Slowly Varying Pipe Flow of Thixotropic Fluids

Andrew I. Croudace
Department of Mathematics and Statistics
University of Strathclyde
Glasgow, Scotland, UK
September 2018

This thesis is submitted to the University of Strathclyde for the degree of Doctor of Philosophy in the Faculty of Science.

This thesis is the result of the author's original research. It has been composed by the author and has not been previously submitted for examination which has led to the award of a degree.

Signed: Date:

To Barry, Edwina, Pamela, and Selwyn

Acknowledgements

I would like to thank the Engineering and Physical Sciences Research Council (EPSRC) for providing funding for my research, training, and conference attendance.

I would also like to thank my supervisors, David Pritchard and Stephen Wilson, for going beyond the call of duty in many aspects of my studies, and for providing their knowledge, experience, and support.

Finally, I would like to thank my friends and family, who have supported me through my tough times, both in and out of university, as well as through their own, and for making my time in Glasgow more rewarding and enjoyable than I could've imagined.

Abstract

In this thesis we study lubrication flows of thixotropic and antithixotropic fluids in two flow problems: unsteady flow in a slowly varying 3D pipe, and oscillating flow in a uniform cylindrical pipe. We consider two fluid models which exhibit interesting non-Newtonian behaviour: the viscous Moore–Mewis–Wagner (MMW) model, and the viscoplastic Houška model.

In Chapters 2–6 we study unsteady thixotropic flow in a slowly varying pipe, in a particular regime in which the thixotropic effects are considered 'weak', with the aim of determining whether we may describe generally the qualitative behaviour of thixotropic fluids in such flows. Previous work by Pritchard et al. [*Journal of Non-Newtonian Fluid Mechanics*, 238: 140–157, 2016] in the related problem of steady 2D channel flow suggests that such a description may be available. After obtaining the governing equations for this problem, we perform a detailed analysis of the flow for the MMW and Houška models, and determine all of the possible behaviours of these models. This analysis shows that the results and physical interpretations of Pritchard et al. are insightful but not complete. We also study the application of an off-the-shelf finite element program to determine the suitability of such programs for studying slowly varying thixotropic flows.

In Chapter 7 we study the similar but simpler problem of unsteady thixotropic pipe flow driven by an oscillating pressure gradient. This problem is simpler than the problem considered in Chapters 2–6, which allows us to explore a wider range of thixotropic behaviours, in which the thixotropic effects range from 'weak' to 'strong'. We are able to describe the full range of thixotropic behaviour using a combination of analytical and numerical methods.

Contents

Chapter 1

Introduction

1.1 Complex fluids

This thesis concerns complex fluids. Fluids may be described as either Newtonian or non-Newtonian, depending on how they deform when stressed. Newtonian fluids are the simplest fluids, which deform at a rate linearly proportional to the stress, where the constant of proportionality in simple shear flow is the viscosity [1]. Of course, no real fluid is perfectly Newtonian, but the behaviour of some, including air and water, is similar enough to Newtonian behaviour for it to be an accurate approximation [1, 2].

In contrast, many common fluids, including various foods, oils, blood, and paints, exhibit non-Newtonian behaviour [2, 3], and are therefore known as non-Newtonian fluids, or complex fluids [4]. Such fluids, for example, may increase or decrease in viscosity when deformed, or may resist flow until a critical stress is reached. In this thesis, we focus on a category of complex fluids called thixotropic fluids, which we will briefly introduce here and discuss in more detail in Section 1.2.

In this introductory chapter, we discuss four types of non-Newtonian behaviour. A fluid may have a viscosity that varies with the rate of deformation. Shear-thinning and shear-thickening fluids decrease and increase in viscosity, respectively, as the rate of deformation increases [2]. Paint is an example of a shear-

thinning fluid, which becomes less viscous when it is being applied, allowing for an even coat, but increases in viscosity after application to reduce dripping [2].

Viscoplastic, or yield-stress fluids are solid under low stresses, but 'yield' and flow like viscous liquids when a sufficiently large stress is applied [2]. A common example is mayonnaise [5], which retains peaks and knife marks rather than flowing to find its level.

Viscoelastic fluids are time-dependent and both stretch like an elastic solid and flow like a viscous fluid under stress [2]. The timescale of the deformation has a significant effect on the behaviour of viscoelastic fluids. When the timescale is long, fluids have a viscous response, but when the timescale is short, as in impacts, the response is elastic [2]. Between these extremes fluids exhibit both viscous and elastic effects. Silly putty is a well-known example of a viscoelastic fluid [6], which flows under gravity when left on a surface, but bounces when dropped from a height. The important difference between flow under gravity and under impact in this example is the timescale: flows under gravity are much slower than impacts. The ratio of the timescale of the flow (or process) and the characteristic timescale of the fluid, which is an intrinsic characteristic of the fluid, is called a Deborah number, and will play and important role in this thesis.

Thixotropic fluids are also time-dependent fluids, and are the focus of this thesis. Thixotropic fluids behave differently depending on how they were deformed in the past, often referred to as the flow history or shear history [7]. An example is ketchup [8], which is a thixotropic shear-thinning fluid: when a bottle of ketchup is shaken, the liquid gradually becomes less viscous, allowing for easy pouring; when the bottle is left to rest, the fluid slowly increases in viscosity, gradually tending towards its original, unshaken viscosity.

Thixotropy is manifested as a time-dependent aspect of the viscous, plastic, or elastic properties of a fluid. In addition to the thixotropic shear-thinning behaviour seen in ketchup, thixotropic shear-thickening behaviour [9], thixotropic viscoplasticity [10, 11], and thixotropic viscoelasticity [11, 12] also exist. We discuss each of these behaviours and the impact of thixotropy on them in more detail in Sections 1.2.2 and 1.2.3.

The prevalence and wide range of behaviours of complex fluids makes understand-

ing them important to many industries, such as the oil industry (see e.g. [13, 14]), and also provides an interesting area of scientific study. Rheology is the science of the deformation and flow of matter [2]. More specifically, in the context of this thesis, it is the study of the relationships between the deformation of a complex fluid and the stress that deforms it.

The rheology of complex fluids is studied experimentally using rheometers, which measure the properties of a sample of fluid [2]. Rheometers may use shear flows, also called 'rheometric' or 'viscometric' flows (e.g. flow between two parallel moving plates) or extensional flows (e.g. stretching a fluid sample between two plates). [4]. Rheometers typically impose either a constant deformation or a constant stress, and provide data on the stress or deformation, respectively [4]. The data obtained is used to identify qualitative phenomena, such as shear-thickening or yield-stress behaviour (see e.g. [15]), and is used to guide the construction and calibration of mathematical models [9, 16, 17], called rheological models, which describe in general terms the relationship between deformation and stress. Rheological models can then be combined with the other governing equations of fluid dynamics to predict the flow of complex fluids in non-rheometric settings [17].

The macroscopic rheological behaviour of complex fluids often depends on the interaction of suspended microscopic particles [3]. In particular, these particles may arrange into larger mesoscopic structures, including flocs [3, 7], which affect the macroscopic behaviour of the fluid. Examples of such mesoscopic structures include entanglements of molecules in polymer solutions [3, 18] and "house-of-cards" arrangements of platelets [19]. Mesoscopic structures often depend on both present and past flow conditions, which yields time-dependent behaviour, including the focus of this thesis — thixotropy [3, 7, 20].

When studying complex fluids, it may or may not be necessary or the desire of the rheologist to know the precise details of all the particle interactions. For example, Swan et al. [21] consider the 'microrheology' of a fluid for which the interactions between individual particles must be known, whereas Hewitt and Balmforth [22] consider the macroscopic behaviour of a fluid, so only the macroscopic effects of the particle interactions are important, rather than the details. In this thesis, we consider fluid models of the latter kind, which assume all particle interactions

may be modelled by a single scalar 'structure parameter' [7].

As well as identifying the rheological properties of a fluid, one may also wish to understand how a particular rheological property affects its flow. For example, in the case of avalanche-like behaviour of rock and mud slides [22], in which a fluid-like material resists flow down an inclined plane under gravity for a time, before catastrophically destructuring and flowing rapidly down the plane, the run-out at the bottom of the slope is important. In the flow of waxy crude oils along pipelines, the complex rheology of oil makes restarting flow after maintenance tricky [23]. The scale of such flows makes them impractical to study experimentally, so studying the effects of various rheological properties theoretically is often advantageous. There are two dominant approaches to studying theoretically how rheological properties affect flow. One builds complexity from simplicity, while the other approach is complex from the outset.

The first approach is to consider rheometric flows. Depending on the particular rheological model used, the governing equations of rheometric flows are often simple enough for analytical and numerical progress to be made towards describing the behaviour [24, 25]. Analytical and numerical simulations may be compared and verified, which provides mutual support and a solid grounding for the numerical model so that more complex behaviour not accessible by analytical methods may be studied [26, 27]. While the simplicity of rheometric flows has advantages over flows in complicated geometries, it also has the disadvantage of being rather idealised compared to many practical situations. In addition, to observe complex fluid behaviours, some degree of complexity in the flow is required, such as start-up flows [28] or non-uniform geometries [29], for example.

The second approach is to consider complex geometries motivated by particular practical situations, for instance flow in extrusion dies [30] or mixing tanks [31]. While some analytical simplification of the set-up may be possible [21, 32, 33, 34, 35], such flows are typically too complex for much analytical progress to be made, so numerical simulations are usually the only way to approach them [36, 37]. If analytical progress is unlikely, then the rheological models employed do not need to be particularly simple, and their complexity is limited by the computational power available. Highly complex rheological models typically give

rise to a wealth of rheological behaviour, which often comes at the expense of a limited understanding of how each component of the model affects the flow, which decreases its practical usefulness.

It is clear there is a need for studies which lie somewhere between these two extremes and which inherit some of the advantages of both: simplicity from the former and practicality from the latter. In particular, there is a need for studies which are simple enough to clearly highlight the effect of a rheological property on a flow and to determine whether a particular aspect of a flow is generic, both of which require a detailed analysis of the flow. On the other hand, we wish to use this approach to study flows complex enough to yield non-trivial results which may be used as a benchmark for numerical models.

Lubrication flows, also called "slowly varying" or "slender" flows, provide an opportunity for such studies. In these flows, the typical lengthscale of variation in one dimension is significantly smaller than the lengthscales in the other dimensions [38]. Lubrication theory was first formulated by Reynolds [39] to model the behaviour of lubricating Newtonian fluid in bearings, and yields a significant simplification of the governing equations of the set-up. Lubrication theory has been applied to a wide range of complex fluids, including viscous non-Newtonian fluids [24, 40], viscoplastic fluids [41, 42, 43, 44, 45], and thixotropic fluids [29, 46], and, in particular, to the free-surface flows of muds and lavas [47, 48]. It has also been used to simplify complex fluid flows before they are studied numerically [33, 34]. Substantial reviews on slowly varying flows have been provided by Oron et al. [49] and more recently by Craster and Matar [50]. Both reviews discuss mainly slowly varying flows of Newtonian fluids, and focus on free-surface flows, which is indicative of the comparatively limited research in the areas of complex fluids and constrained flows. We discuss lubrication theory in more detail in Section 1.3.

In this thesis, we build on the asymptotic approach for steady 2D thixotropic lubrication flows developed by Pritchard et al. [29] in two important ways. We extend the approach to include unsteady flows, which are often an important feature of complex flow set-ups [28, 46]. In addition, we extend the approach to model axisymmetric geometries, with the particular aim of studying unsteady

slowly varying pipe flows, which arise in several industrial processes which use thixotropic fluids, including liquid foods [10, 51, 52], drilling muds, and oils [23, 46, 53]. We obtain a number of theoretical results using analytical methods which provide a physical insight into the mechanisms of the flow, and which we use to determine whether generic behaviour exists, and whether artefacts of widely used rheological models play a significant role.

Following the analytical investigation of the flow, we study the application of a standard numerical method (namely finite-element methods (FEM) as implemented in the commercial package COMSOL [54]) to such problems. We use our analytical results to provide a stern benchmarking test for the numerical method. This initial numerical testing brings to light the challenges of studying thixotropic lubrication flows numerically, and provides some guidance for future attempts in the area.

Finally, we study the simpler but related unsteady set-up of periodically forced, or oscillating, flow in a uniform pipe. The flow in this case provides further insight into the unsteady flow of complex fluids, a substantial amount of which can be obtained through analytical methods. These results provide new benchmark solutions and important insights into the physical mechanisms of thixotropic flow.

1.2 Rheological models

In this section, we introduce rheological models, which are constructed with the aim of modelling one or more aspects of fluid behaviour. Naturally, owing to the wide range of behaviours of fluids, there are numerous models of varying complexity, accuracy, and generality. We cover these in approximate order of complexity from Newtonian fluids to complex fluids with multiple physical properties and modelling approaches.

The flow of an incompressible (constant-density) fluid is governed by the Navier–Stokes equation (see [38]), which is given by

$$\rho\frac{\mathrm{D}\mathbf{u}}{\mathrm{D}t} = -\nabla p + \rho\mathbf{g} + \nabla\cdot\underline{\underline{\tau}}, \tag{1.2.1}$$

where ρ is the density, $\mathrm{D}(\cdot)/\mathrm{D}t = \partial(\cdot)/\partial t + \mathbf{u}\cdot\nabla(\cdot)$ is the material derivative, $\mathbf{u}$ is the velocity, p is the pressure, $\mathbf{g}$ is gravity, and $\underline{\underline{\tau}}$ is the stress tensor, and where the fluid satisfies the incompressibility condition

$$\nabla \cdot \mathbf{u} = 0. \tag{1.2.2}$$

The stress experienced by a fluid element is given by the stress tensor $\underline{\underline{\tau}}$, which depends on the shear-rate tensor e_{ij}, which describes the way the fluid deforms as it flows. In this thesis, we are concerned primarily with fluid flow along cylindrical pipes, so we write the shear-rate tensor in cylindrical co-ordinates (see [38]) as

$$e_{ij} = \begin{bmatrix} 2\dfrac{\partial u}{\partial r} & r\dfrac{\partial}{\partial r}\left(\dfrac{v}{r}\right) + \dfrac{1}{r}\dfrac{\partial u}{\partial \theta} & \dfrac{\partial u}{\partial z} + \dfrac{\partial w}{\partial r} \\ r\dfrac{\partial}{\partial r}\left(\dfrac{v}{r}\right) + \dfrac{1}{r}\dfrac{\partial u}{\partial \theta} & 2\left(\dfrac{1}{r}\dfrac{\partial v}{\partial \theta} + \dfrac{u}{r}\right) & \dfrac{1}{r}\dfrac{\partial w}{\partial \theta} + \dfrac{\partial v}{\partial z} \\ \dfrac{\partial u}{\partial z} + \dfrac{\partial w}{\partial r} & \dfrac{1}{r}\dfrac{\partial w}{\partial \theta} + \dfrac{\partial v}{\partial z} & 2\dfrac{\partial w}{\partial z} \end{bmatrix}, \tag{1.2.3}$$

where r, θ, and z are the radial, azimuthal, and axial co-ordinates, respectively, with the respective velocities u, v, and w. We define the total shear rate $\dot{\gamma}$ (where γ is the shear) and total stress τ, using Einstein summation notation, as

$$\dot{\gamma} = \sqrt{\frac{1}{2}e_{ij}e_{ij}} \quad \text{and} \quad \tau = \sqrt{\frac{1}{2}\tau_{ij}\tau_{ij}}, \tag{1.2.4}$$

respectively, where τ_{ij} are elements of $\underline{\underline{\tau}}$.

An integral part of any rheological model is the constitutive relation (also known as the constitutive equation), which describes the relationship between the shear rate and the shear stress. We present a range of constitutive relations in the following sections.

1.2.1 Newtonian fluid

The simplest and most familiar model of fluid behaviour is the Newtonian model. In a Newtonian fluid, the stress experienced by a fluid element is proportional to

the shear rate, where the constant of proportionality is the viscosity η (though μ is also commonly used to denote viscosity). The constitutive relation for a Newtonian fluid is therefore given by

$$\tau_{ij} = \eta e_{ij}. \tag{1.2.5}$$

Deviations from the behaviour described by (1.2.5) are called non-Newtonian behaviour, which is the subject of the next section.

1.2.2 Non-thixotropic non-Newtonian fluids

A wide variety of rheological models exist, designed to capture different rheological behaviour. We discuss purely viscous behaviour in Section 1.2.2.1, viscoplasticity in Section 1.2.2.2, viscoelasticity in Section 1.2.2.3. We discuss thixotropic behaviour in Section 1.2.3 and present a range of approaches to modelling it in Section 1.2.4.

1.2.2.1 Purely viscous behaviour

Purely viscous non-Newtonian fluids differ from Newtonian fluids, presented in Section 1.2.1, in one crucial way: the viscosity relating the shear stress and the shear-rate tensor varies with the shear rate or other factors, i.e. η in (1.2.5) is not constant. A class of such fluids are the generalised Newtonian fluids, whose constitutive relations have the form

$$\tau_{ij} = \eta(\dot{\gamma}) e_{ij}, \tag{1.2.6}$$

where the viscosity $\eta(\dot{\gamma})$ depends on the total shear rate. (There are some models similar to generalised Newtonian models which have a constitutive relation of the form shown (1.2.6) but have non-monotonic stress–strain relations, and so are not generalised Newtonian fluids. We discuss some examples of these models in Sections 1.2.2.2 and 1.2.4.2.)

Table 1.1 shows examples of models for generalised Newtonian fluids, with the

Model	$\eta(\dot{\gamma})$	Refs
Power-law model	$\eta_0 \dot{\gamma}^{n-1}$	[24, 39]
Carreau model	$\eta_\infty + (\eta_0 - \eta_\infty)\left(1 + (\lambda\dot{\gamma})^2\right)^{(n-1)/2}$	[2, 24]
Ellis model	$\eta_0 \left(1 + \lvert\tau/\tau_{1/2}\rvert^{\alpha-1}\right)^{-1}$	[2, 24]
Cross model	$\eta_\infty + (\eta_0 - \eta_\infty)\left(1 + (\lambda\dot{\gamma})^{1-n}\right)^{-1}$	[2]

Table 1.1: Examples of common models for generalised Newtonian fluids.

corresponding forms of $\eta(\dot{\gamma})$. The various parameters and exponents in these models are chosen to model a range of viscous behaviours. In particular, η_0 and η_∞ are the viscosities at zero and infinite shear rate, respectively, λ is a constant parameter with the dimension of time, $\tau_{1/2}$ is the shear stress at which the viscosity is $\eta_0/2$, and α is a dimensionless parameter.

In the power-law model, the exponent n describes the tendency of a fluid to become more or less viscous with varying shear rate. When $n < 1$, the viscosity decreases with increasing shear, known as shear-thinning (or pseudoplastic) behaviour. When $n > 1$, the viscosity increases with increasing shear, known as shear-thickening (or dilatant) behaviour. When $n = 1$, the viscosity no longer depends on the shear rate, so we recover Newtonian behaviour; such model simplifications are common in many areas of rheological modelling. Figure 1.1 shows the relationship between the shear rate $\dot{\gamma}$ and the shear stress τ for the power-law model, for various values of n.

Each of the models in Table 1.1 has strengths and weaknesses. For example, the power-law model, which arises later in this thesis, has the advantage of being very simple and is therefore widely used, but a significant drawback is that it yields physically unrealistic behaviour in low-shear and high-shear conditions. In contrast, the Carreau model may be preferable as it yields physically realistic behaviour in all flow conditions, but its relative complexity, as noted by Myers [24], means that even for simple set-ups, such as free-surface flow down an inclined plane, it may be difficult to make significant analytical progress. Such limitations should be taken into account when a rheological model is chosen for a flow set-up.

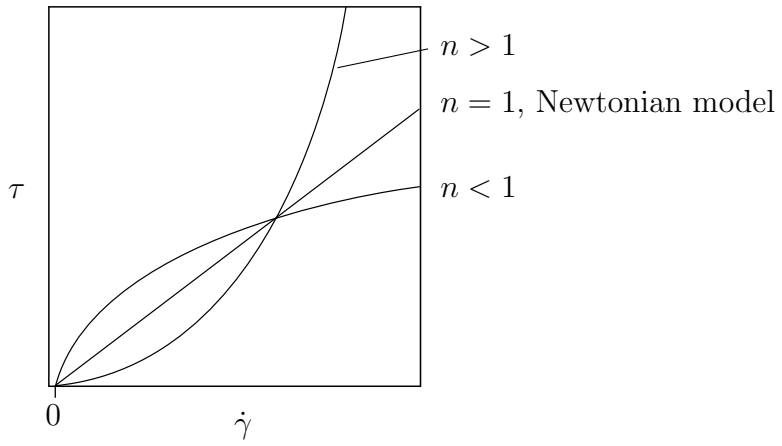

Figure 1.1: Shear-stress–shear-rate curves for the power-law model, which contains the Newtonian model as a special case when $n = 1$. In this model, $n < 1$ corresponds to shear-thinning behaviour and $n > 1$ corresponds to shear-thickening behaviour.

1.2.2.2 Purely viscoplastic behaviour

In addition to viscosity, many fluids also exhibit plasticity, and are therefore referred to as viscoplastic (VP) fluids. Viscoplasticity, also known as yield-stress behaviour, is the property of a fluid of resisting shear under increasing stress until a critical stress is reached, called the yield stress, denoted τ_{y}, after which the fluid 'yields' and flows like a viscous fluid [19]. Viscoplastic fluids arise in both industrial settings, including drilling muds and crude oil, and in everyday settings, such as mayonnaise [51].

Many VP rheologies have a constitutive relation of the form

$$\begin{cases} \tau = \left(\eta(\dot{\gamma}) + \dfrac{\tau_{\mathrm{y}}}{\dot{\gamma}}\right) e_{ij} & \text{when} \quad \tau \geq \tau_{\mathrm{y}}, \\ \dot{\gamma} = 0 & \text{otherwise}, \end{cases} \tag{1.2.7}$$

where the viscosity $\eta(\dot{\gamma})$ may be Newtonian or generalised Newtonian. The simplest VP model, and one of the most widely used, is the Bingham model (see [19]), in which the viscosity is constant. In the Bingham model, the fluid remains rigid when the applied stress is below the yield stress, but flows with constant

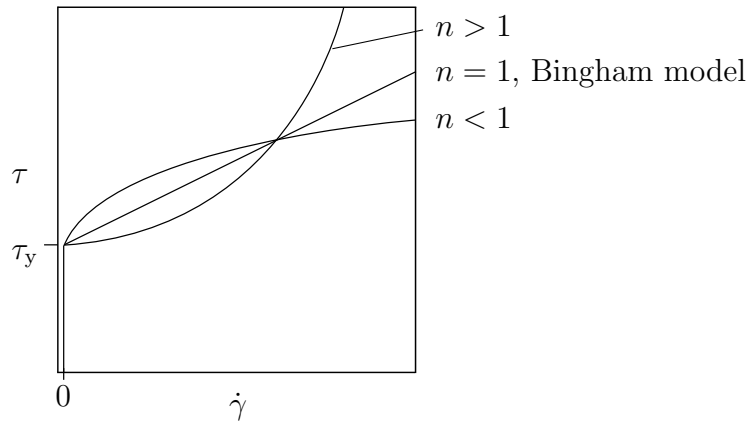

Figure 1.2: Shear-stress–shear-rate curves for the Herschel–Bulkley model, which contains the Bingham model as a special case when $n = 1$. In this model, $n < 1$ corresponds to shear-thinning post-yield behaviour and $n > 1$ corresponds to shear-thickening post-yield behaviour. The yield stress for the Herschel–Bulkley model is denoted τ_y.

viscosity like a Newtonian fluid when the yield stress is exceeded, as in (1.2.5). A slightly more complex model, and an example which uses a generalised Newtonian viscosity, is the Herschel–Bulkley model (see [19]), in which the fluid exhibits power-law behaviour post-yield. Figure 1.2 shows the shear-stress–shear-rate relationship for a Bingham fluid ($n = 1$) and two Herschel–Bulkley fluids, one shear thinning ($n < 1$) and one shear thickening ($n > 1$).

True viscoplasticity is exhibited when the shear rate in a fluid remains zero until the yield stress is reached, after which the fluid yields and flows like a purely viscous fluid, as described by the Bingham and Herschel–Bulkley models. When the stress is below the yield stress, the viscosity diverges, the fluid solidifies and shearing ceases. The debate on the existence of true yield-stress behaviour is ongoing — many theoreticians and experimentalists continue to use the simple and traditional VP models (e.g. Balmforth and Craster [41] and Frigaard and Ryan [43]), and others are moving away from these models in favour of a more complete and physics-based approach to viscoplasticity (e.g. Coussot et al. [55]). In many viscoplastic fluids, some small 'creeping' flow is observed experimentally when the fluid is unyielded. Many (e.g. Barnes and Walters [56], Renardy [57]) theorise that

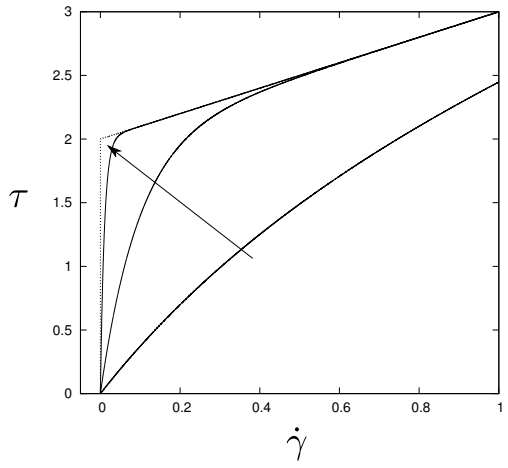

Figure 1.3: Stress–shear-rate relationship for the Papanastasiou-regularised Bingham model (solid lines) for examples for the regularisation parameter $(1, 10, 100)$, and for the unregularised Bingham model (dotted line). The arrow shows the direction of increasing regularisation parameter; as this parameter becomes large, the Papanastasiou model approximates the true Bingham model more and more closely.

true plasticity does not exist, and that yield-stress behaviour is a myth. Rather, as supported by experiments (e.g. Coussot et al. [55]), proponents of yield-stress as a myth consider viscoplasticity to be simply purely viscous behaviour in which the viscosity rapidly decreases when the 'yield stress' is exceeded.

One approach to allow the continued use of the traditional VP models is to regularise them. In the context of viscoplasticity, model regularisation slightly modifies a model so that the fluid is not completely rigid for stresses below the yield stress. As an illustrative example, Papanastasiou [58] presents an example of a regularisation for the Bingham model. Regularisation is often considered in the limiting case of minimal divergence from the original model. In the case of the Papanastasiou model, increasing the regularisation parameter yields behaviour which more and more closely approximates the behaviour of the unregularised Bingham model. Figure 1.3 shows how regularisation affects the stress–shear-rate curve.

Another approach to including creeping behaviour in models is to use a model

with two characteristic viscosities, a low-shear viscosity and a high-shear viscosity (the Carreau, Ellis, and Cross models given in Table 1.1 are examples of this approach), and by assuming the transition from one viscosity to the other occurs over a small change in the shear rate. Such models are constructed so that for low stresses, the fluid flows with the higher viscosity, which is similar to plug-like flow. When the stress reaches a critical stress, equivalent to a yield stress, the viscosity decreases to the lower viscosity, which is equivalent to a yielded fluid. In such a model, there is a 1-to-1 correspondence between the shear rate and the shear stress, and the high-viscosity (unyielded) fluid may deform.

1.2.2.3 Purely viscoelastic behaviour

In addition to viscosity, many fluids exhibit elasticity, and are therefore referred to as viscoelastic (VE) fluids. In everyday settings, viscoelasticity is most noticeable in fluids that have a "springy" or "bouncy" quality, such as silly putty [6]. More formally, elasticity and viscosity are the properties of a fluid in which, under strain, the stresses experienced by a fluid element due to elasticity and viscosity depend on the strain γ and the rate of strain $\dot{\gamma}$, respectively [59]. These stresses are referred to as the elastic and viscous stresses.

The viscous and elastic stresses are analogous to the forces involved in deforming dashpots and extending springs, respectively, and so provide useful mechanical analogies for visualising viscoelastic behaviour [59]. Springs and dashpots can be combined in various ways to construct models of fluids with particular behaviours. The two simplest combinations are given by the Maxwell model, which contains a spring and dashpot connected in series as shown in Figure 1.4(a), and the Kelvin–Voigt model, which contains a spring and dashpot connected in parallel as shown in Figure 1.4(b).

In the Maxwell model, both the spring and the dashpot experience the applied stress τ fully, but they deform independently, with deformations γ_e and γ_v, respectively. In the Kelvin–Voigt model, the applied stress is shared by the spring and the dashpot, with stresses τ_e and τ_v, respectively, but as these components are connected in parallel, they experience the same deformation γ. We may write

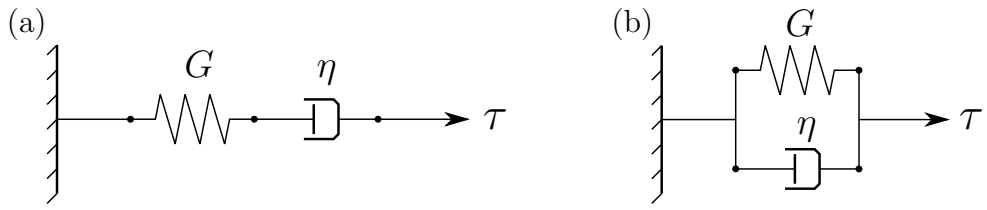

Figure 1.4: Mechanical analogies for (a) the Maxwell model and (b) the Kelvin–Voigt model. The spring has elastic modulus G and the dashpot has viscosity η.

the total stress τ and total strain γ in each of these models as

$$\text{Maxwell:} \qquad \tau = \tau_{\mathrm{e}} = \tau_{\mathrm{v}} \quad \text{and} \quad \gamma = \gamma_{\mathrm{e}} + \gamma_{\mathrm{v}}, \tag{1.2.8}$$

$$\text{Kelvin–Voigt:} \qquad \tau = \tau_{\mathrm{e}} + \tau_{\mathrm{v}} \quad \text{and} \quad \gamma = \gamma_{\mathrm{e}} = \gamma_{\mathrm{v}}. \tag{1.2.9}$$

As the elastic and viscous stresses are proportional to the strain and the rate of strain, respectively, we may write

$$\tau_{\mathrm{e}} = G\gamma_{\mathrm{e}} \quad \text{and} \quad \tau_{\mathrm{v}} = \eta\dot{\gamma}_{\mathrm{v}}, \tag{1.2.10}$$

respectively, where G is the elastic modulus and η is the viscosity. So the stress–strain relations for the Maxwell and Kelvin–Voigt models are given by

$$\frac{\dot{\tau}}{G} + \frac{\tau}{\eta} = \dot{\gamma} \quad \text{and} \quad \tau = G\gamma + \eta\dot{\gamma}, \tag{1.2.11}$$

respectively.

A notable feature of VE fluids is the presence of more than one timescale over which the fluid behaves. Over short timescales, under sudden impact or rapid shearing for example, elastic effects dominate over viscous effects, so a VE fluid exhibits behaviour similar to rubber. Over long timescales, as when a lump of VE fluid is left to slump under gravity, viscous effects dominate over elastic effects and VE fluids behave similarly to purely viscous fluids.

While VE effects have an absolute timescale which depends on the fluid, it is more useful to consider the timescale of viscoelasticity compared to the timescale of the fluid flow, referred to as the 'process'. When modelling the flow of time-

dependent fluids, one often obtains a dimensionless Deborah number, which is the ratio of the timescale of fluid to the timescale of the process. On one hand, if the timescale of the process is much longer than the timescale of the fluid, for example in the slumping of a small piece of highly viscous VE fluid under gravity, the Deborah number is small and the time-dependent effects do not greatly affect the flow. On the other hand, if the timescale of the process is shorter than the timescale of the fluid, for example in a quickly oscillating flow of a VE fluid, the Deborah number is large and the time-dependence of the fluid has a significant effect on the flow.

1.2.3 Thixotropic behaviour

In all the models discussed in the previous sections, the properties of the fluid are assumed to respond immediately to changes in the stress acting on the fluid. In many fluids these properties are subject to variation with the duration and history of stresses in the fluid, which is called thixotropy.

There is no universally agreed definition of thixotropy, though Mewis and Wagner [7] present three characteristics which essentially define thixotropic behaviour, which we quote here exactly: (i) it is based on viscosity; (ii) it implies a time-dependent decrease of the viscosity induced by flow; (iii) the effect is reversible when the flow is decreased or arrested. Here, 'based on viscosity' implies that thixotropy does not affect elasticity or plasticity, or any other fluid property aside from viscosity.

Whilst this definition of thixotropy essentially covers the more common time-dependent decrease of viscosity (time-dependent shear-thinning behaviour), less commonly fluids (e.g. carbon black suspensions [9]) exhibit a time-dependent increase in viscosity, usually referred to as *antithixotropy* or rheopexy. (Mewis and Wagner [7] define rheopexy as a slightly different phenomenon to antithixotropy, though such a distinction is not necessary here.) For convenience throughout this thesis, we refer to both time-dependent shear-thinning and time-dependent shear-thickening behaviour as 'thixotropy', though where further clarification is necessary, we use 'thixotropy' and 'antithixotropy' accordingly, which will be

made clear by the context. Purely viscous thixotropic fluids, whether thixotropic or antithixotropic, are also referred to as 'ideal' thixotropic fluids, following the definition of Larson [60].

1.2.3.1 Non-ideal thixotropic behaviour

In addition to viscosity, the effects of elasticity and plasticity may also be time-dependent in a similar way to purely viscous thixotropy. For example, when a VP fluid is sheared above its yield stress for an extended time, the yield stress may decrease so that, following a cessation of shearing and subsequent re-shearing, the fluid yields at a lower stress. This behaviour creates problems when measuring the yield stress experimentally [61]. Such effects are occasionally referred to as the 'ageing' of fluid, and often arise in the context of thixotropy over long timescales.

Many everyday fluids exhibit a combination of thixotropic, elastic, viscous and plastic behaviours, depending on the flow conditions. For example, at small and slow rates of deformation, the behaviour of mayonnaise is characteristically elastic [51], though for larger and quicker deformations the behaviour is viscous shear thinning. So mayonnaise could be described as an elastoviscoplastic (EVP) material in general, with specific behaviours arising in varying flow conditions.

The full range of behaviours of thixoelastoviscoplastic (TEVP) fluids [12] are difficult to model accurately in their entirety, so rheological models tend to focus on a single or a few behaviours in a specific environment, whilst neglecting other, relatively weak behaviours. Using again the example of mayonnaise, one rheological model could describe the purely elastic response of the fluid and another could describe the viscoplastic response, which would be confined to small deformations and large deformations, respectively. As such, navigating the TEVP space of models in search of an appropriate model for an experiment, for example, is not a task with a clear approach. However, a recent conceptual attempt has been made by Ewoldt and McKinley [11] to construct a map of TEVP behaviour by extending the map of elastoviscous behaviour constructed by Pipkin [62].

1.2.4 Thixotropic models

It is generally agreed that there are three methods for modelling thixotropy mathematically [3, 7]. A popular approach among theoreticians is the structure parameter-based approach, which is not concerned with the details of the build-up and breakdown of the mesoscopic structure in the fluid. Instead, the instantaneous state of the structure is represented by a single scalar variable, usually denoted by λ and called the structure parameter (not to be confused with the timescale of a fluid, occasionally denoted the same way), which is governed by an appropriate evolution equation. The local value of λ then may affect the viscosity, yield stress, and elastic modulus of the fluid.

Another approach is the viscoelasticity-based approach, examples of which are presented by Renardy and co-workers [27, 57, 63]. Models of this form do not use a structure parameter, rather they focus on thixotropic behaviour in the form of ageing, which arises in a limiting case of VE behaviour, and can exhibit complex fluid behaviour such as shear banding and hysteresis. Finally, the least commonly used approach is to model the micro-physics of suspended particles and their interactions directly. Naturally, these three approaches to modelling thixotropy vary in accuracy, simplicity, and applicability; we discuss each of them in the following sections.

1.2.4.1 Manifestations of thixotropy

Thixotropy may have a 'strong' or a 'weak' effect on the behaviour of the fluid. Thixotropic effects occur over a timescale which depends on the fluid, a relevant example of which is the timescale over which suspended particles rearrange under shearing. It is therefore more useful to consider the timescale of thixotropy compared to the characteristic timescale of a process, expressed mathematically as a dimensionless Deborah number, as for the case of VE fluids, discussed in Section 1.2.2.3.

Whilst thixotropy is a time-dependent effect, the flow of a thixotropic fluid need not be unsteady for thixotropy to affect the flow. For example, suspended particles in a fluid may be advected to a region of higher or lower shear rate. For this

reason, we identify two processes, with independent timescales. The first we term the 'temporal effect of thixotropy' or, for brevity, 'temporal thixotropy', which has an associated temporal Deborah number. In temporal thixotropy, the process which builds up and breaks down the fluid is the time-dependence of the flow, which may arise, for example, from a time-dependent pressure gradient. The second we term the 'advective effect of thixotropy' or 'advective thixotropy', which has an associated advective Deborah number. In advective thixotropy, the process which builds up and breaks down the fluid is the advection of the structure of the fluid to regions with higher or lower shear rates. Whilst we have referred to two kinds of thixotropy, a thixotropic fluid has only one thixotropic property (we do not consider two independent fluid structures with separate timescales), so the temporal and advective effects of thixotropy are manifestations of thixotropy in the context of a particular process.

1.2.4.2 Structure-parameter-based models

The structure parameter λ is bounded below by $\lambda = 0$, which represents a completely destructured state, but may or may not be bounded above; in either case the maximum value of λ represents a fully structured state. Depending on the shear rate and the current state of the structure, the structure of the fluid evolves according to a structure evolution equation of the form

$$\frac{\mathrm{D}\lambda}{\mathrm{D}t} = f(\dot{\gamma}, \lambda), \tag{1.2.12}$$

where $f(\dot{\gamma}, \lambda)$ describes the dependence of the evolution of the structure on the shear rate and the current state of the structure.

A variety of choices of $f(\dot{\gamma}, \lambda)$ made by previous authors are extensively reviewed by Mewis and Wagner [7], who propose a general form of $f(\dot{\gamma}, \lambda)$, given by

$$f(\dot{\gamma}, \lambda) = -k_1 \dot{\gamma}^a \lambda^b + k_2 \dot{\gamma}^c (1 - \lambda)^d, \tag{1.2.13}$$

where the parameters a, b, c, and d are non-negative, and k_1 and k_2 are positive breakdown and build-up rate constants, respectively. This function (1.2.13) con-

Model	Breakdown	Build-up	Refs
Mujumbar et al.	$k_1\dot{\gamma}\lambda$	$k_2(1-\lambda)$	[64]
Pinder	$k_1\lambda^2$	k_2	[65]
Houška model	$k_1\dot{\gamma}^a\lambda$	$k_2(1-\lambda)$	[10, 66]
Coussot model	$k_1\dot{\gamma}\lambda$	k_2	[55]
Billingham & Ferguson*	$k_1\dot{\gamma}\lambda$	$k_2(1-\lambda)$	[67]

Table 1.2: Examples of models which use Mewis and Wagner's structure equation (1.2.13). *Billingham and Ferguson [67] add a diffusive term to their structure equation.

tains a breakdown term $k_1\dot{\gamma}^a\lambda^b$, which vanishes when $\lambda = 0$, i.e. when the fluid is completely destructured. This function also contains a build-up term $k_2\dot{\gamma}^c(1-\lambda)^d$, which adds Brownian restructuring when $c = 0$ and shear-driven restructuring when $c > 0$; in addition, when $d > 0$ the structure is bounded above by $\lambda = 1$, but when $d = 0$, λ may grow without bound.

Table 1.2 shows examples of several models used by previous authors which are special cases of Mewis and Wagner's structure evolution equation (1.2.13). We note that the model of Billingham and Ferguson [67] adds a term to (1.2.12) representing the diffusion of structure. It is therefore not a true special case of Mewis and Wagner's structure evolution equation, but is cited here as a closely related approach.

In purely viscous structure-parameter models, the constitutive relation is assumed to be generalised Newtonian in form (see (1.2.6)), except that the viscosity is modified to depend on the structure:

$$\tau_{ij} = \eta(\dot{\gamma}, \lambda)e_{ij}. \tag{1.2.14}$$

Some models incorporate a structure parameter to model viscoplastic behaviour, including the Houška model [10, 66]. In such models, the yield-stress term is modified to depend on the structure. By allowing the yield stress to depend on the structure, the phenomenon of ageing is incorporated. Structure parameter models are also used to model viscoelastic behaviour, an example of which is the Dullaert and Mewis model [68].

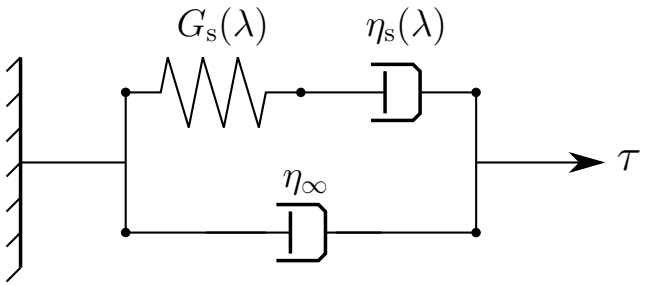

Figure 1.5: Mechanical analogy of the TEVP components of de Souza Mendes [70, 71]. In the Maxwell element (cf. Figure 1.4), the elastic modulus G_s and the structural viscosity η_s depend on the structure parameter λ. The additional viscous element η_∞, connected in parallel to the Maxwell element, is the infinite shear-rate viscosity.

A series of models by de Souza Mendes and co-workers [69, 70, 71] model both viscoplasticity and viscoelasticity, or elastoviscoplasticity, in the framework of structure-based thixotropy, yielding a so-called thixoelastoviscoplastic (TEVP) model. These models are modifications and extensions of the viscoelastic Maxwell model. The initial modification by de Souza Mendes [69] consists of a Maxwell element in which the elastic modulus and the viscosity depend on a structure parameter λ, which itself evolves according to a structure evolution equation. This model was extended by de Souza Mendes [70] to include an additional viscosity term not dependent on the structure parameter, which is shown to improve the ability of the model to predict certain experimental results. In the mechanical analogy, this additional dashpot is connected in parallel to the Maxwell element, as shown in Figure 1.5, with constant viscosity η_∞. Thixotropy is directly incorporated into these models via a structure evolution equation of the form

$$\frac{\mathrm{d}\lambda}{\mathrm{d}t} = \frac{1}{t_{\mathrm{eq}}} g(\lambda, \tau), \tag{1.2.15}$$

where $g(\lambda, \tau)$ contains the build-up and breakdown terms, which depend on the structure λ and the stress τ. The term t_{eq} is the equilibrium time, the characteristic timescale of the change of λ. We note that breakdown is driven by stress, which is a departure from the more familiar shear-driven structure build-up and

breakdown rates (cf. (1.2.12)), such as those in the review by Mewis and Wagner [7]. We note also that (1.2.15) contains only the time-derivative of the structure (rather than the full material derivative, as in (1.2.12)), so the equilibrium time t_{eq} represents the strength of temporal thixotropy. As mentioned by de Souza Mendes [70], a further addition could be made to the models discussed above by using the full material derivative of the structure (as done by Oishi et al. [36]), which would introduce advective thixotropy, in addition to temporal thixotropy.

Hewitt and Balmforth [22] constructed a structure-parameter model to study the thixoviscoplastic behaviour observed in avalanche flows by Coussot and co-workers [37, 55]. They were also able to model the viscosity bifurcation observed by [72], which occurs in thixoviscoplastic (TVP) fluids. Below the yield stress, TVP fluids have a high viscosity and the structure is said to be 'jammed'. When a TVP fluid yields under stress, the fluid destructures and the viscosity decreases significantly, and due to thixotropy the yield stress also decreases. When the fluid is allowed to rest, the structure rebuilds and the viscosity begins to increase. Once shearing begins again, the behaviour of the fluid depends on how long the fluid was allowed to rest between periods of shearing. If the rest time is short, the structure breaks down again and the viscosity decreases, but if the rest time is long enough, the structure rebuilds to a jammed state. So depending on the rest time, a TVP fluid may behave drastically differently for only a small difference in the applied stress, if the applied stress is similar to the yield stress of the fluid.

Hewitt and Balmforth construct a variation of a generalised Newtonian, structure-parameter-based model, but unlike other similar models, they consider the limiting case of instantaneous structure-parameter adjustment, and therefore instantaneous viscosity adjustment, i.e. $f(\dot{\gamma}, \lambda) = 0$ in (1.2.12). In this limit, their model defines a non-monotonic shear-stress–shear-rate curve, so that the stress τ may or may not define a unique shear-rate $\dot{\gamma}$. In fact, the value of $\dot{\gamma}$ for a given τ depends on the shear history of the fluid. For a fluid in a fully structured and rigid state, as the stress increases the viscosity is high and the shear rate is low until τ reaches a critical value at which the fluid suddenly yields, the viscosity decreases and the shear rate increases. This critical stress may be likened to the yield stress of VP fluids. When the stress decreases, the now destructured fluid continues to flow, even for stresses lower than the original critical stress, until

a second lower critical stress is reached at which point the fluid becomes rigid and the shear rate decreases to zero. This change in the apparent yield stress, and the resulting hysteretic behaviour, is the main way thixotropy arises in the model of Hewitt and Balmforth [22], who refer to the 'jumping' up and down between branches of the stress–shear-rate curve as a viscosity bifurcation. As noted by Hewitt and Balmforth [22], this definition differs slightly from that presented by Coussot et al. [72], which only applies to the initial 'yielding', and not the 'unyielding', of the fluid.

Hewitt and Balmforth [22] improve the flexibility of their model by including an ageing effect via a constant ageing-time parameter λ_0, which affects the yield stress of the fluid. This ageing effect adds a very strongly thixotropic effect, in which the typical timescale of structure adjustment is much longer than the typical timescale of the flow, hence λ_0 may be assumed to be constant. One way to extend their model to study more complex thixotropic behaviour would be to include structure-parameter adjustment over a short timescale, i.e. to consider the case where $f(\dot{\gamma}, \lambda) \neq 0$. Another would be to consider the case where the ageing parameter λ_0 is not constant. These extensions would allow one to study complex thixotropic behaviour over multiple timescales.

1.2.4.3 Viscoelasticity-based models

For many of those who study and model thixotropy, the explicit inclusion of thixotropy via a structure parameter assumes thixotropy is a fundamental property of a fluid, in the same way plasticity or elasticity is. An alternative approach used by Renardy and co-workers eliminates the need for a structure parameter [57, 63], and suggests that thixotropy arises naturally from a combination of viscous, plastic, and elastic effects, without the need for its deliberate inclusion. A similar line of thought is promoted by some experimental rheologists, who note the difficulty of using structure-parameter models with experiments.

Following Barnes and Walters [56], Renardy [57] described true yield-stress behaviour as a myth, citing significant disagreement between experimental yield-stress behaviour and the behaviour predicted by yield-stress rheological models. These disagreements mainly stem from a yield stress that depends on the shear

history of the fluid, which leads to behaviour including stress–strain hysteresis, stress overshoots, and fast and slow yielding. Thixotropy also arises in the form of the Mullins effect — the dependence of the elastic response of a fluid on the history of the strain applied to the fluid [73]. In particular, the slow yielding and unyielding of fluid means that fluid prestrained above the yield stress remains unyielded for an extended time after the stress is removed. This complex yield-stress behaviour implies that yield-stress fluids do not have a definitive yield stress, and so there is no 'true' yield-stress behaviour.

Renardy [57] constructs a model which exhibits complex yield-stress behaviour in a particular limiting case of a viscoelastic model. He draws an analogy with his model to the yield-stress behaviour of the viscoplastic Bingham model that arises as a limiting case of a regularised yield-stress model, referencing the model of Papanastasiou [58] in particular (discussed in Section 1.2.2.2). Unlike the TEVP models of de Souza Mendes [69, 70, 71], and indeed a significant proportion of other thixotropic models, Renardy avoids the need for a phenomenological structure parameter.

The model constructed by Renardy is a modification of the Partially Extending strand Convection (PEC) model originally described by Larson [74], in which the shear stress is a non-monotonic function of the shear rate. In the PEC model, in qualitative terms, as the shear rate increases, the shear stress increases to a maximum, then decreases to zero as the shear rate becomes large. A sketch of the flow curve of the PEC model is shown as a dotted line in Figure 1.6. For large relaxation times, the shear rate at which the shear stress is a maximum is low, tending to zero in the limit of large relaxation times. In this limit, the maximum in the flow curve resembles an apparent yield stress which, for a fluid at rest, must be overcome to initiate flow. Renardy modifies the PEC model so that the shear stress has two components. The first of these components is a modification of the elastic component of the PEC model, which provides the non-monotonicity of the shear stress–shear rate relation. Renardy generalises this component so that the shear stress tends to τ_{PECR}, a non-negative value, as the shear rate becomes large, forming the PEC–Renardy (PECR) model, shown as a dashed line in Figure 1.6. The second component is a Newtonian component, so that, post-yielding, the shear stress increases linearly with the shear rate, forming

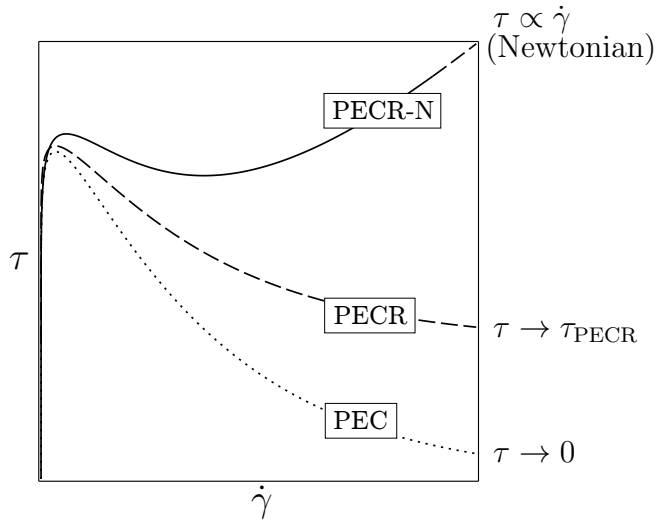

Figure 1.6: Shear stress–shear rate curves for the PEC (dotted), PECR (dashed), and PECR-N (solid) models. In the PEC model, $\tau \to 0$ as $\dot{\gamma} \to \infty$; in the PECR model, $\tau \to \tau_{\mathrm{PECR}} \geq 0$ as $\dot{\gamma} \to \infty$; in the PECR-N model, $\tau \propto \dot{\gamma}$ as $\dot{\gamma} \to \infty$ (i.e. Newtonian behaviour post-yielding). Adapted from [63].

the PECR-N model, shown as a solid line in Figure 1.6.

The large relaxation times and apparent yield-stress behaviour of the PECR-N model results in 'fast' and 'slow' timescales, leading to hysteresis, shear banding (see [75, 76]), and thixotropy. The PECR-N model (along with similar models) is an important step forward in the study of thixotropic behaviour as it eliminates the tricky task of measuring the value of the structure parameter experimentally (a problem encountered recently by Jeon and Hodges [77]). However, the ability of these models to exhibit thixotropy is limited to the Mullins effect, so they cannot be used to model weak thixotropy.

1.2.4.4 Microphysics-based models

Thixotropy may also be modelled by considering the underlying physical mechanisms which lead to thixotropic behaviour. The interaction of suspended particles with each other and with the suspending fluid often yields non-Newtonian behaviour. Modelling fluids this way is complex as it involves a full description of the structure or suspended particles, a complexity which is avoided in

structure-parameter-based models.

Some authors (e.g. Patel and Russel [78]) model suspended flocs which vary in size depending on the stress, and so affect the properties of the fluid in different ways. Others, including Swan et al. [21], model suspended spherical particles which diffuse in the fluid via Brownian motion over varying timescales. When the particles diffuse slowly compared to the timescale of the flow, thixotropic behaviour may be strong enough to affect the flow.

1.3 Slowly varying flows

In this thesis, we will consider the unsteady axisymmetric flow of thixotropic fluid along a uniform cylindrical pipe and a cylindrical pipe of slowly varying radius, which is a case of slowly varying flow. Following the application of lubrication theory, we expand the governing equations to study a flow at various orders of approximation. The benefit of applying lubrication theory for a slowly varying flow is that the leading-order behaviour is simply that of uniform flow. Geometrical corrections to account for the slowly varying radius enter the expansion at second order in the expansion, not first order, meaning that lubrication theory allows one to approximate slowly varying flow to a high accuracy by considering an equivalent uniform set-up. Since Reynolds [39], lubrication theory has been used to model flow in various geometries and for various fluids, which we discuss in the following sections.

1.3.1 Lubrication flow of non-Newtonian fluids

Non-Newtonian fluids arise in the context of lubrication flows in a variety of settings, including in avalanches, in which snow may be modelled as a VP fluid [55], and in crude oil transportation [23]. Myers [24] studied and compared the flow of generalised Newtonian fluids, specifically the power-law, Carreau, and Ellis fluids, in 2D channels and down inclined planes. A well-known problem of the power-law model is its unphysical behaviour in low shear rates, so Myers presents the behaviour of non-pathological models which could be preferred over

the power-law model. He notes that a more physically realistic model comes at the expense of simplicity.

Wilson et al. [79] studied the steady lubrication flow of a rivulet of power-law fluid. This work was extended by Yatim et al. [80] to unsteady behaviour of power-law fluid, and most recently by Al Mukahal et al. [81, 82]. These works provide an important baseline for studying more complex fluids, such as thixotropic fluids. Yatim et al. [80] also study the limiting behaviour of the power-law model. In particular, they consider the so-called shear-thinning limit, in which the power-law exponent tends to zero ($n \to 0$), and the shear-thickening limit ($n \to \infty$).

Lubrication flow of viscoplastic fluids typically features regions of yielded, purely viscous flow, and regions of unyielded, 'plug-like' flow. In the case of pipe flow, for example, a VP fluid is yielded near the wall of the pipe where the shear stress is high, and unyielded near the centre of the pipe where the shear stress is low. The viscous flow near the wall lubricates the plug near the centreline, which is bounded by a 'yield surface'. The higher the yield stress of a fluid, the wider the plug will be. Lubrication theory for VP fluids, particularly Bingham and Herschel–Bulkley fluids, predicts the plug to be completely unyielded, and the yield surface divides purely viscous and purely plug-like flow. Conversely, the same approach yields solutions which describe flow within the supposedly rigid plug. This disagreement has been termed the 'Bingham paradox', the 'lubrication paradox', and the 'yield-stress paradox'.

One way to avoid this paradox is to relax the rheological model, an example of which was presented by Wilson [83]. Instead of assuming the fluid is completely rigid when unyielded, Wilson assumes the fluid has two characteristic viscosities, often referred to as a bi-viscous model, with one viscosity being much larger than the other. This model is constructed so that for low stresses, the fluid flows with the higher viscosity, which is similar to plug-like flow. When the stress reaches a critical stress, equivalent to the yield stress, the viscosity rapidly, but smoothly, decreases to the lower viscosity, which is equivalent to a yield fluid. In such a model, there is a 1-to-1 correspondence between the shear rate and the shear stress, and the high-viscosity (unyielded) fluid may deform. This process of relaxing a rheological model is also referred to as a 'regularisation' of the model,

and will be encountered later in this thesis.

Balmforth and Craster [41] present a consistent lubrication theory for the free surface flow of a viscoplastic fluid. Specifically, they use the exact Bingham model, but unlike Wilson [83], they allow for no relaxation or regularisation of the model. Following an expansion of the governing equations, they show that the plug does in fact yield 'weakly' at a higher order, and so they define a 'pseudo-plug' accordingly, which is bounded by a 'fake' yield surface. Frigaard and Ryan [43] studied Bingham flow along a 2D channel of slowly varying width. Pritchard et al. [84] studied free-surface flow of power-law and Carreau fluids, as well as the viscoplastic Bingham and Casson fluids, on inclined planes of varying gradient. Huilgol [85] reviews analytical solutions for VP fluids in a range of geometries, including channel and pipe flows, and free-surface flows. Huilgol notes similar difficulties to Myers [24], specifically of obtaining analytical solutions for VP fluids which are non-linear post-yield, such as Herschel–Bulkley fluids.

1.3.2 Lubrication flow of thixotropic fluids

Due to the complexity of thixotropic fluids, simplifying methods, which include lubrication theory or making assumptions on λ in fluid layers, are often used when studying slowly varying flows of thixotropic fluids. Interest in slowly varying flows of thixotropic fluids arose from studies of avalanche behaviour, though Pearson and Tardy [86] proposed using lubrication theory to study thixotropic flows in porous media. Avalanche experiments of yield-stress fluids are usually performed by placing a blob of yield-stress fluid at one end of a plane and allowing the fluid to rest for an extended time. The plane is then inclined until the fluid yields and flows, with the distance travelled by the leading 'head' of the fluid being of particular interest. Coussot et al. [55] showed that while theory predicts that the fluid flows quickly after yielding, and gradually slows, an experiment showed that the flow is initially slow after yielding, occasionally referred to a creeping flow, then accelerates and flows well past the predicted stopping point of the leading head (see their Figure 2(b)). Coussot et al. conclude that thixotropy has the effect of breaking down the structure of the fluid after yielding, decreasing the viscosity, and eventually allowing the fluid to flow rapidly down the plane, further

decreasing the viscosity leading to a long runout.

Following further studies by Coussot and co-workers [37, 72], and Chanson et al. [87], Hewitt and Balmforth [22] constructed a structure-parameter-based rheological model to study the thixotropic yield-stress behaviour observed by Coussot and co-workers. Their model emphasised the decrease of the apparent yield stress of the fluid due to thixotropy, and incorporated viscosity bifurcations (discussed in Section 1.2.4.2), and, repeating Coussot's experiments, found rough qualitative agreement between their theoretical and experimental results. Hewitt and Balmforth note some differences between their results, which highlight the difficulty constructing a rheological model for thixotropic fluids. In addition, Pritchard and Pearson [88] studied the flow of thixotropic fluid in a porous medium and in fracture of varying width. Chanson et al. [87] and Pritchard and Pearson [88] both reduced the governing equations by assuming that the structure over a cross-section could be averaged, yielding a single quantity characteristic of the state of the structure. Chanson et al. [87] averaged the structure parameter vertically, while Pritchard and Pearson [88] averaged the value of the fluidity in a version of Bautista et al.'s model [89].

Dullaert and Mewis [68] propose a structure parameter-based model for a thixoviscoelastic fluid, in which the structure of a suspension affects the elastic modulus of the elastic component and the viscosity of the viscous component. The suspension is itself suspended in an inelastic medium of constant viscosity. The authors were keen to demonstrate an agreement between the behaviour of structure-parameter-based models and experimental behaviour of thixoviscoelastic fluids. Recently, Ahmadpour and Sadeghy [28] studied start-up flows of Dullaert–Mewis thixotropic fluids in axisymmetric pipelines, with emphasis on the effect of elasticity on success or failure of restarting flow in oil pipelines. Whilst the authors did not use lubrication theory, we are able to compare their results for a uniform pipe directly to the leading-order behaviour of a slowly varying pipe in the present work. In particular, we are able to use Ahmadpour and Sadeghy's results to match a limiting case of the MMW model in the present work to a limiting case of the Houška model.

Livescu et al. [90] study the levelling of a thin sinusoidally rippled film of thixotropic

fluid. They use Moore's structure-based model [91], which uses a special case of Mewis and Wagner's structure equation (1.2.13). To simplify the mathematical problem further, they use the results of numerical simulations to approximate the inverse of the viscosity across the thin film, using the boundary conditions for the viscosity at the substrate and the free surface. A downside to this approach is that in order to simplify the problem further following lubrication theory, one must perform a numerical study for the full problem.

Recently, Uppal et al. [35] used lubrication theory to study the spreading of a thixotropic droplet, modelled using Moore's structure-parameter model [91]. In addition to simplifying the problem using lubrication theory, they also employ a cross-sectional averaging over the depth of the droplet to obtain a '1.5D' model, in which the structure evolution equation retains vertical dependence explicitly and the continuity equation is depth-integrated.

The work of Pritchard et al. [29]

Recently Pritchard et al. [29] (hereafter PWM) studied the steady flow of a purely viscous thixotropic fluid and a thixoviscoplastic fluid along a slowly varying 2D channel, and derived a general theory for thixotropic lubrication flow for a general rheology. They study the so-called weakly advective regime of thixotropy in which the structure of the fluid is advected through wider and narrow regions of the channel. They obtain an advective Deborah number, which is the ratio of the timescale of the structure evolution to the timescale of the advection of structure along the channel. The timescale of the structure evolution, or structure response, of a real-world fluid is difficult to determine. Dullaert and Mewis [92] found typical timescales of 0.1s to 10s for a suspension of fumed silica particles, Boek et al. [93] found timescales of 1s to 100s for a wormlike micellar solution, and Ardakani et al. [30] found a timescales of around 10s for toothpaste.

Pritchard et al. use Mewis and Wagner's structure evolution equation [7], given by (1.2.13), with a version of Moore's constitutive relation [91], to form the Moore–Mewis–Wagner (MMW) model. This model has also been used recently in the similar context of the Stokes boundary layer problem [94] Unlike others who use Mewis and Wagner's structure equation, Pritchard et al. make significant

analytical progress without specifying values of the parameters a, b, c, and d, and obtain general leading-order and perturbation solutions for the velocity and structure parameter. We discuss the results of Pritchard et al. in more detail in Section 3.3.1, where we are able to make comparisons between their results and the results in this thesis.

In this thesis, we build on the results of Pritchard et al. [29] in two main ways: we generalise their approach further by allowing for unsteady flow; and we study the related geometry of a slowly varying cylindrical pipe. Unlike Pritchard et al. we perform an in-depth analysis of the behaviour of the fluid for three rheological models, and attempt to determine what general statements can be made about the behaviour of thixotropic fluids in slowly varying geometries.

1.4 Overview of thesis

In this thesis, we study the behaviour of thixotropic fluids in a uniform and a non-uniform cylindrical pipe, in both steady and unsteady flow conditions. Chapters 2–5 focus on the unsteady flow of a thixotropic fluid in a slowly varying pipe. In particular, in Chapter 2 we derive the governing equations for unsteady thixotropic flow in a slowly varying pipe, and obtain thixotropic regimes of various characteristic thixotropic strengths through an asymptotic expansion. By focussing on the weakly thixotropic behaviour in Chapter 3, we obtain solutions for unsteady thixotropic pipe flow for a general rheology in the weakly thixotropic regimes. Thixotropic behaviour in these regimes is characterised by a structure timescale which lies between instantaneous and the timescale driving structure evolution. We use the previous work of Pritchard et al. [29] to define a reference case for thixotropic behaviour against which we compare the weakly thixotropic behaviour is this thesis. In Chapters 4 and 5, we present the fluid behaviour for the simplified MMW model, the full MMW model, and the viscoplastic Houška model, and determine whether we are able to make generic statements about the behaviour thixotropic fluid in pipe flow.

General solutions are not available for all thixotropic regimes as they are in the weakly thixotropic regime. Consequently, in Chapter 6, we attempt to implement

unsteady thixotropic flow in a slowly varying pipe numerically using the finite element analysis software package COMSOL [54] to verify and expand the results of Chapters 2–5. We have some limited success with this implementation, and indicate where likely challenges lie in the numerical problem.

In Chapter 7, we focus on the oscillating flow of a thixotropic fluid in a uniform pipe, which is related to the set-up studied in Chapters 2–5. A key difference between the slowly varying set-up and the oscillating set-up is that the latter is simpler. Two key advantages of the simpler set-up are that we can make more analytical progress than in the former set-up, particulars in studying thixotropic regimes other than the weakly thixotropic regime, and that we can obtain more accurate numerical solutions. Indeed, we are able to build a full picture of oscillating thixotropic pipe flow using both analytical and numerical methods.

Finally, in Chapter 8, we summarise the findings of this thesis and indicate possible directions for further study in this area.

1.5 Presentations and publications

The main results of Chapter 3 of this thesis have been presented at the following conferences: the British Applied Mathematics Colloquia (BAMC) at the University of Oxford in April 2016, and the University of Surrey in April 2017; the Scottish Fluid Mechanics Meetings (SFMM) at the University of Edinburgh in May 2016, and the University of Strathclyde in May 2017; the British Society of Rheology Mid-Winter Meetings at the University of Glasgow in December 2015, and the University of Reading in December 2016; the Society of Industrial and Applied Mathematics (SIAM) Annual Meeting (AN17) in July 2017 in Pittsburgh, USA; the European Coating Symposium (ECS) in November 2017 in Fribourg, Switzerland. The main results of Chapter 3 have been published in *Physics of Fluids* [95].

Chapter 2

Model Formulation

In this chapter, we formulate the problem of unsteady thixotropic flow in a slowly varying pipe of small aspect ratio δ. As mentioned in the Chapter 1, we consider a slowly varying pipe because the flow will be complex enough to yield interesting thixotropic behaviour, while remaining simple enough to thoroughly explore analytically. We begin by deriving the governing equations for the unsteady flow of an incompressible fluid in an axisymmetric geometry in Section 2.1. We then rescale and non-dimensionalise these equations, and obtain two Deborah numbers in Section 2.2. Using lubrication theory, we expand the governing equations and obtain equations at leading order and first order in δ in Section 2.3. We define various regimes of the Deborah numbers in Section 2.4. Finally, in Section 2.5, we introduce three rheological models: the simplified Moore–Mewis–Wagner (sMMW) model, the full Moore–Mewis–Wagner (MMW) model, and the regularised Houška model. In this chapter, a distinction between thixotropic and antithixotropic behaviour is not necessary, so for brevity we refer to time-dependent shear-thinning or -thickening behaviour as thixotropy.

2.1 Governing equations

We consider the unsteady flow of an incompressible thixotropic fluid along a pipe of slowly varying radius, using cylindrical co-ordinates $(\hat{r}, \theta, \hat{z})$. Here, as with

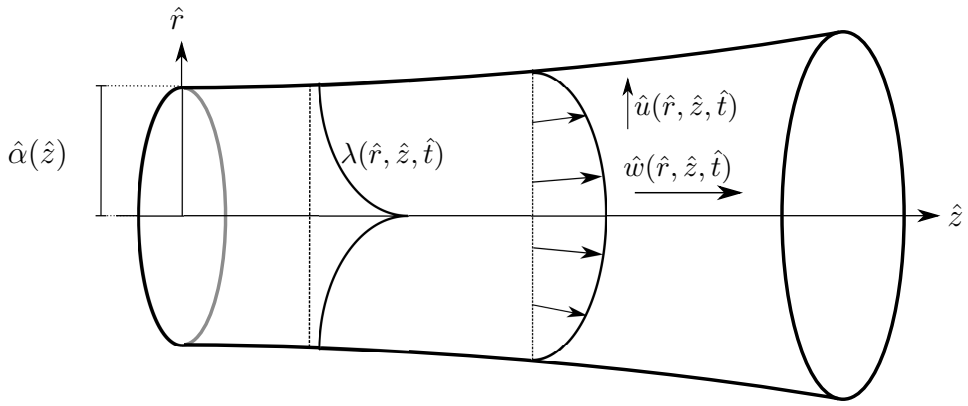

Figure 2.1: Sketch of unsteady axisymmetric flow of a thixotropic fluid along a pipe of slowly varying radius $\hat{r} = \hat{\alpha}(\hat{z})$.

terms below, a circumflex represents a dimensional quantity and dimensionless terms are unadorned. In particular, we assume that the typical lengthscale of the flow $\hat{L}$ is much larger than the typical radius $\hat{R}$, i.e. $\hat{R}/\hat{L} = \delta \ll 1$, where δ is the small aspect ratio of the flow. We assume thixotropic behaviour arises from the time-dependent build-up and breakdown of a mesoscopic internal structure, which we model using the scalar structure parameter λ.

We assume the flow along the pipe is axisymmetric, with no swirl, so the velocity has the form $\hat{\mathbf{u}} = (\hat{u}(\hat{r},\hat{z},\hat{t}), 0, \hat{w}(\hat{r},\hat{z},\hat{t}))$. The radius of the pipe varies slowly with distance in the $\hat{z}$-direction, and is given by $\hat{r} = \hat{\alpha}(\hat{z})$, so that any transverse cross section of the pipe is circular, and $\hat{\alpha}'(\hat{z}) = \mathcal{O}(\delta)$. Figure 2.1 shows a sketch illustrating the geometry of this set-up.

This problem involves the flow of viscous fluid, which is governed by the Navier–Stokes equation

$$\hat{\rho}\frac{\mathrm{D}\hat{\mathbf{u}}}{\mathrm{D}\hat{t}} = -\nabla\hat{p} + \mu\nabla^2\underline{\underline{\hat{\tau}}}, \tag{2.1.1}$$

where $\hat{\rho}$ is the constant density, $\hat{p}$ is the pressure, $\underline{\underline{\hat{\tau}}}$ is the stress tensor, and $\mathrm{D}/\mathrm{D}\hat{t}$ is the material derivative. We take $\underline{\underline{\hat{\tau}}}$ to depend on the shear rate via an extended generalised Newtonian constitutive relation in which the viscosity $\hat{\eta}$ depends on

the total shear rate $\dot{\gamma}$ and the structure parameter λ, i.e.

$$\hat{\tau}_{ij} = \hat{\eta}(\dot{\gamma}, \lambda)\hat{e}_{ij}, \tag{2.1.2}$$

where $\hat{e}_{ij}$ are terms of the shear-rate tensor and $\dot{\gamma} = \sqrt{\hat{e}_{ij}\hat{e}_{ij}/2}$ is the total shear rate. The shear-rate tensor, in cylindrical co-ordinates $(\hat{r}, \theta, \hat{z})$, for axisymmetric flow with no swirl, i.e. with all terms and derivatives in θ set equal to zero, is given by [38]:

$$\hat{e}_{ij} = \begin{pmatrix} 2\dfrac{\partial \hat{u}}{\partial \hat{r}} & 0 & \dfrac{\partial \hat{u}}{\partial \hat{z}} + \dfrac{\partial \hat{w}}{\partial \hat{r}} \\ 0 & 2\dfrac{\hat{u}}{\hat{r}} & 0 \\ \dfrac{\partial \hat{u}}{\partial \hat{z}} + \dfrac{\partial \hat{w}}{\partial \hat{r}} & 0 & 2\dfrac{\partial \hat{w}}{\partial \hat{z}} \end{pmatrix}. \tag{2.1.3}$$

We assume the fluid is incompressible, so its velocity satisfies the mass conservation equation $\hat{\nabla} \cdot \hat{\mathbf{u}} = 0$, i.e.

$$\frac{1}{\hat{r}}\frac{\partial}{\partial \hat{r}}(\hat{r}\hat{u}) + \frac{\partial \hat{w}}{\partial \hat{z}} = 0. \tag{2.1.4}$$

We assume the usual no-slip and no-penetration boundary conditions apply at the pipe wall, along with the symmetry condition at the centreline of the pipe, given by

$$\hat{\mathbf{u}} = \mathbf{0} \quad \text{at} \quad \hat{r} = \hat{\alpha}(\hat{z}) \quad \text{and} \quad \hat{\tau}_{rz} = 0 = \hat{u} \quad \text{at} \quad \hat{r} = 0, \tag{2.1.5}$$

respectively. The flow is driven by a time-dependent pressure gradient and has volume flux $\hat{Q}(\hat{t})$ given by

$$\hat{Q}(\hat{t}) = 2\pi \int_0^{\hat{\alpha}(\hat{z})} \hat{w}(\hat{r}, \hat{z}, \hat{t})\hat{r}\, \mathrm{d}\hat{r}. \tag{2.1.6}$$

We note that by incompressibility (2.1.4), the flux is independent of the streamwise co-ordinate $\hat{z}$. We will have the option to prescribe either the pressure gradient or the volume flux. We choose to prescribe the volume flux, which will allow us to obtain general solutions at a later stage, and to compare the solutions with those of PWM.

The flow has zero Reynolds number, so we may neglect the inertial term of the Navier–Stokes equation (2.1.1), yielding, in component form, the Cauchy momentum equations:

$$\frac{\partial \hat{p}}{\partial \hat{r}} = \frac{1}{\hat{r}}\frac{\partial}{\partial \hat{r}}\left(\hat{r}\hat{\tau}_{rr}\right) + \frac{\partial \hat{\tau}_{rz}}{\partial \hat{z}}, \tag{2.1.7}$$

$$\frac{\partial \hat{p}}{\partial \hat{z}} = \frac{1}{\hat{r}}\frac{\partial}{\partial \hat{r}}\left(\hat{r}\hat{\tau}_{zr}\right) + \frac{\partial \hat{\tau}_{zz}}{\partial \hat{z}}, \tag{2.1.8}$$

for the $\mathbf{e}_r$- and $\mathbf{e}_z$-components respectively. Using the constitutive relation (2.1.2) and the shear-rate tensor (2.1.3), equations (2.1.7) and (2.1.8) become

$$\frac{\partial \hat{p}}{\partial \hat{r}} = \frac{1}{\hat{r}}\frac{\partial}{\partial \hat{r}}\left(2\hat{r}\hat{\eta}\frac{\partial \hat{u}}{\partial \hat{r}}\right) + \frac{\partial}{\partial \hat{z}}\left[\hat{\eta}\left(\frac{\partial \hat{u}}{\partial \hat{z}} + \frac{\partial \hat{w}}{\partial \hat{r}}\right)\right], \tag{2.1.9}$$

$$\frac{\partial \hat{p}}{\partial \hat{z}} = \frac{1}{\hat{r}}\frac{\partial}{\partial \hat{r}}\left[\hat{r}\hat{\eta}\left(\frac{\partial \hat{u}}{\partial \hat{z}} + \frac{\partial \hat{w}}{\partial \hat{r}}\right)\right] + \frac{\partial}{\partial \hat{z}}\left(2\hat{\eta}\frac{\partial \hat{w}}{\partial \hat{z}}\right), \tag{2.1.10}$$

respectively.

For convenience, we define

$$\hat{\Gamma} = \dot{\gamma}^2 = 2\left(\frac{\partial \hat{u}}{\partial \hat{r}}\right)^2 + \left(\frac{\partial \hat{u}}{\partial \hat{z}} + \frac{\partial \hat{w}}{\partial \hat{r}}\right)^2 + 2\left(\frac{\partial \hat{w}}{\partial \hat{z}}\right)^2. \tag{2.1.11}$$

The structure evolves according to an advection-kinetic equation

$$\frac{\mathrm{D}\lambda}{\mathrm{D}\hat{t}} = \hat{f}(\hat{\Gamma}, \lambda), \tag{2.1.12}$$

where the function $\hat{f}$ is the structure evolution rate, which describes the shear-driven build-up and breakdown of the structure. The structure evolution rate $\hat{f}(\hat{\Gamma}, \lambda)$ and the viscosity $\hat{\eta}(\dot{\gamma}, \lambda)$, given in (2.1.2), describe the rheological properties of the fluid, and together form the rheological model. We do not specify a particular rheological model at this stage as we are able to make significant progress toward solutions for the velocities and the structure parameter, whilst keeping the rheological model general.

2.2 Non-dimensionalisation

We now rescale and non-dimensionalise the governing equations introduced in Section 2.1, to which end we define dimensionless quantities, with the scaling δ, via

$$\begin{gathered}\hat{r} = \hat{R}r, \quad \hat{z} = \frac{\hat{R}z}{\delta}, \quad \hat{u} = \frac{\delta\hat{Q}_{\text{ref}}u}{\hat{R}^2}, \quad \hat{w} = \frac{\hat{Q}_{\text{ref}}w}{\hat{R}^2}, \\ \hat{\Gamma} = \frac{\hat{Q}_{\text{ref}}^2\Gamma}{\hat{R}^6}, \quad \hat{Q} = \hat{Q}_{\text{ref}}Q, \quad \hat{p} = \frac{\hat{\mu}_0\hat{Q}_{\text{ref}}p}{\delta\hat{R}^3}, \quad \hat{\eta} = \hat{\mu}_0\eta, \\ \hat{\alpha}(\hat{z}) = \hat{R}\alpha(z), \quad \hat{t} = \hat{T}t, \quad \text{and} \quad \hat{f}(\hat{\Gamma}, \lambda) = \hat{f}_0 f(\Gamma, \lambda),\end{gathered} \tag{2.2.1}$$

where $\hat{R}$ is the typical radius of the pipe, δ is the small aspect ratio of the flow, $\hat{\mu}_0$ is the typical viscosity, $\hat{Q}_{\text{ref}}$ is the typical volume flux, and $\hat{T}$ is the typical timescale of the flow.

Following non-dimensionalisation, the mass conservation equation (2.1.4) simply becomes

$$\frac{1}{r}\frac{\partial}{\partial r}(ru) + \frac{\partial w}{\partial z} = 0. \tag{2.2.2}$$

The Cauchy momentum equations (2.1.9) and (2.1.10) non-dimensionalise and simplify to

$$\frac{\partial p}{\partial r} = \delta^2\left[\frac{1}{r}\frac{\partial}{\partial r}\left(2r\eta\frac{\partial u}{\partial r}\right) + \frac{\partial}{\partial z}\left(\eta\frac{\partial w}{\partial r}\right)\right] + \delta^4\frac{\partial}{\partial z}\left(\eta\frac{\partial u}{\partial z}\right), \tag{2.2.3}$$

$$\frac{\partial p}{\partial z} = \frac{1}{r}\frac{\partial}{\partial r}\left(r\eta\frac{\partial w}{\partial r}\right) + \delta^2\left[\frac{1}{r}\frac{\partial}{\partial r}\left(r\eta\frac{\partial u}{\partial z}\right) + \frac{\partial}{\partial z}\left(2\eta\frac{\partial w}{\partial z}\right)\right], \tag{2.2.4}$$

respectively.

The equation for $\hat{\Gamma}$ (2.1.11) non-dimensionalises and simplifies to

$$\Gamma = \left(\frac{\partial w}{\partial r}\right)^2 + \delta^2\left[2\left(\frac{\partial u}{\partial r}\right)^2 + 2\frac{\partial u}{\partial z}\frac{\partial w}{\partial r} + 2\left(\frac{\partial w}{\partial z}\right)^2\right] + \delta^4\left(\frac{\partial u}{\partial z}\right)^2. \tag{2.2.5}$$

We also non-dimensionalise the boundary conditions (2.1.5) to obtain

$$u = 0 = w \quad \text{at} \quad r = \alpha(z) \quad \text{and} \quad \eta(\dot{\gamma}, \lambda)\frac{\partial w}{\partial r} = 0 = u \quad \text{at} \quad r = 0, \tag{2.2.6}$$

and the volume flux condition (2.1.6) non-dimensionalises simply to

$$Q(t) = 2\pi \int_0^{\alpha(z)} w(r, z, t) r \, \mathrm{d}r. \tag{2.2.7}$$

Finally, we non-dimensionalise the structure evolution equation (2.1.12) to obtain

$$\mathcal{D}_\mathrm{t}\frac{\partial \lambda}{\partial t} + \mathcal{D}_\mathrm{a}\left(u\frac{\partial \lambda}{\partial r} + w\frac{\partial \lambda}{\partial z}\right) = f(\Gamma, \lambda), \tag{2.2.8}$$

$$\text{where} \quad \mathcal{D}_\mathrm{a} = \frac{\hat{Q}_\mathrm{ref}\delta}{\hat{f}_0\hat{R}^3} \quad \text{and} \quad \mathcal{D}_\mathrm{t} = \frac{1}{\hat{f}_0\hat{T}},$$

where $\mathcal{D}_\mathrm{a}$ is the advective Deborah number and $\mathcal{D}_\mathrm{t}$ is the temporal Deborah number. These dimensionless numbers are the ratios of the structure response timescale to, respectively, the timescales of advection and of an unsteady applied pressure gradient. So there are two manifestations of thixotropy: advective thixotropy in which the shear rate acting on a fluid element changes as the fluid is advected to wider or narrower sections of the pipe, and temporal thixotropy in which the shear rate acting on a fluid element changes as the pressure gradient increases or decreases. We provide more discussion of the Deborah numbers, including a description of the effect of their magnitude on the flow, in Section 2.4.

2.3 General expansion scheme

Using lubrication theory to simplify the governing equations, we consider the flow in the limit $\delta \to 0$, and seek asymptotic solutions for the velocity and the structure parameter at various orders of δ. To this end, we now expand the

pressure, velocities and structure parameter in powers of the aspect ratio δ:

$$(p, w, u, \lambda) = \sum_{i=0}^{\infty} \delta^i (p_i, w_i, u_i, \lambda_i). \tag{2.3.1}$$

We note from equation (2.2.3) that the pressure only depends on the radial coordinate r at $\mathcal{O}(\delta^2)$, so p_0 and p_1 are functions of z and t only. Aside from p_0 and p_1, all quantities in (2.3.1) are functions of r, z, and t.

We also expand $\eta(\Gamma, \lambda)$ and $f(\Gamma, \lambda)$ to obtain

$$\eta = \sum_{i=0}^{\infty} \delta^i \eta_i, \quad \text{and} \quad f = \sum_{i=0}^{\infty} \delta^i f_i, \tag{2.3.2}$$

where η_i and f_i are the i^{th}-order terms, evaluated at (Γ_0, λ_0).

We now insert the expanded quantities (2.3.1) into the mass conservation equation (2.2.2), the momentum equation (2.2.4), and the equation for Γ (2.2.5). In addition, we insert the expanded quantities into the boundary conditions (2.2.6), the flux condition (2.2.7), and the structure evolution equation (2.2.8). Using (2.3.1), we expand the mass conservation equation (2.2.2), which yields

$$\frac{1}{r}\frac{\partial}{\partial r}(r u_k) + \frac{\partial w_k}{\partial z} = 0, \tag{2.3.3}$$

and the momentum equation (2.2.4), which yields

$$\frac{\partial p_k}{\partial z} = \frac{1}{r}\frac{\partial}{\partial r} \sum_{i=0}^{k} \delta^i r \eta_i \frac{\partial w_{k-i}}{\partial r} = -G_k(z, t), \tag{2.3.4}$$

where G_k is the k-th order pressure gradient. The equation for Γ (2.2.5) yields

$$\begin{aligned} \Gamma = \sum_{i=0}^{\infty} \delta^i \sum_{j=0}^{i} \Bigg\{ & \frac{\partial w_j}{\partial r}\frac{\partial w_{i-j}}{\partial r} \\ & + 2\delta^2 \left(\frac{\partial u_j}{\partial r}\frac{\partial u_{i-j}}{\partial r} + \frac{\partial u_j}{\partial z}\frac{\partial w_{i-j}}{\partial r} + \frac{\partial w_j}{\partial z}\frac{\partial w_{i-j}}{\partial z} \right) + \delta^4 \frac{\partial u_j}{\partial z}\frac{\partial u_{i-j}}{\partial z} \Bigg\}. \end{aligned} \tag{2.3.5}$$

We apply the expansion 2.3.1 to the boundary conditions (2.2.6), which yield

$$u_k = 0 = w_k \quad \text{at} \quad r = \alpha(z), \tag{2.3.6}$$

$$\sum_{i=0}^{k} \eta_k \frac{\partial w_{k-i}}{\partial r} = 0 = u_k \quad \text{at} \quad r = 0, \tag{2.3.7}$$

and to the volume flux condition (2.2.7), which yields

$$Q(t) = 2\pi \int_0^{\alpha(z)} w_0(r,z,t) r \,\mathrm{d}r \quad \text{and} \quad 0 = \int_0^{\alpha(z)} w_k(r,z,t) r \,\mathrm{d}r, \quad k \geq 1. \tag{2.3.8}$$

Finally, using (2.3.1), we expand the structure evolution equation (2.2.8), which yields

$$\mathcal{D}_\mathrm{t} \sum_{k=0}^{\infty} \delta^k \lambda_{k,t} + \mathcal{D}_\mathrm{a} \sum_{k=0}^{\infty} \delta^k \phi_k = \sum_{k=0}^{\infty} \delta^k f_k, \tag{2.3.9}$$

where for brevity we have defined

$$\lambda_{k,t} = \frac{\partial \lambda_k}{\partial t} \quad \text{and} \quad \phi_k = \sum_{i=0}^{k} u_i \frac{\partial \lambda_{k-i}}{\partial r} + w_i \frac{\partial \lambda_{k-i}}{\partial z}. \tag{2.3.10}$$

It is clear from (2.3.9) that the role of thixotropy depends on the relative magnitudes of the temporal and advective Deborah numbers $\mathcal{D}_\mathrm{t}$ and $\mathcal{D}_\mathrm{a}$, and the aspect ratio δ. Again, we provide more discussion of the Deborah numbers in Section 2.4.

We consider the behaviour at the lowest and next-lowest orders of δ with non-trivial solutions, i.e. at leading order and first order. We use the governing equations at these orders to obtain solutions for the leading-order streamwise velocity w_0, transverse velocity u_0, structure parameter λ_0, the streamwise velocity perturbation w_1, and structure parameter perturbation λ_1.

The leading-order terms of Γ (2.3.5), and the viscosity η and the structure evo-

lution rate f (2.3.2) are

$$\Gamma_0 = \left(\frac{\partial w_0}{\partial r}\right)^2, \quad \text{and} \quad \Gamma_1 = 2\frac{\partial w_0}{\partial r}\frac{\partial w_1}{\partial r}, \tag{2.3.11}$$

$$\eta_0 = \eta(\Gamma_0, \lambda_0), \quad \text{and} \quad \eta_1 = \eta_\Gamma \Gamma_1 + \eta_\lambda \lambda_1, \tag{2.3.12}$$

$$f_0 = f(\Gamma_0, \lambda_0), \quad \text{and} \quad f_1 = f_\Gamma \Gamma_1 + f_\lambda \lambda_1, \tag{2.3.13}$$

where for convenience we define

$$\eta_\Gamma = \left.\frac{\partial \eta}{\partial \Gamma}\right|_{(\Gamma_0,\lambda_0)}, \quad \text{and} \quad \eta_\lambda = \left.\frac{\partial \eta}{\partial \lambda}\right|_{(\Gamma_0,\lambda_0)}, \tag{2.3.14}$$

$$f_\Gamma = \left.\frac{\partial f}{\partial \Gamma}\right|_{(\Gamma_0,\lambda_0)}, \quad \text{and} \quad f_\lambda = \left.\frac{\partial f}{\partial \lambda}\right|_{(\Gamma_0,\lambda_0)}. \tag{2.3.15}$$

At leading order and first order in δ, the governing equations, excluding the structure evolution equation, are the mass conservation equation (2.3.3), the momentum equation (2.3.4), the boundary conditions (2.3.6) and (2.3.7), and the flux condition (2.3.8), with $k = 0$ and $k = 1$, respectively. So at leading order the governing hydrodynamic equations are:

$$\frac{1}{r}\frac{\partial}{\partial r}(r u_0) + \frac{\partial w_0}{\partial z} = 0, \tag{2.3.16}$$

$$\frac{1}{r}\frac{\partial}{\partial r}\left(r\eta_0 \frac{\partial w_0}{\partial r}\right) = -G_0(z,t), \tag{2.3.17}$$

$$u_0 = 0 = w_0 \quad \text{at} \quad r = \alpha(z), \tag{2.3.18}$$

$$\eta_0 \frac{\partial w_0}{\partial r} = 0 = u_0 \quad \text{at} \quad r = 0, \tag{2.3.19}$$

$$2\pi \int_0^{\alpha(z)} w_0(r,z,t) r \, \mathrm{d}r = Q(t). \tag{2.3.20}$$

At first order the governing hydrodynamic equations are:

$$\frac{1}{r}\frac{\partial}{\partial r}(ru_1) + \frac{\partial w_1}{\partial z} = 0, \tag{2.3.21}$$

$$\frac{1}{r}\frac{\partial}{\partial r}\left[r\left(\eta_0\frac{\partial w_1}{\partial r} + \left(2\eta_\Gamma\frac{\partial w_0}{\partial r}\frac{\partial w_1}{\partial r} + \eta_\lambda\lambda_1\right)\frac{\partial w_0}{\partial r}\right)\right] = -G_1(z,t), \tag{2.3.22}$$

$$u_1 = 0 = w_1 \quad \text{at} \quad r = \alpha(z), \tag{2.3.23}$$

$$\eta_0\frac{\partial w_1}{\partial r} + \left(2\eta_\Gamma\frac{\partial w_0}{\partial r}\frac{\partial w_1}{\partial r} + \eta_\lambda\lambda_1\right)\frac{\partial w_0}{\partial r} = 0 = u_1 \quad \text{at} \quad r = 0, \tag{2.3.24}$$

$$\int_0^{\alpha(z)} w_1(r,z,t)r\,\mathrm{d}r = 0. \tag{2.3.25}$$

In the following section, we discuss the importance of the magnitudes of the Deborah numbers, and present the structure evolution equation (2.3.9) at leading order and first order for the various regimes of the Deborah numbers.

2.4 Regimes of the Deborah numbers

The structure evolution equations at leading order and first order in δ depend on the magnitudes of the Deborah numbers $\mathcal{D}_\mathrm{t}$ and $\mathcal{D}_\mathrm{a}$, and the aspect ratio δ.

When the Deborah numbers are $\mathcal{O}(\delta^2)$ (or smaller) in magnitude, the thixotropic effects are too weak to affect the flow at leading order ($\mathcal{O}(1)$) or first order ($\mathcal{O}(\delta)$), so the fluid does not exhibit any thixotropic effects, and the behaviour is entirely dependent on the local build-up and breakdown rates. When the Deborah numbers are $\mathcal{O}(\delta)$ in magnitude, the thixotropic effects enter as perturbations to the leading-order behaviour. The case when the Deborah numbers are $\mathcal{O}(\delta)$ in magnitude is the focus of Chapters 3–5. When the Deborah numbers are $\mathcal{O}(1)$ in magnitude, the thixotropic effects are similar in magnitude to local build-up and breakdown. We expect this regime of behaviour to be particularly complicated. When the Deborah numbers are $\mathcal{O}(\delta^{-1})$ or $\mathcal{O}(\delta^{-2})$ in magnitude, the thixotropic effects are strong compared to local build-up and breakdown, and the flow is dominated by the upstream behaviour.

For convenience, we define the regime $\mathfrak{R}_{m,n}$ as the regime in which $\mathcal{D}_\mathrm{t} = \mathcal{O}(\delta^m)$

and $\mathcal{D}_\mathrm{a} = \mathcal{O}(\delta^n)$. We may write $\mathcal{D}_\mathrm{t} = \delta^m \mathcal{D}_\mathrm{t}^*$ and $\mathcal{D}_\mathrm{a} = \delta^n \mathcal{D}_\mathrm{a}^*$, where $\mathcal{D}_\mathrm{t}^* = \mathcal{O}(1)$ and $\mathcal{D}_\mathrm{a}^* = \mathcal{O}(1)$, so that (2.3.9) becomes

$$\delta^m \mathcal{D}_\mathrm{t}^* \sum_{k=0}^{\infty} \delta^k \lambda_{k,t} + \delta^n \mathcal{D}_\mathrm{a}^* \sum_{k=0}^{\infty} \delta^k \phi_k = \sum_{k=0}^{\infty} \delta^k f_k. \tag{2.4.1}$$

By selecting a regime we obtain the structure evolution equation at leading order and first order from (2.4.1). For example, for the regime $\mathfrak{R}_{1,0}$, $m = 1$ and $n = 0$, so (2.4.1) becomes

$$\delta \mathcal{D}_\mathrm{t}^* (\lambda_{0,t} + \delta \lambda_{1,t} + \cdots) + \mathcal{D}_\mathrm{a}^* (\phi_0 + \delta \phi_1 + \cdots) = f_0 + \delta f_1 + \cdots, \tag{2.4.2}$$

from which collecting terms in δ yields

$$\mathcal{D}_\mathrm{a}^* \phi_0 = f_0, \tag{2.4.3}$$

$$\mathcal{D}_\mathrm{t}^* \lambda_{0,t} + \mathcal{D}_\mathrm{a}^* \phi_1 = f_1, \tag{2.4.4}$$

at leading order and first order, respectively. Tables 2.1 and 2.2 show the structure evolution equation (2.4.1) at leading order and first order, respectively, for $m, n = -2, -1, 0, 1, 2$ (which is the full range of interesting regimes, and m and n outside these values do not yield new unique regimes).

We name the regimes according to the strengths of temporal and advective thixotropy. When $\mathcal{D}_\mathrm{t}$ is small, the structure adjusts quickly to changes in the flux, compared to the build-up and breakdown rates, and when $\mathcal{D}_\mathrm{t}$ is large, the structure adjusts slowly. As in PWM, when $\mathcal{D}_\mathrm{a}$ is small, the effect of advection is weak compared to the build-up and breakdown, and when $\mathcal{D}_\mathrm{a}$ is large, the effect of advection is strong.

We deduce that several of the regimes $\mathfrak{R}_{m,n}$ share behaviour or have behaviour which is a simplified case of another regime. We note from (2.2.3), (2.2.4), and (2.2.5) that at $\mathcal{O}(1)$ the behaviour is that of generalised Newtonian laminar flow in a pipe, with geometrical corrections at $\mathcal{O}(\delta^2)$, so there is a 'gap' in the expansion at $\mathcal{O}(\delta)$. The regimes are:

- Weakly thixotropic regimes ($\mathfrak{R}_{1,1}$, $\mathfrak{R}_{1,2}$, $\mathfrak{R}_{2,1}$, and $\mathfrak{R}_{2,2}$): In $\mathfrak{R}_{1,1}$, the quickly

$\mathcal{D}_\mathrm{t}$ \ $\mathcal{D}_\mathrm{a}$	$\mathcal{O}(\delta^{-2})$	$\mathcal{O}(\delta^{-1})$	$\mathcal{O}(1)$	$\mathcal{O}(\delta)$	$\mathcal{O}(\delta^2)$
$\mathcal{O}(\delta^{-2})$	$\mathcal{D}_\mathrm{t}^*\lambda_{0,t} + \mathcal{D}_\mathrm{a}^*\phi_0 = 0$	$\mathcal{D}_\mathrm{t}^*\lambda_{0,t} = 0$	$\mathcal{D}_\mathrm{t}^*\lambda_{0,t} = 0$	$\mathcal{D}_\mathrm{t}^*\lambda_{0,t} = 0$	$\mathcal{D}_\mathrm{t}^*\lambda_{0,t} = 0$
$\mathcal{O}(\delta^{-1})$	$\mathcal{D}_\mathrm{a}^*\phi_0 = 0$	$\mathcal{D}_\mathrm{t}^*\lambda_{0,t} + \mathcal{D}_\mathrm{a}^*\phi_0 = 0$	$\mathcal{D}_\mathrm{t}^*\lambda_{0,t} = 0$	$\mathcal{D}_\mathrm{t}^*\lambda_{0,t} = 0$	$\mathcal{D}_\mathrm{t}^*\lambda_{0,t} = 0$
$\mathcal{O}(1)$	$\mathcal{D}_\mathrm{a}^*\phi_0 = 0$	$\mathcal{D}_\mathrm{a}^*\phi_0 = 0$	$\mathcal{D}_\mathrm{t}^*\lambda_{0,t} + \mathcal{D}_\mathrm{a}^*\phi_0 = f_0$	$\mathcal{D}_\mathrm{t}^*\lambda_{0,t} = f_0$	$\mathcal{D}_\mathrm{t}^*\lambda_{0,t} = f_0$
$\mathcal{O}(\delta)$	$\mathcal{D}_\mathrm{a}^*\phi_0 = 0$	$\mathcal{D}_\mathrm{a}^*\phi_0 = 0$	$\mathcal{D}_\mathrm{a}^*\phi_0 = f_0$	$0 = f_0$	$0 = f_0$
$\mathcal{O}(\delta^2)$	$\mathcal{D}_\mathrm{a}^*\phi_0 = 0$	$\mathcal{D}_\mathrm{a}^*\phi_0 = 0$	$\mathcal{D}_\mathrm{a}^*\phi_0 = f_0$	$0 = f_0$	$0 = f_0$

Table 2.1: Structure evolution equation (2.4.1) for each regime, at leading order.

$\mathcal{D}_\mathrm{t}$ \ $\mathcal{D}_\mathrm{a}$	$\mathcal{O}(\delta^{-2})$	$\mathcal{O}(\delta^{-1})$	$\mathcal{O}(1)$	$\mathcal{O}(\delta)$	$\mathcal{O}(\delta^2)$
$\mathcal{O}(\delta^{-2})$	$\mathcal{D}_\mathrm{t}^*\lambda_{1,t} + \mathcal{D}_\mathrm{a}^*\phi_1 = 0$	$\mathcal{D}_\mathrm{t}^*\lambda_{1,t} + \mathcal{D}_\mathrm{a}^*\phi_0 = 0$	$\mathcal{D}_\mathrm{t}^*\lambda_{1,t} = 0$	$\mathcal{D}_\mathrm{t}^*\lambda_{1,t} = 0$	$\mathcal{D}_\mathrm{t}^*\lambda_{1,t} = 0$
$\mathcal{O}(\delta^{-1})$	$\mathcal{D}_\mathrm{t}^*\lambda_{0,t} + \mathcal{D}_\mathrm{a}^*\phi_1 = 0$	$\mathcal{D}_\mathrm{t}^*\lambda_{1,t} + \mathcal{D}_\mathrm{a}^*\phi_1 = f_0$	$\mathcal{D}_\mathrm{t}^*\lambda_{1,t} + \mathcal{D}_\mathrm{a}^*\phi_0 = f_0$	$\mathcal{D}_\mathrm{t}^*\lambda_{1,t} = f_0$	$\mathcal{D}_\mathrm{t}^*\lambda_{1,t} = f_0$
$\mathcal{O}(1)$	$\mathcal{D}_\mathrm{a}^*\phi_1 = 0$	$\mathcal{D}_\mathrm{t}^*\lambda_{0,t} + \mathcal{D}_\mathrm{a}^*\phi_1 = f_0$	$\mathcal{D}_\mathrm{t}^*\lambda_{1,t} + \mathcal{D}_\mathrm{a}^*\phi_1 = f_1$	$\mathcal{D}_\mathrm{t}^*\lambda_{1,t} + \mathcal{D}_\mathrm{a}^*\phi_0 = f_1$	$\mathcal{D}_\mathrm{t}^*\lambda_{1,t} = f_1$
$\mathcal{O}(\delta)$	$\mathcal{D}_\mathrm{a}^*\phi_1 = 0$	$\mathcal{D}_\mathrm{a}^*\phi_1 = f_0$	$\mathcal{D}_\mathrm{t}^*\lambda_{0,t} + \mathcal{D}_\mathrm{a}^*\phi_1 = f_1$	$\mathcal{D}_\mathrm{t}^*\lambda_{0,t} + \mathcal{D}_\mathrm{a}^*\phi_0 = f_1$	$\mathcal{D}_\mathrm{t}^*\lambda_{0,t} = f_1$
$\mathcal{O}(\delta^2)$	$\mathcal{D}_\mathrm{a}^*\phi_1 = 0$	$\mathcal{D}_\mathrm{a}^*\phi_1 = f_0$	$\mathcal{D}_\mathrm{a}^*\phi_1 = f_1$	$\mathcal{D}_\mathrm{a}^*\phi_0 = f_1$	$0 = f_1$

Table 2.2: Structure evolution equation (2.4.1) for each regime, at first order.

adjusting and weakly advective regime, when $\mathcal{D}_\mathrm{t} = \mathcal{O}(\delta)$ and $\mathcal{D}_\mathrm{a} = \mathcal{O}(\delta)$, the thixotropic behaviour enters the expansion as a perturbation to the $\mathcal{O}(1)$ generalised Newtonian behaviour. As we show in Chapter 3, the perturbations are composed of a combination of a temporal term (proportional to $\mathcal{D}_\mathrm{t}Q'$) and an advective term (proportional to $\mathcal{D}_\mathrm{a}\alpha'$) (see equation (3.3.4) in particular). By setting $\mathcal{D}_\mathrm{t}Q' = 0$ or $\mathcal{D}_\mathrm{a}\alpha' = 0$, we can eliminate temporal or advective thixotropy respectively, and obtain the weakly advective (and very quickly adjusting) regime $\mathfrak{R}_{2,1}$ or the quickly adjusting (and very weakly advective) regime $\mathfrak{R}_{1,2}$, respectively. By setting $\mathcal{D}_\mathrm{t}Q' = \mathcal{D}_\mathrm{a}\alpha' = 0$, we obtain the regime $\mathfrak{R}_{2,2}$, in which thixotropy enters at $\mathcal{O}(\delta^2)$ or higher and so does not affect the flow at $\mathcal{O}(1)$ or $\mathcal{O}(\delta)$.

- Regime groups: Consider as an example the regimes $\mathfrak{R}_{2,-2}$, $\mathfrak{R}_{1,-2}$, and $\mathfrak{R}_{0,-2}$, i.e. when $\mathcal{D}_\mathrm{a} = \mathcal{O}(\delta^{-2})$ and $\mathcal{D}_\mathrm{t} = \mathcal{O}(1)$ or smaller. These regimes are identical (at leading order and first order) because temporal thixotropy is too weak to affect the behaviour at either leading order or first order (in this case, $\mathcal{O}(\delta^{-2})$ and $\mathcal{O}(\delta^{-1})$ respectively). We can see that they are identical by noting that their corresponding structure evolution equations are identical, as shown by the box at the bottom-left of Tables 2.1 and 2.2. Following this reasoning, we identify four regime groups of identical behaviour (at leading order and first order), and name them accordingly. These groups are

$$\begin{aligned}
\mathfrak{R}_{-2,0} = \mathfrak{R}_{-2,1} = \mathfrak{R}_{-2,2}, &\quad \text{'Very Slowly Adjusting Group'},\\
\mathfrak{R}_{-1,1} = \mathfrak{R}_{-1,2}, &\quad \text{'Slowly Adjusting Group'},\\
\mathfrak{R}_{0,-2} = \mathfrak{R}_{1,-2} = \mathfrak{R}_{2,-2}, &\quad \text{'Very Strongly Advective Group'},\\
\mathfrak{R}_{1,-1} = \mathfrak{R}_{2,-1}, &\quad \text{'Strongly Advective Group'},
\end{aligned}$$

  and are indicated in Tables 2.1 and 2.2.

In total, there are 19 unique regimes, which are shown in Table 2.3. Indicated at the bottom-right of Table 2.3 are the weakly thixotropic regimes $\mathfrak{R}_{2,1}$, $\mathfrak{R}_{1,2}$, and $\mathfrak{R}_{2,2}$, the behaviour of which can be obtained from the behaviour in regime $\mathfrak{R}_{1,1}$, and is the focus of Chapters 3–5. Also indicated in Table 2.3 are the regime groups. In summary, we consider this problem at leading order and first

$\mathcal{D}_\mathrm{t}\backslash\mathcal{D}_\mathrm{a}$	$\mathcal{O}(\delta^{-2})$	$\mathcal{O}(\delta^{-1})$	$\mathcal{O}(1)$	$\mathcal{O}(\delta)$	$\mathcal{O}(\delta^2)$
$\mathcal{O}(\delta^{-2})$	$\mathfrak{R}_{-2,-2}$	$\mathfrak{R}_{-2,-1}$	$\mathfrak{R}_{-2,0}$	$\mathfrak{R}_{-2,1}$	$\mathfrak{R}_{-2,2}$
$\mathcal{O}(\delta^{-1})$	$\mathfrak{R}_{-1,-2}$	$\mathfrak{R}_{-1,-1}$	$\mathfrak{R}_{-1,0}$	$\mathfrak{R}_{-1,1}$	$\mathfrak{R}_{-1,2}$
$\mathcal{O}(1)$	$\mathfrak{R}_{0,-2}$	$\mathfrak{R}_{0,-1}$	$\mathfrak{R}_{0,0}$	$\mathfrak{R}_{0,1}$	$\mathfrak{R}_{0,2}$
$\mathcal{O}(\delta)$	$\mathfrak{R}_{1,-2}$	$\mathfrak{R}_{1,-1}$	$\mathfrak{R}_{1,0}$	$\mathfrak{R}_{1,1}$	$\mathfrak{R}_{1,2}$
$\mathcal{O}(\delta^2)$	$\mathfrak{R}_{2,-2}$	$\mathfrak{R}_{2,-1}$	$\mathfrak{R}_{2,0}$	$\mathfrak{R}_{2,1}$	$\mathfrak{R}_{2,2}$

Table 2.3: Regimes considered for the problem, where $\mathcal{D}_\mathrm{t}$ and $\mathcal{D}_\mathrm{a}$ are the temporal and advective Deborah numbers, respectively.

order, the equations for which are given by (2.3.16)–(2.3.20) and (2.3.21)–(2.3.25), respectively, along with the appropriate structure evolution equations, given in Tables 2.1 and 2.2.

2.5 Rheological models

In this section, we introduce the three rheological models that we use in the remainder of this thesis. They are the simplified Moore–Mewis–Wagner (sMMW) model and the full Moore–Mewis–Wagner (MMW) model [7, 91], which exhibit viscous non-Newtonian behaviour, and the viscoplastic Houška model [10, 66].

2.5.1 The Moore–Mewis–Wagner model

In this model, the viscosity is taken to be a version of Moore's constitutive relation [91], which is given in dimensional form by

$$\hat{\eta} = \hat{\mu}_0 \lambda, \tag{2.5.1}$$

and the structure parameter λ satisfies Mewis and Wagner's structure evolution rate [7], which is given in dimensional form by

$$\hat{f}(\hat{\Gamma}, \lambda) = -\hat{k}_1 \hat{\Gamma}^{a/2} \lambda^b + \hat{k}_2 \hat{\Gamma}^{c/2} (1-\lambda)^d. \tag{2.5.2}$$

The parameters a, b, c, and d are non-negative, and the first and second terms on the right-hand side of (2.5.2) are the breakdown and build-up terms, with the associated positive rate constants $\hat{k}_1$ and $\hat{k}_2$, respectively.

We non-dimensionalise the constitutive relation (2.5.1) and the structure evolution rate (2.5.2) using the quantities defined in (2.2.1) and

$$\hat{f}_0 = \frac{\hat{k}_1 \hat{Q}_{\text{ref}}^a}{\hat{R}^{3a}} \quad \text{and} \quad \kappa = \frac{\hat{k}_2 \hat{Q}_{\text{ref}}^{c-a}}{\hat{k}_1 \hat{R}^{3(c-a)}}, \tag{2.5.3}$$

to obtain

$$\eta = \lambda, \tag{2.5.4}$$

and

$$f(\Gamma, \lambda) = -\Gamma^{a/2} \lambda^b + \kappa \Gamma^{c/2} (1-\lambda)^d, \tag{2.5.5}$$

respectively. At equilibrium, when the build-up and breakdown rates are balanced, denoted $\lambda = \lambda_{\text{eq}}$, the structure evolution rate is zero, i.e. $f(\Gamma, \lambda_{\text{eq}}) = 0$, so from (2.5.5) we obtain

$$\frac{\lambda_{\text{eq}}^b}{(1-\lambda_{\text{eq}})^d} = \kappa \Gamma^{(c-a)/2}. \tag{2.5.6}$$

We are not able to isolate λ_{eq} in (2.5.6) for general a, b, c, and d. However, in the special case of $d = 0$, in which we obtain the sMMW model, (2.5.6) yields

$$\eta = \lambda_{\text{eq}} = \kappa^{1/b} \Gamma^{(n-1)/2}, \quad \text{where} \quad n = \frac{c-a}{b} + 1. \tag{2.5.7}$$

So at equilibrium, the constitutive relation (2.5.7) is that of a power-law fluid, where n is the familiar power-law exponent (for which we require $n > 0$ for physical behaviour) and $\kappa^{1/b}$ is a dimensionless consistency parameter.

When $d > 0$, the build-up term in (2.5.5) bounds λ above, but when $d = 0$, λ may become large. For the sMMW model, we are able to obtain explicit solutions for the leading-order and first-order quantities in the weakly thixotropic regimes, which we present in Chapter 4. There are other special cases of the MMW model, aside from the sMMW model, which yield a constitutive relation simple enough to obtain explicit solutions, which we discuss briefly in Appendix B.

2.5.2 The regularised Houška model

We also consider fluids with yield-stress behaviour described by the Houška model — a thixotropic model, introduced by Houška [66], which exhibits structure-dependent yield-stress behaviour by incorperating a Herschel–Bulkley constitutive relation [96], and a structure-dependent viscosity parameter. The constitutive relation is

$$\begin{cases} \hat{\eta}(\dot{\gamma}, \lambda) = \dfrac{\hat{\tau}_{\mathrm{y}}(\lambda)}{\dot{\gamma}} + \hat{\eta}_{\mathrm{H}}(\lambda)\dot{\gamma}^{n-1} & \text{if} \quad \hat{\tau} > \hat{\tau}_{\mathrm{y}}(\lambda), \\ \dot{\gamma} = 0 & \text{if} \quad \hat{\tau} \leq \hat{\tau}_{\mathrm{y}}(\lambda), \end{cases} \tag{2.5.8}$$

where $\dot{\gamma}$ is the shear rate, $\hat{\eta}$ is the viscosity, $\hat{\tau}_{\mathrm{y}}$ is the yield stress, and $\hat{\eta}_{\mathrm{H}}$ is the viscosity parameter. Houška takes $\hat{\tau}_{\mathrm{y}}$ and $\hat{\eta}_{\mathrm{H}}$ to be linear functions of λ, i.e.

$$\hat{\tau}_{\mathrm{y}}(\lambda) = \hat{\tau}_{\mathrm{y}0} + \lambda\hat{\tau}_{\mathrm{y}1} \quad \text{and} \quad \hat{\eta}_{\mathrm{H}}(\lambda) = \hat{\eta}_{\mathrm{H}0} + \lambda\hat{\eta}_{\mathrm{H}1}, \tag{2.5.9}$$

where $\lambda \in [0, 1]$. We assume the viscosity parameter $\hat{\eta}_{\mathrm{H}}$ and the yield stress $\hat{\tau}_{\mathrm{y}}$ increase as the structure increases, hence we assume that $\hat{\eta}_{\mathrm{H}1} > 0$ and $\hat{\tau}_{\mathrm{y}1} > 0$. The structure evolves according to a special case of the structure evolution equation described by Mewis and Wagner [7], given by (2.5.2), in which $a = 1$, $b = 1$, $c = 0$, and $d = 1$, i.e.

$$\hat{f}(\hat{\Gamma}, \lambda) = -\hat{k}_1\hat{\Gamma}^{1/2}\lambda + \hat{k}_2(1 - \lambda). \tag{2.5.10}$$

We can select $n < 1$, $n = 1$, or $n > 1$ in the constitutive relation (2.5.8) for shear-thinning, Bingham, or shear-thickening yield-stress behaviour, respectively, though here we take $n = 1$ for simplicity. The constitutive relation is only differentiable at $\hat{\tau} = \hat{\tau}_{\mathrm{y}}$ when $n < 1$, but for $n \geq 1$ it is not, and the stress–shear-rate relation is not well defined at $\dot{\gamma} = 0$. We regularise the constitutive relation so that it exhibits 'pseudo-yield-stress' behaviour using a single, smooth function incorporating a regularisation parameter $\hat{k}$, as done by Papanastasiou [58]. When $\hat{k}$ is numerically large, we approximate true yield-stress behaviour without the associated numerical difficulties. To this end, we follow PWM and

Papanastasiou [58] and amend (2.5.8) so that

$$\hat{\eta}(\dot{\gamma},\lambda) = \frac{\hat{\tau}_{\mathrm{y}}(\lambda)(1-\mathrm{e}^{-\hat{k}\dot{\gamma}})}{\dot{\gamma}} + \hat{\eta}_{\mathrm{H}}(\lambda)\dot{\gamma}^{n-1}, \tag{2.5.11}$$

for all values of $\dot{\gamma}$. We non-dimensionalise (2.5.10) and (2.5.11) using the quantities defined in (2.2.1) and (2.5.3), together with the scale $\hat{\mu}_0 = \hat{\eta}_{\mathrm{H0}}$ and

$$\eta_{\mathrm{H1}} = \frac{\hat{\eta}_{\mathrm{H1}}}{\hat{\eta}_{\mathrm{H0}}}, \quad k = \frac{\hat{k}\hat{Q}_{\mathrm{ref}}}{\hat{R}^3}, \quad \tau_{\mathrm{y0}} = \frac{\hat{\tau}_{\mathrm{y0}}\hat{R}^3}{\hat{\eta}_{\mathrm{H0}}\hat{Q}_{\mathrm{ref}}}, \quad \text{and} \quad \tau_{\mathrm{y1}} = \frac{\hat{\tau}_{\mathrm{y1}}\hat{R}^3}{\hat{\eta}_{\mathrm{H0}}\hat{Q}_{\mathrm{ref}}}, \tag{2.5.12}$$

which (with $n = 1$) yields

$$f(\Gamma,\lambda) = -\Gamma^{1/2}\lambda + \kappa(1-\lambda), \tag{2.5.13}$$

$$\eta(\dot{\gamma},\lambda) = \frac{(\tau_{\mathrm{y0}} + \lambda\tau_{\mathrm{y1}})(1-\mathrm{e}^{-k\dot{\gamma}})}{\dot{\gamma}} + 1 + \lambda\eta_{\mathrm{H1}}, \tag{2.5.14}$$

respectively. The constitutive relation (2.5.14) now exhibits pseudo-yield-stress behaviour as $k \to \infty$, in which limit we recover true yield-stress behaviour.

Generally, pipe flow of a viscoplastic fluid consists of a yielded region of fluid near the wall of the pipe in which the yield stress is exceeded and the fluid is viscous, and a 'plugged' region at the centre of the pipe where the fluid is not yielded and the viscosity is at its maximum. At the boundary between the yielded and unyielded fluid there is a 'fake' yield surface [41]. As viscoplasticity is a common property of complex fluids, we are keen to see how it affects the flow of a thixotropic fluid. In addition, by studying the Houška model, we will be able to compare the qualitative behaviour between a viscoplastic model and a purely viscous model, and therefore obtain insight into the generality of flow features across models. This comparison is important for determining whether we may describe the qualitative behaviour of thixotropic fluid flow.

Chapter 3

General Solutions in the Weakly Thixotropic Regimes

In this chapter, we obtain general solutions for the unsteady flow of a thixotropic or antithixotropic fluid in the weakly thixotropic regimes — the quickly adjusting (and very weakly advective) regime $\mathfrak{R}_{1,2}$, the weakly advective (and very quickly adjusting) regime $\mathfrak{R}_{2,1}$, and the quickly adjusting and weakly advective regime $\mathfrak{R}_{1,1}$. The governing equations for these regimes were derived in Chapter 2.

In the weakly thixotropic regimes, the Deborah numbers are $\mathcal{O}(\delta)$ in magnitude or smaller. At leading order ($\mathcal{O}(1)$), fluid flowing in the weakly thixotropic regimes exhibits generalised Newtonian behaviour, with no thixotropic behaviour. At first order ($\mathcal{O}(\delta)$), thixotropic effects enter as perturbations to the leading-order behaviour. As discussed in Section 2.4, we do not need to consider each of the weakly thixotropic regimes separately from the outset because we can obtain the solutions in $\mathfrak{R}_{1,2}$, $\mathfrak{R}_{2,1}$, and $\mathfrak{R}_{2,2}$ by setting the appropriate Deborah number(s) to zero in the solutions in $\mathfrak{R}_{1,1}$.

After obtaining the general solutions, we study the leading-order behaviour and perturbations for three rheological models, introduced in Section 2.5. In Chapter 4, we study the simplified MMW (sMMW, with $d = 0$) and full MMW (with $d > 0$) models, which both exhibit purely viscous behaviour. In Chapter 5, we study the regularised viscoplastic Houška model. To guide the discussion of the

behaviour of these models, we refer to the work of Pritchard et al. [29] (PWM), who studied the steady flow of thixotropic and antithixotropic fluids in a slowly varying 2D channel. From their results, we obtain the qualitative behaviour of the perturbations for a thixotropic (shear-thinning) fluid in a widening channel, and a corresponding physical interpretation of the behaviour based on physical intuition. We define the behaviour in this reference case in Section 3.3.1, and aim to determine whether this reference case and corresponding interpretation obtained from PWM provide a qualitative description of thixotropic pipe flow in general.

We present the governing equations for unsteady thixotropic pipe flow in the quickly adjusting and weakly advective regime in Section 3.1. The then use these solutions to study the behaviour for the three rheologies in the following chapters.

3.1 Governing equations

At leading order, the weakly thixotropic regimes $\mathfrak{R}_{1,1}$, $\mathfrak{R}_{1,2}$, $\mathfrak{R}_{2,1}$, and $\mathfrak{R}_{2,2}$ share the same governing equations: the mass conservation equation (2.3.16), the momentum equation (2.3.17), and the corresponding structure evolution equation from Table 2.1. We rewrite these equations here for reference:

$$\frac{1}{r}\frac{\partial}{\partial r}(ru_0) + \frac{\partial w_0}{\partial z} = 0, \tag{3.1.1}$$

$$\frac{1}{r}\frac{\partial}{\partial r}\left(r\eta_0\frac{\partial w_0}{\partial r}\right) = -G_0(z,t), \tag{3.1.2}$$

$$0 = f_0. \tag{3.1.3}$$

Equations (3.1.1)–(3.1.3) are subject to the no-slip and no-penetration conditions at the wall (2.3.18), the symmetry condition at the centreline (2.3.19), and the

flux condition (2.3.20):

$$u_0 = 0 = w_0 \quad \text{at} \quad r = \alpha(z), \tag{3.1.4}$$

$$\eta_0 \frac{\partial w_0}{\partial r} = 0 = u_0 \quad \text{at} \quad r = 0, \tag{3.1.5}$$

$$2\pi \int_0^{\alpha(z)} w_0(r, z, t) r \, \mathrm{d}r = Q(t). \tag{3.1.6}$$

At first order, the governing equations for the quickly adjusting and weakly advective regime $\mathfrak{R}_{1,1}$ are the mass conservation equation (2.3.21), the momentum equation (2.3.22), and the corresponding structure evolution equation from Table 2.2. We rewrite these equations here for reference:

$$\frac{1}{r}\frac{\partial}{\partial r}(r u_1) + \frac{\partial w_1}{\partial z} = 0, \tag{3.1.7}$$

$$\frac{1}{r}\frac{\partial}{\partial r}\left[r\left(\eta_0 \frac{\partial w_1}{\partial r} + \left(2\eta_\Gamma \frac{\partial w_0}{\partial r}\frac{\partial w_1}{\partial r} + \eta_\lambda \lambda_1\right)\frac{\partial w_0}{\partial r}\right)\right] = -G_1(z, t), \tag{3.1.8}$$

$$\mathcal{D}_\mathrm{t}^* \frac{\partial \lambda_0}{\partial t} + \mathcal{D}_\mathrm{a}^*\left(u_0 \frac{\partial \lambda_0}{\partial r} + w_0 \frac{\partial \lambda_0}{\partial z}\right) = 2 f_\Gamma \frac{\partial w_0}{\partial r}\frac{\partial w_1}{\partial r} + f_\lambda \lambda_1. \tag{3.1.9}$$

Equations (3.1.7)–(3.1.9) are subject to the no-slip and no-penetration conditions at the wall (2.3.23), the symmetry condition at the centreline (2.3.24), and the flux condition (2.3.25):

$$u_1 = 0 = w_1 \quad \text{at} \quad r = \alpha(z), \tag{3.1.10}$$

$$\eta_0 \frac{\partial w_1}{\partial r} + \left(2\eta_\Gamma \frac{\partial w_0}{\partial r}\frac{\partial w_1}{\partial r} + \eta_\lambda \lambda_1\right)\frac{\partial w_0}{\partial r} = 0 = u_1 \quad \text{at} \quad r = 0, \tag{3.1.11}$$

$$\int_0^{\alpha(z)} w_1(r, z, t) r \, \mathrm{d}r = 0. \tag{3.1.12}$$

We can obtain the governing equations for the weakly advective regime or the quickly adjusting regime by setting $\mathcal{D}_\mathrm{t}^* = 0$ or $\mathcal{D}_\mathrm{a}^* = 0$, respectively, in (3.1.9).

We are able to solve the governing equations in the weakly thixotropic regimes in general, without specifying a particular rheology, i.e. for general $\eta(\Gamma, \lambda)$ and $f(\Gamma, \lambda)$, to obtain asymptotic solutions in terms of integrals. In Section 3.2, we obtain general solutions for the leading-order streamwise velocity w_0, transverse

velocity u_0, structure parameter λ_0, and pressure gradient G_0. In Section 3.3, we obtain general solutions for the streamwise velocity perturbation w_1, the structure parameter perturbation λ_1, and the pressure gradient perturbation G_1.

3.2 General solutions at $\mathcal{O}(1)$

In this section, we solve the leading-order governing equations (3.1.1)– (3.1.3) subject to (3.1.4)–(3.1.6) for general $\eta(\Gamma, \lambda)$ and $f(\Gamma, \lambda)$. We begin by adapting the method of PWM [29], and define a variable q equal to the leading-order shear rate, so at equilibrium ($f(\Gamma, \lambda) = 0$) we may write the stress τ as

$$\tau(q) = \eta(q^2, \lambda)q, \quad \text{subject to} \quad f(q^2, \lambda) = 0, \quad \text{where} \quad q = \frac{\partial w_0}{\partial r}. \tag{3.2.1}$$

We rewrite the leading-order momentum equation (3.1.2) using (3.2.1), which yields

$$\frac{1}{r}\frac{\partial}{\partial r}\left(r\tau(q)\right) = -G_0(z,t). \tag{3.2.2}$$

Rearranging and integrating (3.2.2) with respect to r yields

$$\tau(q) = -\frac{G_0(z,t)r}{2} \quad \text{or} \quad q = \tau^{-1}\left(-\frac{G_0(z,t)r}{2}\right), \tag{3.2.3}$$

where we have applied the symmetry condition (3.1.5). We note that for (3.2.3) to be valid, $\tau(q)$ must be invertible (which is a constraint on the rheological models we may use). To obtain the general solution for w_0, we integrate the second of (3.2.3) with respect to r, which yields

$$w_0(r,z,t) = -\int_r^{\alpha(z)} \tau^{-1}\left(-\frac{G_0(z,t)r'}{2}\right) \mathrm{d}r'. \tag{3.2.4}$$

Using the substitution $\xi = -G_0(z,t)r'/2$, so $\mathrm{d}r' = -(2/G_0(z,t))\mathrm{d}\xi$, (3.2.4) becomes

$$w_0(r,z,t) = \frac{2}{G_0(z,t)}\int_{-G_0(z,t)r/2}^{-G_0(z,t)\alpha(z)/2} \tau^{-1}(\xi)\,\mathrm{d}\xi, \tag{3.2.5}$$

which we evaluate using quadrature.

To obtain the general solution for u_0, we rearrange and integrate the mass conservation equation (3.1.1) with respect to r, which yields

$$u_0(r,z,t) = \frac{1}{r}\int_r^{\alpha(z)} r' \frac{\partial w_0}{\partial z}\,\mathrm{d}r'. \tag{3.2.6}$$

We require $\partial w_0/\partial z$, which we obtain by differentiating (3.2.5) with respect to z, which yields

$$\frac{\partial w_0}{\partial z} = \frac{2}{G_0}\frac{\partial}{\partial z}\int_{-G_0 r/2}^{-G_0\alpha/2} \tau^{-1}(\xi)\,\mathrm{d}\xi - \frac{2G_{0,z}}{G_0^2}\int_{-G_0 r/2}^{-G_0\alpha/2} \tau^{-1}(\xi)\,\mathrm{d}\xi, \tag{3.2.7}$$

where $G_{0,z} \equiv \partial G_0/\partial z$. Evaluating the integrals in (3.2.7) using Leibniz's rule for differentiation under an integral sign yields

$$\begin{aligned}\frac{\partial w_0}{\partial z} = \frac{2}{G_0}\Bigg[&-\tau^{-1}\left(-\frac{G_0\alpha}{2}\right)\frac{\partial}{\partial z}\left(\frac{G_0\alpha}{2}\right) + \tau^{-1}\left(-\frac{G_0 r}{2}\right)\frac{\partial}{\partial z}\left(\frac{G_0 r}{2}\right) \\ &+ \int_{-G_0 r/2}^{-G_0\alpha/2} \frac{\partial}{\partial z}\tau^{-1}(\xi)\,\mathrm{d}\xi\Bigg] - \frac{2G_{0,z}}{G_0^2}\int_{-G_0 r/2}^{-G_0\alpha/2} \tau^{-1}(\xi)\,\mathrm{d}\xi.\end{aligned} \tag{3.2.8}$$

We define the leading-order shear rate at the wall as

$$q_\mathrm{w} = q(\alpha(z),z,t) \quad \text{so that} \quad \tau(q_\mathrm{w}) = -\frac{G_0(z,t)\alpha(z)}{2}. \tag{3.2.9}$$

By using the second of (3.2.3) and by comparing the last term on the right-hand side of (3.2.8) with (3.2.5), (3.2.8) becomes

$$\frac{\partial w_0}{\partial z} = \frac{2}{G_0}\left[-q_\mathrm{w}\frac{\partial}{\partial z}\left(\frac{G_0\alpha}{2}\right) + q\frac{\partial}{\partial z}\left(\frac{G_0 r}{2}\right)\right] - \frac{G_{0,z}}{G_0}w_0, \tag{3.2.10}$$

which simplifies to

$$\frac{\partial w_0}{\partial z} = \frac{1}{G_0}\frac{\partial G_0}{\partial z}(qr - w_0) - \frac{q_\mathrm{w}}{G_0}\frac{\partial}{\partial z}(G_0\alpha). \tag{3.2.11}$$

By replacing $\partial w_0/\partial z$ in (3.2.6) with (3.2.11), (3.2.6) becomes

$$\begin{aligned} u_0(r,z,t) = \frac{1}{G_0(z,t)r}\frac{\partial G_0}{\partial z}\int_r^{\alpha(z)} qr'^2 - r'w_0(r',z,t)\,\mathrm{d}r' \\ - \frac{q_\mathrm{w}(z,t)}{G_0(z,t)r}\frac{\partial}{\partial z}\left(G_0(z,t)\alpha(z)\right)\int_r^{\alpha(z)} r'\,\mathrm{d}r'. \end{aligned} \tag{3.2.12}$$

We evaluate the first integral on the right-hand side of (3.2.12) by parts to obtain

$$\int_r^{\alpha(z)} qr'^2 - r'w_0(r',z,t)\,\mathrm{d}r' = \left[w_0(r',z,t)r'^2\right]_r^{\alpha(z)} - 3\int_r^{\alpha(z)} r'w_0(r',z,t)\,\mathrm{d}r'. \tag{3.2.13}$$

After applying the no-slip boundary condition at the wall (3.1.4) and evaluating the second integral in (3.2.12), we obtain

$$\begin{aligned} u_0(r,z,t) = -\frac{1}{G_0(z,t)r}\frac{\partial G_0}{\partial z}\left(w_0(r,z,t)r^2 + 3\int_r^{\alpha(z)} r'w_0(r',z,t)\,\mathrm{d}r'\right) \\ - \frac{q_\mathrm{w}(z,t)}{2G_0(z,t)r}\frac{\partial}{\partial z}\left(G_0(z,t)\alpha(z)\right)\left(\alpha^2 - r^2\right). \end{aligned} \tag{3.2.14}$$

Following some simplification and evaluating the integral in (3.2.14) by integrating by parts, we obtain

$$\begin{aligned} u_0(r,z,t) = \frac{r}{2G_0}\left(2\frac{\partial G_0}{\partial z}w_0 - q_\mathrm{w}\frac{\partial}{\partial z}\left(G_0\alpha\right)\right) - \frac{q_\mathrm{w}\alpha^2}{2G_0 r}\frac{\partial}{\partial z}\left(G_0\alpha\right) \\ + \frac{3}{2G_0 r}\frac{\partial G_0}{\partial z}\left(r^2 w_0 + \int_r^{\alpha} r'^2\frac{\partial w_0}{\partial r}\,\mathrm{d}r'\right). \end{aligned} \tag{3.2.15}$$

We perform a variable change in the integral in (3.2.15) from r to q. To achieve this change, we differentiate the first of (3.2.3) with respect to r using the chain rule, which yields

$$\frac{\mathrm{d}\tau}{\mathrm{d}q}\frac{\partial q}{\partial r} = -\frac{G_0(z,t)}{2}, \tag{3.2.16}$$

and so, after rearranging, we find

$$\mathrm{d}r = -\frac{2\tau'(q)}{G_0(z,t)}\,\mathrm{d}q. \tag{3.2.17}$$

In addition, by rearranging the first of (3.2.3) to isolate r, we obtain

$$r = -\frac{2\tau(q)}{G_0(z,t)}. \tag{3.2.18}$$

Now, using (3.2.9), we can rewrite (3.2.15) as

$$\begin{aligned} u_0(r,z,t) = \frac{r}{2G_0}\left(2\frac{\partial G_0}{\partial z}w_0 - q_\mathrm{w}\frac{\partial}{\partial z}\left(G_0\alpha\right)\right) - \frac{q_\mathrm{w}\alpha^2}{2G_0 r}\frac{\partial}{\partial z}\left(G_0\alpha\right) \\ + \frac{3r}{2G_0}\frac{\partial G_0}{\partial z}w_0 - \frac{12}{G_0^4 r}\frac{\partial G_0}{\partial z}\int_q^{q_\mathrm{w}} q\tau^2\tau'\,\mathrm{d}q. \end{aligned} \tag{3.2.19}$$

We also require general solutions for G_0, $\partial G_0/\partial z$, and $\partial G_0/\partial t$ to use with (3.2.5) and (3.2.19). To find these solutions, we use the leading-order flux condition (3.1.6) and change variables following Weissenberg (see PWM and [84]). In particular, we evaluate the integral in (3.1.6) by integrating by parts, which yields

$$Q(t) = 2\pi\left(\left[\frac{r^2}{2}w_0(r,z,t)\right]_0^{\alpha(z)} - \int_0^{\alpha(z)}\frac{r^2}{2}\frac{\partial w_0}{\partial r}\,\mathrm{d}r\right). \tag{3.2.20}$$

The no-slip condition (3.1.4) requires that $w_0 = 0$ at $r = \alpha$, so (3.2.20) becomes

$$Q(t) = -\pi\int_0^{\alpha(z)} r^2\frac{\partial w_0}{\partial r}\,\mathrm{d}r. \tag{3.2.21}$$

From here, we perform a variable change from r to q following the same process used for the integral in (3.2.15). We note that at the centreline the shear rate is zero, so the lower limit of the integral $r = 0$ in (3.2.21) becomes $q = 0$. Following the variable transformation, we obtain

$$Q(t) = \frac{8\pi}{G_0^3(z,t)}\int_0^{q_\mathrm{w}} q\tau^2(q)\tau'(q)\,\mathrm{d}q. \tag{3.2.22}$$

We rearrange (3.2.22) for $G_0^3(z,t)$ to obtain

$$G_0^3(z,t) = \frac{8\pi}{Q(t)}\int_0^{q_\mathrm{w}} q\tau^2(q)\tau'(q)\,\mathrm{d}q. \tag{3.2.23}$$

We find the derivatives of G_0 by differentiating and rearranging (3.2.23) appropriately. First, we find the derivative of $\partial G_0/\partial z$ by differentiating (3.2.23) with respect to z, which yields

$$3G_0^2(z,t)\frac{\partial G_0}{\partial z} = \frac{2\pi}{Q(t)}q_{\mathrm{w}}(z,t)G_0^2(z,t)\alpha^2(z)\frac{\partial}{\partial z}\left(-\frac{G_0(z,t)\alpha(z)}{2}\right), \quad (3.2.24)$$

and rearranges to

$$\frac{\partial G_0}{\partial z} = -\frac{\pi q_{\mathrm{w}}(z,t)G_0(z,t)\alpha^2(z)\alpha'(z)}{3Q(t)+\pi q_{\mathrm{w}}(z,t)\alpha^3(z)}. \quad (3.2.25)$$

Now, for the derivative of G_0 with respect to t, we find

$$\begin{aligned} 3G_0^2(z,t)\frac{\partial G_0}{\partial t} = &-\frac{8\pi}{Q^2(t)}Q'(t)\int_0^{q_{\mathrm{w}}} q\tau^2(q)\tau'\,\mathrm{d}q \\ &+\frac{2\pi}{Q(t)}q_{\mathrm{w}}(z,t)G_0^2(z,t)\alpha^2(z)\frac{\partial}{\partial t}\left(-\frac{G_0(z,t)\alpha(z)}{2}\right), \end{aligned} \quad (3.2.26)$$

which rearranges to

$$\frac{\partial G_0}{\partial t} = -\frac{8\pi Q'(t)}{G_0^2(z,t)Q(t)\left[3Q(t)+\pi q_{\mathrm{w}}(z,t)\alpha^3(z)\right]}\int_0^{q_{\mathrm{w}}} q\tau^2(q)\tau'\,\mathrm{d}q. \quad (3.2.27)$$

We are able to obtain a general solution for λ_0, as it is defined implicitly by

$$f(q^2(r,z,t),\lambda_0(r,z,t)) = 0. \quad (3.2.28)$$

We also require various derivatives to obtain the general solutions at first order (presented in Section 3.3). We find these derivatives by implicitly differentiating (3.2.28) with respect to r, z, and t, which yields

$$\frac{\partial f}{\partial x} = 2qf_\Gamma(q^2,\lambda_0)\frac{\partial q}{\partial x} + f_\lambda(q^2,\lambda_0)\frac{\partial \lambda_0}{\partial x} = 0, \quad (3.2.29)$$

where $x \in \{r,z,t\}$. By rearranging (3.2.29) we obtain

$$\frac{\partial \lambda_0}{\partial x} = -\frac{2qf_\Gamma(q^2,\lambda_0)}{f_\lambda(q^2,\lambda_0)}\frac{\partial q}{\partial x}. \quad (3.2.30)$$

Using (3.2.3), we find the derivatives of q with respect to r, z, and t, given by

$$\frac{\partial q}{\partial r} = -\frac{G_0(z,t)}{2\tau'(q)}, \quad \frac{\partial q}{\partial z} = -\frac{\partial G_0}{\partial z}\frac{r}{2\tau'(q)}, \quad \text{and} \quad \frac{\partial q}{\partial t} = -\frac{\partial G_0}{\partial t}\frac{r}{2\tau'(q)}, \tag{3.2.31}$$

respectively.

We have now obtained general solutions for w_0, u_0, λ_0, and G_0, and the various associated derivatives. After selecting the rheological model by defining $f(\Gamma,\lambda)$ and $\eta(\Gamma,\lambda)$, we evaluate the integrals in (3.2.5), (3.2.19), and (3.2.23) using the computer algebra package Maple. For some rheologies, such as the sMMW model, we are able to obtain explicit solutions for the leading-order behaviour.

3.3 General solutions at $\mathcal{O}(\delta)$

In this section, we solve the first-order governing equations (3.1.7)–(3.1.9) subject to (3.1.10)–(3.1.12) for general $\eta(\Gamma,\lambda)$ and $f(\Gamma,\lambda)$. We begin by isolating λ_1 in (3.1.9) to obtain

$$\lambda_1 = \frac{1}{f_\lambda}\left[\mathcal{D}^*_{\mathrm{t}}\frac{\partial\lambda_0}{\partial t} + \mathcal{D}^*_{\mathrm{a}}\left(u_0\frac{\partial\lambda_0}{\partial r} + w_0\frac{\partial\lambda_0}{\partial z}\right)\right] - 2\frac{f_\Gamma}{f_\lambda}\frac{\partial w_0}{\partial r}\frac{\partial w_1}{\partial r}. \tag{3.3.1}$$

Replacing λ_1 in (3.1.8) using (3.3.1) yields

$$\frac{1}{r}\frac{\partial}{\partial r}\left[rA(r,z,t)\frac{\partial w_1}{\partial r} + rB(r,z,t)\right] = -G_1(z,t), \tag{3.3.2}$$

where

$$A(r,z,t) = \eta_0 + 2\left(\eta_\Gamma - \eta_\lambda\frac{f_\Gamma}{f_\lambda}\right)\left(\frac{\partial w_0}{\partial r}\right)^2, \tag{3.3.3}$$

$$B(r,z,t) = \frac{\eta_\lambda}{f_\lambda}\left[\mathcal{D}^*_{\mathrm{t}}\frac{\partial\lambda_0}{\partial t} + \mathcal{D}^*_{\mathrm{a}}\left(u_0\frac{\partial\lambda_0}{\partial r} + w_0\frac{\partial\lambda_0}{\partial z}\right)\right]\frac{\partial w_0}{\partial r}, \tag{3.3.4}$$

where $B(r,z,t)$ is the additional stress due to thixotropy, which we refer to as the *thixotropic stress term*. By rearranging (3.3.2) and integrating with respect

to r, we obtain

$$A(r,z,t)\frac{\partial w_1}{\partial r} + B(r,z,t) = -\frac{1}{2}G_1(z,t)r + \frac{C}{r}, \tag{3.3.5}$$

where C is a constant of integration. For (3.3.5) to be well defined as $r \to 0$, we require $C = 0$. Now, rearranging (3.3.5) for $\partial w_1/\partial r$ yields

$$\frac{\partial w_1}{\partial r} = -\frac{G_1(z,t)r}{2A(r,z,t)} + \frac{B(r,z,t)}{A(r,z,t)}. \tag{3.3.6}$$

Integrating (3.3.6) with respect to r, using the no-slip condition at the wall (3.1.10), yields the general solution for w_1:

$$w_1(r,z,t) = \frac{1}{2}G_1(z,t)\int_r^{\alpha(z)} \frac{r'}{A(r',z,t)}\,\mathrm{d}r' + \int_r^{\alpha(z)} \frac{B(r',z,t)}{A(r',z,t)}\,\mathrm{d}r'. \tag{3.3.7}$$

Finally, by integrating (3.3.7) with respect to r, applying the flux condition (3.1.12), and rearranging, we obtain the general solution for G_1:

$$G_1(z,t) = -\frac{2\displaystyle\int_0^{\alpha(z)} r\int_r^{\alpha(z)} \frac{B(r',z,t)}{A(r',z,t)}\,\mathrm{d}r'\mathrm{d}r}{\displaystyle\int_0^{\alpha(z)} r\int_r^{\alpha(z)} \frac{r'}{A(r',z,t)}\,\mathrm{d}r'\mathrm{d}r}. \tag{3.3.8}$$

The solutions for w_1, λ_1, and G_1, given by (3.3.7), (3.3.1), and (3.3.8), respectively, are the perturbation solutions for general η and f. In some cases we are able to obtain explicit solutions, such as the sMMW model and a few special cases of the MMW model (presented in Appendix B), which provide results against which we have verified the implementation of the general solutions in Maple. Before presenting examples of the perturbation quantities, we use the results of PWM to define a reference case for the 'expected' behaviour of the perturbations w_1 and λ_1.

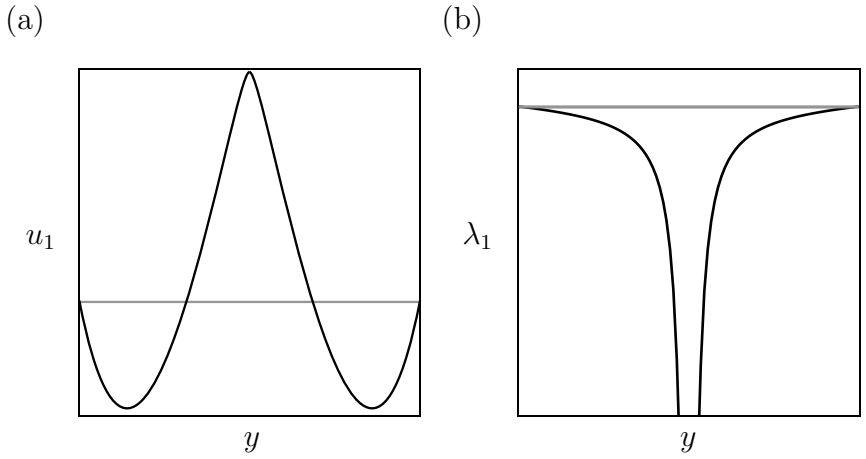

Figure 3.1: Sketches of (a) the streamwise velocity perturbation u_1 and (b) the structure parameter perturbation λ_1 for a thixotropic fluid in a widening channel in the weakly advective regime, as found by PWM. We refer to this behaviour as the thixotropic reference case (TRC).

3.3.1 Thixotropic reference case (TRC)

When studying the perturbation quantities in the present flow set-up, we use the recent results of PWM as a reference case. PWM studied the steady flow of a thixotropic or antithixotropic fluid in a widening 2D channel in the weakly advective regime. Figure 3.1 shows, retaining the notation of PWM in which y is the transverse co-ordinate, the qualitative behaviour of the streamwise velocity perturbation u_1 (equivalent to w_1 in the present work) and the structure parameter perturbation λ_1 for a thixotropic fluid.

We refer to the behaviour shown in Figure 3.1, in which the streamwise velocity perturbation is positive at the centre of the channel and negative at the walls, and the structure parameter perturbation is negative and largest at the centre of the channel, as the *thixotropic reference case* (TRC).

The behaviour in the TRC agrees with physical intuition, because in a widening pipe the shear rate is higher upstream than downstream, so the structure is broken down upstream. As the fluid flows downstream, the structure is advected from a region of high shear to a region of low shear. In the absence of thixotropy, the structure would build up immediately as the shear rate decreases, but ad-

vective thixotropy slows the build-up, so the structure remains broken down, as indicated by the negative structure parameter perturbation in Figure 3.1(b). PWM reason that fluid with a lower structure shears more readily, so flows more quickly, yielding a positive perturbation to the streamwise velocity at the centre of the channel where advection is strongest, i.e. where the leading-order velocity is largest, as shown in Figure 3.1(a). The streamwise velocity is negative near the walls to maintain the prescribed volume flux. We show in a later section that this reasoning does not fully explain all of the behaviour of the perturbations, but it will suffice for the following examples.

In addition to the TRC, we also pose two analogies that we expect, using the physical intuition described above, to hold. The first analogy is a thixotropy/ antithixotropy analogy, in which we expect the behaviour of the perturbations for antithixotropic fluids to be opposite to those for thixotropic fluids, i.e. to be the opposite of the behaviour shown in Figure 3.1. This analogy holds for the examples of antithixotropic fluids provided by PWM, but we shall see that it is not sufficient in all cases. The second analogy is a widening/decelerating analogy, in which we expect the behaviour of a fluid in a widening pipe in the weakly advective regime to be qualitatively similar to that in a decelerating flow in the quickly adjusting regime, because in both cases the shear rate decreases following a fluid element. As for the thixotropy/antithixotropy analogy, we will find that the widening/decelerating analogy does not hold in all cases.

In the following sections, we obtain and present the leading-order and perturbation solutions for the three rheological models, and determine the limits of the TRC and the analogies described above, and where the physical intuition behind them breaks down. When we describe a perturbation quantity as agreeing or disagreeing with the TRC, we assume that the appropriate analogy or analogies are applied.

3.4 Summary

In this chapter, we used the governing equations for unsteady and slowly varying thixotropic pipe flow derived in Chapter 2 to obtain general solutions for

flow in the quickly adjusting and weakly advective regimes. In addition, we constructed a reference case from the results of PWM, the TRC, for the perturbations to the streamwise velocity and the structure parameter, and presented a corresponding interpretation based on physical intuition. In further addition to the TRC, we posed two analogies: the thixotropic/antithixotropic analogy and the widening/decelerating analogy, which we used to extend the descriptive range of the TRC to antithixotropic fluids, and from the weakly advective regime to the quickly adjusting regime.

Having solutions for a general rheology, we are at liberty to choose specific rheologies that provide insight into thixotropic flows. In the following chapters, we use the general solutions obtained in this chapter, along with the TRC and analogies, to determine whether general statements can be made on the behaviour of unsteady thixotropic flows in a slowly varying pipe by thoroughly analysing the behaviour for three rheological models. In particular, in Chapter 4 we study the purely viscous sMMW and full MMW models, and in Chapter 5 we study the viscoplastic Houška model.

Chapter 4

Results for the sMMW and MMW models

In this chapter, we study the purely viscous models sMMW and full MMW models, introduced in Section 2.5.1. For the sMMW model, we are able to obtain closed-form solutions and thus we may present a full analysis of the behaviour of the fluid. For the MMW model, we use the general solutions obtained in Chapter 3 to present an extensive analysis of the behaviour of the fluid. In both cases, we find examples of behaviour that agree with the TRC and examples that do not. The latter behaviours indicate that the TRC and the analogies do not describe purely viscous thixotropic flow in general. For each model, we obtain the qualitative behaviour for the range of their respective parameters, and indictate which parameters yield TRC-like behaviour and which do not.

4.1 Results for the sMMW model

In this section, we obtain and discuss solutions for the leading-order behaviour and the perturbations for the sMMW model, introduced and non-dimensionalised in Section 2.5.1. The sMMW model is given by

$$\eta = \lambda \quad \text{and} \quad f = -\Gamma^{a/2}\lambda^b + \kappa\Gamma^{c/2}, \tag{4.1.1}$$

where the dimensionless quantities are defined via (2.2.1) and (2.5.3):

$$\hat{r} = \hat{R}r, \quad \hat{z} = \frac{\hat{R}z}{\delta}, \quad \hat{u} = \frac{\delta\hat{Q}_{\mathrm{ref}}u}{\hat{R}^2}, \quad \hat{w} = \frac{\hat{Q}_{\mathrm{ref}}w}{\hat{R}^2}, \quad \hat{\Gamma} = \frac{\hat{Q}_{\mathrm{ref}}^2\Gamma}{\hat{R}^6},$$
$$\hat{Q} = \hat{Q}_{\mathrm{ref}}Q, \quad \hat{p} = \frac{\hat{\mu}_0\hat{Q}_{\mathrm{ref}}p}{\delta\hat{R}^3}, \quad \hat{\eta} = \hat{\mu}_0\eta, \quad \hat{\alpha}(\hat{z}) = \hat{R}\alpha(z), \quad \hat{t} = \hat{T}t, \tag{4.1.2}$$
$$\hat{f}(\hat{\Gamma}, \lambda) = \hat{f}_0 f(\Gamma, \lambda), \quad \hat{f}_0 = \frac{\hat{k}_1\hat{Q}_{\mathrm{r}}^a}{\hat{R}^{3a}} \quad \text{and} \quad \kappa = \frac{\hat{k}_2\hat{Q}_{\mathrm{r}}^{c-a}}{\hat{k}_1\hat{R}^{3(c-a)}}.$$

For this model we are able to obtain explicit solutions, which will provide a validation test for the later implementation of the general solutions in Maple. We obtain the leading-order solutions in Section 4.1.1 and present examples of the behaviour in Section 4.1.2, and we obtain the perturbation solutions in Section 4.1.3 with examples in Sections 4.1.4–4.1.8.

4.1.1 Leading-order solutions

In this section, we obtain the solutions for the leading-order quantities w_0, λ_0, u_0, and G_0. Recalling from (2.3.11) that $\Gamma_0 = (\partial w_0/\partial r)^2$ and using (2.5.7), at leading order, we obtain

$$\eta_0 = \lambda_0 = \kappa^{1/b}\left|\frac{\partial w_0}{\partial r}\right|^{n-1}, \tag{4.1.3}$$

where n is the power-law exponent, defined in (2.5.7). By rearranging and integrating the leading-order momentum equation (3.1.2) with respect to r, and applying the symmetry condition at the centreline, given by (3.1.5), we obtain

$$\eta_0\frac{\partial w_0}{\partial r} = -\frac{1}{2}G_0 r. \tag{4.1.4}$$

Substituting η_0 in (4.1.3) into (4.1.4) yields

$$\left(\frac{\partial w_0}{\partial r}\right)^{n-1}\frac{\partial w_0}{\partial r} = -\frac{1}{2}\kappa^{-1/b}G_0 r. \tag{4.1.5}$$

By rearranging and integrating (4.1.5) with respect to r we obtain

$$w_0(r,z,t) = \frac{n}{n+1}\left(\frac{1}{2}\kappa^{-1/b}G_0\right)^{1/n}\alpha^{(n+1)/n}\left(1-\left(\frac{r}{\alpha}\right)^{(n+1)/n}\right), \tag{4.1.6}$$

using the no-slip boundary condition (3.1.4). This is the streamwise velocity of a power-law fluid in pipe flow (see, for example, [1]).

By using (4.1.6) with the flux condition (3.1.6) we obtain

$$Q(t) = \frac{2\pi n}{n+1}\left(\frac{\kappa^{-1/b}G_0(t)}{2}\right)^{1/n}\int_0^\alpha \left(\alpha^{(n+1)/n} - r^{(n+1)/n}\right) r\,\mathrm{d}r, \tag{4.1.7}$$

which yields

$$Q(t) = \frac{\pi n}{3n+1}\left(\frac{\kappa^{-1/b}G_0}{2}\right)^{1/n}\alpha^{(3n+1)/n}. \tag{4.1.8}$$

Rearranging (4.1.8) yields the leading-order pressure gradient G_0 in terms of known quantities:

$$G_0(z,t) = 2\kappa^{1/b}\alpha^{-(3n+1)}\left(\frac{3n+1}{\pi n}Q\right)^n. \tag{4.1.9}$$

Substituting (4.1.9) for G_0 in (4.1.6) yields the solution for w_0:

$$w_0(r,z,t) = \frac{3n+1}{\pi(n+1)}\frac{Q}{\alpha^2}\left(1-\left(\frac{r}{\alpha}\right)^{(n+1)/n}\right). \tag{4.1.10}$$

Using (4.1.10) with (4.1.3) yields the solution for λ_0:

$$\lambda_0(r,z,t) = \kappa^{1/b}\left(\frac{3n+1}{\pi n}Q\alpha^{-(3n+1)/n}\right)^{n-1} r^{(n-1)/n}. \tag{4.1.11}$$

Finally, we rearrange and integrate the mass conservation equation (3.1.1) with respect to r to obtain

$$u_0 = \frac{1}{r}\int_r^\alpha \frac{\partial w_0}{\partial z} r'\,\mathrm{d}r', \tag{4.1.12}$$

which with (4.1.10) yields the solution for u_0:

$$u_0(r,z,t) = \frac{3n+1}{\pi(n+1)}\frac{Q}{\alpha^2}\frac{\alpha'}{\alpha}r\left(1-\left(\frac{r}{\alpha}\right)^{(n+1)/n}\right). \tag{4.1.13}$$

The leading-order solutions are important to understanding the behaviour of the perturbations, so in the following section, we briefly present and discuss examples of the leading-order behaviour.

4.1.2 Examples of leading-order quantities

In this section, we present examples of the leading-order quantities w_0, λ_0, u_0, and G_0, given by (4.1.10), (4.1.11), (4.1.13), and (4.1.9), respectively. Figures 4.1(a)–(c) show examples these quantities, respectively, in a widening pipe ($\alpha' > 0$) for various values of n. We note that the dimensionless quantities (4.1.2) vary with a and c (and so vary with n), so here, and in subsequent figures, profiles for different values of a, b, or c are not directly comparable. In this figure, the arrows indicate the direction of increasing n. In addition, Figure 4.1(d) shows an example of G_0 as a function of n.

Figure 4.1(a) shows examples of the leading-order streamwise velocity w_0, given by (4.1.10), which exhibits the well-known behaviour of a power-law fluid (e.g. see [1]). In particular, when $n = 1$, the profile of w_0 is that of classic Poiseuille flow of a Newtonian fluid along a pipe. When $n < 1$, i.e. for thixotropic fluids, the profile of w_0 near the centre of the pipe is flatter than when $n = 1$, indicating plug-like flow, with a steeper gradient near the wall of the pipe, indicating a high shear rate. When $n > 1$, i.e. for antithixotropic fluids, the profile of w_0 near the centre of the pipe is sharper than when $n = 1$, with a shallower gradient near the wall.

Figure 4.1(b) shows examples of the leading-order structure parameter λ_0, given by (4.1.11). In particular, when $n = 1$ the fluid is Newtonian, so the structure does not depend on the shear rate, so $\lambda_0 = \kappa^{1/b} = 1$ across the width of the pipe. In the example shown in Figure 4.1(b), we choose $\kappa = 1$ and $b = 1$, so $\lambda_0 = 1$. When $n < 1$, λ_0 diverges at the centre of the pipe, and so the viscosity

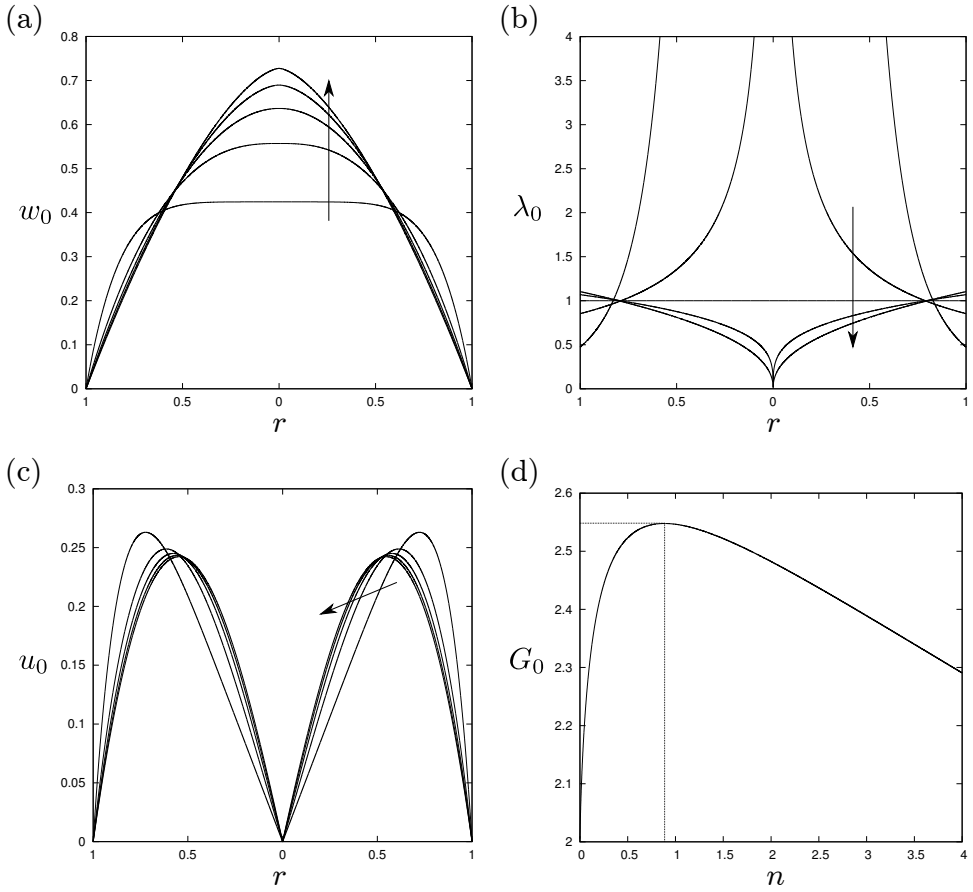

Figure 4.1: sMMW model: profiles of (a) w_0, (b) λ_0, and (c) u_0 for various values of n, and (d) G_0 as a function of n. In (a,b,c) $n = 0.4$ ($c = 0.4$, $G_0 = 2.502$), $n = 0.7$ ($c = 0.7$, $G_0 = 2.543$), $n = 1$ ($c = 1$, $G_0 = 2.546$), $n = 1.3$ ($c = 1.3$, $G_0 = 2.534$), and $n = 1.6$ ($c = 1.6$, $G_0 = 2.515$). The common parameters are $\kappa = 1$, $Q(t) = 1$, $\alpha(z) = 1$, $\alpha'(z) = 1$, $a = 1$, and $b = 1$. The arrows show the direction of increasing n, i.e. from thixotropic to antithixotropic behaviour.

also diverges here (as $\eta_0 = \lambda_0$). When $n > 1$, λ_0 decreases monotonically from the wall to zero at the centre of the pipe, and so the viscosity is also zero at the centre.

Figure 4.1(c) shows examples of the transverse velocity u_0. In general for a widening pipe, u_0 is positive everywhere, indicating that the direction of flow is away from the centre, as expected, and u_0 is largest between the centre of the pipe and the wall. The behaviour of u_0 does not vary substantially with n, except that u_0 is larger near the wall for $n < 1$ than for $n > 1$. Figure 4.1(d) shows G_0 as a function of n. We note that the pressure gradient required to drive the prescribed flux is largest when n is slightly less than unity. It is not clear why this is the case.

The leading-order behaviour shown in Figure 4.1 agrees with physical intuition. For thixotropic fluids, the fluid is highly structured near the centreline where the shear rate is low, leading to a flat profile near the centreline. Near the wall, the shear rate is high which de-structures the fluid and decreases the viscosity, allowing the fluid to flow more easily, which lubricates the high-viscosity fluid near the centreline. For antithixotropic fluids, the behaviour is reversed. Near the wall, the high shear rate builds up the structure and the viscosity, which means the fluid flows less readily, so to maintain the prescribed volume flux, flow is increased near the centreline where the viscosity is low.

4.1.3 Perturbation solutions

In this section, we obtain the solutions for the perturbation quantities w_1, λ_1, and G_1. To find the solutions for the perturbations we use the general solutions obtained in Section 3.3. In particular, we use equations (3.3.7), (3.3.1), and (3.3.8) to find solutions for w_1, λ_1, and G_1, respectively. We also require the terms $A(r, z, t)$ and $B(r, z, t)$, given by (3.3.3) and (3.3.4), respectively, and the leading-order solutions (4.1.10), (4.1.11), (4.1.13), and (4.1.9). We begin by finding $A(r, z, t)$ and $B(r, z, t)$, where, for the sMMW model, η_Γ and η_λ, given by

(2.3.14), and f_Γ and f_λ, given by (2.3.15), are

$$\eta_\Gamma = 0, \qquad f_\Gamma = -\frac{a}{2}\Gamma_0^{a/2-1}\lambda_0^b + \frac{c}{2}\kappa\Gamma_0^{c/2-1}, \tag{4.1.14}$$

$$\eta_\lambda = 1, \qquad f_\lambda = -b\Gamma_0^{a/2}\lambda_0^{b-1}, \tag{4.1.15}$$

where $\eta(\Gamma,\lambda)$ and $f(\Gamma,\lambda)$ are given by (4.1.1). So (3.3.3) and (3.3.4) become

$$A(r,z,t) = \lambda_0 - \frac{1}{b}\left(a\lambda_0 - c\kappa\Gamma_0^{(c-a)/2}\lambda_0^{1-b}\right), \tag{4.1.16}$$

$$B(r,z,t) = -\frac{1}{b}\Gamma_0^{(1-a)/2}\lambda_0^{1-b}\left[\mathcal{D}_{\rm t}^*\frac{\partial\lambda_0}{\partial t} + \mathcal{D}_{\rm a}^*\left(u_0\frac{\partial\lambda_0}{\partial r} + w_0\frac{\partial\lambda_0}{\partial z}\right)\right], \tag{4.1.17}$$

respectively. Now, using the solution for λ_0 with (4.1.16) and (4.1.17), we obtain

$$\begin{aligned} A(r,z,t) = \kappa^{1/b}&\left(\frac{3n+1}{\pi n}Q\alpha^{-(3n+1)/n}r^{1/n}\right)^{n-1} \\ &\times\left[1 - \frac{1}{b}\left(a - c\Gamma_0^{(c-a)/2}\left(\frac{3n+1}{\pi n}Q\alpha^{-(3n+1)/n}r^{1/n}\right)^{-b(n-1)}\right)\right], \end{aligned} \tag{4.1.18}$$

and

$$\begin{aligned} B(r,z,t) = -\frac{1}{b}(n-1)\Gamma_0^{(1-a)/2}\kappa^{(2-b)/b}&\left(\frac{3n+1}{\pi n}Q\alpha^{-(3n+1)/n}r^{1/n}\right)^{(n-1)(2-b)} \\ &\times\left[\mathcal{D}_{\rm t}^*\frac{Q'}{Q} + \mathcal{D}_{\rm a}^*\frac{3(3n+1)}{\pi(n+1)}\frac{Q}{\alpha^2}\frac{\alpha'}{\alpha}\left(1 - \left(\frac{r}{\alpha}\right)^{(n+1)/n}\right)\right], \end{aligned} \tag{4.1.19}$$

respectively. Recalling that $\Gamma_0 = (\partial w_0/\partial r)^2$, we use (4.1.10) to obtain

$$\Gamma_0 = \left(\frac{3n+1}{\pi n}Q\alpha^{-(3n+1)/n}r^{1/n}\right)^2, \tag{4.1.20}$$

so now (4.1.18) and (4.1.19) become

$$A(r,z,t) = \kappa^{1/b}n\left(\frac{3n+1}{\pi n}Q\alpha^{-(3n+1)/n}r^{1/n}\right)^{n-1} \quad (= n\lambda_0 \geq 0), \tag{4.1.21}$$

and

$$B(r,z,t) = \frac{1}{b}\kappa^{(2-b)/b}(n-1)\left(\frac{3n+1}{\pi n}Q\alpha^{-(3n+1)/n}r^{1/n}\right)^{2n-c-1} \times \left[\mathcal{D}_{\mathrm{t}}^{*}\frac{Q'}{Q} - \mathcal{D}_{\mathrm{a}}^{*}\frac{3(3n+1)}{\pi(n+1)}\frac{Q}{\alpha^2}\frac{\alpha'}{\alpha}\left(1-\left(\frac{r}{\alpha}\right)^{(n+1)/n}\right)\right], \tag{4.1.22}$$

respectively. We note from (4.1.21) that $A(r,z,t) \geq 0$, which will be important later in this chapter.

In the general solutions for w_1 and G_1, given by (3.3.7) and (3.3.8) respectively, we must evaluate the integrals

$$\int_r^{\alpha} \frac{r'}{A(r',z,t)}\,\mathrm{d}r', \quad \text{and} \quad \int_r^{\alpha} \frac{B(r',z,t)}{A(r',z,t)}\,\mathrm{d}r', \tag{4.1.23}$$

which we do now to simplify the subsequent presentation. Using (4.1.21), the first integral in (4.1.23) is

$$\int_r^{\alpha} \frac{r'}{A(r',z,t)}\,\mathrm{d}r' = \frac{\kappa^{-1/b}}{n}\left(\frac{3n+1}{\pi n}Q\alpha^{-(3n+1)/n}\right)^{1-n}\int_r^{\alpha} r'r'^{(1-n)/n}\,\mathrm{d}r', \tag{4.1.24}$$

which, upon evaluating the integral on the right-hand side, yields

$$\int_r^{\alpha} \frac{r'}{A(r',z,t)}\,\mathrm{d}r' = \frac{\kappa^{-1/b}}{n+1}\left(\frac{3n+1}{\pi n}Q\alpha^{-(3n+1)/n}\right)^{1-n}\left(\alpha^{(n+1)/n} - r^{(n+1)/n}\right). \tag{4.1.25}$$

Using (4.1.21) and (4.1.22), the second integral in (4.1.23) is

$$\int_r^{\alpha} \frac{B(r',z,t)}{A(r',z,t)}\,\mathrm{d}r' = \kappa^{(1-b)/b}\frac{n-1}{b}\left(\frac{3n+1}{\pi n}Q\alpha^{-(3n+1)/n}\right)^{n-c} \times \int_r^{\alpha}\left[\mathcal{D}_{\mathrm{t}}^{*}\frac{Q'}{Q} - \mathcal{D}_{\mathrm{a}}^{*}\frac{3(3n+1)}{\pi(n+1)}\frac{Q}{\alpha^2}\frac{\alpha'}{\alpha}\left(1-\left(\frac{r'}{\alpha}\right)^{(n+1)/n}\right)\right] r'^{(n-c)/n}\,\mathrm{d}r', \tag{4.1.26}$$

which, upon evaluating the integral on the right-hand side, yields

$$\begin{aligned}\int_r^\alpha \frac{B(r',z,t)}{A(r',z,t)}\,\mathrm{d}r' &= \kappa^{(1-b)/b}\frac{n-1}{b}\left(\frac{3n+1}{\pi n}Q\alpha^{-(3n+1)/n}\right)^{n-c} \\ &\times\left[\left(\mathcal{D}_{\mathrm{t}}^*\frac{Q'}{Q}-\mathcal{D}_{\mathrm{a}}^*\frac{3(3n+1)}{\pi(n+1)}\frac{Q}{\alpha^2}\frac{\alpha'}{\alpha}\right)\frac{\alpha^{(2n-c)/n}}{2n-c}\left(1-\left(\frac{r}{\alpha}\right)^{(2n-c)/n}\right)\right. \\ &\left.+\,\mathcal{D}_{\mathrm{a}}^*\frac{3(3n+1)Q\alpha'\alpha^{-(n+c)/n}}{\pi(n+1)(3n-c+1)}\left(1-\left(\frac{r}{\alpha}\right)^{(3n-c+1)/n}\right)\right].\end{aligned} \tag{4.1.27}$$

For convenience, we briefly write (4.1.27) as

$$\int_r^\alpha \frac{B(r',z,t)}{A(r',z,t)}\,\mathrm{d}r' = D_1\left[D_2+D_3-D_2\left(\frac{r}{\alpha}\right)^{(2n-c)/n}-D_3\left(\frac{r}{\alpha}\right)^{(3n-c+1)/n}\right], \tag{4.1.28}$$

where

$$D_1 = \kappa^{(1-b)/b}\frac{n-1}{b}\left(\frac{3n+1}{\pi n}Q\alpha^{-(3n+1)/n}\right)^{n-c}, \tag{4.1.29}$$

$$D_2 = \left(\mathcal{D}_{\mathrm{t}}^*\frac{Q'}{Q}-\mathcal{D}_{\mathrm{a}}^*\frac{3(3n+1)}{\pi(n+1)}\frac{Q}{\alpha^2}\frac{\alpha'}{\alpha}\right)\frac{\alpha^{(2n-c)/n}}{2n-c}, \tag{4.1.30}$$

$$D_3 = \mathcal{D}_{\mathrm{a}}^*\frac{3(3n+1)Q\alpha'\alpha^{-(n+c)/n}}{\pi(n+1)(3n-c+1)}. \tag{4.1.31}$$

We can now use the general solution for the pressure gradient perturbation G_1, given by (3.3.8), with (4.1.25) and (4.1.28), to obtain the solution for G_1:

$$G_1(z,t) = -\frac{2D_1\left[\frac{1}{2}(D_2+D_3)-\frac{n}{4n-c}D_2-\frac{n}{5n-c+1}D_3\right]\alpha^2}{\frac{\kappa^{-1/b}}{2(3n+1)}\left(\frac{3n+1}{\pi n}Q\alpha^{-(3n+1)/n}\right)^{1-n}\alpha^{(3n+1)/n}}. \tag{4.1.32}$$

Replacing D_1, given by (4.1.29), and simplifying we obtain

$$\begin{aligned}G_1(z,t) = -\kappa^{(2-b)/b}&\frac{2(3n+1)(n-1)}{b\alpha^{(n+1)/n}}\left(\frac{3n+1}{\pi n}Q\alpha^{-(3n+1)/n}\right)^{2n-c-1} \\ &\times\left[D_2+D_3-\frac{2n}{4n-c}D_2-\frac{2n}{5n-c+1}D_3\right].\end{aligned} \tag{4.1.33}$$

Using (4.1.30) and (4.1.31) we find

$$D_2 + D_3 = \mathcal{D}_{\mathrm{t}}^* \frac{Q'}{Q} \frac{\alpha^{(2n-c)/n}}{2n-c} - \mathcal{D}_{\mathrm{a}}^* \frac{3(3n+1)Q\alpha'\alpha^{-(n+c)/n}}{\pi(2n-c)(3n-c+1)}, \tag{4.1.34}$$

$$-\frac{2n}{4n-c} D_2 = -\mathcal{D}_{\mathrm{t}}^* \frac{Q'}{Q} \frac{2n\alpha^{(2n-c)/n}}{(2n-c)(4n-c)} + \mathcal{D}_{\mathrm{a}}^* \frac{6n(3n+1)Q\alpha'\alpha^{-(n+c)/n}}{\pi(n+1)(2n-c)(4n-c)}, \tag{4.1.35}$$

$$-\frac{2n}{5n-c+1} D_3 = -\mathcal{D}_{\mathrm{a}}^* \frac{6n(3n+1)Q\alpha'\alpha^{-(n+c)/n}}{\pi(n+1)(3n-c+1)(5n-c+1)}. \tag{4.1.36}$$

By collecting terms in $\mathcal{D}_{\mathrm{t}}^*$ and terms in $\mathcal{D}_{\mathrm{a}}^*$, we obtain the solution for G_1:

$$G_1(z,t) = -\kappa^{(2-b)/b} \frac{2(3n+1)(n-1)}{b(4n-c)} \left(\frac{3n+1}{\pi n} Q\alpha^{-(3n+1)/n} \right)^{2n-c-1} \alpha^{(n-c-1)/n} \times \left[\mathcal{D}_{\mathrm{t}}^* \frac{Q'}{Q} - \mathcal{D}_{\mathrm{a}}^* \frac{3(3n+1)}{\pi(5n-c+1)} \frac{Q\alpha'}{\alpha^3} \right]. \tag{4.1.37}$$

The general solution for the streamwise velocity perturbation w_1 is given by (3.3.7). By using the integrals evaluated in (4.1.25) and (4.1.27) with (3.3.7) we obtain

$$\begin{aligned} w_1(r,z,t) = {} & \frac{1}{2} G_1 \frac{\kappa^{-1/b}}{n+1} \left(\frac{3n+1}{\pi n} Q\alpha^{-(3n+1)/n} \right)^{1-n} \alpha^{(n+1)/n} \left(1 - \left(\frac{r}{\alpha} \right)^{(n+1)/n} \right) \\ & + \kappa^{(1-b)/b} \frac{n-1}{b} \left(\frac{3n+1}{\pi n} Q\alpha^{-(3n+1)/n} \right)^{n-c} \\ & \times \left[\left(\mathcal{D}_{\mathrm{t}}^* \frac{Q'}{Q} - \mathcal{D}_{\mathrm{a}}^* \frac{3(3n+1)}{\pi(n+1)} \frac{Q}{\alpha^2} \frac{\alpha'}{\alpha} \right) \frac{\alpha^{(2n-c)/n}}{2n-c} \left(1 - \left(\frac{r}{\alpha} \right)^{(2n-c)/n} \right) \right. \\ & \left. + \mathcal{D}_{\mathrm{a}}^* \frac{3(3n+1)Q\alpha'\alpha^{-(n+c)/n}}{\pi(n+1)(3n-c+1)} \left(1 - \left(\frac{r}{\alpha} \right)^{(3n-c+1)/n} \right) \right]. \end{aligned} \tag{4.1.38}$$

Substituting G_1, given by (4.1.37), into (4.1.38) and simplifying yields the solution

for w_1:

$$
\begin{aligned}
w_1(r,z,t) = -\kappa^{(1-b)/b}\frac{n-1}{b}\left(\frac{3n+1}{\pi n}Q\alpha^{-(3n+1)/n}\right)^{n-c}\alpha^{(2n-c)/n} \\
\times\left[\left(\mathcal{D}_{\mathrm{t}}^{*}\frac{Q'}{Q}-\mathcal{D}_{\mathrm{a}}^{*}\frac{3(3n+1)}{\pi(5n-c+1)}\frac{Q\alpha'}{\alpha^3}\right)\frac{3n+1}{(4n-c)(n+1)}\left(1-\left(\frac{r}{\alpha}\right)^{(n+1)/n}\right)\right. \\
-\left(\mathcal{D}_{\mathrm{t}}^{*}\frac{Q'}{Q}-\mathcal{D}_{\mathrm{a}}^{*}\frac{3(3n+1)}{\pi(n+1)}\frac{Q\alpha'}{\alpha^3}\right)\frac{1}{2n-c}\left(1-\left(\frac{r}{\alpha}\right)^{(2n-c)/n}\right) \\
\left.-\mathcal{D}_{\mathrm{a}}^{*}\frac{3(3n+1)}{\pi(n+1)}\frac{Q\alpha'}{\alpha^3}\frac{1}{3n-c+1}\left(1-\left(\frac{r}{\alpha}\right)^{(3n-c+1)/n}\right)\right].
\end{aligned}
\tag{4.1.39}
$$

Using the leading-order solutions (4.1.10), (4.1.11), and (4.1.13), and the streamwise velocity perturbation (4.1.39), and simplifying yields the solution for λ_1 (3.3.1):

$$
\begin{aligned}
\lambda_1 = -\kappa^{(2-b)/b}\frac{n-1}{bn}\left(\frac{3n+1}{\pi n}Q\alpha^{-(3n+1)/n}\right)^{2n-c-2}r^{(2n-c-2)/n} \\
\times\left[\mathcal{D}_{\mathrm{t}}^{*}\frac{Q'}{Q}-\mathcal{D}_{\mathrm{a}}^{*}\frac{3(3n+1)}{\pi(n+1)}\frac{Q\alpha'}{\alpha^3}\left(1-\left(\frac{r}{\alpha}\right)^{(n+1)/n}\right)\right. \\
\left.+\frac{(n-1)(3n+1)}{4n-c}\left(\mathcal{D}_{\mathrm{t}}^{*}\frac{Q'}{Q}-\mathcal{D}_{\mathrm{a}}^{*}\frac{3(3n+1)}{\pi(5n-c+1)}\frac{Q\alpha'}{\alpha^3}\right)\left(\frac{r}{\alpha}\right)^{(-n+c+1)/n}\right].
\end{aligned}
\tag{4.1.40}
$$

We note from the solutions for w_1 and λ_1, given by (4.1.39) and (4.1.40) respectively, that in the quickly adjusting regime $\mathfrak{R}_{1,2}$ (when $\mathcal{D}_{\mathrm{t}}^{*}=\mathcal{O}(1)$ and $\mathcal{D}_{\mathrm{a}}^{*}=0$), w_1 and λ_1 are proportional to $\mathcal{D}_{\mathrm{t}}^{*}Q'(t)$. Similarly, in the weakly advective regime $\mathfrak{R}_{2,1}$ (when $\mathcal{D}_{\mathrm{a}}^{*}=\mathcal{O}(1)$ and $\mathcal{D}_{\mathrm{t}}^{*}=0$), w_1 and λ_1 are proportional to $\mathcal{D}_{\mathrm{a}}^{*}\alpha'(z)$. Consequently, we do not gain any extra insight into $\mathfrak{R}_{1,2}$ by considering both a decelerating flow ($Q'(t)<0$) and an accelerating flow ($Q'(t)>0$), or into $\mathfrak{R}_{2,1}$ by considering both a widening pipe ($\alpha'(z)>0$) and a narrowing pipe ($\alpha'(z)<0$). Unless stated otherwise, when discussing the perturbations for the sMMW model in the following sections, and indeed for the full MMW model and the Houška model, we only consider a decelerating flow in a widening pipe ($Q'(t)<0$ and $\alpha'(z)>0$). The behaviour for accelerating flows or narrowing pipes can be obtained by simply reversing the signs of w_1 and λ_1 accordingly.

4.1.4 Examples of perturbation quantities

In this section, we present examples of the perturbation quantities w_1 and λ_1, given by (4.1.39) and (4.1.40), respectively, for the sMMW model. We discuss G_1, given by (4.1.37), in detail in Section 4.1.8. Whilst these solutions are for the quickly adjusting and weakly advective regime $\mathfrak{R}_{1,1}$, in order to study the effect of thixotropy in an unsteady flow and in a varying pipe, we consider the quickly adjusting regime $\mathfrak{R}_{1,2}$ and the weakly advective regime $\mathfrak{R}_{2,1}$ separately. To this end, we consider $\mathcal{D}_{\mathrm{t}}^* = 1$ and $\mathcal{D}_{\mathrm{a}}^* = 0$ for $\mathfrak{R}_{1,2}$, and $\mathcal{D}_{\mathrm{a}}^* = 1$ and $\mathcal{D}_{\mathrm{t}}^* = 0$ for $\mathfrak{R}_{2,1}$ separately. As stated at the end of Section 4.1.3, we consider decelerating flow in a widening pipe. Specifically, we set $Q' = -1$ and $\alpha' = 1$. We present profiles of w_1 and λ_1 here for illustrative purposes, and provide a more detailed analysis of the full range of behaviours of w_1 and λ_1 in Section 4.1.5, where we determine when the TRC describes the perturbations, and when it does not.

Figures 4.2(a) and (b) show examples of w_1 and λ_1 in the quickly adjusting regime for various values of n (the arrows show the direction of increasing n). For thixotropic fluids ($n < 1$), w_1 is positive near the centre of the pipe and, to preserve the prescribed volume flux, negative near the wall, and λ_1 is negative and largest near the centre of the pipe. For antithixotropic fluids ($n > 1$), w_1 is negative near the centre of the pipe and positive near the wall, and λ_1 is positive and largest near the centre of the pipe.

Figures 4.2(c) and (d) show examples for w_1 and λ_1 in the weakly advective regime, for various values of n (the arrow shows increasing n). The velocity and structure perturbations in the weakly advective regime are qualitatively similar to those in the quickly adjusting regime, shown in Figures 4.2(a) and (b), respectively.

Each of the examples of w_1 and λ_1 shown in Figure 4.2 agree with the TRC, discussed in Section 3.3.1 and shown in Figure 3.1, using the thixotropic/ antithixotropic and widening/decelerating analogies. However, in cases of strong antithixotropy there are other behaviours of w_1 and λ_1 which do not agree with the TRC.

Figures 4.3(a) and (b) show examples of w_1 and λ_1 respectively, in the quickly

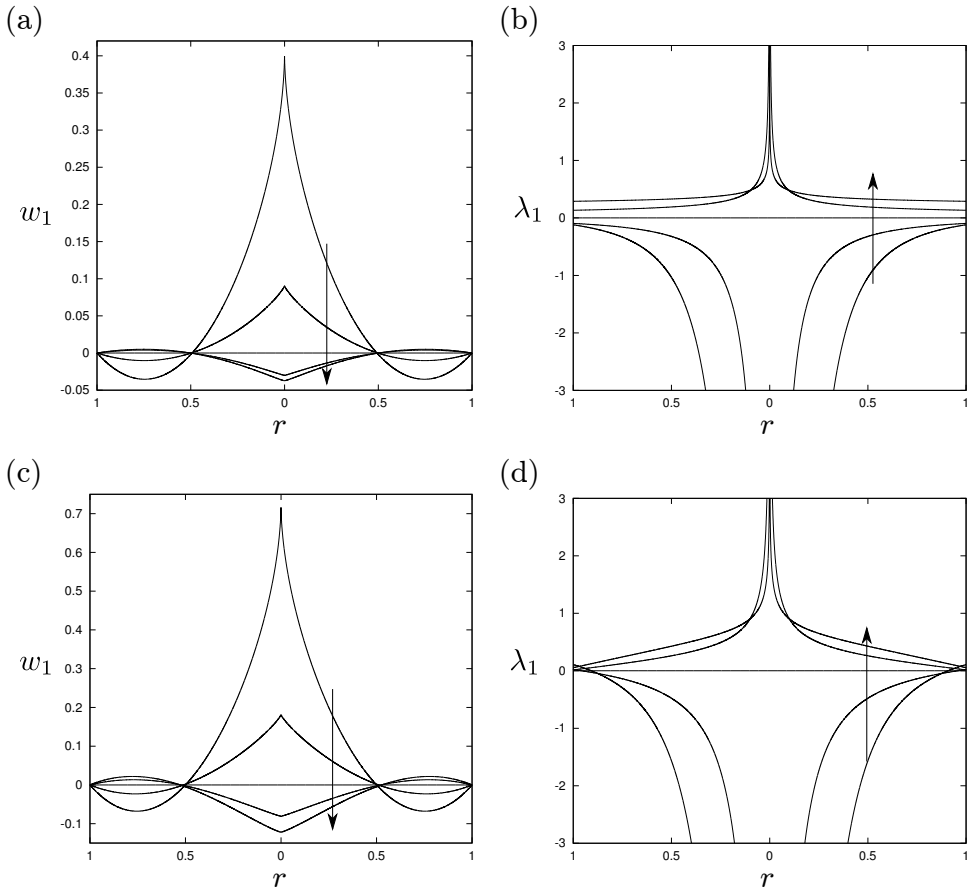

Figure 4.2: sMMW model: profiles of (a,c) w_1 and (b,d) λ_1 in (a,b) the quickly adjusting regime $\mathfrak{R}_{1,2}$ and (c,d) the weakly advective regime $\mathfrak{R}_{2,1}$. The parameters are $n = 0.7$ ($a = 1.3$, $G_1 = -0.8410$ ($\mathfrak{R}_{1,2}$), $G_1 = -0.7113$ ($\mathfrak{R}_{2,1}$)), $n = 0.85$ ($a = 1.15$, $G_1 = -0.4074$ ($\mathfrak{R}_{1,2}$), $G_1 = -0.3250$ ($\mathfrak{R}_{2,1}$)), $n = 1$ ($a = 1$, $G_1 = 0$ ($\mathfrak{R}_{1,2}$), $G_1 = 0$ ($\mathfrak{R}_{2,1}$)), $n = 1.15$ ($a = 0.85$, $G_1 = 0.3948$ ($\mathfrak{R}_{1,2}$), $G_1 = 0.2917$ ($\mathfrak{R}_{2,1}$)), and $n = 1.3$ ($a = 0.7$, $G_1 = 0.7808$ ($\mathfrak{R}_{1,2}$), $G_1 = 0.5621$ ($\mathfrak{R}_{2,1}$)). The common parameters are $\kappa = 1$, $Q(t) = 1$, $Q'(t) = -1$, $\alpha(z) = 1$, $\alpha'(z) = 1$, $b = 1$, and $c = 1$, and (a,b) $\mathcal{D}_{\mathrm{t}}^* = 1$, $\mathcal{D}_{\mathrm{a}}^* = 0$ and (c,d) $\mathcal{D}_{\mathrm{a}}^* = 1$, $\mathcal{D}_{\mathrm{t}}^* = 0$. The arrows show the direction of increasing n, i.e. from thixotropic to antithixotropic behaviour.

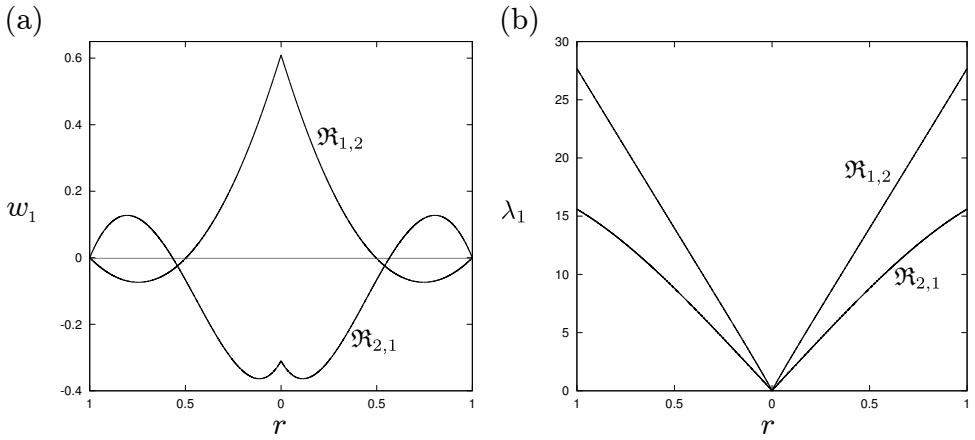

Figure 4.3: sMMW model: profiles of (a) w_1 and (b) λ_1 in the quickly adjusting regime $\mathfrak{R}_{1,2}$ and weakly advective regime $\mathfrak{R}_{2,1}$ (labelled accordingly). The common parameters are $a = 0.1$, $b = 0.2$, $c = 4$ ($n = 20.5$, $G_1 = 53.08$ ($\mathfrak{R}_{1,2}$), $G_1 = 31.84$ ($\mathfrak{R}_{2,1}$)), $\kappa = 1$, $Q(t) = 1$, $Q'(t) = -1$, $\alpha(z) = 1$, $\alpha'(z) = 1$, and ($\mathfrak{R}_{1,2}$) $\mathcal{D}_{\mathrm{t}}^* = 1$, $\mathcal{D}_{\mathrm{a}}^* = 0$ and ($\mathfrak{R}_{2,1}$) $\mathcal{D}_{\mathrm{a}}^* = 1$, $\mathcal{D}_{\mathrm{t}}^* = 0$.

adjusting regime $\mathfrak{R}_{1,2}$ and the weakly advective regime $\mathfrak{R}_{2,1}$ which do not agree with the TRC. Using the TRC and the analogies, we expect these profiles to be similar to those of the antithixotropic fluids shown in Figure 4.2, i.e. we expect w_1 to be negative near the centre of the pipe and positive at the wall.

For the case plotted in the weakly advective regime $\mathfrak{R}_{2,1}$, w_1, shown in Figure 4.3(a), is similar to the TRC, but there is an extra change in the sign of $\partial w_1/\partial r$ near the centreline of the pipe, yielding a local maximum at the centreline, rather than a local minimum. For the case plotted in the quickly adjusting regime $\mathfrak{R}_{1,2}$, w_1 is the opposite to what we would expect for an antithixotropic fluid. Instead, w_1 is qualitatively similar to that of a thixotropic fluid (cf. $\mathfrak{R}_{1,2}$ in Figure 4.3(a) and the profiles for thixotropic fluids in Figure 4.2(a)), so it does not agree with the TRC.

In both cases plotted in Figure 4.3(b), λ_1 is qualitatively different from the TRC. With the thixotropy/antithixotropy and widening/decelerating analogies, we would expect λ_1 to be positive and largest at the centreline in both regimes, similar to λ_1 for the antithixotropic fluids shown in Figures 4.2(b) and (d). Instead, λ_1 is zero at the centreline and positive and largest at the wall.

The behaviours of w_1 and λ_1 shown in Figure 4.3 indicate that the TRC, the accompanying analogies and corresponding physical interpretation are insuffient to full describe the behaviour of antithixotropic flow in some cases. This result is important because it provides proof by counter example that it is not possible to make general statements regarding the qualitative behaviour of the perturbations, and, hence, the flow. The behaviours also indicate that the more pronounced features of thixotropic flow may be caused by a subtle process which is overlooked by an intuitive physical interpretation.

We study the anomalous behaviour of w_1 and λ_1 shown in Figure 4.3 in the following section by considering the centreline behaviour of the perturbations. In particular, we highlight the ways in which the analogies break down and in Section 4.1.6 we discuss the physical mechanisms leading to the anomalous behaviour.

4.1.5 Centreline behaviour of perturbations

In this section, we present the behaviour of w_1 and λ_1 near the centreline, which we obtain by analysing the solutions, given by (4.1.39) and (4.1.40), as $r \to 0$. This analysis will allow us to determine the full range of qualitative behaviours for the sMMW model, and thus determine when the behaviour agrees with the TRC, and when it does not. We present the results of this analysis here; the details are presented for w_1 in Appendix A.1 and for λ_1 in Appendix A.2. In the appendices, we determine the sign and the boundedness of the perturbations at the centreline, and the nature of their radial derivatives as $r \to 0$, which are what determines the qualitative behaviour of the perturbations. We find a range of qualitatively distinct behaviours for the perturbations, which we organise into a regime diagram of the parameter space of the sMMW model. In addition, we find exactly for which parameters the behaviours of perturbations agree with the TRC, and for which they do not, which allows an in-depth study of the anomalous behaviour shown in Figure 4.3.

4.1.5.1 Regime diagrams

We summarise the behaviour of w_1 and λ_1 at the centreline in the quickly adjusting regime and in the weakly advective regime as follows. The critical lines of the parameter space (a, b, c) of the sMMW model, obtained in Appendices A.1 and A.2, are $n-1=0$, $n-c=0$, $2n-c-2=0$, $2n-c=0$, $4n-c=0$, and $n-c-1=0$, which, using $n=(c-a)/b+1$, are $a=c$, $a=b+c(1-b)$, $a=c(1-b/2)$, $a=b+c(1-b/2)$, $a=b+c(1-b/4)$, and $a=c(1-b)$, respectively. We note that, given that $a, b, c \geq 0$, the line $a=c(1-b/2)$ only exists in this quadrant of (c, a)-space when $b<2$, and similarly the line $a=c(1-b)$ only exists in this quadrant when $b<1$. By plotting these lines in (c, a)-space (for $a, c \geq 0$) we obtain a regime diagram for all possible behaviours of w_1 and λ_1. Figure 4.4 shows examples of this regime diagram, for $b=0.8$ and $b=1.2$.

The labels in Figure 4.4 refer to regions of qualitatively similar centreline behaviour of w_1, for decelerating flow in a widening pipe. Regions $\bar{\mathrm{T}}_{\mathrm{II}}$–$\bar{\mathrm{T}}_{\mathrm{IV}}$ contain only thixotropic behaviour (note there is no region $\bar{\mathrm{T}}_{\mathrm{I}}$), characterised by

- Region $\bar{\mathrm{T}}_{\mathrm{II}}$: w_1 is positive and flat at the centreline,
- Region $\bar{\mathrm{T}}_{\mathrm{III}}$: w_1 is positive and has a cusp at the centreline,
- Region $\bar{\mathrm{T}}_{\mathrm{IV}}$: w_1 is positive and singular at the centreline.

Regions $\bar{\mathrm{A}}_{\mathrm{II}}$–$\bar{\mathrm{A}}_{\mathrm{IV}}$ contain only antithixotropic behaviour, characterised by

- Region $\bar{\mathrm{A}}_{\mathrm{II}}$: w_1 is negative and flat at the centreline,
- Region $\bar{\mathrm{A}}_{\mathrm{III}}$: w_1 is negative and has a cusp at the centreline,
- Region $\bar{\mathrm{A}}_{\mathrm{IV}}$: w_1 is negative and singular at the centreline.

Finally, regions $\bar{\mathrm{A}}_{\mathrm{I}}^{1,2}$ and $\bar{\mathrm{A}}_{\mathrm{I}}^{2,1}$ are characterised by

- Region $\bar{\mathrm{A}}_{\mathrm{I}}^{1,2}$: in the quickly adjusting regime, w_1 is positive and flat at the centreline,

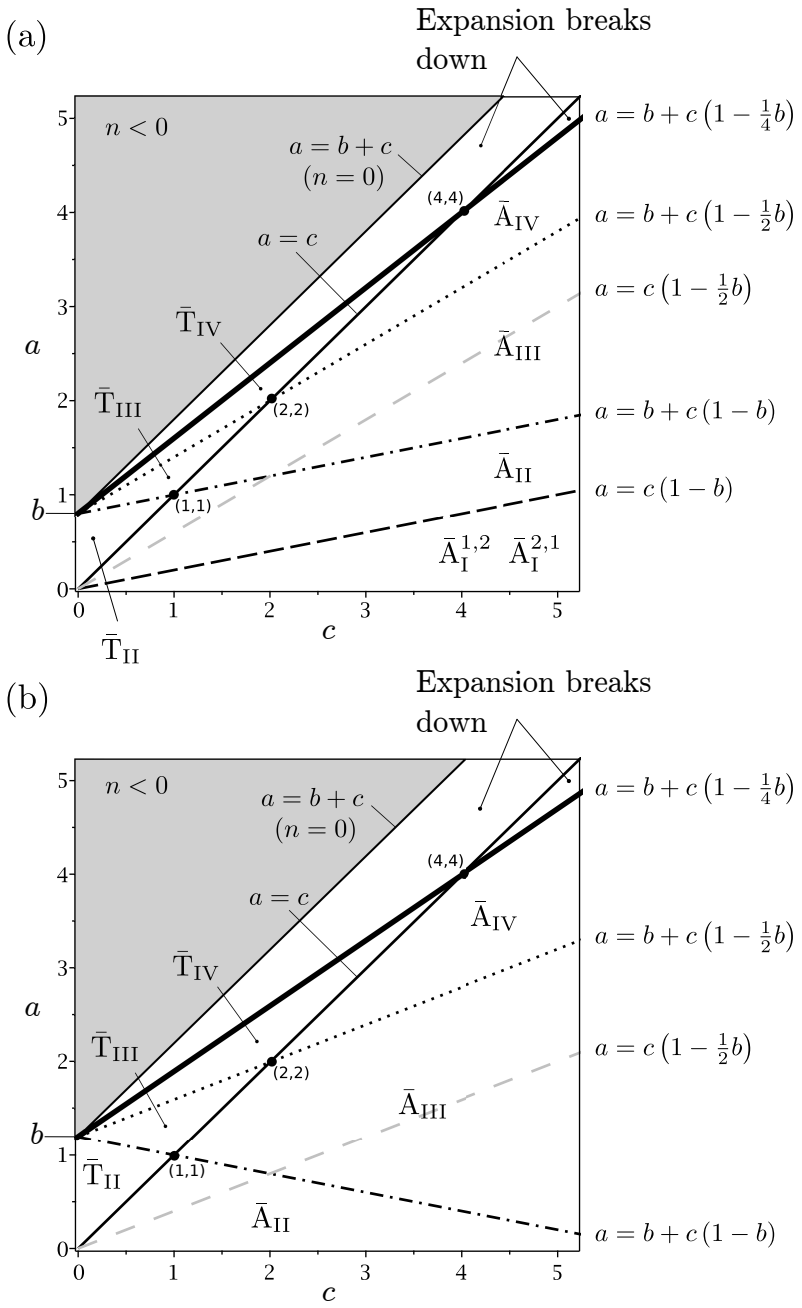

Figure 4.4: sMMW model: regime diagrams in (c, a)-space for (a) $b = 0.8$ and (b) $b = 1.2$, for the centreline behaviour of w_1 and λ_1. The lines $a = c(1 - b)$ (dashed), $a = b + c(1 - b)$ (dot-dashed), and $a = b + c(1 - b/2)$ (dotted) apply to w_1 only. The line $a = c(1 - b/2)$ (space-dashed, grey) applies to λ_1 only. The lines $a = c$ (solid) applies to both w_1 and λ_1. The labels $\bar{\mathrm{T}}_{\mathrm{II}}$, $\bar{\mathrm{A}}_{\mathrm{II}}$, etc. denote regions of qualitatively similar centreline behaviour of w_1.

- Region $\bar{\mathrm{A}}_{\mathrm{I}}^{2,1}$: in the weakly advective regime, w_1 is negative and flat at the centreline.

Regions $\bar{\mathrm{A}}_{\mathrm{I}}^{1,2}$ and $\bar{\mathrm{A}}_{\mathrm{I}}^{2,1}$ are bounded above by the line $a = c(1-b)$. When $b < 1$, these regions are present in the regime diagram, as shown in Figure 4.4(a), but when $b > 1$, these regions are absent, as shown in Figure 4.4(b).

When $a < c(1-b/2)$, λ_1 is zero and has a cusp at the centreline, when $c(1-b/2) < a < c$, λ_1 is positive and singular at the centreline, and when $a > c$, λ_1 is negative and singular at the centreline.

The thick solid lines in Figure 4.4 denote $a = b + c(1 - b/4)$, and we require $a < b + c(1 - b/4)$ (or $4n - c > 0$) for our small-δ asymptotic expansion to be valid (which relies on the flux (3.1.12) being integrable, see Appendix A.1). In addition, the thin solid lines in Figure 4.4 denote $a = b + c$ (i.e. $n = 0$), and we require $a < b + c$ (i.e. $n > 0$), for the sMMW model to be physically meaningful. So there is a region of the parameter space $(b + c(1 - b/4) < a < b + c$, labelled 'Expansion breaks down' in Figure 4.4 which is physically meaningful but beyond the scope of the expansion scheme. In this region, the asymptotic approach we have used is not appropriate because the perturbations 'jump' order, and the leading-order behaviour is no longer independent of thixotropy. We require a different technique, such as numerical methods, to access the behaviour of w_1 and λ_1 in this region.

Figure 4.5 shows a table of schematics: sketches of the leading-order quantities w_0 and λ_0, and the perturbations w_1 and λ_1 in each of the regions of the regime diagram, for a widening pipe and a decelerating flow. This table is a summary of all qualitative behaviours of the sMMW model in the weakly advective regime and in the quickly adjusting regime that we may obtain using our expansion scheme. The vertical and horizontal lines represent the boundaries between the regions of the regime diagram, shown in Figure 4.4. The vertical line, labelled $a = c$ denotes the boundary between thixotropic fluids to the left and antithixotropic fluids to the right. The grey box indicates the behaviours that agree with the TRC, using the thixotropy/antithixotropy and widening/decelerating analogies, and so the profile sketches outwith this box do not agree with the TRC.

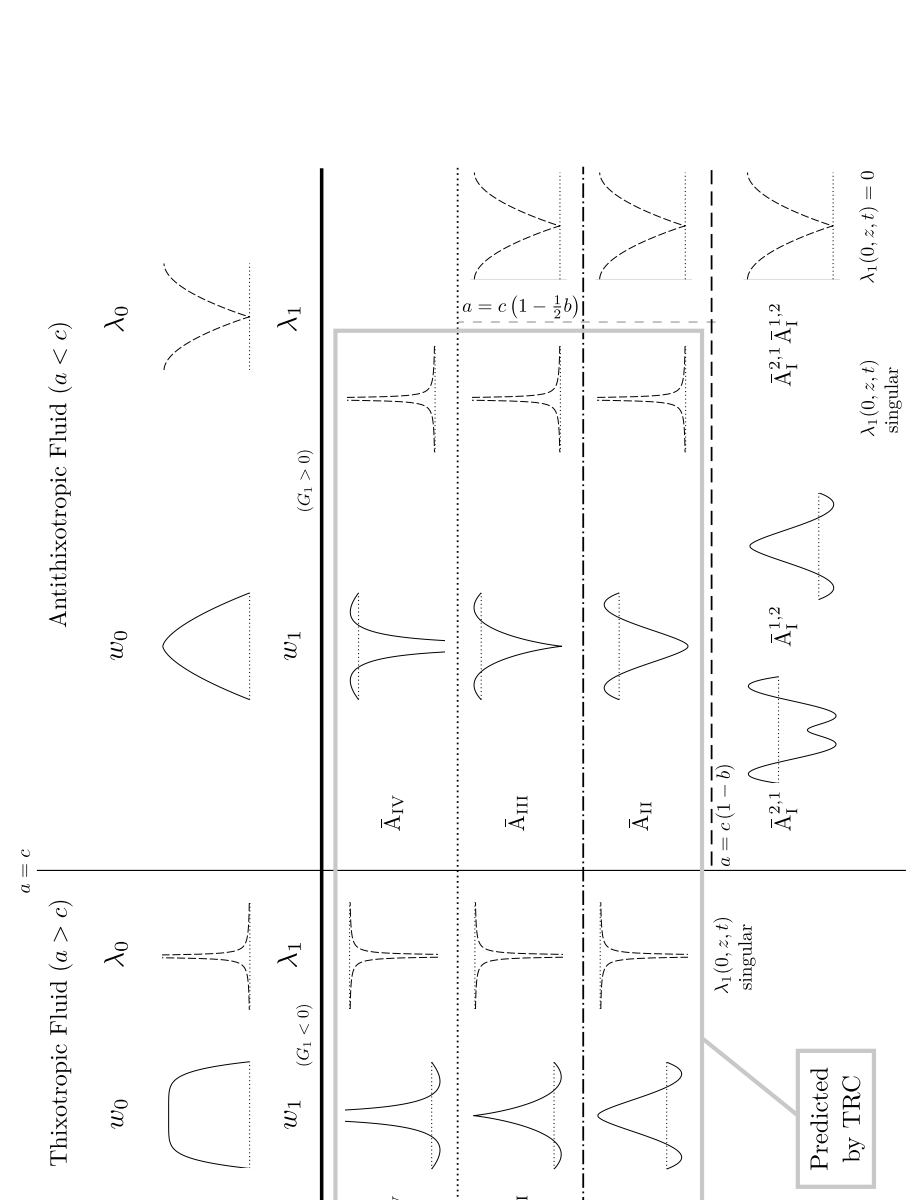

Figure 4.5: sMMW model: table of schematics for w_0 and w_1 (solid), and λ_0 and λ_1 (dashed). The characteristic centreline behaviour of w_1 in each of the regions is noted at the left of the table, and the characteristic behaviour of λ_1 is noted at the bottom of the table. The vertical and horizontal lines represent the boundaries between the regions of the regime diagram, shown in Figure 4.4, and the region labels are noted. Profiles inside the grey box agree with the TRC, and those outwith do not.

For thixotropic fluids, in regions $\bar{\mathrm{T}}_{\mathrm{II}}$–$\bar{\mathrm{T}}_{\mathrm{IV}}$, in both the weakly advective regime and in the quickly adjusting regime, w_1 is positive near the centreline, with some qualitative variation, and negative near the wall. In addition, λ_1 is negative and largest at the centreline. So the behaviours of w_1 and λ_1 agree with the TRC using the widening/decelerating analogy. We conclude that the thixotropic behaviour of the sMMW model may be qualitatively described in general. In particular, the behaviour is described by the TRC.

For the antithixotropic fluids in regions $\bar{\mathrm{A}}_{\mathrm{II}}$–$\bar{\mathrm{A}}_{\mathrm{IV}}$, in both the weakly advective regime and in the quickly adjusting regime, w_1 is negative near the centreline, with some qualitative variation, and positive near the wall, i.e. the opposite of thixotropic fluids. In these regions, w_1 agrees with the TRC using the thixotropy/antithixotropy and widening/decelerating analogies. Region $\bar{\mathrm{A}}_{\mathrm{I}}^{2,1}$ contains antithixotropic fluids in the weakly advective regime. As illustrated in Figure 4.5, w_1 for fluids in region $\bar{\mathrm{A}}_{\mathrm{I}}^{2,1}$ do not agree with the TRC. Whilst w_1 is negative near the centreline and positive near the wall, as for antithixotropic fluids in regions $\bar{\mathrm{A}}_{\mathrm{II}}$–$\bar{\mathrm{A}}_{\mathrm{IV}}$, there is an extra change in the sign of the gradient of w_1 near the centreline not described by the TRC. So for fluids in region $\bar{\mathrm{A}}_{\mathrm{I}}^{2,1}$, the thixotropy/antithixotropy analogy does not hold and so the physical explanation of the behaviour of the perturbations must be refined. Region $\bar{\mathrm{A}}_{\mathrm{I}}^{1,2}$ contains antithixotropic fluids in the quickly adjusting regime. As illustrated in Figure 4.5, w_1 for fluids in region $\bar{\mathrm{A}}_{\mathrm{I}}^{1,2}$ do not agree with the TRC. Unlike fluids in region $\bar{\mathrm{A}}_{\mathrm{I}}^{2,1}$, w_1 is the opposite of what the TRC describes, i.e. w_1 is positive near the centreline and negative near the wall, and so is qualitatively similar to thixotropic fluids in regions $\bar{\mathrm{T}}_{\mathrm{II}}$–$\bar{\mathrm{T}}_{\mathrm{IV}}$. So for fluids in region $\bar{\mathrm{A}}_{\mathrm{I}}^{1,2}$, the widening/decelerating and thixotropy/antithixotropy analogies do not hold and so the physical explanation of the behaviour of the perturbations must again be refined. We discuss the physical mechanisms behind the anomalous behaviour in regions $\bar{\mathrm{A}}_{\mathrm{I}}^{2,1}$ and $\bar{\mathrm{A}}_{\mathrm{I}}^{1,2}$ in Section 4.1.6.

We have not defined regions for the behaviour of λ_1, but we note that when $a > c(1 - b/2)$, which includes all thixotropic fluids and some antithixotropic fluids, λ_1 agrees with the TRC using the analogies. When $a < c(1 - b/2)$, which includes only strongly antithixotropic fluids, shown in the right-most column in Figure 4.5, λ_1 does not agree with the TRC.

4.1.6 Mechanisms for behaviour of w_1

We find the source of the anomalous behaviour exhibited by w_1 in regions $\bar{\mathrm{A}}_{\mathrm{I}}^{2,1}$ and $\bar{\mathrm{A}}_{\mathrm{I}}^{1,2}$ in the equation for the radial derivative $\partial w_1/\partial r$. The general form of this equation is given by (3.3.6), which we rewrite here for convenience:

$$\frac{\partial w_1}{\partial r} = -\left[\frac{1}{2}G_1(z,t)r - B(r,z,t)\right]\frac{1}{A(r,z,t)}, \tag{4.1.41}$$

where G_1 is the pressure gradient perturbation (4.1.37), B is the thixotropic stress term (4.1.22), and A is non-negative (4.1.21). It is clear from (4.1.41) that the sign of $\partial w_1/\partial r$ is determined by the relative sizes of the terms $G_1 r/2$ and B: when $G_1 r/2 \lessgtr B$, $\partial w_1/\partial r \gtrless 0$.

We are interested in how the relative size of these terms differs between regions $\bar{\mathrm{A}}_{\mathrm{I}}^{2,1}$ and $\bar{\mathrm{A}}_{\mathrm{II}}$ in the weakly advective regime, and between regions $\bar{\mathrm{A}}_{\mathrm{I}}^{1,2}$ and $\bar{\mathrm{A}}_{\mathrm{II}}$ in the quickly adjusting regime, so it will be useful to plot an example of $-G_1 r/2$ and B in each of these regions. Such examples are shown in Figure 4.6(a) and (b) for the weakly advective regime and in Figure 4.6(c) and (d) for the quickly adjusting regime. Figures 4.6(a) and (c) show profiles in region $\bar{\mathrm{A}}_{\mathrm{II}}$, and Figures 4.6(b) and (d) show profiles in regions $\bar{\mathrm{A}}_{\mathrm{I}}^{2,1}$ and $\bar{\mathrm{A}}_{\mathrm{I}}^{1,2}$ respectively, and use the same parameters as the profiles in Figure 4.3.

The term $-G_1 r/2$ is linear in r, so always takes the form shown by the dotted lines in Figure 4.6. The general form of the thixotropic stress term B (3.3.4) is given by

$$B(r,z,t) = \frac{\eta_\lambda}{f_\lambda}\left[\mathcal{D}_{\mathrm{t}}^*\frac{\partial \lambda_0}{\partial t} + \mathcal{D}_{\mathrm{a}}^*\left(u_0\frac{\partial \lambda_0}{\partial r} + w_0\frac{\partial \lambda_0}{\partial z}\right)\right]\frac{\partial w_0}{\partial r}. \tag{4.1.42}$$

We note from (4.1.42) that because the shear rate $\partial w_0/\partial r$ vanishes at the centreline, B also always vanishes at the centreline.

In the weakly advective regime ($\mathcal{D}_{\mathrm{t}}^* = 0$), B is proportional to the advective derivative $\mathbf{u}_0 \cdot \nabla \lambda_0$, and is forced to equal zero at the wall by the no-slip condition. The constraints on B at the centreline and at the wall mean that B must take the particular form shown by the solid lines in Figures 4.6(a) and (b). Given that

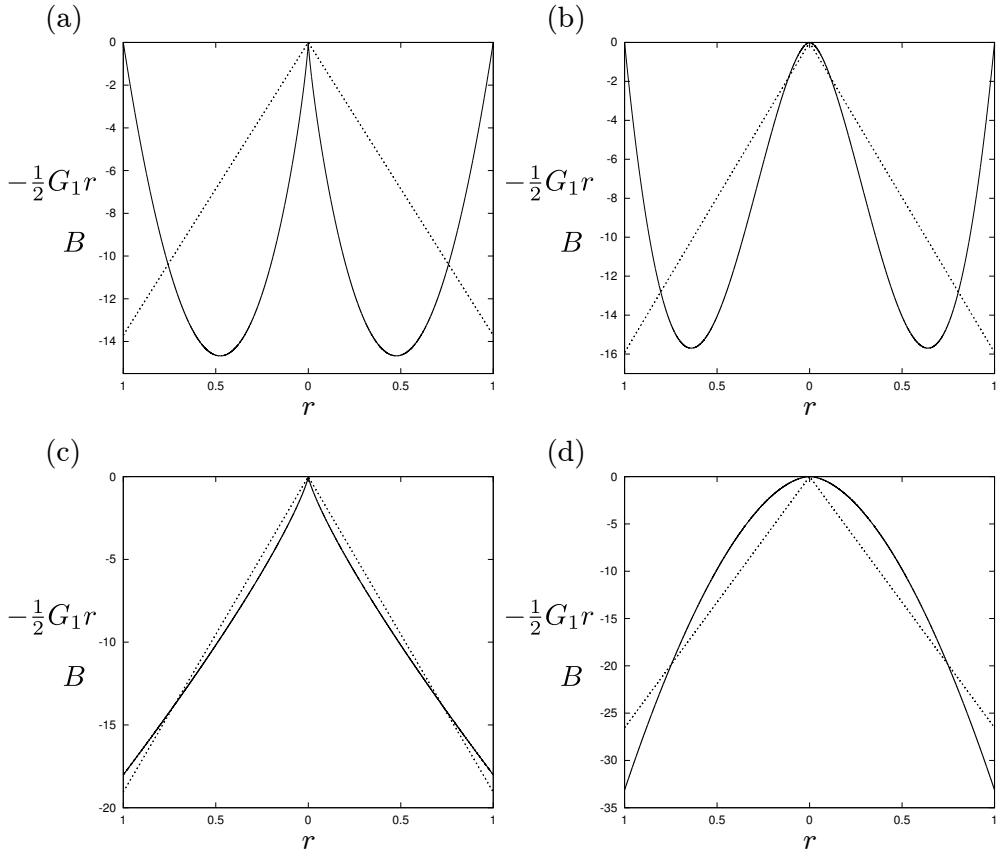

Figure 4.6: sMMW model: profiles of $-\frac{1}{2}G_1 r$ (dotted) and B (solid) in (a) region $\bar{\mathrm{A}}_{\mathrm{II}}$ and (b) region $\bar{\mathrm{A}}_{\mathrm{I}}^{2,1}$ in the weakly advective regime, and (c) region $\bar{\mathrm{A}}_{\mathrm{II}}$ and (d) region $\bar{\mathrm{A}}_{\mathrm{I}}^{1,2}$ in the quickly adjusting regime. The parameters are (a,c) $a = 3.35$ and (b,d) $a = 0.1$. The common parameters are $\kappa = 1$, $Q(t) = 1$, $Q'(t) = -1$, $\alpha(z) = 1$, $\alpha'(z) = 1$, $b = 0.2$, and $c = 4$, and (a,b) $\mathcal{D}_{\mathrm{a}}^* = 1$, $\mathcal{D}_{\mathrm{t}}^* = 0$ and (c,d) $\mathcal{D}_{\mathrm{t}}^* = 1$, $\mathcal{D}_{\mathrm{a}}^* = 0$. The profiles in (b,d) are the profiles of $-\frac{1}{2}G_1 r$ and B for the parameters used in Figure 4.3.

B is always zero at the wall and $-G_1 r/2$ is always negative at the wall, $\partial w_1/\partial r$ is always negative at the wall, so w_1 must be positive near the wall, as shown by the sketches of w_1 in regions $\bar{\mathrm{A}}_{\mathrm{I}}^{2,1}$ and $\bar{\mathrm{A}}_{\mathrm{II}}$ in Figure 4.5.

In region $\bar{\mathrm{A}}_{\mathrm{II}}$ (Figure 4.6(a)), $|B| > |-G_1 r/2|$ near the centreline, so $\partial w_1/\partial r$ is positive near the centreline. In region $\bar{\mathrm{A}}_{\mathrm{I}}^{2,1}$ (Figure 4.6(b)), B has a different concavity which decreases its value near the centreline so that $|B| < |-G_1 r/2|$, and consequently $\partial w_1/\partial r$ is negative near the centreline. It is clear then that a slight change in the concavity of $|B|$ leads to a localised change in the gradient of w_1, which yields the difference in behaviour of w_1 near the centreline in regions $\bar{\mathrm{A}}_{\mathrm{I}}^{2,1}$ and $\bar{\mathrm{A}}_{\mathrm{II}}$. We interpret the decrease of $|B|$ near the centreline as a weakening of thixotropy.

In the quickly adjusting regime ($\mathcal{D}_{\mathrm{a}}^* = 0$), B is proportional to the time derivative $\partial\lambda_0/\partial t$, which is not zero at the wall in general. So, in contrast to the weakly advective regime, B is only constrained to equal zero at the centreline, and can vary significantly at the wall, as shown by the solid lines in Figures 4.6(c) and (d). In fact, as shown by Figure 4.6(c) and (d), B is similar to $-G_1 r/2$ across the width of the pipe, and $\partial w_1/\partial r$ is determined by a fine balance between the two terms. In region $\bar{\mathrm{A}}_{\mathrm{II}}$, shown in Figures 4.6(c), $|B| > |-G_1 r/2|$ near the centreline and $|B| < |-G_1 r/2|$ near the wall, so $\partial w_1/\partial r$ is positive and negative at these locations respectively, which yields the profile sketched for region $\bar{\mathrm{A}}_{\mathrm{II}}$ in Figure 4.5. As in the weakly advective regime, a slight change in the concavity of B leads to a decrease in $|B|$, as shown in Figures 4.6(d). The fine balance between B and $G_1 r/2$ means that this change in the concavity of B leads to a reversal of the sign of $\partial w_1/\partial r$ across the pipe, which reverses w_1, as shown by the profile sketched for region $\bar{\mathrm{A}}_{\mathrm{I}}^{1,2}$ in Figure 4.5.

We note that on the boundary $a = c(1-b)$, between regions $\bar{\mathrm{A}}_{\mathrm{I}}^{1,2}$ and $\bar{\mathrm{A}}_{\mathrm{II}}$, B, given by (4.1.22), is

$$B(r,z,t) = \mathcal{D}_{\mathrm{t}}^* \kappa^{(2-b)/b} \frac{c}{b} \frac{Q'}{Q} \left(\frac{3c+4}{\pi(c+1)} Q \alpha^{-(3c+4)/(c+1)} \right)^{c+1} r = -\frac{1}{2} G_1 r. \quad (4.1.43)$$

So on this boundary, $\partial w_1/\partial r = 0$, so $w_1 = 0$, and thus antithixotropy does not affect the streamwise velocity, but it does affect the structure parameter and the

pressure gradient.

In summary, in both the weakly advective regime and the quickly adjusting regime, the anomalous behaviour of regions $\bar{\mathrm{A}}_{\mathrm{I}}^{2,1}$ and $\bar{\mathrm{A}}_{\mathrm{I}}^{1,2}$, respectively, arises from a change in the concavity of the thixotropic stress term B. In the weakly advective regime, this change in concavity only affects the flow near the centreline, so it only has a localised effect on w_1. In the quickly adjusting regime, this change in concavity affects w_1 across the width of the pipe and results in a reversal of w_1.

4.1.7 Cancellation of thixotropic effects

In this section, we discuss the possible 'cancellation' of advective thixotropy and temporal thixotropy in the quickly adjusting and weakly advective regime ($\mathfrak{R}_{1,1}$). In previous sections, we have studied decelerating flow ($Q'(t) < 0$) in a widening pipe ($\alpha'(z) > 0$), in which advective thixotropy and temporal thixotropy have similar effects on the flow in most cases (excluding fluids in regions $\bar{\mathrm{A}}_{\mathrm{I}}^{2,1}$ and $\bar{\mathrm{A}}_{\mathrm{I}}^{1,2}$ of the regime diagram). Here we study accelerating flow ($Q'(t) > 0$) in a widening pipe ($\alpha'(z) > 0$), in which advective thixotropy and temporal thixotropy have opposite effects on the flow in most cases.

There are several ways we could choose to define the thixotropic effects as being cancelled, such as minimising the magnitude of the streamwise velocity perturbation or the structure perturbation. We choose to define the thixotropic effects as being cancelled when $G_1 = 0$, i.e. when there is no perturbation to the pressure gradient, despite the presence of thixotropy. In the quickly adjusting and weakly advective regime, G_1 is given by (4.1.37). By setting $G_1 = 0$ in this equation, we obtain

$$0 = -\kappa^{(2-b)/b}\frac{2(3n+1)(n-1)}{b(4n-c)}\left(\frac{3n+1}{\pi n}Q\alpha^{-(3n+1)/n}\right)^{2n-c-1}\alpha^{(n-c-1)/n} \times\left[\mathcal{D}_{\mathrm{t}}^{*}\frac{Q'}{Q}-\mathcal{D}_{\mathrm{a}}^{*}\frac{3(3n+1)}{\pi(5n-c+1)}\frac{Q\alpha'}{\alpha^{3}}\right]. \tag{4.1.44}$$

As $\kappa, b, n, Q, \alpha > 0$, (4.1.44) is satisfied when either $n = 1$, the trivial Newtonian

case in which all perturbations are zero, or when

$$0 = \mathcal{D}_{\mathrm{t}}^{*}\frac{Q'}{Q} - \mathcal{D}_{\mathrm{a}}^{*}\frac{3(3n+1)}{\pi(5n-c+1)}\frac{Q\alpha'}{\alpha^3}, \tag{4.1.45}$$

which, following some rearrangement, yields

$$\frac{\mathcal{D}_{\mathrm{t}}^{*}Q'}{\mathcal{D}_{\mathrm{a}}^{*}\alpha'} = \frac{3(3n+1)}{\pi(5n-c+1)}\frac{Q^2}{\alpha^3}. \tag{4.1.46}$$

The terms $\mathcal{D}_{\mathrm{t}}^{*}Q'$ and $\mathcal{D}_{\mathrm{a}}^{*}\alpha'$ determine the strengths of temporal and advective thixotropy respectively, so the term on the L.H.S. of (4.1.46) is the ratio of thixotropic strengths.

We recall that for the volume flux perturbation condition to be satisfied, $4n-c>0$, so $5n-c+1>0$ always, so the right-hand side of (4.1.46) is always positive. It is only possible for the thixotropic effects to cancel (with $G_1=0$) when $\mathcal{D}_{\mathrm{t}}^{*}Q'$ and $\mathcal{D}_{\mathrm{a}}^{*}\alpha'$ have the same sign. For the following examples we consider an accelerating flow in a widening pipe (with $Q'=1$ and $\alpha'=1$), then tune $\mathcal{D}_{\mathrm{t}}^{*}$ and $\mathcal{D}_{\mathrm{a}}^{*}$ so that (4.1.46) is satisfied.

Figure 4.7 shows an example of w_1 and λ_1 from each of the regions of the regime diagram (Figure 4.4), with $G_1=0$. In all of the examples (and for all behaviour in $\mathfrak{R}_{1,1}$) the centreline behaviour of w_1 and λ_1 matches that described in the regime diagram and in the table of schematics (Figure 4.5). In contrast to $\mathfrak{R}_{1,2}$ and $\mathfrak{R}_{2,1}$, w_1 in region $\bar{\mathrm{A}}_{\mathrm{I}}$ when $G_1=0$ does not exhibit any anomalous behaviour, so is qualitatively similar to behaviour in region $\bar{\mathrm{A}}_{\mathrm{II}}$.

We note that for the examples in Figure 4.7(a), w_1 is similar to the behaviour of w_1 in $\mathfrak{R}_{2,1}$ in a widening pipe (cf. Figure 4.2(c)), rather than w_1 in $\mathfrak{R}_{1,2}$ in an accelerating flow, which is the sign-reverse of the behaviour in Figure 4.2(a).

4.1.8 Behaviour of pressure gradient perturbation G_1

In this section, we explore the behaviour of the pressure gradient perturbation G_1, given by (4.1.37), in the quickly adjusting regime and in the weakly advective regime.

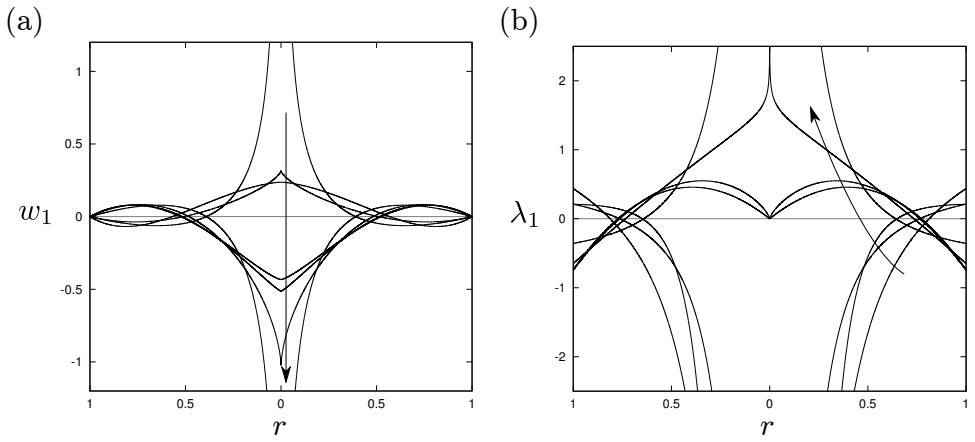

Figure 4.7: sMMW model: profiles of (a) w_1 and (b) λ_1 in the quickly adjusting and weakly advective regime $\mathfrak{R}_{1,1}$, where $G_1 = 0$. The parameters are $a = 0.6$ and $c = 0.25$ ($n = 0.5625$, region $\bar{\mathrm{T}}_{\mathrm{II}}$, $\mathcal{D}_{\mathrm{t}}^* = 0.7204$), $a = 1.2$ and $c = 1$ ($n = 0.75$, region $\bar{\mathrm{T}}_{\mathrm{III}}$, $\mathcal{D}_{\mathrm{t}}^* = 0.8276$), $a = 2.2$ and $c = 2$ ($n = 0.75$, region $\bar{\mathrm{T}}_{\mathrm{IV}}$, $\mathcal{D}_{\mathrm{t}}^* = 1.129$), $a = 0.1$ and $c = 4$ ($n = 5.875$, region $\bar{\mathrm{A}}_{\mathrm{I}}$, $\mathcal{D}_{\mathrm{t}}^* = 0.6743$), $a = 1$ and $c = 4$ ($n = 4.75$, region $\bar{\mathrm{A}}_{\mathrm{II}}$, $\mathcal{D}_{\mathrm{t}}^* = 0.7018$), $a = 2.5$ and $c = 4$ ($n = 2.875$, region $\bar{\mathrm{A}}_{\mathrm{III}}$, $\mathcal{D}_{\mathrm{t}}^* = 0.808$), $a = 3.5$ and $c = 4$ ($n = 1.625$, region $\bar{\mathrm{A}}_{\mathrm{IV}}$, $\mathcal{D}_{\mathrm{t}}^* = 1.095$). The common parameters are $\kappa = 1$, $Q(t) = 1$, $Q'(t) = 1$, $\alpha(z) = 1$, $\alpha'(z) = 1$, $b = 1$, and $\mathcal{D}_{\mathrm{a}}^* = 1$. The arrows show the direction $\bar{\mathrm{T}}_{\mathrm{II}}$–$\bar{\mathrm{T}}_{\mathrm{IV}}$ and $\bar{\mathrm{A}}_{\mathrm{I}}$–$\bar{\mathrm{A}}_{\mathrm{IV}}$.

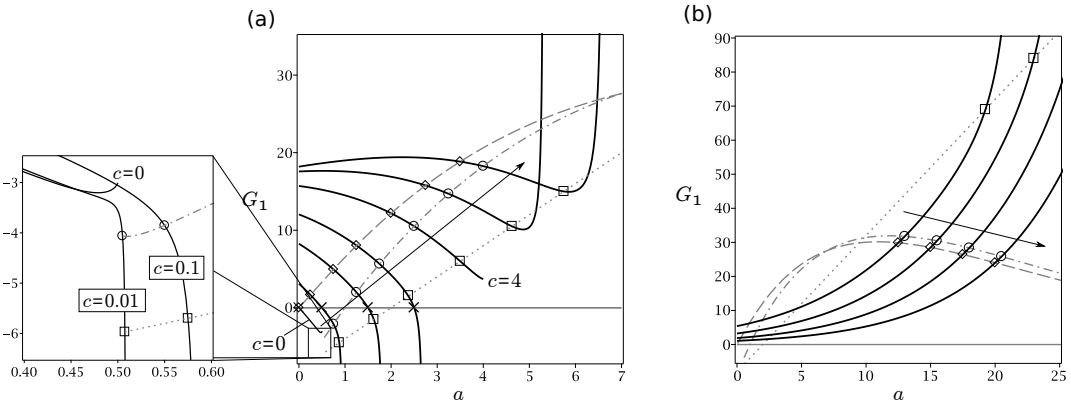

Figure 4.8: sMMW model: plots of the pressure gradient perturbation G_1 as a function of a for (a) $c = 0, 0.5, 1.5, 2.5, 4, 5.5, 7$ (for inset $c = 0, 0.01, 0.1$) and (b) $c = 25, 30, 35, 40$ (black, solid lines). Also shown are the boundaries $a = c$ (grey, solid, intersects G_1 at crosses), $a = c(1-b)$ (grey, dashed, intersects G_1 at diamonds), $a = b + c(1-b)$ (grey, dot-dashed, intersects G_1 at circles) and $a = b + c(2-b)/2$ (grey, dotted, intersects G_1 at squares) from the regime diagram shown in Figure 4.4. The parameters are $\kappa = 1$, $\alpha(z) = 1$, $\alpha'(z) = 1$, $Q(t) = 1$, $b = 0.5$, $\mathcal{D}_{\mathrm{t}}^* = 0$ and $\mathcal{D}_{\mathrm{a}}^* = 1$. The arrows show the direction of increasing c.

Figures 4.8(a) and (b) show G_1 as a function of the parameter a for various values of c (black, solid lines), in the weakly advective regime. Also shown for reference are the boundaries from the regime diagram (Figure 4.4); these are $a = c$ (grey, solid, $G_1 = 0$), $a = c(1-b)$ (grey, dashed), $a = b + c(1-b)$ (grey, dot-dashed) and $a = b + c(2-b)/2$ (grey, dotted), which intersect G_1 at crosses, diamonds, circles and squares, respectively. It is clear from (4.1.37) and Figure 4.8(a) that $G_1 < 0$ for thixotropic fluids ($n < 1$, $a > c$), $G_1 > 0$ for antithixotropic fluids ($n > 1$, $a < c$), and $G_1 = 0$ on the boundary ($n = 1$, $a = c$), on which the fluid is a generalised-Newtonian fluid at equilibrium.

As Figure 4.8 shows, when $c < 4$, G_1 decreases monotonically as a increases, and becomes singular and negative as a approaches the line $n = c/4$, i.e. as $a \to b + c(4-b)/4$ (shown as a thick, solid line in Figure 4.4), at which the expansion scheme breaks down. When c is not too much larger than $c = 4$ (specifically for $4 < c \lesssim 10.54$ when $b = 0.5$, as in Figure 4.8(a)), G_1 decreases to a minimum as a increases, before increasing unboundedly as $a \to b + c(4-b)/4$. For larger values of c (specifically for $c \gtrsim 10.54$ when $b = 0.5$, as in Figure 4.8(b)), G_1

increases monotonically as a increases, and becomes singular as $a \to b+c(4-b)/4$.

The plot of G_1 for $c = 4$ and $b = 0.5$ is labelled in Figure 4.8(a), and is characteristic of the plot of G_1 when $c = 4$ for all values of b. The plot of G_1 for $c = 4$ and $a = 4$ lies on the line $a = c$ between thixotropic and antithixotropic fluids, where we expect $G_1 = 0$, and on the line $a = b + c(4 - b)/4$, where the expansion scheme breaks down and we expect G_1 to be singular. In the double limit $c \to 4$ and $a \to 4$, the terms $n - 1$ and $4n - c$, in the numerator and denominator of G_1 respectively, both tend to zero, and the value G_1 takes depends on how this limit is approached. In particular, upon fixing $c = 4$, $(n-1)/(4n-c) = (c-a)/(4(c-a)-b(4-c)) = 1/4$ for all values of a. Similarly, upon fixing $a = 4$, $(n-1)/(4n-c) = (c-a)/(4(c-a)-b(4-c)) = 1/(4-b)$ for all values of c.

The plot of G_1 for $c = 0$ and $b = 0.5$ is labelled in the inset of Figure 4.8(a), and is characteristic of the plot of G_1 for $c = 0$ for all values of b. The point $c = 0$ and $a = b$ lies on the line $a = b + c(4 - b)/4$, where the expansion scheme breaks down and we expect G_1 to be singular. It is clear in the inset of Figure 4.8(a) that when $a = b$, G_1 is singular as $c \to 0$ (as shown by the plots labelled $c = 0.1, 0.01$), but when $c = 0$, G_1 remains finite as $a \to b$ (as shown by the plot labelled $c = 0$), so the value of G_1 in the limit $c \to 0$ and $a \to b$ depends on how we approach it, which can be shown in a similar way to method shown for the limit $c \to 4$ and $a \to 4$.

Figures 4.9(a) and (b) show G_1 as a function of a for various values of c (black, solid lines), in the quickly adjusting regime. Also shown for reference are the boundaries from the regime diagram (Figure 4.4). As in the weakly advective regime, $G_1 < 0$ for thixotropic fluids ($n < 1$, $a > c$), $G_1 > 0$ for antithixotropic fluids ($n > 1$, $a < c$), and $G_1 = 0$ on the boundary ($n = 1$, $a = c$), where the fluid is a generalised-Newtonian fluid at equilibrium.

The plots of G_1 in the quickly adjusting regime, shown in Figure 4.9, are qualitatively similar to those in the weakly advective regime, shown in Figure 4.8, so no further discussion is required.

The analysis of the sMMW model presented in this section has shown that even in simple rheological models of purely viscous fluids, anomalous behaviour can

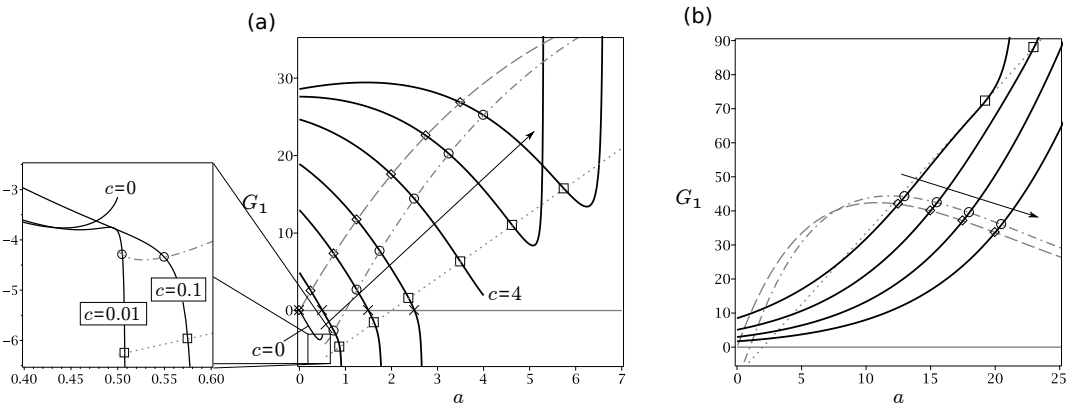

Figure 4.9: sMMW model: plots of the pressure gradient perturbation G_1 as a function of a (black, solid lines) for (a) $c = 0, 0.5, 1.5, 2.5, 4, 5.5, 7$ (for inset $c = 0, 0.01, 0.1$) and (b) $c = 25, 30, 35, 40$. Also shown are the boundaries $a = c$ (grey, solid), $a = c(1-b)$ (grey, dashed), $a = b + c(1-b)$ (grey, dot-dashed) and $a = b + c(2-b)/2$ (grey, dotted) from the regime diagram shown in Figure 4.4. The parameters are $\kappa = 1$, $\alpha(z) = 1$, $\alpha'(z) = 1$, $Q(t) = 1$, $Q'(t) = -1$, $b = 0.5$, $\mathcal{D}_{\mathrm{t}}^* = 1$ and $\mathcal{D}_{\mathrm{a}}^* = 0$. The arrows show the direction of increasing c.

arise. These anomalous cases demonstrate that the TRC and the accompanying physical interpretation are not valid in general. In the following section, we study the full MMW model, for which we find similar anomalous behaviour to the sMMW model and additional anomalous behaviour not present in the sMMW model. We find some similarities between the sMMW and MMW models, so we present a conclusion for the results in this section and in the following section at the end of the chapter, where we may highlight such similarities in the context of the larger question of this thesis: whether we may make general statements regarding the behaviour of thixotropic flows.

4.2 Results for the full MMW model

In Section 4.1, we obtained asymptotic solutions for the sMMW model. By simplifying the model this way, we were able to obtain explicit solutions for the leading-order and perturbation quantities. In this section, we consider the full MMW model with $d > 0$, introduced in Section 2.5.1, given in dimensionless form

by

$$\eta = \lambda \quad \text{and} \quad f = -\Gamma^{a/2}\lambda^b + \kappa\Gamma^{c/2}(1-\lambda)^d, \tag{4.2.1}$$

where the dimensionless quantities are given by (4.1.2) and are presented again here for convenience:

$$\begin{gathered}\hat{r} = \hat{R}r, \quad \hat{z} = \frac{\hat{R}z}{\delta}, \quad \hat{u} = \frac{\delta\hat{Q}_{\mathrm{ref}}u}{\hat{R}^2}, \quad \hat{w} = \frac{\hat{Q}_{\mathrm{ref}}w}{\hat{R}^2}, \quad \hat{\Gamma} = \frac{\hat{Q}_{\mathrm{ref}}^2\Gamma}{\hat{R}^6}, \\ \hat{Q} = \hat{Q}_{\mathrm{ref}}Q, \quad \hat{p} = \frac{\hat{\mu}_0\hat{Q}_{\mathrm{ref}}p}{\delta\hat{R}^3}, \quad \hat{\eta} = \hat{\mu}_0\eta, \quad \hat{\alpha}(\hat{z}) = \hat{R}\alpha(z), \quad \hat{t} = \hat{T}t, \\ \hat{f}(\hat{\Gamma},\lambda) = \hat{f}_0 f(\Gamma,\lambda), \quad \hat{f}_0 = \frac{\hat{k}_1\hat{Q}_{\mathrm{r}}^a}{\hat{R}^{3a}} \quad \text{and} \quad \kappa = \frac{\hat{k}_2\hat{Q}_{\mathrm{r}}^{c-a}}{\hat{k}_1\hat{R}^{3(c-a)}}.\end{gathered} \tag{4.2.2}$$

When $d > 0$, we are not able to isolate λ_{eq} in (2.5.6) for general a, b, c, and d, so we are unable to obtain explicit solutions for leading-order and perturbation quantities. Instead, we use the general solutions obtained in Sections 3.2 and 3.3. We use the computer-algebra package Maple to evaluate the integrals in the general solutions using quadrature, and obtain 'semi-analytical' solutions for leading-order and perturbation quantities. In limited cases, such as when $b = d = 1$, we can obtain explicit solutions. We present an example of such a case in Appendix B.1, for which we are able to match our solutions with those for a limiting case of the Houška model (see Ahmadpour and Sadeghy [26]). Whilst we are unable to analyse the full MMW model in as much depth as the sMMW model, we can use the semi-analytical solutions, along with an asymptotic analysis of the centreline behaviour of the MMW model, to construct a regime diagram and the corresponding sketches of the behaviour similar to those for the sMMW model (shown in Figures 4.4 and 4.5 respectively). We highlight the similarities and differences between the sMMW and the MMW models, and discuss whether the TRC and the associated analogies, presented in Section 3.3.1, agree with the behaviour of the MMW model.

In Section 4.2.1, as done for the sMMW model, we present solutions for the leading-order quantities w_0, λ_0, and u_0, which apply to the three weakly thixotropic regimes $\mathfrak{R}_{2,1}$, $\mathfrak{R}_{1,2}$, and $\mathfrak{R}_{1,1}$. In Section 4.2.2, we present solutions for the perturbation quantities w_1 and λ_1 in the quickly adjusting regime and in the weakly advective regime.

4.2.1 Examples of leading-order quantities

In this section, we present examples of the leading-order quantities w_0, λ_0, and u_0, given by (3.2.5), (3.2.28), and (3.2.19), respectively. Figure 4.10 shows examples of the leading-order quantities w_0, λ_0, and u_0 in a widening pipe ($\alpha' > 0$) for various values of c with $a = b = d = 1$. In this figure, the arrows indicate the direction of increasing c.

Figure 4.10(a) shows examples of the streamwise velocity w_0. In particular, when $a > c$, i.e. for thixotropic fluids, the profile of w_0 is flat near the centre of the pipe, indicating plug-like flow. When $a = c$, w_0 is that of classic Poiseuille flow of a Newtonian fluid along a pipe. When $a < c$, i.e. for antithixotropic fluids, the profile of w_0 is sharp near the centre of the pipe. The behaviour of w_0 is qualitatively similar to that of the sMMW model (cf. Figure 4.1(a), which uses the same values of a, b, and c as Figure 4.10), though the variation of w_0 with c (via n) in the sMMW model is larger than in the MMW model.

Figure 4.10(b) shows examples of the structure parameter λ_0. The behaviour of λ_0 for antithixotropic fluids and when $a = c$ is qualitatively similar to that in the sMMW model (cf. Figure 4.1(b)). For thixotropic fluids, λ_0 is positive and largest at the centreline, as for the sMMW model, but it is bounded above by $\lambda_0 = 1$. This upper bound of λ_0 is built into the model. When $d > 0$, the term $(1 - \lambda)^d$ in the build-up term in (4.2.1) vanishes when $\lambda = 1$, so the structure does not build up further.

Figure 4.10(c) shows examples of the transverse velocity u_0. The behaviour of u_0 is qualitatively similar to that of the sMMW model (cf. Figure 4.1(c)), though, as for w_0, u_0 varies more significantly with c (via n) in the sMMW model than in the MMW model.

4.2.2 Examples of perturbation quantities

In this section, we present examples of the perturbation quantities w_1 and λ_1, given by (3.3.7) and (3.3.1), respectively. As for the sMMW model in Section 4.1.4, we consider the quickly adjusting regime $\mathfrak{R}_{1,2}$ and the weakly advective

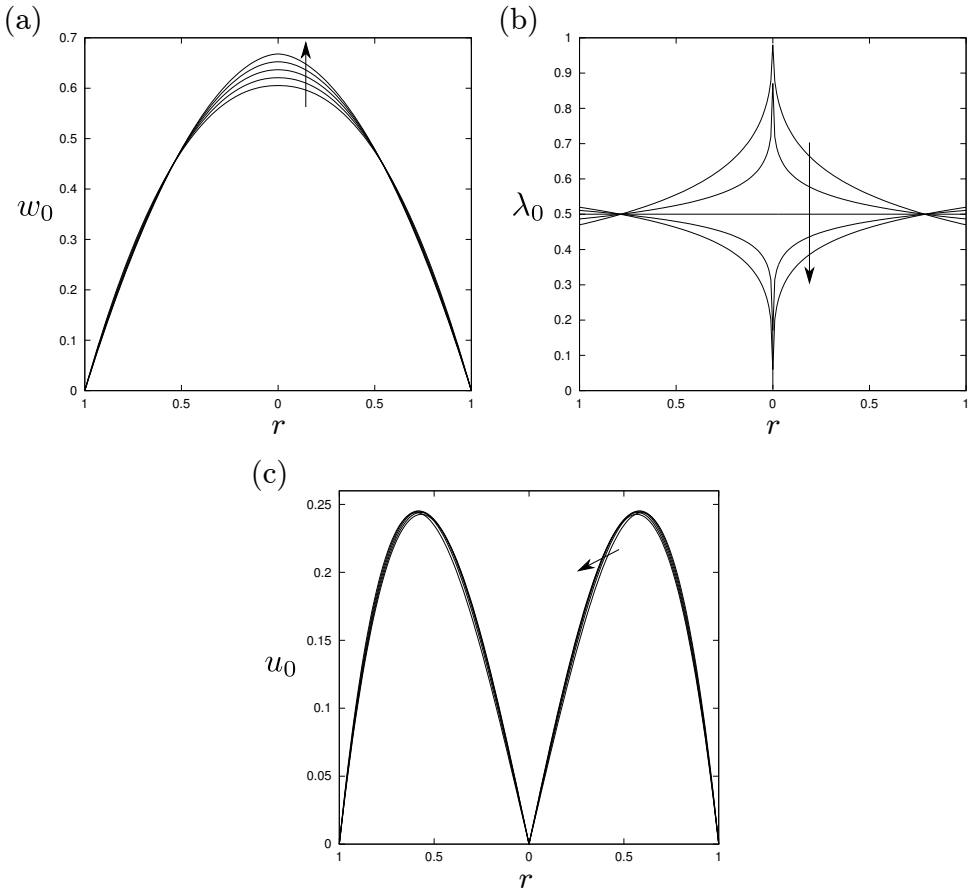

Figure 4.10: MMW model: profiles of (a) w_0, (b) λ_0, and (c) u_0 for various values of c. The parameters are $c = 0.4$ ($G_0 = 1.266$), $c = 0.7$ ($G_0 = 1.273$), $c = 1$ ($G_0 = 1.273$), $c = 1.3$ ($G_0 = 1.270$), and $c = 1.6$ ($G_0 = 1.265$). The common parameters are $\kappa = 1$, $Q(t) = 1$, $\alpha(z) = 1$, $\alpha'(z) = 1$, $a = 1$, $b = 1$, and $d = 1$. The arrows show the direction of increasing c, i.e. from thixotropic to antithixotropic behaviour.

regime $\mathfrak{R}_{2,1}$ separately. To this end, we consider $\mathcal{D}_{\mathrm{t}}^{*} = 1$ and $\mathcal{D}_{\mathrm{a}}^{*} = 0$ for $\mathfrak{R}_{1,2}$, and $\mathcal{D}_{\mathrm{a}}^{*} = 1$ and $\mathcal{D}_{\mathrm{t}}^{*} = 0$ for $\mathfrak{R}_{2,1}$ separately. As stated at the end of Section 4.1.3, we consider decelerating flow in a widening pipe. Specifically, we set $Q' = -1$ and $\alpha' = 1$. We present profiles of w_1 and λ_1 here for illustrative purposes, and provide a more detailed analysis of the full range of behaviours of w_1 and λ_1 in Section 4.2.3.

Figures 4.11(a) and (b) show examples of w_1 and λ_1, in the quickly adjusting regime for various values of c with $a = b = d = 1$ (the arrows show the direction of increasing c (and n)). For thixotropic fluids ($a > c$), the velocity perturbation is positive near the centre of the pipe and negative near the wall. The structure parameter perturbation is negative and singular at the centre of the pipe. For antithixotropic fluids ($a < c$), the velocity perturbation is negative near the centre of the pipe and, to preserve the prescribed volume flux, positive near the wall. The structure parameter perturbation is positive and singular at the centre of the pipe.

Figures 4.11(c) and (d) show examples of w_1 and λ_1 in the weakly advective regime. The streamwise velocity and structure parameter perturbations in the weakly advective regime are qualitatively similar to those in the quickly adjusting regime.

The behaviour in the quickly adjusting regime and in the weakly advective regime shown in Figure 4.11 is qualitatively similar to the behaviour of the sMMW model, for the same values of the parameters a, b, and c (cf. Figure 4.2).

Each of the examples of w_1 and λ_1 in Figure 4.11 agree with the TRC (discussed in Section 3.3.1), using the thixotropic/antithixotropic and widening/decelerating analogies. However, in cases of strong thixotropy and strong antithixotropy, there are other behaviours of w_1 and λ_1 which do not agree with the TRC.

Figure 4.12 shows examples of w_1 and λ_1 for strongly antithixotropic fluids in the quickly adjusting regime $\mathfrak{R}_{1,2}$ and in the weakly advective regime $\mathfrak{R}_{2,1}$ which do not agree with the TRC. Using the TRC and the analogies, we expect these profiles to be similar to that of the antithixotropic fluids shown in Figure 4.11, i.e. we expect w_1 to be negative near the centre of the pipe and positive near the wall.

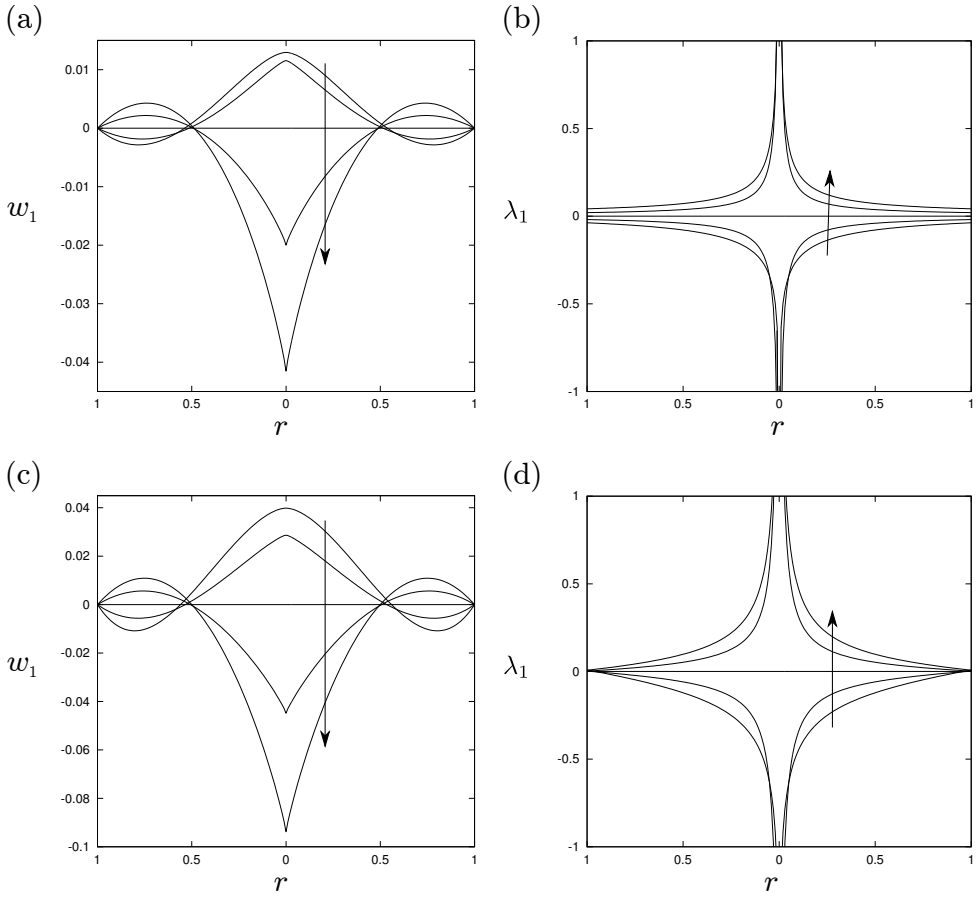

Figure 4.11: MMW model: profiles of (a,c) w_1 and (b,d) λ_1 in (a,b) the quickly adjusting regime $\mathfrak{R}_{1,2}$ and (c,d) the weakly advective regime $\mathfrak{R}_{2,1}$. The parameters are $c = 0.6$ ($G_1 = -0.8410$ ($\mathfrak{R}_{1,2}$), $G_1 = -0.7113$ ($\mathfrak{R}_{2,1}$)), $c = 0.8$ ($G_1 = -0.4074$ ($\mathfrak{R}_{1,2}$), $G_1 = -0.3250$ ($\mathfrak{R}_{2,1}$)), $c = 1$ ($G_1 = 0$ ($\mathfrak{R}_{1,2}$), $G_1 = 0$ ($\mathfrak{R}_{2,1}$)), $c = 1.2$ ($G_1 = 0.3948$ ($\mathfrak{R}_{1,2}$), $G_1 = 0.2917$ ($\mathfrak{R}_{2,1}$)), and $c = 1.4$ ($G_1 = 0.7808$ ($\mathfrak{R}_{1,2}$), $G_1 = 0.5621$ ($\mathfrak{R}_{2,1}$)). The common parameters are $\kappa = 1$, $Q(t) = 1$, $Q'(t) = -1$, $\alpha(z) = 1$, $\alpha'(z) = 1$, $a = 1$, $b = 1$, $d = 1$, and (a,b) $\mathcal{D}_{\mathrm{t}}^* = 1$, $\mathcal{D}_{\mathrm{a}}^* = 0$ and (c,d) $\mathcal{D}_{\mathrm{a}}^* = 1$, $\mathcal{D}_{\mathrm{t}}^* = 0$. The arrows show the direction of increasing c, i.e. from thixotropic to antithixotropic behaviour.

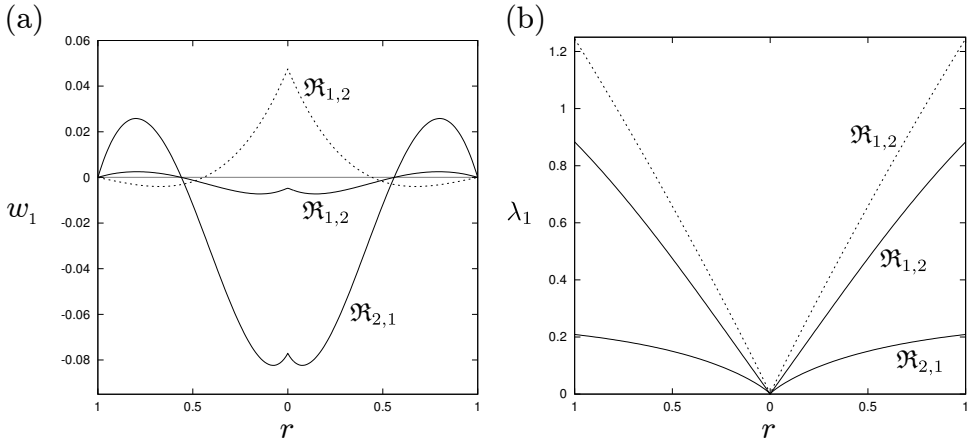

Figure 4.12: MMW model: profiles of (a) w_1, (b) λ_1 for strongly antithixotropic fluids in the quickly adjusting regime $\mathfrak{R}_{1,2}$ and weakly advective regime $\mathfrak{R}_{2,1}$ (labelled accordingly). The parameters are $c = 0.75$ (solid, $G_1 = 0.4709$, $\mathfrak{R}_{1,2}$), $c = 4$ (dotted, $G_1 = 2.444$, $\mathfrak{R}_{1,2}$), $c = 10$ (solid, $G_1 = 9.823$, $\mathfrak{R}_{2,1}$). The common parameters are $a = 0.1$, $b = 0.2$, $d = 1$, $Q(t) = 1$, $Q'(t) = -1$, $\alpha(z) = 1$, $\alpha'(z) = 1$, and $\kappa = 1$, and ($\mathfrak{R}_{1,2}$) $\mathcal{D}_{\mathrm{t}}^* = 1$, $\mathcal{D}_{\mathrm{a}}^* = 0$ and ($\mathfrak{R}_{2,1}$) $\mathcal{D}_{\mathrm{a}}^* = 1$, $\mathcal{D}_{\mathrm{t}}^* = 0$.

In the example shown from $\mathfrak{R}_{2,1}$, w_1 is similar to the TRC, but there is an extra change in the sign of $\partial w_1/\partial r$ near the centreline of the pipe, as shown by the solid line labelled $\mathfrak{R}_{2,1}$ in Figure 4.12(a), yielding a local maximum at the centreline, rather than a local minimum as in the TRC. This behaviour is qualitatively similar to the equivalent fluids in the sMMW model (cf. Figure 4.3(a)).

In contrast to the sMMW model, this behaviour is also seen in $\mathfrak{R}_{1,2}$ (as shown by the solid line labelled $\mathfrak{R}_{1,2}$ in Figure 4.12(a)). Meanwhile, for some strongly antithixotropic fluids in $\mathfrak{R}_{1,2}$, the profile of w_1 is the opposite of the TRC, as shown by the dotted profile in Figure 4.12(a), which is qualitatively similar to the corresponding fluids in the sMMW model (cf. Figure 4.3(a)). So there is an additional behaviour of w_1 for the MMW model that is not present in the sMMW model, one in which w_1 in $\mathfrak{R}_{1,2}$ is qualitatively similar to that in $\mathfrak{R}_{2,1}$. The profile of λ_1 in these anomalous cases does not agree with the TRC. Instead λ_1 is qualitatively similar to the strongly antithixotropic fluids in the sMMW model (cf. Figure 4.3(b)).

In the sMMW model in $\mathfrak{R}_{1,2}$, for increasingly strongly antithixotropic behaviour,

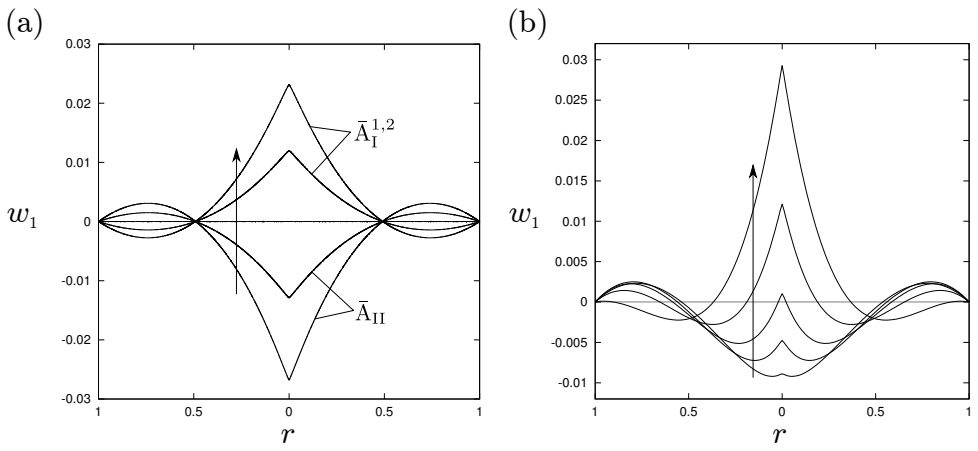

Figure 4.13: Profiles of w_1 for (a) the sMMW model and (b) the MMW model in the quickly adjusting regime $\mathfrak{R}_{1,2}$, illustrating the reversal of w_1 for strongly antithixotropic fluids. The parameters are (a) $a = 0.8$, $b = 0.8$, $d = 0$, and $c = 3, 3.5, 4, 4.5, 5$, and (b) $a = 0.1$, $b = 0.2$, $d = 1$, and $c = 0.5, 0.75, 1, 1.5, 2.5$. The common parameters are $\kappa = 1$, $Q(t) = 1$, $Q'(t) = -1$, $\alpha(z) = 1$, $\alpha'(z) = 1$, $\mathcal{D}_{\mathrm{t}}^* = 1$, and $\mathcal{D}_{\mathrm{a}}^* = 0$. The arrows show the direction of increasing c, i.e. of increasingly strong antithixotropic behaviour.

w_1 and $\partial w_1/\partial r$ change sign when crossing from region $\bar{\mathrm{A}}_{\mathrm{II}}$ to $\bar{\mathrm{A}}_{\mathrm{I}}^{1,2}$, with $w_1 = 0$ on the boundary ($a = c(1 - b)$). This change in behaviour is illustrated in Figure 4.13(a), in which the arrow shows the direction of increasingly strongly antithixotropic behaviour (increasing n via increasing c). In contrast, in the MMW model w_1 is not zero across the width of the pipe when w_1 reverses sign. In the MMW model, for increasingly strongly antithixotropic fluids, $\partial w_1/\partial r$ changes sign first, then for more strongly antithixotropic behaviour w_1 changes sign at the centreline and eventually becomes the opposite of that described by the TRC. This change in behaviour is illustrated in Figure 4.13(b), in which the arrow shows the direction of increasingly strongly antithixotropic behaviour (increasing c).

Figure 4.14 shows examples of w_1 and λ_1 for strongly thixotropic fluids in the quickly adjusting regime $\mathfrak{R}_{1,2}$ and the weakly advective regime $\mathfrak{R}_{2,1}$ which do not agree with the TRC. Using the TRC and the analogies, we expect these profiles to be similar to the profiles of thixotropic fluids shown in Figure 4.11, i.e. we expect w_1 to be positive near the centre of the pipe and negative near the wall.

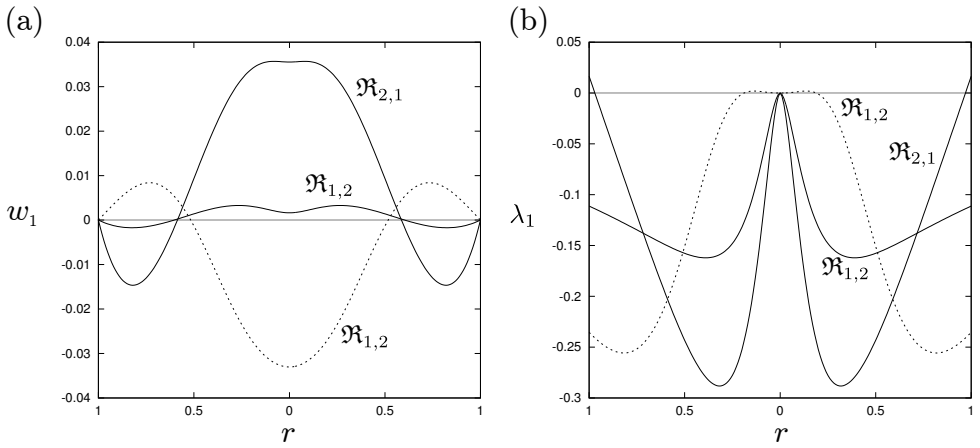

Figure 4.14: MMW model: profiles of (a) w_1, (b) λ_1 for strongly thixotropic fluids in the quickly adjusting regime $\mathfrak{R}_{1,2}$ and weakly advective regime $\mathfrak{R}_{2,1}$ (labelled accordingly). The parameters are $c = 0.62$ (solid, $G_1 = -0.3270$, $\mathfrak{R}_{1,2}$), $c = 0.5$ (dotted, $G_1 = -0.6076$, $\mathfrak{R}_{1,2}$), $c = 0.62$ (solid, $G_1 = -0.2115$, $\mathfrak{R}_{2,1}$). The common parameters are $a = 0.75$, $b = 0.5$, $d = 0.1$, $Q(t) = 1$, $Q'(t) = -1$, $\alpha(z) = 1$, $\alpha'(z) = 1$, and $\kappa = 1$, and ($\mathfrak{R}_{1,2}$) $\mathcal{D}_{\mathrm{t}}^* = 1$, $\mathcal{D}_{\mathrm{a}}^* = 0$ and ($\mathfrak{R}_{2,1}$) $\mathcal{D}_{\mathrm{a}}^* = 1$, $\mathcal{D}_{\mathrm{t}}^* = 0$.

In $\mathfrak{R}_{2,1}$, w_1 is similar to the TRC, as shown in Figure 4.14(a), but there is an extra change in the sign of $\partial w_1/\partial r$ near the centreline of the pipe, yielding a local minimum at the centreline, rather than a local maximum as in the TRC.

For some thixotropic fluids in $\mathfrak{R}_{1,2}$, w_1 is similar to the TRC, as shown by the solid profile labelled $\mathfrak{R}_{1,2}$ in Figure 4.14(a), but there is an extra change in the sign of $\partial w_1/\partial r$ near the centreline of the pipe, yielding a local minimum at the centreline, rather than a local maximum as in the TRC. For some strongly thixotropic fluids in $\mathfrak{R}_{1,2}$ only, the profile of w_1 is the opposite of the TRC, as shown by the dotted profile in Figure 4.14(a). The profile of w_1 reverses in a similar way to w_1 for antithixotropic fluids, as shown in Figure 4.13: first $\partial w_1/\partial r$ changes sign, then w_1 changes sign at the centreline, and eventually, as c (and n) increases, w_1 completely reverses.

The profiles of λ_1 in these anomalous cases, shown in Figure 4.14(b) do not agree with the TRC. As for the strongly antithixotropic fluids in the MMW model, shown in Figure 4.12(b), $\lambda_1 = 0$ at the centreline. In contrast to the antithixotropic fluids, $|\lambda_1|$ has a maximum between the wall and the centre of the

pipe, and in $\mathfrak{R}_{2,1}$ λ_1 changes sign near the wall. In some cases in $\mathfrak{R}_{1,2}$, λ_1 changes sign near the centreline, as shown by the dotted profile in Figure 4.14(b).

The range of behaviours of w_1 and λ_1 shown in Figures 4.11– 4.14 cast doubt on the validity of the thixotropy/antithixotropy and widening/decelerating analogies. In the following section, we study the anomalous behaviour of the perturbations in the MMW model, as done for the sMMW model in Section 4.1.5, by considering the centreline behaviour of the perturbations. We then go on in Section 4.2.4 to consider the ways in which the analogies break down and the physical mechanisms causing this breakdown.

4.2.3 Centreline behaviour of perturbations

In this section, we discuss the behaviour of w_1 and λ_1 near the centreline. Unlike for the sMMW model, we do not have explicit asymptotic solutions for the full MMW model, but we can study the centreline behaviour by considering the behaviour in the asymptotic limit $r \to 0$. We must consider thixotropic and antithixotropic fluids separately, thus we obtain approximations to w_1 and λ_1 for $a > c$ and for $a < c$, which are valid for $0 < r \ll 1$. We use this asymptotic behaviour to study the boundedness and nature of the perturbations at the centreline in Appendices B.2 and B.3. We find a range of qualitatively distinct behaviours for w_1 and λ_1, which we organise into a regime diagram of the parameter space of the MMW model. We study thixotropic fluids in Section 4.2.3.1, followed by antithixotropic fluids in Section 4.2.3.2.

4.2.3.1 Centreline behaviour of thixotropic fluids

To obtain the asymptotic behaviour of w_1 and λ_1 as $r \to 0$ for thixotropic fluids ($a > c$), we seek an expansion in r for $0 < r \ll 1$ of the form

$$\begin{gathered} w_0(r,z,t) \sim W_{00}(z,t) - W_{01}(z,t) r^{\omega}, \quad \lambda_0(r,z,t) \sim 1 - \Lambda_{01}(z,t) r^{\zeta}, \\ \text{and} \quad u_0(r,z,t) \sim U_{00}(z,t) r, \end{gathered} \tag{4.2.3}$$

where we assume $\omega > 0$ and $\zeta > 0$. From (4.2.3) we find the derivatives

$$\begin{gathered}\frac{\partial w_0}{\partial r} \sim -\omega W_{01} r^{\omega-1}, \quad \frac{\partial \lambda_0}{\partial r} \sim -\zeta \Lambda_{01} r^{\zeta-1}, \\ \frac{\partial \lambda_0}{\partial z} \sim -\frac{\partial \Lambda_{01}}{\partial z} r^{\zeta}, \quad \text{and} \quad \frac{\partial \lambda_0}{\partial t} \sim -\frac{\partial \Lambda_{01}}{\partial t} r^{\zeta}.\end{gathered} \tag{4.2.4}$$

We substitute terms from (4.2.3) and (4.2.4) into the leading-order momentum equation (3.1.2), given by

$$\frac{1}{r}\frac{\partial}{\partial r}\left(r\eta_0 \frac{\partial w_0}{\partial r}\right) = -G_0(z,t), \tag{4.2.5}$$

which, recalling that $\eta_0 = \lambda_0$ in the MMW model, yields

$$\frac{1}{r}\frac{\partial}{\partial r}\left[-\omega W_{01} r^{\omega}\right] \sim -G_0. \tag{4.2.6}$$

By performing the differentiation in (4.2.6) we find

$$\omega^2 W_{01} r^{\omega-2} = G_0, \quad \text{so} \quad \omega = 2. \tag{4.2.7}$$

We also use (4.2.3) and (4.2.4) with the structure evolution equation (3.1.3), via (2.5.6), to find

$$\frac{1}{(\Lambda_{01} r^{\zeta})^d} \sim \kappa (2W_{01} r)^{c-a}. \tag{4.2.8}$$

By comparing the exponents of r in each side of (4.2.8) we find

$$r^{-\zeta d} = r^{c-a}, \quad \text{so} \quad \zeta = \frac{a-c}{d}. \tag{4.2.9}$$

By comparing the coefficients of r in (4.2.8), using (4.2.7), we find

$$\Lambda_{01}^{-d} = \kappa (2W_{01})^{c-a}, \quad \text{so} \quad \Lambda_{01} = \kappa^{-1/d} (2W_{01})^{\zeta} = \kappa^{-1/d} \left(\frac{G_0}{2}\right)^{\zeta}. \tag{4.2.10}$$

To find the solutions for the perturbations we must also use $\eta(\Gamma,\lambda)$ and $f(\Gamma,\lambda)$, given by (4.2.1), along with their derivatives, given by

$$\eta_\Gamma(\Gamma_0,\lambda_0)=0,\quad f_\Gamma(\Gamma_0,\lambda_0)=-\frac{a}{2}\Gamma_0^{a/2-1}\lambda_0^b+\frac{c}{2}\kappa\Gamma_0^{c/2-1}(1-\lambda_0)^d, \tag{4.2.11}$$

$$\eta_\lambda(\Gamma_0,\lambda_0)=1,\quad f_\lambda(\Gamma_0,\lambda_0)=-b\Gamma_0^{a/2}\lambda_0^{b-1}-d\kappa\Gamma_0^{c/2}(1-\lambda_0)^{d-1}. \tag{4.2.12}$$

Recalling that $\Gamma_0=(\partial w_0/\partial r)^2\sim(G_0 r/2)^2$ and substituting (4.2.3) and (4.2.4) into the equations for f_Γ and f_λ we find

$$f_\Gamma(\Gamma_0,\lambda_0)\sim-\frac{a}{2}\left(\frac{G_0}{2}r\right)^{a-2}+\frac{c}{2}\kappa\left(\frac{G_0}{2}r\right)^{c-2}\kappa^{-1}\left(\frac{G_0}{2}r\right)^{\zeta d}, \tag{4.2.13}$$

$$=\frac{1}{2}(c-a)\left(\frac{G_0}{2}\right)^{a-2}r^{a-2}, \tag{4.2.14}$$

and

$$f_\lambda(\Gamma_0,\lambda_0)\sim-b\left(\frac{G_0}{2}r\right)^{a}-d\kappa\left(\frac{G_0}{2}r\right)^{c}\kappa^{(1-d)/d}\left(\frac{G_0}{2}r\right)^{\zeta(d-1)}, \tag{4.2.15}$$

$$=-b\left(\frac{G_0}{2}r\right)^{a}-d\kappa^{1/d}\left(\frac{G_0}{2}r\right)^{a-\zeta}, \tag{4.2.16}$$

respectively. As $\zeta>0$ and therefore $a>a-\zeta$, (4.2.16) reduces to

$$f_\lambda(\Gamma_0,\lambda_0)\sim-d\kappa^{1/d}\left(\frac{G_0}{2}\right)^{a-\zeta}r^{a-\zeta}. \tag{4.2.17}$$

We can now find $A(r,z,t)$ and $B(r,z,t)$, given by (3.3.3) and (3.3.4) respectively, which we rewrite here for convenience:

$$A(r,z,t)=\eta_0+2\left(\eta_\Gamma-\eta_\lambda\frac{f_\Gamma}{f_\lambda}\right)\left(\frac{\partial w_0}{\partial r}\right)^2, \tag{4.2.18}$$

$$B(r,z,t)=\frac{\eta_\lambda}{f_\lambda}\left[\mathcal{D}_{\mathrm{t}}^*\frac{\partial\lambda_0}{\partial t}+\mathcal{D}_{\mathrm{a}}^*\left(u_0\frac{\partial\lambda_0}{\partial r}+w_0\frac{\partial\lambda_0}{\partial z}\right)\right]\frac{\partial w_0}{\partial r}. \tag{4.2.19}$$

So for $A(r,z,t)$ we obtain

$$A(r,z,t) \sim 1 - \Lambda_{01} r^{\zeta} - 2 \left(\frac{\frac{1}{2}(c-a)\left(\frac{G_0}{2}\right)^{a-2} r^{a-2}}{-d\kappa^{1/d}\left(\frac{G_0}{2}\right)^{a-\zeta} r^{a-\zeta}} \right) \left(\frac{G_0}{2} r\right)^2, \tag{4.2.20}$$

$$= 1 - \frac{\zeta+1}{\kappa^{1/d}} \left(\frac{G_0}{2}\right)^{\zeta} r^{\zeta}, \tag{4.2.21}$$

and for $B(r,z,t)$ we obtain

$$B(r,z,t) \sim \frac{1}{-d\kappa^{1/d}\left(\frac{G_0}{2}\right)^{a-\zeta} r^{a-\zeta}} \tag{4.2.22}$$

$$\times \left[-\mathcal{D}_{\mathrm{t}}^* \frac{\partial \Lambda_{01}}{\partial t} r^{\zeta} + \mathcal{D}_{\mathrm{a}}^* \left(-U_{00}\zeta\Lambda_{01} r^{\zeta} - (W_{00} - W_{01} r^2) \frac{\partial \Lambda_{01}}{\partial z} r^{\zeta} \right) \right] \frac{G_0}{2} r,$$

$$= \frac{\zeta}{d\kappa^{2/d}} \left(\frac{G_0}{2}\right)^{2\zeta-a+1} r^{2\zeta-a+1} \tag{4.2.23}$$

$$\times \left[\mathcal{D}_{\mathrm{t}}^* \frac{1}{G_0} \frac{\partial G_0}{\partial t} + \mathcal{D}_{\mathrm{a}}^* \left(U_{00} + \left(W_{00} - \left(\frac{G_0}{4}\right) r^2 \right) \frac{1}{G_0} \frac{\partial G_0}{\partial z} \right) \right],$$

$$\sim \frac{\zeta}{d\kappa^{2/d}} \left[\mathcal{D}_{\mathrm{t}}^* \frac{1}{G_0} \frac{\partial G_0}{\partial t} + \mathcal{D}_{\mathrm{a}}^* \left(U_{00} + W_{00} \frac{1}{G_0} \frac{\partial G_0}{\partial z} \right) \right] \left(\frac{G_0}{2}\right)^{2\zeta-a+1} r^{2\zeta-a+1}. \tag{4.2.24}$$

We see from (4.2.21) that $A \to 1$ as $r \to 0$. In addition, we see from (4.2.24) that $B \to 0$ as $r \to 0$ if the exponent $2\zeta - a + 1 > 0$, and B becomes unbounded as $r \to 0$ if $2\zeta - a + 1 < 0$.

Using (4.2.21) and (4.2.24) with the equation for $\partial w_1/\partial r$, given by (3.3.6), we obtain

$$\frac{\partial w_1}{\partial r} \sim -\frac{G_1(z,t) r}{2} \tag{4.2.25}$$

$$- \frac{\zeta}{d\kappa^{2/b}} \left[\mathcal{D}_{\mathrm{t}}^* \frac{1}{G_0} \frac{\partial G_0}{\partial t} + \mathcal{D}_{\mathrm{a}}^* \left(U_{00} + W_{00} \frac{1}{G_0} \frac{\partial G_0}{\partial z} \right) \right] \left(\frac{G_0}{2}\right)^{2\zeta-a+1} r^{2\zeta-a+1},$$

which we then integrate with respect to r to find w_1:

$$w_1 \sim -\frac{G_1(z,t)r^2}{4} - \frac{\zeta}{d\kappa^{2/d}(2\zeta - a + 2)} \times \left[\mathcal{D}_{\mathrm{t}}^* \frac{1}{G_0}\frac{\partial G_0}{\partial t} + \mathcal{D}_{\mathrm{a}}^* \left(U_{00} + W_{00}\frac{1}{G_0}\frac{\partial G_0}{\partial z}\right)\right] \left(\frac{G_0}{2}\right)^{2\zeta-a+2} r^{2\zeta-a+2} + C, \tag{4.2.26}$$

where C is a constant of integration.

Now we can find the solution for λ_1 using equation (3.3.1):

$$\lambda_1 = \mathcal{D}_{\mathrm{t}}^* \frac{1}{f_\lambda}\frac{\partial \lambda_0}{\partial t} + \mathcal{D}_{\mathrm{a}}^* \frac{1}{f_\lambda}\left(u_0\frac{\partial \lambda_0}{\partial r} + w_0\frac{\partial \lambda_0}{\partial z}\right) - 2\frac{f_\Gamma}{f_\lambda}\frac{\partial w_0}{\partial r}\frac{\partial w_1}{\partial r}. \tag{4.2.27}$$

Using (4.2.3), (4.2.4), and (4.2.26) we obtain

$$\begin{aligned}\lambda_1 \sim{}& \mathcal{D}_{\mathrm{t}}^* \frac{\zeta}{d\kappa^{2/d}}\left(\frac{G_0}{2}\right)^{2\zeta-a} r^{2\zeta-a}\frac{1}{G_0}\frac{\partial G_0}{\partial t} \\ &+ \mathcal{D}_{\mathrm{a}}^* \frac{\zeta}{d\kappa^{2/d}}\left(\frac{G_0}{2}\right)^{2\zeta-a} r^{2\zeta-a}\left(U_{00} + \left(W_{00} - \frac{G_0}{4}r^2\right)\frac{1}{G_0}\frac{\partial G_0}{\partial z}\right) \\ &- \zeta\kappa^{-1/d}\left(\frac{G_0}{2}\right)^{\zeta-1} r^{\zeta-1}\Bigg(- \frac{G_1 r}{2} - \frac{\zeta}{d\kappa^{2/d}} \\ &\times \left[\mathcal{D}_{\mathrm{t}}^* \frac{1}{G_0}\frac{\partial G_0}{\partial t} + \mathcal{D}_{\mathrm{a}}^* \left(U_{00} + W_{00}\frac{1}{G_0}\frac{\partial G_0}{\partial z}\right)\right] \left(\frac{G_0}{2}\right)^{2\zeta-a+1} r^{2\zeta-a+1}\Bigg),\end{aligned} \tag{4.2.28}$$

which simplifies to

$$\begin{aligned}\lambda_1 \sim{}& \frac{\zeta}{d\kappa^{2/d}}\left[\mathcal{D}_{\mathrm{t}}^* \frac{1}{G_0}\frac{\partial G_0}{\partial t} + \mathcal{D}_{\mathrm{a}}^* \left(U_{00} + W_{00}\frac{1}{G_0}\frac{\partial G_0}{\partial z}\right)\right] \\ &\times \left[\left(\frac{G_0}{2}\right)^{2\zeta-a} r^{2\zeta-a} + \zeta\kappa^{-1/d}\left(\frac{G_0}{2}\right)^{3\zeta-a} r^{3\zeta-a}\right].\end{aligned} \tag{4.2.29}$$

As $\zeta = (a-c)/d > 0$, we see that $2\zeta - a < 3\zeta - a$, so the term with the exponent $2\zeta - a$ will dominate as $r \to 0$, hence

$$\lambda_1 \sim \frac{\zeta}{d\kappa^{2/d}}\left[\mathcal{D}_{\mathrm{t}}^* \frac{1}{G_0}\frac{\partial G_0}{\partial t} + \mathcal{D}_{\mathrm{a}}^* \left(U_{00} + W_{00}\frac{1}{G_0}\frac{\partial G_0}{\partial z}\right)\right] \left(\frac{G_0}{2}\right)^{2\zeta-a} r^{2\zeta-a}. \tag{4.2.30}$$

We note that in the limit $d \to 0$, $\zeta \to \infty$ and the exponent of λ_0, given in

(4.2.3) diverges, so the centreline behaviour obtained in this section only applies to $d > 0$, and cannot be used for the sMMW model.

4.2.3.2 Centreline behaviour of antithixotropic fluids

To obtain the asymptotic behaviour of w_1 and λ_1 as $r \to 0$ for antithixotropic fluids ($a < c$), we seek an expansion in r for $0 < r \ll 1$ of the form

$$\begin{gathered} w_0(r,z,t) \sim W_{00}(z,t) - W_{01}(z,t)r^{\chi}, \quad \lambda_0(r,z,t) \sim \Lambda_{01}(z,t)r^{\xi}, \\ \text{and} \quad u_0(r,z,t) \sim U_{00}(z,t)r, \end{gathered} \tag{4.2.31}$$

where we assume $\chi > 0$ and $\xi > 0$. From (4.2.31) we find the derivatives

$$\begin{gathered} \frac{\partial w_0}{\partial r} \sim -\chi W_{01} r^{\chi-1}, \quad \frac{\partial \lambda_0}{\partial r} \sim \xi \Lambda_{01} r^{\xi-1}, \\ \frac{\partial \lambda_0}{\partial z} \sim \frac{\partial \Lambda_{01}}{\partial z} r^{\xi}, \quad \text{and} \quad \frac{\partial \lambda_0}{\partial t} \sim \frac{\partial \Lambda_{01}}{\partial t} r^{\xi}. \end{gathered} \tag{4.2.32}$$

We substitute terms from (4.2.31) and (4.2.32) into the leading-order momentum equation (3.1.2), given by

$$\frac{1}{r}\frac{\partial}{\partial r}\left(r\eta_0 \frac{\partial w_0}{\partial r}\right) = -G_0(z,t), \tag{4.2.33}$$

which, recalling that $\eta_0 = \lambda_0$, yields

$$\frac{1}{r}\frac{\partial}{\partial r}\left[-\chi \Lambda_{01} W_{01} r^{\xi+\chi}\right] \sim -G_0. \tag{4.2.34}$$

By performing the differentiation in (4.2.34) we find

$$\xi + \chi = 2 \quad \text{and} \quad 2\chi \Lambda_{01} W_{01} = G_0. \tag{4.2.35}$$

We also use (4.2.31) and (4.2.32) with the structure evolution equation (3.1.3), via (2.5.6), to find

$$(\Lambda_{01} r^{\xi})^b \sim \kappa (\chi W_{01} r^{\chi-1})^{c-a}. \tag{4.2.36}$$

By comparing the exponents and coefficients of r in (4.2.36), using (4.2.35), we find

$$\xi = \frac{n-1}{n} \quad \text{and} \quad \chi = \frac{n+1}{n}, \quad \text{where} \quad n = \frac{c-a}{b} + 1, \tag{4.2.37}$$

and

$$\Lambda_{01}^b = \kappa(\chi W_{01})^{c-a}, \quad \text{so} \quad \Lambda_{01} = \kappa^{1/b}(\chi W_{01})^{n-1} = \kappa^{1/b}\left(\frac{G_0}{2}\right)^{\xi}. \tag{4.2.38}$$

To find the solutions for the perturbations we must also use $\eta(\Gamma, \lambda)$ and $f(\Gamma, \lambda)$, given by (4.2.1), along with their derivatives, given by (4.2.11) and (4.2.12).

Recalling that $\Gamma_0 = (\partial w_0/\partial r)^2 \sim (G_0 r/2)^2$ and substituting (4.2.31) and (4.2.32) into the equations for f_Γ and f_λ we find

$$f_\Gamma \sim -\frac{a}{2}\left(\frac{G_0}{2}r\right)^{(a-2)/n} \kappa\left(\frac{G_0}{2}r\right)^{\xi b} + \frac{c}{2}\kappa\left(\frac{G_0}{2}r\right)^{(c-2)/n}, \tag{4.2.39}$$

$$= \frac{1}{2}\kappa\,(c-a)\left(\frac{G_0}{2}\right)^{(c-2)/n} r^{(c-2)/n}, \tag{4.2.40}$$

and

$$f_\lambda \sim -b\left(\frac{G_0}{2}r\right)^{a/n} \kappa^{(b-1)/b}\left(\frac{G_0}{2}r\right)^{\xi(b-1)} - d\kappa\left(\frac{G_0}{2}r\right)^{c/n}, \tag{4.2.41}$$

$$= -b\kappa^{(b-1)/b}\left(\frac{G_0}{2}r\right)^{c/n-\xi} - d\kappa\left(\frac{G_0}{2}r\right)^{c/n}, \tag{4.2.42}$$

respectively. As $\xi > 0$, and therefore $c/n - \xi < c/n$, (4.2.42) reduces to

$$f_\lambda \sim -b\kappa^{(b-1)/b}\left(\frac{G_0}{2}r\right)^{(c-n+1)/n}. \tag{4.2.43}$$

We can now find $A(r, z, t)$ and $B(r, z, t)$, given by (4.2.18) and (4.2.19) respec-

tively. For $A(r,z,t)$ we obtain

$$A(r,z,t) \sim \Lambda_{01} r^{\xi} - 2 \left(\frac{\frac{1}{2}\kappa\,(c-a) \left(\frac{G_0}{2}\right)^{(c-2)/n} r^{(c-2)/n}}{-b\kappa^{(b-1)/b} \left(\frac{G_0}{2}\right)^{(c-n+1)/n} r^{(c-n+1)/n}} \right) \left(\frac{G_0}{2} r\right)^{2/n}, \tag{4.2.44}$$

$$= \kappa^{1/b} n \left(\frac{G_0}{2}\right)^{(n-1)/n} r^{(n-1)/n}, \tag{4.2.45}$$

and for $B(r,z,t)$ we obtain

$$B(r,z,t) \sim -\frac{\kappa^{(1-b)/b}}{b} \left(\frac{G_0}{2}\right)^{\xi - c/n} r^{\xi - c/n} \left(\frac{G_0}{2} r\right)^{1/n} \tag{4.2.46}$$

$$\times \left[\mathcal{D}_{\mathrm{t}}^{*} \frac{\partial \Lambda_{01}}{\partial t} r^{\xi} + \mathcal{D}_{\mathrm{a}}^{*} \left(U_{00} r \xi \Lambda_{01} r^{\xi - 1} + (W_{00} - W_{01} r^{\chi}) \frac{\partial \Lambda_{01}}{\partial z} r^{\xi} \right) \right],$$

$$\sim -\frac{\kappa^{(1-b)/b}}{b} \xi \left[\mathcal{D}_{\mathrm{t}}^{*} \frac{G_{0,t}}{G_0} + \mathcal{D}_{\mathrm{a}}^{*} \left(U_{00} + W_{00} \frac{G_{0,z}}{G_0} \right) \right] \left(\frac{G_0}{2} r\right)^{(2n-c-1)/n}. \tag{4.2.47}$$

We see from (4.2.45) that $A \to 0$ as $r \to 0$. In addition, we see from (4.2.47) that $B \to 0$ as $r \to 0$ if the exponent $2n - c - 1 > 0$, and B becomes unbounded as $r \to 0$ if $2n - c - 1 < 0$.

Using (4.2.45) and (4.2.47) with the equation for $\partial w_1 / \partial r$, given by (3.3.6), we obtain

$$\frac{\partial w_1}{\partial r} \sim -\frac{G_1}{2} \frac{\kappa^{-1/b}}{n} \left(\frac{G_0}{2}\right)^{(1-n)/n} r^{1/n} \tag{4.2.48}$$

$$+ \frac{\kappa^{-1}}{bn} \xi \left[\mathcal{D}_{\mathrm{t}}^{*} \frac{G_{0,t}}{G_0} + \mathcal{D}_{\mathrm{a}}^{*} \left(U_{00} + W_{00} \frac{G_{0,z}}{G_0} \right) \right] \left(\frac{G_0}{2}\right)^{(n-c)/n} r^{(n-c)/n},$$

which we then integrate with respect to r to find w_1:

$$w_1 \sim -\frac{G_1}{2}\frac{\kappa^{-1/b}}{n+1}\left(\frac{G_0}{2}\right)^{(1-n)/n} r^{(n+1)/n} + \frac{\xi}{b}\frac{\kappa^{-1/b}}{2n-c}\left[\mathcal{D}_{\mathrm{t}}^*\frac{G_{0,t}}{G_0} + \mathcal{D}_{\mathrm{a}}^*\left(U_{00} + W_{00}\frac{G_{0,z}}{G_0}\right)\right]\left(\frac{G_0}{2}\right)^{(n-c)/n} r^{(2n-c)/n} + C, \tag{4.2.49}$$

where C is a constant of integration. We can now find the behaviour of λ_1 near the centreline using (4.2.27), (4.2.31), (4.2.32), and (4.2.49), which yields λ_1:

$$\lambda_1 \sim \frac{c\kappa - a}{c\kappa - a + b}\left(\frac{G_0}{2}r\right)^{(n-1)/n}\frac{G_1}{G_0} - \frac{\xi}{b}\kappa^{(2-b)/b}\left[\mathcal{D}_{\mathrm{t}}^*\frac{G_{0,t}}{G_0} + \mathcal{D}_{\mathrm{a}}^*\left(U_{00} + W_{00}\frac{G_{0,z}}{G_0}\right)\right]\left(\frac{G_0}{2}r\right)^{(2n-c-2)/n}. \tag{4.2.50}$$

Having obtained asymptotic solutions for w_1 and λ_1 for thixotropic and antithixotropic fluids, we analyse them to determine the centreline behaviour of these quantities. The details of these analyses are presented for w_1 in Appendix B.2 and for λ_1 in Appendix B.3. We find a range of qualitatively distinct behaviours for w_1 and λ_1, which we organise into a regime diagram of the parameter space of the MMW model. As for the sMMW model, we find that the parameter space (a, b, c, d) of the MMW model can be divided into various regions of qualitatively similar behaviour of w_1 and λ_1. In addition, we find exactly for which parameter values the behaviours of w_1 and λ_1 agree with the TRC, and for which they do not, which allows an in-depth study of the anomalous behaviour shown in Figures 4.12 and 4.14.

4.2.3.3 Regime diagrams

We summarise the behaviour of w_1 and λ_1 at the centreline in the quickly adjusting regime and in the weakly advective regime as follows. We note, given $a, b, c \geq 0$, that the line $a = c(1 - b/2)$ only exists in this quadrant of (c, a)-space when $b < 2$, and similarly the line $a = c(1 - b)$ only exists in this quadrant when $b < 1$. In addition, given that $a, c, d \geq 0$, the line $a = 2c/(2 - d)$ only exists in this quadrant of (c, a)-space when $d < 2$, and similarly the line $a = c/(1 - d)$

only exists in this quadrant when $d < 1$. By plotting these lines in (c, a)-space, we obtain a regime diagram for all possible behaviours of w_1 and λ_1. Figure 4.15 shows an example of this regime diagram, for $b = 0.8$ and $d = 0.8$.

The critical lines for thixotropic fluids, given along the top of Figure 4.15, do not depend on the parameter b, and those for antithixotropic fluids, given along the right of Figure 4.15, do not depend on the parameter d. This suggests that the centreline behaviour of thixotropic fluids is dominated by the build-up term of the structure evolution rate (4.2.1) ($\kappa\Gamma^{c/2}(1-\lambda)^d$), and the centreline behaviour of antithixotropic fluids is dominated by the breakdown term of the structure evolution rate (4.2.1) ($-\Gamma^{a/2}\lambda^b$). In addition, we note that the critical lines for antithixotropic fluids in the full MMW model are identical to those in the sMMW model (cf. the equations along the right of the regime diagram in Figure 4.15 and those along the right of the regime diagrams in Figure 4.4).

The labels in Figure 4.15 refer to regions of qualitatively similar centreline behaviour of w_1, for decelerating flow in a widening pipe. Regions $\mathrm{T_I}$–$\mathrm{T_{IV}}$ contain only thixotropic behaviour, characterised by

- Region $\mathrm{T_I}$: w_1 is positive and flat, with a local minimum at the centreline, rather than a maximum,
- Region $\mathrm{T_{II}}$: w_1 is positive and flat at the centreline,
- Region $\mathrm{T_{III}}$: w_1 is positive and has a cusp at the centreline,
- Region $\mathrm{T_{IV}}$: w_1 is positive and singular at the centreline.

Regions $\mathrm{A_I}$–$\mathrm{A_{IV}}$ contain only antithixotropic behaviour, characterised by

- Region $\mathrm{A_I}$: w_1 is negative and flat, with a local maximum at the centreline, rather than a minimum,
- Region $\mathrm{A_{II}}$: w_1 is negative and flat at the centreline,
- Region $\mathrm{A_{III}}$: w_1 is negative and has a cusp at the centreline,
- Region $\mathrm{A_{IV}}$: w_1 is negative and singular at the centreline.

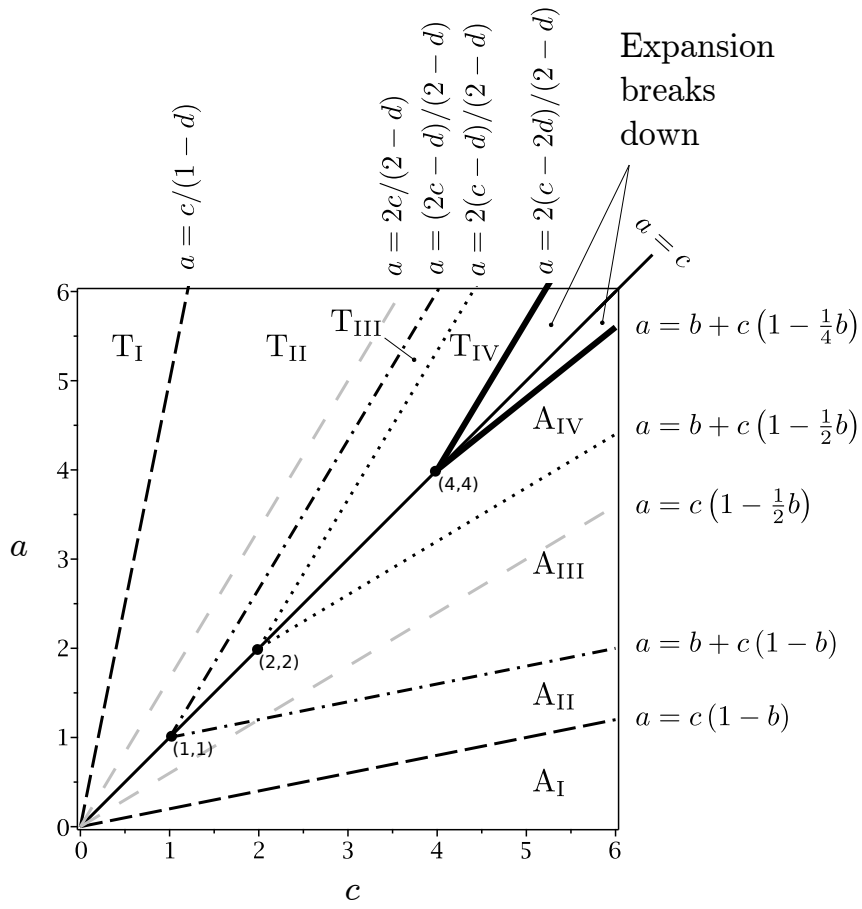

Figure 4.15: MMW model: regime diagram for $b = 0.8$ and $d = 0.8$, for the centreline behaviour of w_1 and λ_1. The critical lines of the parameter space of the MMW model, obtained in Appendices B.2 and B.3, are $a = c$ and, for thixotropic fluids ($a > c$): $a = c/(1-d)$, $a = 2c/(2-d)$, $a = (2c-d)/(2-d)$, $a = 2(c-d)/(2-d)$, $a = 2(c-2d)/(2-d)$, and, for antithixotropic fluids ($a < c$): $a = c(1-b)$, $a = b + c(1-b)$, $a = c(1-b/2)$, $a = b + c(1-b/2)$, and $a = b + c(1-b/4)$.

Region T_I is bounded to the right by $a = c/(1-d)$. When $d < 1$ this region is present in the regime diagram, as shown in Figure 4.15, but when $d > 1$ this region is absent (because it would require $c < 0$). Region A_I is bounded above by $a = c(1-b)$. When $b < 1$ this region is present in the regime diagram, as shown in Figure 4.15, but when $b > 1$ this region is absent (because it would require $a < 0$).

For thixotropic fluids, when $a > 2c/(1-2d)$, λ_1 is zero and has a cusp at the centreline, when $a < 2c/(1-2d)$, λ_1 is negative and singular at the centreline. For antithixotropic fluids, when $a < c(1-b/2)$, λ_1 is zero and has a cusp at the centreline, when $a > c(1-b/2)$, λ_1 is positive and singular at the centreline.

The thick solid lines in Figure 4.15 denote $a = 2(c-2d)/(2-d)$ and $a = b+c(1-b/4)$. For thixotropic fluids we require $a > 2(c-2d)/(2-d)$ for the expansion scheme to be valid, and for antithixotropic fluids we require $a < b + c(1-b/4)$ for the expansion scheme to be valid. So there is a region of the parameter space $(b + c(1-b/4) < a < b + c)$, labelled 'Expansion breaks down' in Figure 4.15 which is physically meaningful but beyond the reach of the expansion scheme. We require a different technique, such as numerical simulation, to access the behaviour of the velocity and structure parameter in this region.

We note that when $b = d$, as in Figure 4.15, the dashed lines ($a = c/(1-d)$ and $a = c(1-b)$), the space-dashed lines ($a = 2c/(2-d)$ and $a = c(1-b/2)$), and the dotted lines ($a = 2(c-d)/(2-d)$ and $a = b+c(1-b/2)$) have reflective symmetry about the thin solid line $a = c$. The dot-dashed lines ($a = (2c-d)/(2-d)$ and $a = b + c(1-b)$) and the thick solid lines ($a = 2(c-2d)/(2-d)$ and $a = b + c(1-b/4)$) are not symmetric about $a = c$, which implies that the thixotropic/antithixotropic analogy does not always hold for the MMW model. For example, in Figure 4.15, the thixotropic region T_{III} lies to the right of the space-dashed line $a = 2c/(2-d)$, so in this region w_1 is positive and has a cusp at the centreline, and λ_1 is always negative and singular at the centreline. However, in the equivalent antithixotropic region A_{III}, w_1 is negative and has a cusp at the centreline, but λ_1 may be positive and singular at the centreline (when $a > c(1-b/2)$) or zero at the centreline (when $a < c(1-b/2)$).

Figure 4.16 shows a table of schematics for the MMW model, the equivalent of

that presented for the sMMW model in Figure 4.5. It shows sketches of the perturbation quantities w_1 and λ_1 in each of the regions $\mathrm{T_I}$–$\mathrm{T_{IV}}$ and $\mathrm{A_I}$–$\mathrm{A_{IV}}$, and so is a summary of all possible qualitative behaviours of the MMW model in the weakly advective regime and in the quickly adjusting regime. The line labelled $a = c$ denotes the boundary between thixotropic fluids to the left and antithixotropic fluids to the right. The grey box indicates the behaviours that agree with the TRC, using the thixotropy/antithixotropy and widening/decelerating analogies, and so profile sketches outwith this box do not agree with the TRC.

For thixotropic fluids, whilst there is some variation in the behaviour at the centreline, w_1 in both the weakly advective regime and in the quickly adjusting regime is positive near the centreline and negative near the wall. In addition, λ_1 is negative and either zero or singular at the centreline. For antithixotropic fluids, whilst there is some variation in the behaviour at the centreline, w_1 in both the weakly advective regime and in the quickly adjusting regime is negative near the centreline and positive near the wall. In addition, λ_1 is positive and either zero or singular at the centreline.

For thixotropic fluids in regions $\mathrm{T_{II}}$–$\mathrm{T_{IV}}$, in both the weakly advective regime and in the quickly adjusting regime, w_1 is positive, with some qualitative variation, near the centreline and negative near the wall. In these regions, w_1 agrees with the TRC using the widening/decelerating analogy. Region $\mathrm{T_I}$ contains strongly thixotropic fluids. Figure 4.16 shows that for fluids in region $\mathrm{T_I}$, w_1 does not agree with the TRC. Whilst w_1 is positive near the centreline and negative near the wall, as for thixotropic fluids in regions $\mathrm{T_{II}}$–$\mathrm{T_{IV}}$, there is an extra change in the sign of the gradient of w_1 near the centreline not described by the TRC. As this anomalous behaviour occurs in both the weakly advective regime and in the quickly adjusting regime, the widening/accelerating analogy holds, so the physical description for the TRC must be refined. We note that for thixotropic fluids in $\mathfrak{R}_{1,2}$, w_1 may be the opposite of the TRC, resembling the reversal of w_1 in $\bar{\mathrm{A}}_{\mathrm{I}}^{1,2}$ for the sMMW model (we recall that there is no corresponding reversal in w_1 for thixotropic fluids in the sMMW model).

For antithixotropic fluids in regions $\mathrm{A_{II}}$–$\mathrm{A_{IV}}$, in both the weakly advective regime and in the quickly adjusting regime, w_1 is negative, with some qualitative varia-

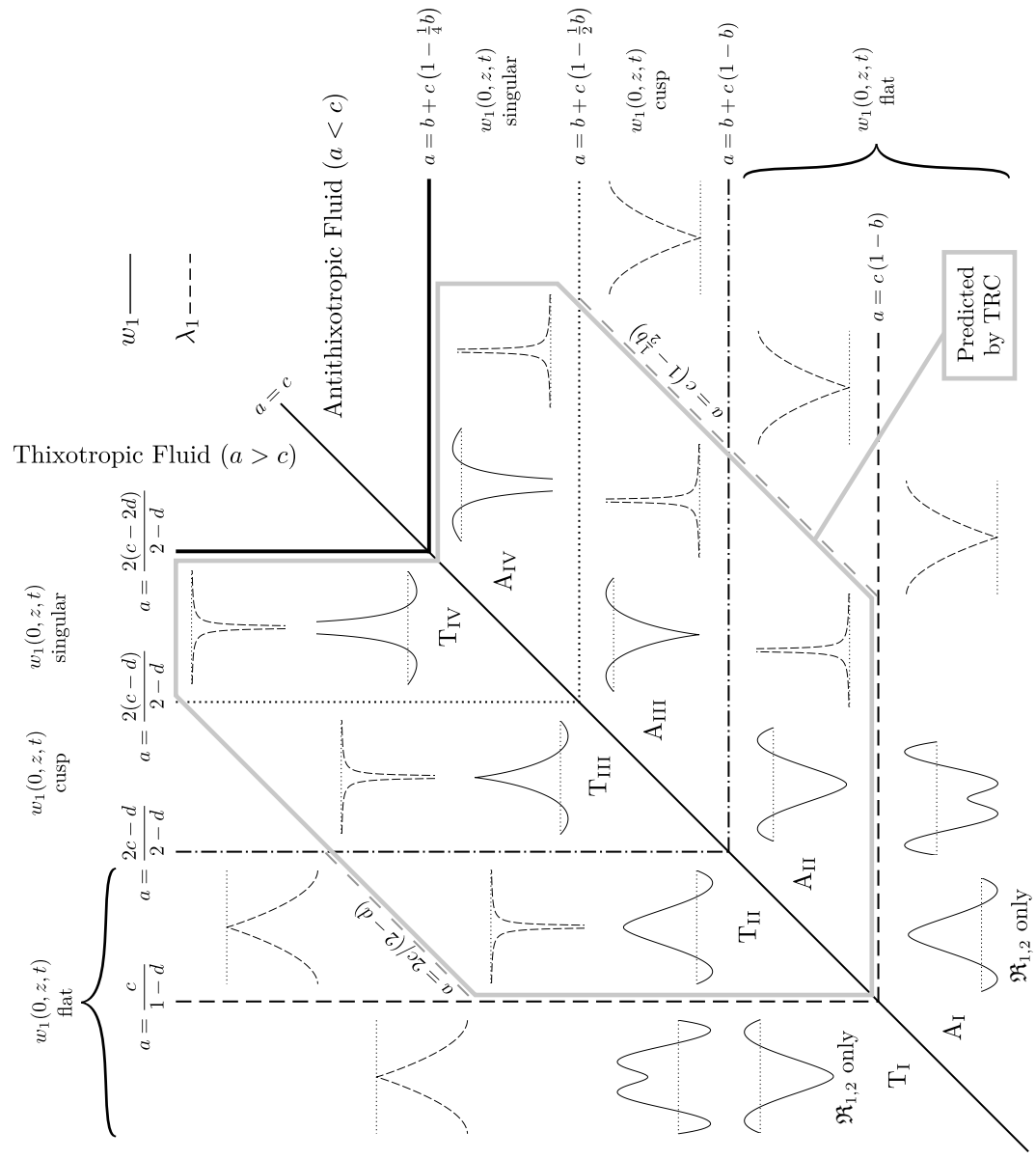

Figure 4.16: MMW model: table of schematics for w_1 (solid) and λ_1 (dashed). The characteristic centreline behaviour of w_1 in each of the regions is noted at the top and the right of the table, and λ_1 is either singular or zero at the centreline. The lines represent the boundaries between the regions of the regime diagram, shown in Figure 4.15, and the region numbers are noted. Profiles inside the grey box agree with the TRC, and those outwith do not. All sketches apply to $\mathfrak{R}_{1,2}$ and $\mathfrak{R}_{2,1}$, except the two at the bottom left, which apply to $\mathfrak{R}_{1,2}$ only.

tion, near the centreline and positive near the wall, i.e. the opposite of thixotropic fluids. In these antithixotropic regions, w_1 agrees with the TRC using the thixotropic/antithixotropic and widening/decelerating analogies. Region $\mathrm{A_I}$ contains strongly antithixotropic fluids. Figure 4.16 shows that for fluids in region $\mathrm{A_I}$, w_1 does not agree with the TRC. Whilst w_1 is negative near the centreline and positive near the wall, as for antithixotropic fluids in regions $\mathrm{A_{II}}$–$\mathrm{A_{IV}}$, there is an extra change in the sign of the gradient of w_1 near the centreline not described by the TRC. As this anomalous behaviour occurs in both the weakly advective regime and in the quickly adjusting regime, as well as occurring for the thixotropic region $\mathrm{T_I}$, the thixotropic/antithixotropic and widening/accelerating analogies hold, so the physical description for the TRC must be refined. As for thixotropic fluids, we note that for antithixotropic fluids in $\mathfrak{R}_{1,2}$, w_1 may be the opposite of the TRC, resembling the reversal of w_1 in $\bar{\mathrm{A}}_{\mathrm{I}}^{1,2}$ for the sMMW model.

We have not defined regions for the behaviour of λ_1, but we note that for thixotropic fluids when $a < 2c/(2-d)$, and antithixotropic fluids when $a > c(1-b/2)$, λ_1 agrees with the TRC using the analogies. When $a > 2c/(2-d)$ or $a < c(1-b/2)$, λ_1 does not agree with the TRC.

4.2.4 Mechanisms for behaviour of w_1

As for the sMMW model, we find the source of the anomalous behaviour exhibited by w_1 in the antithixotropic region $\mathrm{A_I}$ and the thixotropic region $\mathrm{T_I}$ in the equation for the radial derivative $\partial w_1/\partial r$, given by (3.3.6). As discussed in Section 4.1.6 for the sMMW model, the behaviour of $\partial w_1/\partial r$ depends on the interaction between the terms $-G_1 r/2$ and B. We are interested in how the relative size of these terms differs between regions $\mathrm{A_I}$ and $\mathrm{A_{II}}$, and between $\mathrm{T_I}$ and $\mathrm{T_{II}}$, so it will be useful to plot an example of $-G_1 r/2$ and B in each of these four regions, for the weakly advective regime and for the quickly adjusting regime.

We first study the antithixotropic regions $\mathrm{A_I}$ and $\mathrm{A_{II}}$, for which examples of w_1 are shown in Figure 4.12(a). Figures 4.17(a) and (b) show $-G_1 r/2$ (dotted) and B (solid) in regions $\mathrm{A_{II}}$ and $\mathrm{A_I}$ respectively, in the weakly advective regime. These profiles are qualitatively similar to those for the equivalent regions of the sMMW

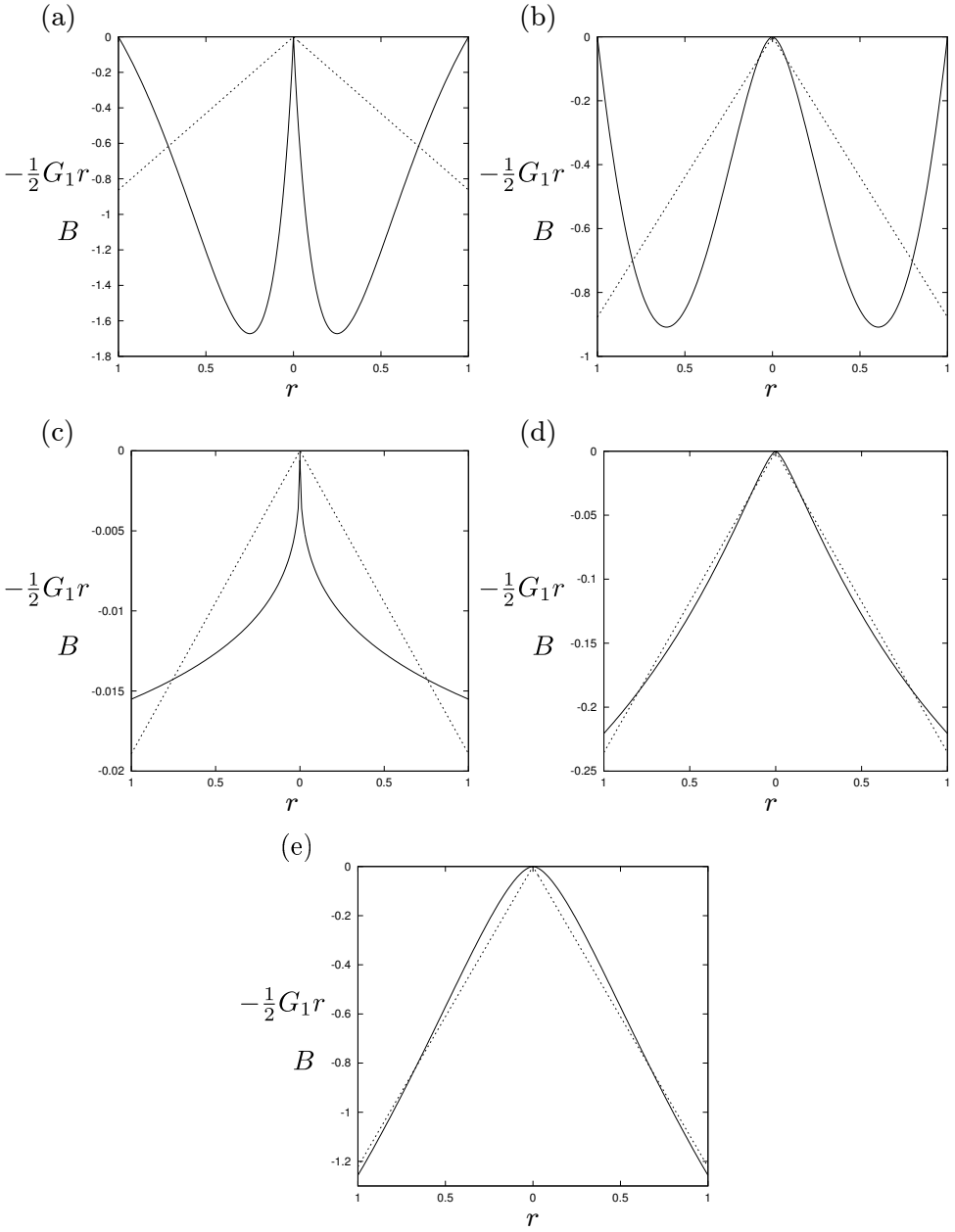

Figure 4.17: MMW model: profiles of $-\frac{1}{2}G_1 r$ (dotted) and $B(r, z, t)$ (solid) in (a) region $\mathrm{A_{II}}$ and (b) region $\mathrm{A_I}$ in the weakly advective regime, and (c) region $\mathrm{A_{II}}$ and (d,e) region $\mathrm{A_I}$ in the quickly adjusting regime. The parameters are (a) $a = 8.1$ and $c = 10$, (b) $a = 0.1$ and $c = 10$, (c) $a = 0.7$ and $c = 0.75$, (d) $a = 0.1$ and $c = 0.75$, and (e) $a = 0.1$ and $c = 4$. The common parameters are $\kappa = 1$, $Q(t) = 1$, $Q'(t) = -1$, $\alpha(z) = 1$, $\alpha'(z) = 1$, $b = 0.2$, and (a,b) $\mathcal{D}_{\mathrm{a}}^* = 1$, $\mathcal{D}_{\mathrm{t}}^* = 0$ and (c,d,e) $\mathcal{D}_{\mathrm{t}}^* = 1$, $\mathcal{D}_{\mathrm{a}}^* = 0$. The profiles in (b,d,e) are the profiles of $-\frac{1}{2}G_1 r$ and B for the parameters used in Figure 4.12.

model (cf. Figures 4.6(a) and (b)), presented in Section 4.1.6, so we omit the corresponding discussion here for brevity.

Figures 4.17(c), (d), and (e) show $-G_1 r/2$ (dotted) and B (solid) in regions $\mathrm{A_{II}}$ and $\mathrm{A_I}$ in the quickly adjusting regime. Figures 4.17(c) and (e) are qualitatively similar to those for the equivalent regions of the sMMW model (cf. Figures 4.6(c) and (d)). However, there is no equivalent of Figure 4.17(d) in the sMMW model, which corresponds to the solid profile of w_1 in Figure 4.12(a) in $\mathfrak{R}_{1,2}$. Figure 4.17(d) shows $-G_1 r/2$ and B for antithixotropic fluids in region $\mathrm{A_I}$, but where w_1 is negative at the centreline. In this case, a change in the shape of B affects w_1 near the centreline only, as in $\mathfrak{R}_{2,1}$ (cf. Figures 4.17(b) and (d)).

We now study the thixotropic regions $\mathrm{T_I}$ and $\mathrm{T_{II}}$, for which examples are shown in Figure 4.14. Figures 4.18(a) and (b) show $-G_1 r/2$ (dotted) and B (solid) in regions $\mathrm{T_{II}}$ and $\mathrm{T_I}$, respectively, in the weakly advective regime. These profiles and the corresponding discussion are qualitatively similar to the sign-reverse of those for the equivalent regions of the sMMW model (cf. Figures 4.6(a) and (b)), presented in Section 4.1.6. Following a similar argument for antithixotropic fluids, we see that an apparent weakening of thixotropy near the centreline in both the weakly advective regime and the quickly adjusting regime leads to a change in the concavity of B, which changes the sign of $\partial w_1/\partial r$.

Figures 4.18(c) and (d) show $-G_1 r/2$ and B in regions $\mathrm{T_{II}}$ and $\mathrm{T_I}$, respectively, in the quickly adjusting regime. In this regime, B is not constrained to equal zero at the wall, in contrast to the weakly advective regime, but in similarity to the weakly advective regime, a weakening of thixotropy near the centreline leads to a change in the concavity of B, which changes the sign of $\partial w_1/\partial r$ near the centreline. Figures 4.18(e) shows $-G_1 r/2$ and B in region $\mathrm{T_I}$ for a case in $\mathfrak{R}_{1,2}$ when w_1 is completely reversed.

4.3 Summary

In this chapter, we studied the unsteady flow of purely viscous thixotropic and antithixotropic fluids in a slowly varying pipe in the quickly adjusting and weakly

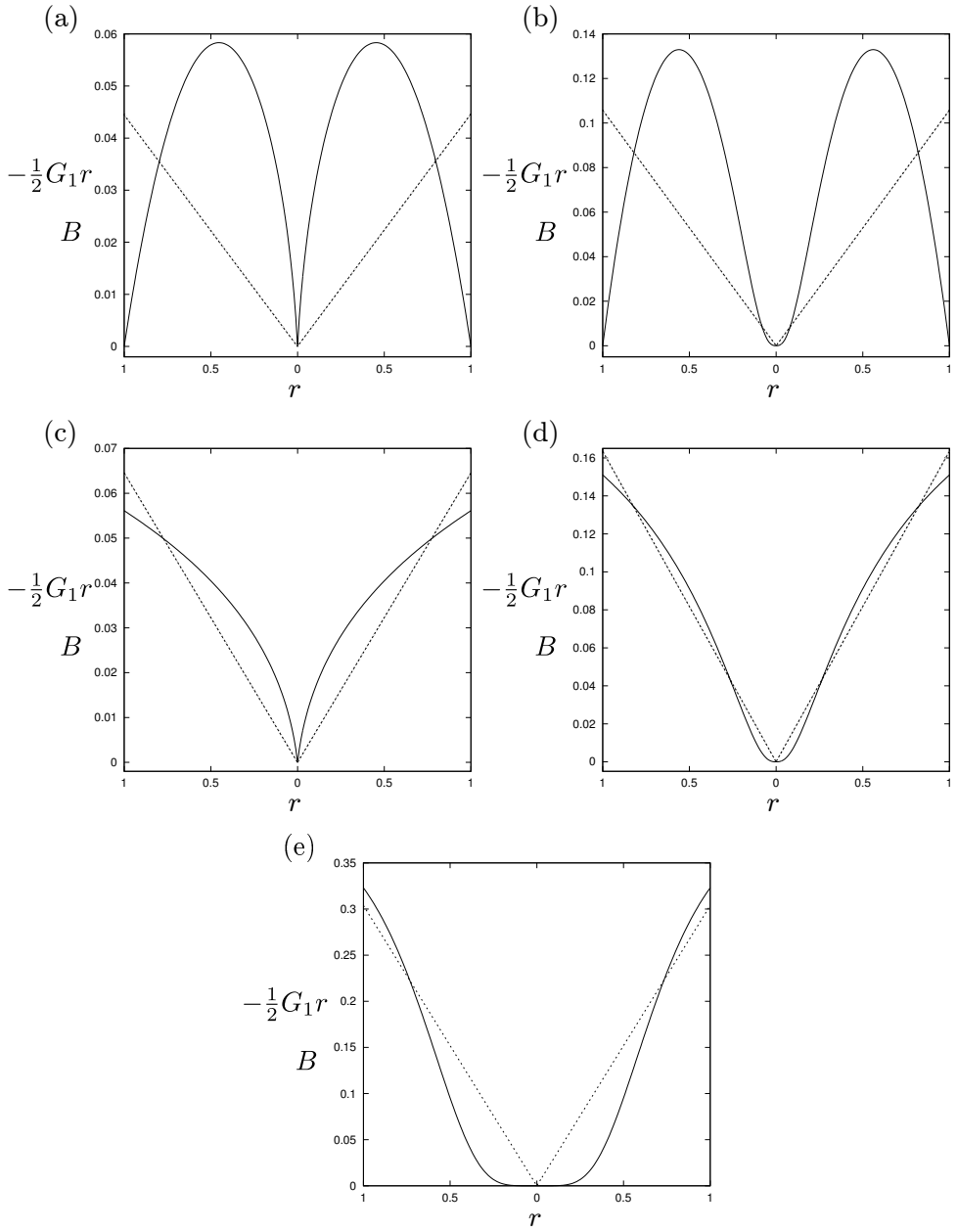

Figure 4.18: MMW model: profiles of $-\frac{1}{2}G_1 r$ (dotted) and $B(r, z, t)$ (solid) in (a) region $\mathrm{T_{II}}$ and (b) region $\mathrm{T_I}$ in the weakly advective regime, and (c) region $\mathrm{T_{II}}$ and (d,e) region $\mathrm{T_I}$ in the quickly adjusting regime. The parameters are (a,c) $a = 0.65$ and $c = 0.62$, (b,d) $a = 0.75$ and $c = 0.62$, and (e) $a = 0.75$ and $c = 0.5$. The common parameters are $\kappa = 1$, $Q(t) = 1$, $Q'(t) = -1$, $\alpha(z) = 1$, $\alpha'(z) = 1$, $b = 0.5$, $d = 0.1$, and (a,b) $\mathcal{D}_{\mathrm{a}}^* = 1$, $\mathcal{D}_{\mathrm{t}}^* = 0$ and (c,d,e) $\mathcal{D}_{\mathrm{t}}^* = 1$, $\mathcal{D}_{\mathrm{a}}^* = 0$. The profiles in (b,d,e) are the profiles of $-\frac{1}{2}G_1 r$ and B for the parameters used in Figure 4.14.

advective regimes. We sought to determine whether or not general statements could be made regarding the effect of thixotropy on pipe flow. More specifically, we used the TRC and the thixotropic/antithixotropic and widening/decelerating analogies, constructed from the results of PWM (see Section 3.3.1), as a reference case for the behaviour of the streamwise velocity and the structure parameter perturbations. We compared the perturbations for two rheological models to the TRC to determine how well and how generally the TRC and the analogies describe thixotropic and antithixotropic flow. These models were the sMMW model ($d = 0$) and the full MMW model ($d > 0$). These models provided a different insight in the behaviour of the flow, and a different test of the TRC.

The first of these models is the purely viscous sMMW model, discussed in Section 4.1. Of the models we consider for this problem (the sMMW and MMW models, and the Houška model, which we study in Chapter 5), this is the only one for which we obtain explicit solutions in general (for the parameters a, b, and c), and so is of particular use because we are able to fully analyse its behaviour. A notable drawback of this model is that it exhibits power-law behaviour at leading order, and so in many cases there are non-physical singularities near the centre of the pipe.

The analysis in this chapter shows that for the sMMW model, the TRC describes the behaviour of the perturbations (w_1 and λ_1) of all thixotropic fluids in both the quickly adjusting regime and the weakly advective regime. The TRC also describes the behaviour in a part of the parameter space of antithixotropic fluids (specifically, those for which $a > c(1-b)$) in both regimes. However, for the rest of the parameter space of antithixotropic fluids (those for which $a < c(1-b)$, in regions $\bar{\mathrm{A}}_{\mathrm{I}}^{2,1}$ and $\bar{\mathrm{A}}_{\mathrm{I}}^{1,2}$ of the regime diagram (see Figure 4.4)) the TRC does not describe the behaviour. In the weakly advective regime, w_1 is similar to the TRC, but the radial gradient of w_1 changes sign twice between the wall and the centre of the pipe, compared to only once in the TRC. In Section 4.1.6 we find the cause of this anomalous behaviour to be a weakening of the thixotropic stress near the centreline for strongly antithixotropic fluids. There is no equivalent behaviour for thixotropic fluids, which implies that the TRC with the thixotropic/antithixotropic analogy does not always hold. In the quickly adjusting regime, w_1 is the complete opposite of the TRC. In Section 4.1.6 we find

that the competition between the terms determining the gradient of w_1 in the quickly adjusting regime is much more finely tuned than in the weakly advective regime. In the quickly adjusting regime, a weakening of thixotropic stress near the centreline for strongly antithixotropic fluids reverses the profile of w_1 across the width of the pipe. The difference between the behaviour of w_1 in region $\bar{\mathrm{A}}_{\mathrm{I}}^{1,2}$ and region $\bar{\mathrm{A}}_{\mathrm{I}}^{2,1}$ implies that the TRC with the widening/decelerating analogy does not always hold. For the sMMW model, we therefore conclude that we are not able to make general statements about the behaviour of the perturbations.

The full MMW model, discussed in Section 4.2, is also a purely viscous model, but unlike the sMMW model, we cannot obtain explicit solutions in general (though we can obtain explicit solutions in some special cases). An advantage of the MMW model over the sMMW model is that the leading-order structure parameter is bounded above by unity (whereas it is unbounded in the sMMW model), so the MMW model exhibits more physically realistic behaviour.

For the MMW model, we find that the behaviour of all antithixotropic fluids, excluding those in the quickly adjusting region $\mathrm{A}_{\mathrm{I}}^{1,2}$, is qualitatively similar to the corresponding fluids in the sMMW model, regardless of the value of d. The TRC describes the behaviour of w_1 and λ_1 when $a > c(1-b)$, but not in the weakly advective region $\mathrm{A}_{\mathrm{I}}^{2,1}$ (when $a < c(1-b)$). In the quickly adjusting region $\mathrm{A}_{\mathrm{I}}^{1,2}$ the behaviour of w_1 is slightly different from the equivalent in the sMMW model. For increasingly strongly antithixotropic behaviour, w_1 eventually reverses to become the opposite of the TRC, but w_1 changes sign in a more complicated way (see Figure 4.13(b)).

The regime diagram for thixotropic fluids in the MMW model (given in Figure 4.15 is significantly different to the sMMW model. For a part of the parameter space of thixotropic fluids (specifically, those for which $a < c/(1-d)$) the TRC describes the behaviour of the perturbations (as in the sMMW model). However, for the rest of the parameter space of thixotropic fluids (those for which $a > c/(1-d)$, regions $\mathrm{T}_{\mathrm{I}}^{2,1}$ and $\mathrm{T}_{\mathrm{I}}^{1,2}$) the TRC does not describe the behaviour. In these regions, the behaviour is qualitatively similar to the sign reverse of the corresponding behaviour in the antithixotropic regions ($\mathrm{A}_{\mathrm{I}}^{2,1}$ and $\mathrm{A}_{\mathrm{I}}^{1,2}$).

As in the sMMW model, the TRC does not hold in general for the MMW model,

and the accelerating/decelerating analogy does not always hold. However, in contrast to the sMMW model, the thixotropic/antithixotropic analogy appears to hold for all parameter values.

Following the analysis presented in this chapter, we conclude that the TRC and the associated physical interpretation is a useful heuristic for the behaviour of purely viscous thixotropic and antithixotropic fluids in pipe flow, but fails to capture the behaviour in the extremes of the models presented. Interestingly, the TRC fails for different reasons in each of the models, making it difficult to make statements on thixotropic pipe flow for general rheologies. In the following chapter, we study the Houška model, which provides a different test of TRC, and use the results of this chapter and Chapter 5 to update the TRC and accompanying physical interpretation.

Chapter 5

Results for the regularised Houška model

In this chapter, we present solutions for the leading-order behaviour and the perturbations for the Papanastasiou-regularised Houška model, introduced in Section 2.5.2. The sMMW and MMW models, studied in Chapter 4, model purely viscous behaviour. In contrast, the Houška model includes the property of plasticity, or yield-stress behaviour, so is a model of viscoplastic behaviour, which allows the study of the effect of plasticity on thixotropic lubrication flows. In addition to exhibiting an interesting physical phenomenon, the Houška model does not have the centreline singularity problems exhibited by the sMMW and MMW models.

5.1 The Houška model

We present the Papanastasiou-regularised Houška model again here for reference. The non-dimensionalised constitutive relation (see Section 2.5.2) is

$$\eta(\dot{\gamma},\lambda) = \frac{(\tau_{\mathrm{y}0} + \lambda\tau_{\mathrm{y}1})(1-\mathrm{e}^{-k\dot{\gamma}})}{\dot{\gamma}} + 1 + \lambda\eta_{\mathrm{H}1}, \tag{5.1.1}$$

where $\dot{\gamma}$ is the shear rate, η is the effective viscosity, $\tau_{\mathrm{y}0}$ is the yield stress of an unstructured fluid ($\lambda = 0$), $\tau_{\mathrm{y}1}$ controls how strongly the yield stress depends on

the structure, η_{H1} controls how strongly the viscosity depends on the structure, and k is the regularisation parameter. The structure evolution rate f is a special case of the MMW model with $a = 1$, $b = 1$, $c = 0$, and $d = 1$:

$$f(\Gamma, \lambda) = -\Gamma^{1/2}\lambda + \kappa(1 - \lambda). \tag{5.1.2}$$

The dimensionless quantities are defined via (2.2.1) and (2.5.3), together with the scale $\hat{\mu}_0 = \hat{\eta}_{\mathrm{H0}}$ and

$$\eta_{\mathrm{H1}} = \frac{\hat{\eta}_{\mathrm{H1}}}{\hat{\eta}_{\mathrm{H0}}}, \quad k = \frac{\hat{k}\hat{Q}_{\mathrm{r}}}{\hat{R}^3}, \quad \tau_{\mathrm{y0}} = \frac{\hat{\tau}_{\mathrm{y0}}\hat{R}^3}{\hat{\eta}_{\mathrm{H0}}\hat{Q}_{\mathrm{r}}}, \quad \text{and} \quad \tau_{\mathrm{y1}} = \frac{\hat{\tau}_{\mathrm{y1}}\hat{R}^3}{\hat{\eta}_{\mathrm{H0}}\hat{Q}_{\mathrm{r}}}. \tag{5.1.3}$$

For this model we are not able to obtain explicit solutions, so we must proceed using the general solutions obtained in Section 3.3, evaluating the integrals using the computer algebra package Maple. In the following sections, we study the effect of varying the regularisation parameter k (Section 5.2), the viscosity parameter η_{H1} (Section 5.3), and the yield-stress parameter τ_{y1} (Section 5.4), on the leading-order and perturbation quantities.

As we are using a regularised Houška model, we cannot observe true yield-stress behaviour, as in the case of the unregularised model. An effect of regularisation is that we instead observe behaviour similar to yield-stress behaviour, but with small deviations from true yield-stress behaviour. For brevity, we refer to aspects of this 'regularised yield-stress' behaviour as follows. When the stress in the fluid is above and below the yield stress $\tau_{\mathrm{y}} = \tau_{\mathrm{y0}} + \lambda\tau_{\mathrm{y1}}$, we say it is 'yielded' and 'unyielded', respectively. For plug-like flow, in which the fluid is unyielded near the centre of the pipe and yielded near the wall, we refer to the unyielded region as a 'pseudo-plug', which is bounded by a 'yield surface'. We use this terminology throughout this section, while remaining aware that we use these terms to refer to regularised yield-stress behaviour, rather than true yield-stress behaviour.

When studying the perturbations for the Houška model, we refer to the TRC, discussed in Section 3.3.1. Whilst the TRC is based on purely viscous behaviour, we use it here as a reference case for the Houška model. Given that $a = 1$ and $c = 0$, the Houška model displays only thixotropic behaviour (as $a > c$), so only

the widening/decelerating analogy is relevant to the following discussion.

5.2 Effect of varying the regularisation parameter k

First we consider the effect of varying k on w_0, λ_0, w_1, and λ_1, in the quickly adjusting regime and in the weakly advective regime. This parameter is an artificial parameter which controls how closely the behaviour of the regularised model matches the behaviour of the unregularised model; larger k yield behaviour more similar to the unregularised model. Figure 5.1 shows examples of these profiles for $k = 1, 10, 100, 1000$. For $k = 1, 10$, the fluid does not exhibit yield-stress behaviour, as shown in Figures 5.1(a) and (b), in which the profiles of w_0 and λ_0 are rounded. As we increase k, a pseudo-plug with defined edges forms, as shown in Figures 5.1(a) and (b), where the pseudo-plug extends from $r = 0$ to $r \approx 0.5$. In the pseudo-plug, the fluid is fully structured ($\lambda_0 = 1$, as shown in Figure 5.1(b)) and the profile of w_0 is flat. Outside the pseudo-plug, where the fluid is yielded, the shear rate is high and the structure is broken down.

Figure 5.1(c) shows the effect of varying k on w_1 in the quickly adjusting regime. When $k = 1$, w_1 is negative near the wall and the centreline, and positive between the wall and the centreline. As k increases, w_1 becomes positive near the centreline while remaining negative near the wall, and a pseudo-plug begins to form. For $k = 100, 1000$ the profile has a distinct plateau, showing strong yield-stress behaviour. We note that an effect of regularisation is that w_1 is slightly larger just outside the pseudo-plug than in the pseudo-plug, though we expect this to vanish as k becomes large, and the behaviour more closely matches the behaviour of the unregularised model.

Figure 5.1(d) shows the effect of varying k on λ_1 in the quickly adjusting regime. The structure remains fully formed at the centreline, i.e. $\lambda_1(0, z, t) = 0$, for all values of k, and as k increases a pseudo-plug forms in the centre, in which $\lambda_1 = 0$, and widens. Immediately outside the pseudo-plug, the increased shear rate breaks down the structure, as shown by the troughs at $r \approx 0.5$ in Figure 5.1(d).

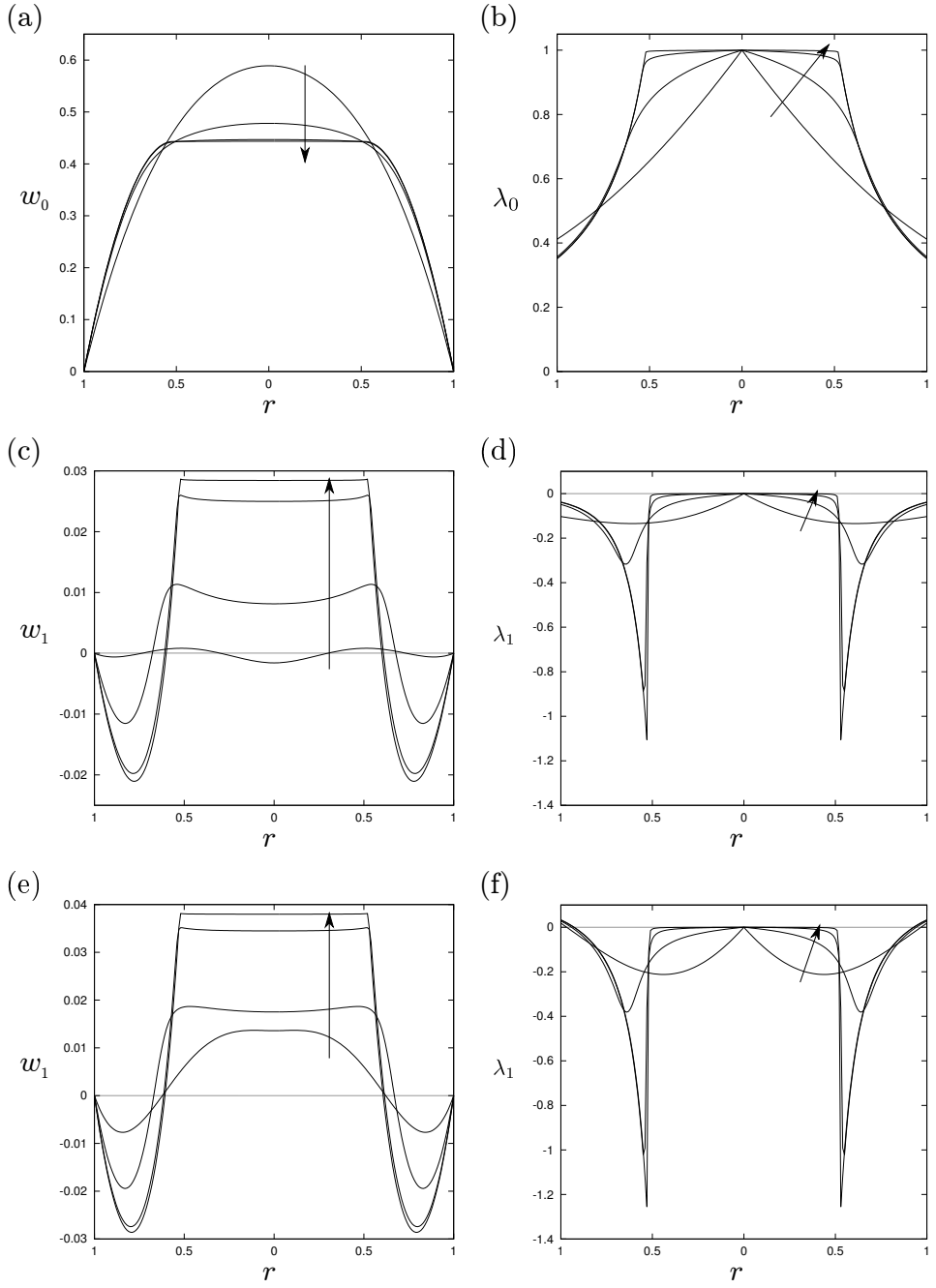

Figure 5.1: Regularised Houška model: profiles for (a) w_0, (b) λ_0, (c,e) w_1 and (d,f) λ_1, for (c,d) $\mathcal{D}_{\mathrm{t}}^* = 1$ and $\mathcal{D}_{\mathrm{a}}^* = 0$, and (e,f) $\mathcal{D}_{\mathrm{a}}^* = 1$ and $\mathcal{D}_{\mathrm{t}}^* = 0$, for $k = 1, 10, 100, 1000$. The common parameters are $\kappa = 1$, $Q(t) = 1$, $Q'(t) = -1$, $\alpha(z) = 1$, $\alpha'(z) = 1$, $\tau_{\mathrm{y}0} = 1$, $\tau_{\mathrm{y}1} = 1$, and $\eta_{\mathrm{H}1} = 1$. The arrows show the direction of increasing k.

Figures 5.1(e) and (f) show the effect of varying k on w_1 and λ_1 respectively, in the weakly advective regime. The profiles show similar behaviour to that in the quickly adjusting regime — a pseudo-plug forms and widens as k increases, and w_1 in the pseudo-plug increases. The behaviour of λ_1 in the weakly advective regime is qualitatively similar to that in the quickly adjusting regime.

We note that in the pseudo-plug the shear rate is zero, so there is nothing to break down or build up the structure, so the structure perturbation in the pseudo-plug is always zero. In the remaining sections we take $k = 1000$, which yields clear yield-stress behaviour with a well-defined pseudo-plug.

5.3 Effect of varying the viscosity parameter $\eta_{\mathrm{H}1}$

In this section, we consider the effect of varying the viscosity parameter $\eta_{\mathrm{H}1}$ on w_0, λ_0, w_1, and λ_1, in the quickly adjusting regime and in the weakly advective regime. Figure 5.2 shows examples of these profiles for $\eta_{\mathrm{H}1} = 1, 10^{1/2}, 10, 10^{3/2}, 100$. Figures 5.2(a) and (b) show the effect of varying $\eta_{\mathrm{H}1}$ on w_0 and λ_0, respectively. It is clear that an increase in $\eta_{\mathrm{H}1}$ leads to a narrowing of the pseudo-plug. As $\eta_{\mathrm{H}1}$ increases the viscosity of the fluid increases, which flows less readily and leads to an increase in the pressure gradient required to maintain the prescribed volume flux. An increase in the pressure gradient, without an increase in the pseudo-yield stress, leads to more unyielded fluid and hence a narrower pseudo-plug. The wider sheared region also means that the shear rate near the wall decreases and so the structure near the wall increases.

Considering the constitutive relation (5.1.1), as $\eta_{\mathrm{H}1}$ becomes large, the effective viscosity η depends more on the viscous contribution than on the yield-stress contribution. In particular, $\eta \sim \lambda\eta_{\mathrm{H}1}$ as $\eta_{\mathrm{H}1} \to \infty$. This constitutive relation is similar to that for the MMW model, given by (2.5.4), except that here the structure λ is scaled by $\eta_{\mathrm{H}1}$.

Figures 5.2(c) and (d) show the effect of varying $\eta_{\mathrm{H}1}$ on w_1 and λ_1 in the quickly adjusting regime $\mathfrak{R}_{1,2}$. When $\eta_{\mathrm{H}1} = 1$, w_1 is positive at the centre of the pipe

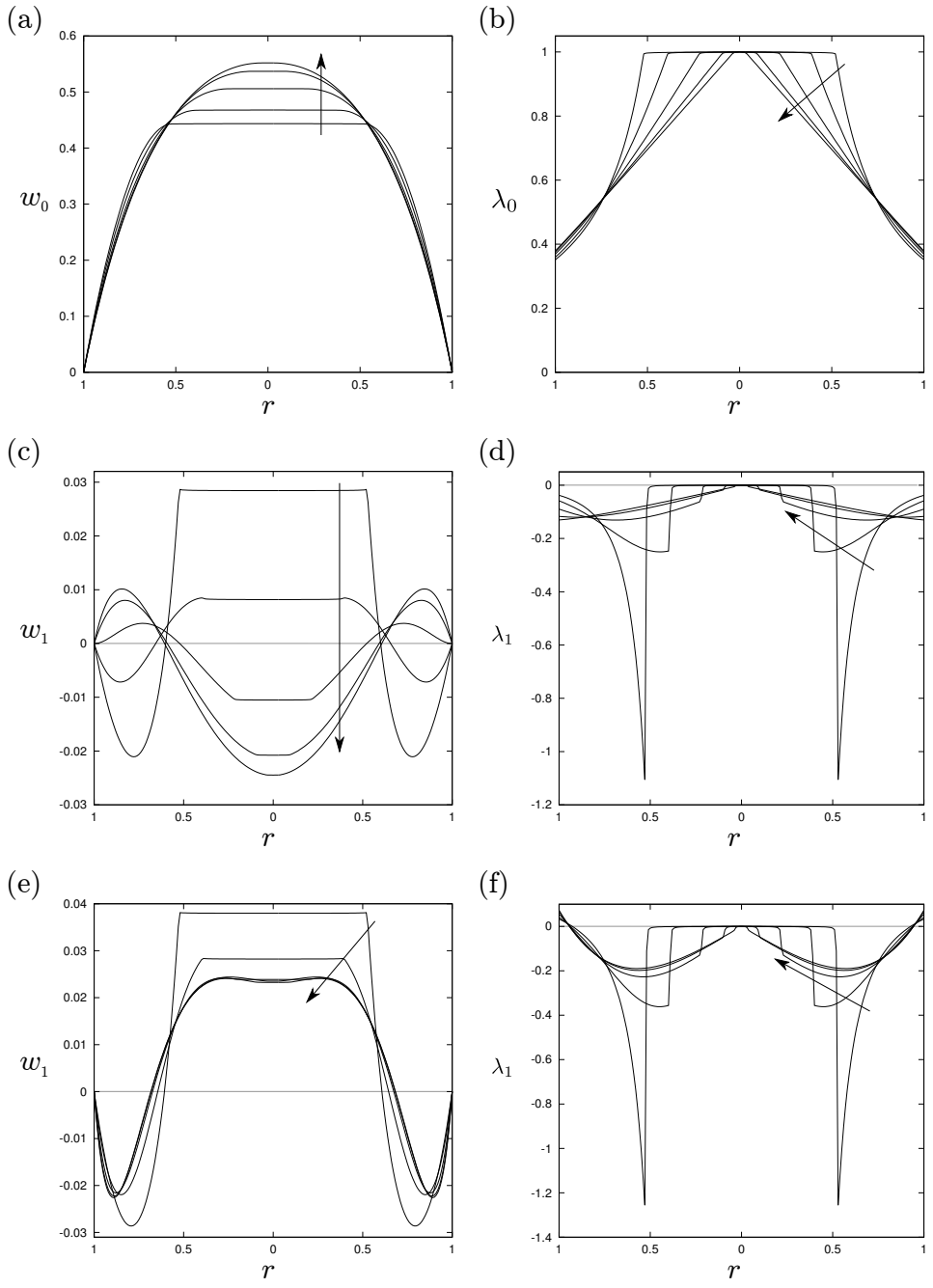

Figure 5.2: Regularised Houška model: profiles for (a) w_0, (b) λ_0, (c,e) w_1 and (d,f) λ_1, for (c,d) $\mathcal{D}_{\mathrm{t}}^* = 1$ and $\mathcal{D}_{\mathrm{a}}^* = 0$, and (e,f) $\mathcal{D}_{\mathrm{a}}^* = 1$ and $\mathcal{D}_{\mathrm{t}}^* = 0$, for $\eta_{\mathrm{H1}} = 1, 10^{1/2}, 10, 10^{3/2}, 100$. The common parameters are $\kappa = 1$, $Q(t) = 1$, $Q'(t) = -1$, $\alpha(z) = 1$, $\alpha'(z) = 1$, $k = 1000$, $\tau_{\mathrm{y}0} = 1$, and $\tau_{\mathrm{y}1} = 1$. The arrows show the direction of increasing η_{H1}.

and negative at the wall, which agrees with the TRC (cf. Figure 3.1(a)). In addition, λ_1 is negative everywhere except in the pseudo-plug, where $\lambda_1 = 0$. As η_{H1} increases, w_1 decreases near the centre, the pseudo-plug narrows and an extra change in the sign of $\partial w_1/\partial r$ appears just outside the pseudo-plug. When η_{H1} is sufficiently large, w_1 becomes negative near the centre and positive near the wall, as shown for $\eta_{\mathrm{H1}} = 10, 10^{3/2}, 100$ in Figure 5.2(c), which is the opposite of what the TRC describes.

Figures 5.2(e) and (f) show the effect of varying η_{H1} on w_1 and λ_1 in the weakly advective regime $\mathfrak{R}_{2,1}$. When $\eta_{\mathrm{H1}} = 1$, w_1 is positive at the centre of the pipe and negative at the wall, which agrees with the TRC (cf. Figure 3.1(a)). In addition, λ_1 is negative everywhere except in the pseudo-plug, where $\lambda_1 = 0$, and at the wall where λ_1 is positive. As η_{H1} increases, w_1 decreases near the centre, the pseudo-plug narrows and an extra change in the sign of $\partial w_1/\partial r$ appears just outside the pseudo-plug. In contrast to the quickly adjusting regime, when η_{H1} is increased, w_1 remains positive near the centre and negative near the wall.

5.4 Effect of varying the yield-stress parameter τ_{y1}

In the section, we consider the effect of varying the yield-stress parameter τ_{y1} on w_0, λ_0, w_1, and λ_1, in the quickly adjusting regime and in the weakly advective regime. Figure 5.3 shows examples of these profiles for $\eta_{\mathrm{H1}} = 0, 0.5, 1, 1.5, 2$. Figures 5.3(a) and (b) show the effect of varying τ_{y1} on w_0 and λ_0, respectively. It is clear that an increase in τ_{y1} leads to a widening of the pseudo-plug, as shown in Figure 5.3(a). As τ_{y1} increases the yield stress of the fluid increases, so less of the fluid is yielded. As the pseudo-plug widens, the shear rate near the wall increases, which breaks down the structure near the wall as shown in Figure 5.3(b). We note that when $\tau_{\mathrm{y1}} = 0$, as in the examples shown in Figure 5.3, the yield stress does not depend on the structure.

Figures 5.3(c) and (d) show the effect of varying τ_{y1} on w_1 and λ_1 in the quickly adjusting regime $\mathfrak{R}_{1,2}$. When $\tau_{\mathrm{y1}} = 1, 1.5, 2$, w_1 is positive at the centre of the

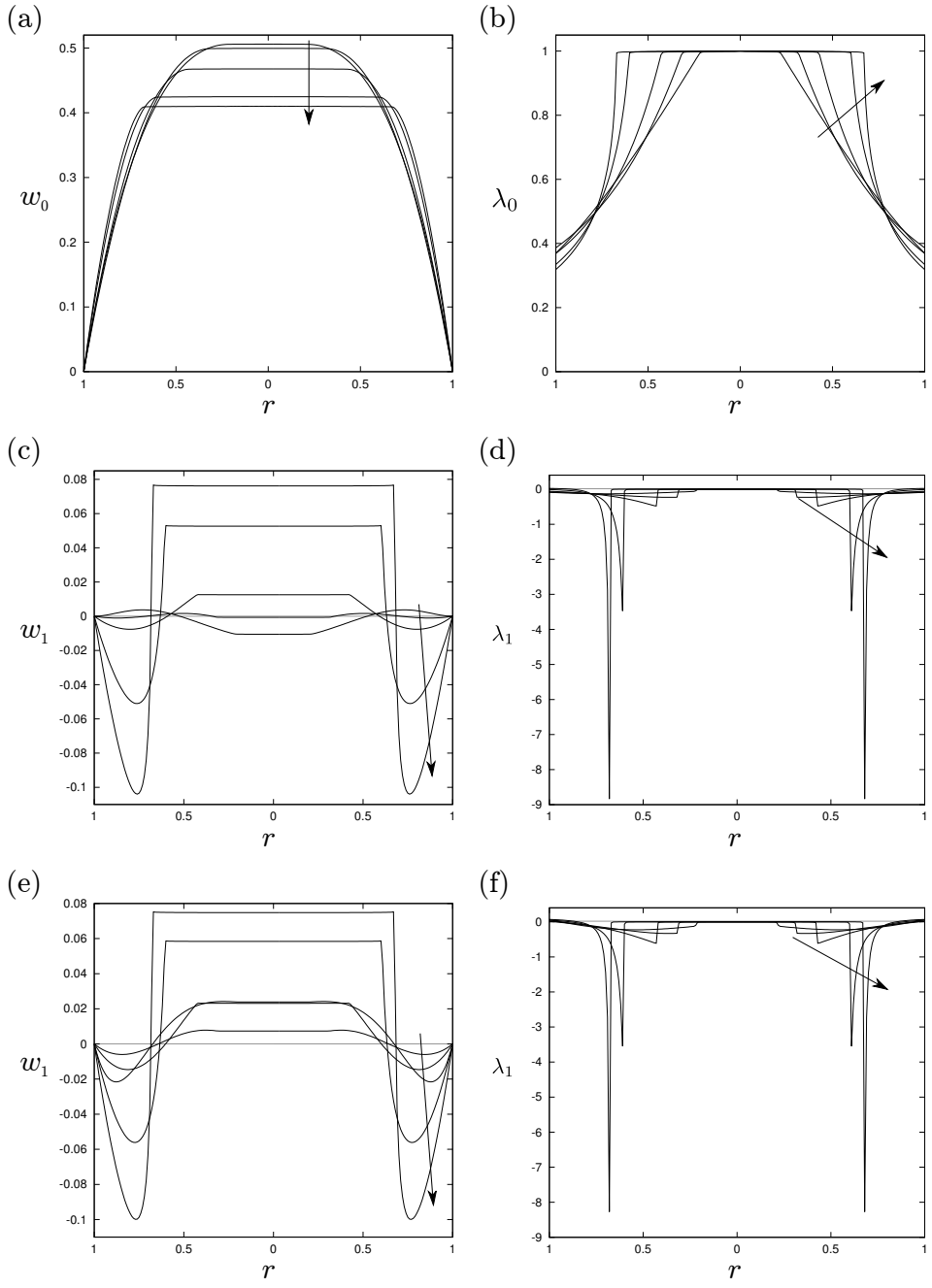

Figure 5.3: Regularised Houška model: profiles for (a) w_0, (b) λ_0, (c,e) w_1 and (d,f) λ_1, for (c,d) $\mathcal{D}_{\mathrm{t}}^* = 1$ and $\mathcal{D}_{\mathrm{a}}^* = 0$, and (e,f) $\mathcal{D}_{\mathrm{a}}^* = 1$ and $\mathcal{D}_{\mathrm{t}}^* = 0$, for $\tau_{\mathrm{y1}} = 0, 0.5, 1, 1.5, 2$. The common parameters are $\kappa = 1$, $Q(t) = 1$, $Q'(t) = -1$, $\alpha(z) = 1$, $\alpha'(z) = 1$, $k = 1000$, $\tau_{\mathrm{y0}} = 1$, and $\eta_{\mathrm{H1}} = 1$. The arrows show the direction of increasing τ_{y1}.

pipe and negative at the wall, which agrees with the TRC (cf. Figure 3.1(a)). In addition, λ_1 is negative everywhere except in the pseudo-plug, where $\lambda_1 = 0$. When τ_{y1} is sufficiently small, such as when $\tau_{y1} = 0$ in Figure 5.3(c), w_1 is negative near the centre and positive at the wall, which is the opposite of what the TRC describes. For a few cases, such as when $\tau_{y1} = 0.5$ in Figure 5.3(c), w_1 changes sign twice across the width of the pipe.

Figures 5.3(e) and (f) show the effect of varying τ_{y1} on w_1 and λ_1 in the weakly advective regime $\mathfrak{R}_{2,1}$. For all values of τ_{y1} in Figure 5.3(e), w_1 is positive at the centre of the pipe and negative at the wall, which agrees with the TRC (cf. Figure 3.1(a)). In addition, λ_1 is negative everywhere except in the pseudo-plug, where $\lambda_1 = 0$.

In both the quickly adjusting regime and the weakly advective regime, a larger yield stress yields a larger velocity perturbation, as shown in Figure 5.3(c) and (e), respectively. A larger yield stress yields a wider pseudo-plug and increases the leading-order shear rate near the wall.

5.5 Mechanisms for behaviour of w_1

We find the source of the anomalous behaviour exhibited by w_1 in Figures 5.2 and 5.3. As discussed in Section 4.1.6 for the sMMW model, the behaviour of $\partial w_1/\partial r$ depends on the interaction between the terms $-G_1 r/2$ and B. We are interested in how the relative size of these terms differs as we vary the parameters η_{H1} and τ_{y1}, so it will be useful to plot examples of $-G_1 r/2$ and B for some of these parameters, for the weakly advective regime and for the quickly adjusting regime.

We first study the effect of varying the viscosity parameter η_{H1}, for which examples are shown in Figures 5.2(e) and (f) for the weakly advective regime and in Figures 5.2(c) and (d) for the quickly adjusting regime. Figures 5.4(a) and (b) show $-G_1 r/2$ (dotted) and B (solid) in the weakly advective regime for two values of η_{H1}: a case which agrees with the TRC ($\eta_{H1} = 10^{1/2}$, Figure 5.4(a)) and a case which does not ($\eta_{H1} = 10^{3/2}$, Figure 5.4(b)). As η_{H1} increases, the

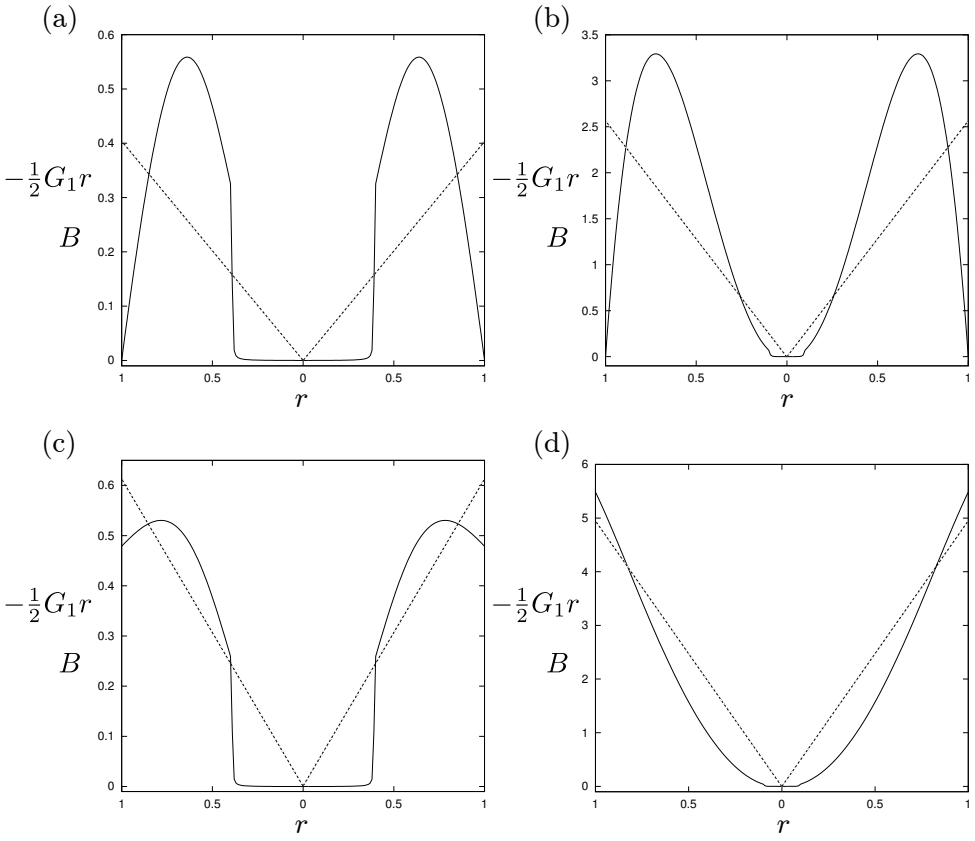

Figure 5.4: Regularised Houška model: profiles of $-\frac{1}{2}G_1 r$ (dotted) and $B(r, z, t)$ (solid) for (a,c) $\eta_{\mathrm{H1}} = 10^{1/2}$ and (b,d) $\eta_{\mathrm{H1}} = 10^{3/2}$ in (a,b) the weakly advective regime, and (c,d) in the quickly adjusting regime. The common parameters are $\kappa = 1$, $Q(t) = 1$, $Q'(t) = -1$, $\alpha(z) = 1$, $\alpha'(z) = 1$, $k = 1000$, $\tau_{\mathrm{y}0} = 1$, $\tau_{\mathrm{y}1} = 1$, and (a,b) $\mathcal{D}^*_{\mathrm{a}} = 1$, $\mathcal{D}^*_{\mathrm{t}} = 0$ and (c,d) $\mathcal{D}^*_{\mathrm{t}} = 1$, $\mathcal{D}^*_{\mathrm{a}} = 0$. The profiles in (b,d) are the profiles of $-\frac{1}{2}G_1 r$ and B for the corresponding parameters used in Figure 5.2.

pseudo-plug becomes narrower and $-G_1 r/2$ and B become more similar in shape near $r = 0$, so the balance between them becomes finer.

Figures 5.4(c) and (d) show $-G_1 r/2$ and B in the quickly adjusting regime for two values of η_{H1}: a case which agrees with the TRC ($\eta_{\mathrm{H1}} = 10^{1/2}$, Figure 5.4(c)) and a case which does not ($\eta_{\mathrm{H1}} = 10^{3/2}$, Figure 5.4(d)). As in the weakly advective regime, the balance between $-G_1 r/2$ and B becomes finer as η_{H1} increases. In contrast to the weakly advective regime, one of the intersections $-G_1 r/2$ and B vanishes (cf. Figures 5.4(c) and (d)), which indicates that one of the turning points of w_1 vanishes, when η_{H1} is sufficiently large. This leads to a reversal of w_1, which only occurs in the quickly adjusting regime, so that it becomes the opposite of the TRC, which brings doubt on the accuracy of the widening/decelerating analogy.

For the yield-stress parameter τ_{y1}, for which examples are shown in Figures 5.3(e) and (f) for the weakly advective regime and in Figures 5.3(c) and (d) for the quickly adjusting regime, the mechanisms for the anomalous behaviour of w_1 are qualitatively similar to that for the viscosity parameter η_{H1}. For brevity, we do not detail the mechanisms leading to the anomalous behaviour of w_1 when τ_{y1} is varied.

5.6 Summary

In this chapter, we studied the unsteady flow of viscoplastic thixotropic and antithixotropic fluids in a slowly varying pipe in the quickly adjusting and weakly advective regimes. As in Chapter 4, we sought to determine whether or not general statements could be made regarding the effect of thixotropy on pipe flow.

Again, we used the TRC and the widening/decelerating analogy, constructed from the results of PWM (see Section 3.3.1), as a reference case for the behaviour of the streamwise velocity and the structure parameter perturbations. We compared the perturbations for the Houška model to the TRC to determine how well and how generally the TRC and the analogies describe thixotropic and antithixotropic flow.

The Houška model provided a different test of the TRC from the (s)MMW models, because an addition feature of the flow, the pseudo-plug, was present. In addition, the Houška model has two distinct advantages over the sMMW and MMW models. One is that it does not yield unphysical singular behaviour near the centreline. The other is that the parameters of the structure evolution rate are fixed ($a = 1$ and $c = 0$, i.e. the Houška model is always thixotropic, so the thixotropic/antithixotropic analogy is not relevant), and the model is tuned using the yield-stress and viscosity parameters in the constitutive relation.

The results of this chapter show that the TRC describes the behaviour of the perturbations when the yield-stress parameter τ_{y1} is sufficiently large, and when the viscosity parameter η_{H1} is sufficiently small. When the yield-stress parameter τ_{y1} is too small, or when the viscosity parameter η_{H1} is too large, w_1 changes sign near the centreline in a similar way to the thixotropic regions $\mathrm{T}_{\mathrm{I}}^{1,2}$ and $\mathrm{T}_{\mathrm{I}}^{2,1}$ in the MMW model. In the quickly adjusting regime w_1 may change sign at the centreline as the parameters are varied, but in the weakly advective regime w_1 does not change sign near the centreline.

Following the analysis presented in this chapter, we conclude that the TRC and the associated physical interpretation is a useful heuristic for the behaviour of thixotropic and antithixotropic fluids in pipe flow, but fails to capture the behaviour in the extremes of the models presented. Interestingly, the TRC fails for different reasons in each of the models, making it difficult to make statements on thixotropic pipe flow for general rheologies.

Using the results in this chapter and in Chapter 4, we are now in a position to update the TRC and the accompanying physical interpretation. PWM presented the following reasoning for the TRC (which we present here for a pipe rather than for a channel): (a) the timescale of advection is strongest where the leading-order flow is fastest, i.e. at the centreline of the pipe, so this is where the advective effect of thixotropy is strongest; (b) fluid with a low structure, and therefore a low viscosity, is more readily sheared than fluid with a high viscosity, so it flows faster; (c) to conserve the prescribed volume flux, an increase in the w_1 near the centre of the pipe must be offset by a decrease near the wall.

We modify this interpretation of the TRC as follows: (a) advection is strongest

at the centreline, but temporal evolution may be strongest at the centreline or at the wall of the pipe; (b) the advective component of the thixotropic stress term is zero at the centreline and the wall, but the temporal component is zero at the centreline and largest at the wall; (c) the pressure gradient perturbation, which maintains the prescribed volume flux, is largest at the wall and smallest at the centreline, so has the largest and smallest contribution to thixotropy-induced shear at these locations, respectively. The advective component of the thixotropic stress term is always weaker at the wall than the pressure gradient perturbation, which gives the characteristic shape of w_1 in the TRC, and this behaviour appears to be generic except very close to the centreline, where a weakening of the thixotropic stress term may alter the shape of w_1. In contrast, the temporal component of the thixotropic stress term may be larger or smaller than the pressure gradient perturbation anywhere across the pipe, so we cannot predict the shape of the profile of w_1 in general.

Chapter 6

Numerical Results for Weak Thixotropy

6.1 Introduction

In Chapter 2, we obtained the governing equations for unsteady thixotropic pipe flow for various regimes of thixotropic strength, from the very weakly to the very strongly thixotropic regimes. In Chapters 3–5, we obtained and analysed asymptotic solutions for unsteady thixotropic pipe flow in the weakly thixotropic regimes $\mathfrak{R}_{2,1}$, $\mathfrak{R}_{1,2}$, and $\mathfrak{R}_{1,1}$, for three rheological models.

We wish now to verify the asymptotic solutions obtained in Chapters 3–5, and extend our understanding of thixotropic pipe flow from the weakly thixotropic regimes, in which the Deborah numbers $\mathcal{D}_{\mathrm{t}} = \mathcal{O}(\delta)$ and/or $\mathcal{D}_{\mathrm{a}} = \mathcal{O}(\delta)$, to the regimes of balanced thixotropy, in which $\mathcal{D}_{\mathrm{t}} = \mathcal{O}(1)$ and/or $\mathcal{D}_{\mathrm{a}} = \mathcal{O}(1)$, and the strongly thixotropic regimes, in which $\mathcal{D}_{\mathrm{t}} = \mathcal{O}(\delta^{-1})$ and/or $\mathcal{D}_{\mathrm{a}} = \mathcal{O}(\delta^{-1})$. To do so, we use the finite element analysis software package COMSOL Multiphysics® [54].

Using COMSOL, we intended to achieve the following three goals: (i) to reproduce and verify the asymptotic solutions presented in Chapters 3–5; (ii) to study the robustness of the lubrication approach, i.e. to find for what range of the aspect ratio δ the perturbation solutions are accurate; and (iii) to study regimes of

strong thixotropy out of the reach of the asymptotic methods developed for weak thixotropy. Although we were able to obtain some partial results which provide useful insights into thixotropic pipe flow, we did not fully achieve these three goals, for reasons which we will describe in this chapter. Consequently, this chapter will be a summary of the partial numerical results obtained using our approach, in which we highlight the main problems encountered and the insights gained so that they may be considered in future work in this area.

Of the three models used in Chapters 3–5, the sMMW, MMW and Houška models, which each have their own individual characteristics, we had to determine which is the most appropriate to begin to tackle the first of the three goals. We decided to focus on the sMMW and Houška models. The sMMW model has the advantage that we were able to analyse fully the behaviour of the model in Chapter 4, but, as that analysis showed, this model has the disadvantage of yielding pathological centreline behaviour for a large range of parameters. The full MMW model exhibits similar pathological centreline behaviour to the sMMW, but without the advantage of having closed-form solutions available, so we do not consider the full MMW model further here. The Houška model is more well-behaved near the centreline than the sMMW and MMW models, but it yields behaviour that is difficult to capture numerically, particularly at the edge of the pseudo-plug. We also found that simulations using the Houška model are highly sensitive to the initial and boundary conditions. For the Houška model, the pathological behaviour arises near the edge of the pseudo-plug in the first-order asymptotic solutions and is difficult to capture numerically. Aside from this problem, we had difficulty in general in obtaining numerical solutions of sufficient accuracy to validate the COMSOL model against the leading-order and first-order asymptotic solutions.

The asymptotic solutions presented in Chapter 3 are formally valid in the limit of small aspect ratio, i.e. as $\delta \to 0$. When simulating this problem in COMSOL, we must set the aspect ratio to be numerically small (e.g. $\delta \approx 10^{-3}$). We found that setting δ too small yields inaccurate numerical solutions, particularly near the centreline, because the perturbation solutions cannot be distinguished from numerical noise. Increasing δ yields behaviour out of the range of validity of the asymptotic solutions.

To begin to work towards achieving the goals stated above, we first implemented the problem of thixotropic pipe flow in COMSOL, which we describe in Section 6.2. In Section 6.3 we present some examples of numerical solutions for the leading-order and perturbation quantities. In Section 6.4 we present a battery of tests used to eliminate various possible errors in the numerical results. In Section 6.5 we present examples of results which provide some insight into the behaviour of the numerical solutions, and the robustness of the lubrication approach. Finally in Section 6.6 we briefly summarise the findings of this chapter.

6.2 Implementation

In this section, we implement the problem of thixotropic pipe flow in COMSOL. In particular, we discuss the implementation of a slowly varying pipe in Section 6.2.1, then introduce some notation to simplify the discussion of the numerical results, and describe how we obtain numerical solutions for the leading-order and perturbation quantities in Section 6.2.2.

For convenience, we rewrite the governing equations for this problem, given by (2.2.2), (2.2.3), (2.2.4), and (2.2.8):

$$\text{mass conservation:} \quad \nabla \cdot \mathbf{u} = 0, \tag{6.2.1}$$

$$\text{Cauchy momentum equation:} \quad \nabla p = \nabla \cdot \underline{\underline{\tau}}, \tag{6.2.2}$$

$$\text{constitutive relation:} \quad \tau_{ij} = \eta(\dot{\gamma}, \lambda) e_{ij}, \tag{6.2.3}$$

$$\text{structure evolution equation:} \quad \mathcal{D}_{\mathrm{t}} \frac{\partial \lambda}{\partial t} + \mathcal{D}_{\mathrm{a}} \left(u \frac{\partial \lambda}{\partial r} + w \frac{\partial \lambda}{\partial z} \right) = f(\dot{\gamma}, \lambda), \tag{6.2.4}$$

where the functions $\eta(\dot{\gamma}, \lambda)$ and $f(\dot{\gamma}, \lambda)$ define the rheological model. We solve equations (6.2.1)–(6.2.4) subject to the boundary conditions, given by (2.2.6):

$$\text{no-slip and no-penetration condition:} \quad \mathbf{u} = \mathbf{0} \quad \text{at} \quad r = \alpha, \tag{6.2.5}$$

$$\text{symmetry conditions:} \quad \tau_{rz} = 0 = u \quad \text{at} \quad r = 0, \tag{6.2.6}$$

where $\alpha = \alpha(z)$ is the radius of the pipe. We note that we do not directly impose the volume flux condition (2.2.7) in COMSOL, rather we prescribe the velocity

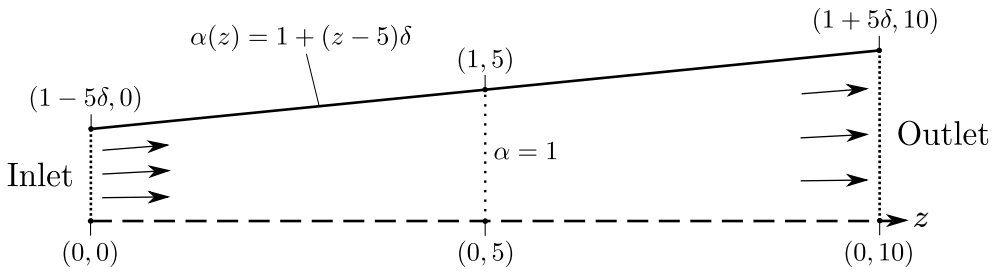

Figure 6.1: Geometry set-up in COMSOL. Profiles are taken along the dotted line at $z = 5$, where $\alpha(5) = 1$ and $\alpha'(5) = \delta$. The centreline ($r = 0$) is shown as a dashed line.

field $\mathbf{u}$ at the inlet, which in turn imposes a specified flux. We discuss this in more detail in Section 6.2.1.

6.2.1 Geometry

We construct a slowly varying axisymmetric pipe as shown in Figure 6.1. We chose a straight pipe wall, shown as a solid line, which is defined by $r = \alpha(z) = 1 + (z-5)\delta$, where δ is the aspect ratio of the pipe, and we chose to consider a pipe 10 units in length. We discuss the reason why this length is appropriate in Section 6.4.2. We can vary the value of δ to vary the rate of widening ($\delta > 0$) or narrowing ($\delta < 0$) of the pipe. The inlet has radius $\alpha(0) = 1 - 5\delta$ and the outlet has radius $\alpha(10) = 1 + 5\delta$. Half way along the pipe (shown as a dotted line) the radius is $\alpha(5) = 1$. We obtain numerical solutions for the velocities and the structure parameter along the entire pipe, and we sample these quantities at $z = 5$, from $r = 0$ to $r = 1$, to compare the numerical solutions to the asymptotic solutions.

We set $Q(t) = Q_\mathrm{i} + Q't$, where $Q(0) = Q_\mathrm{i}$ is the initial value of $Q(t)$, and Q' is the rate of change of the volume flux ($Q' > 0$ for accelerating flows and $Q' < 0$ for decelerating flows). We need to calculate the flow from $t = 0$ to a sufficiently large value that the solutions are no longer affected by the initial conditions, which we refer to as 'settling'. For consistency, when we compare the numerical solutions to the asymptotic solutions, we select the values of Q_i and Q' such that $Q = 1$ for the final value of t. Examples of these values are $Q_\mathrm{i} = 2$ and $Q' = -0.01$ for

$t = [0, 100]$ for a decelerating flow, or $Q_\mathrm{i} = 1$ and $Q' = 0$ for steady flow.

6.2.2 Notation and obtaining numerical solutions

We denote the numerical solutions for the streamwise velocity and the structure parameter we obtain from a simulation in COMSOL by w_N and λ_N, respectively.

We need to extract numerical solutions for the leading-order behaviour, $w_{0,\mathrm{N}}$ and $\lambda_{0,\mathrm{N}}$, and the perturbations, $w_{1,\mathrm{N}}$ and $\lambda_{1,\mathrm{N}}$, from the COMSOL output w_N and λ_N, and determine their accuracy (in the sense which we define below).

To obtain numerical solutions for $w_{0,\mathrm{N}}$ and $\lambda_{0,\mathrm{N}}$, we simply use the numerical solutions for the quantities with the thixotropic effects switched off, i.e. with $\mathcal{D}_\mathrm{a} = \mathcal{D}_\mathrm{t} = 0$. This yields numerical solutions for the leading-order quantities with higher-order corrections at $\mathcal{O}(\delta^2)$. We intended to use $w_{0,\mathrm{N}}$ and $\lambda_{0,\mathrm{N}}$ to verify that we can obtain accurate numerical solutions for the leading-order quantities, which will enable us to use the asymptotic solutions to obtain numerical solutions for the perturbation quantities.

When thixotropic effects are switched on, the numerical solutions are composed of the leading-order behaviour, perturbations due to thixotropy, and higher-order corrections, at $\mathcal{O}(1)$, $\mathcal{O}(\delta)$, and $\mathcal{O}(\delta^2)$ in magnitude, respectively. To obtain numerical solutions for $w_{1,\mathrm{N}}$ and $\lambda_{1,\mathrm{N}}$, we need to remove the leading-order behaviour from the numerical solutions. We can do this by subtracting the appropriate leading-order asymptotic solution from the numerical solutions, which leaves the perturbation quantities and the higher-order corrections, e.g. $\delta w_{1,\mathrm{N}} = w_\mathrm{N} - w_0 + \mathcal{O}(\delta^2)$.

We describe numerical solutions as 'accurate' if the magnitude of the difference between the numerical and the asymptotic solutions, which we refer to as the absolute error of the numerical solutions, is sufficiently small. For the leading-order numerical solutions (without thixotropy), the absolute error, using w as an example, is $w_{0,\mathrm{err}} = |w_{0,\mathrm{N}} - w_0|$. The absolute error of the numerical solutions for the perturbations is $w_{1,\mathrm{err}} = |w_{1,\mathrm{N}} - w_1|$. In particular, we describe the leading-order solutions as accurate if $w_{0,\mathrm{err}} = \mathcal{O}(\delta)$ or smaller, and the perturbations as accurate if $w_{1,\mathrm{err}} = \mathcal{O}(\delta)$ (or $\delta w_{1,\mathrm{err}} = \mathcal{O}(\delta^2)$) or smaller. We cannot, in

general, obtain a higher accuracy (i.e. a smaller absolute error) for w_{N} than $\mathcal{O}(\delta^2)$ because we are limited by the geometrical corrections and higher-order thixotropic behaviour at $\mathcal{O}(\delta^2)$. We note that, as discussed in the analysis of the asymptotic solutions for the sMMW model in Section 4.1, the lubrication approach we have used breaks down for some models and parameters, and leads to unphysical behaviour such as singularities, particularly near the centre of the pipe. The definition of accuracy presented above will be sufficient to verify the asymptotic solutions, but will clearly break down as we move away from weakly thixotropic behaviour, i.e. when δ is not small or when the Deborah numbers are much larger than δ.

6.3 Example of typical numerical solutions

In this section, we present the numerical solutions for a typical set of parameters for the sMMW model which highlight their main problem, i.e. where they disagree with the asymptotic solutions to an extent where we may not rely on the numerical solutions. Figure 6.2 shows the leading-order and first-order streamwise velocities and structure parameters obtained using COMSOL (solid lines) and from the asymptotic solutions (dotted lines with diamonds).

Figure 6.2(a) shows the numerical and asymptotic solutions for the leading-order streamwise velocity, $w_{0,\mathrm{N}}$ and w_0, respectively. This strong similarity is typical for a wide range of the sMMW model parameters, and we may be confident that we can use COMSOL to obtain the leading-order streamwise velocity.

Figure 6.2(b) shows the numerical and asymptotic solutions for the streamwise velocity perturbation, $w_{1,\mathrm{N}}$ and w_1, respectively. The two solutions are in good agreement away from the centre of the pipe, as in the leading-order case. Unlike the leading-order case, the numerical solution does not match the asymptotic solution near the centreline. This disgreement near the centreline is typical for a wide range of the sMMW model parameters (though not for all parameters, as we discuss in Section 6.5). This disagreement is the most significant problem with the numerical solutions, and is what we must eliminate to achieve the goal of verifying the asymptotic solutions.

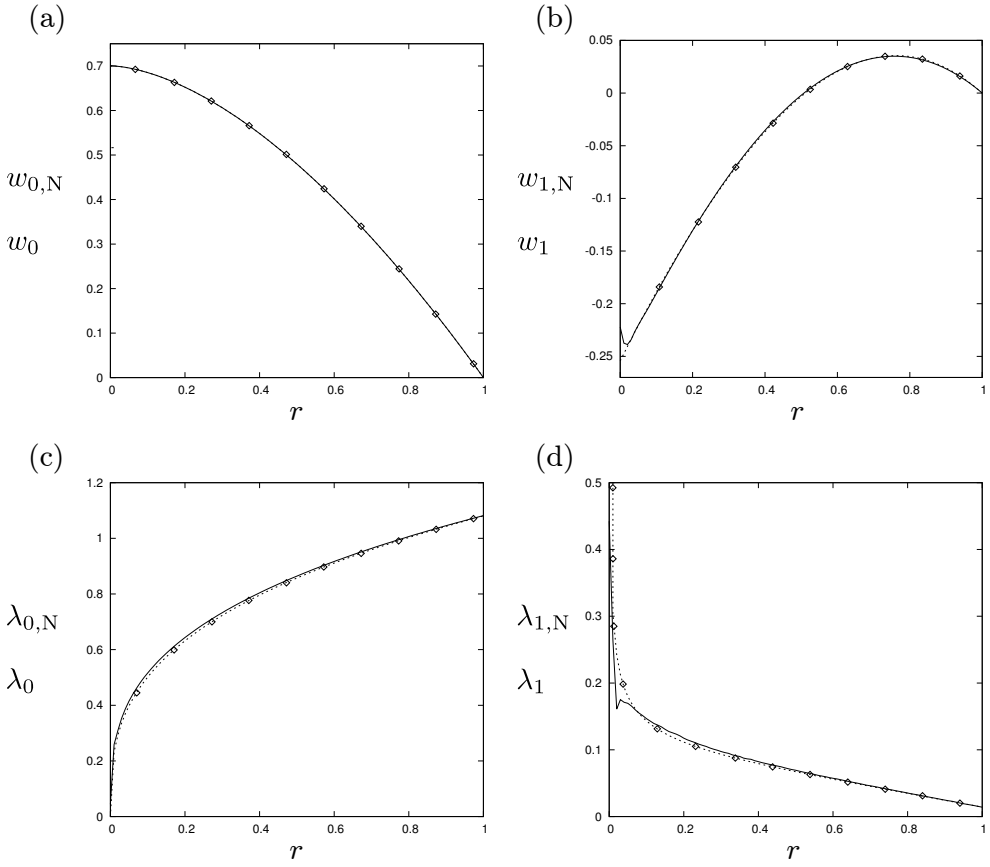

Figure 6.2: Typical numerical (solid lines) and asymptotic (dotted lines with diamonds) solutions for (a) the leading-order streamwise velocity $w_{0,\mathrm{N}}$ and w_0, (b) the streamwise velocity perturbation $w_{1,\mathrm{N}}$ and w_1, (c) the leading-order structure parameter $\lambda_{0,\mathrm{N}}$ and λ_0, The model parameters are $a = 1$, $b = 1$, $c = 1.5$, $\kappa = 1$, $Q(t) = 1$, $\alpha(z) = 1$, $\mathcal{D}_\mathrm{t} Q'(t) = 0$, and $\mathcal{D}_\mathrm{a}\alpha'(z) = 0.01$ ($\delta = 0.01$).

Figure 6.2(c) shows the numerical and asymptotic solutions for the leading-order structure parameter, $\lambda_{0,\mathrm{N}}$ and λ_0, respectively. Figure 6.2(d) shows the numerical and asymptotic solutions for the structure parameter perturbation, $\lambda_{1,\mathrm{N}}$ and λ_1, respectively. In both cases the numerical solutions are less accurate away from the wall than the corresponding solutions for the streamwise velocity. In addition, it is clear that the numerical solutions are least accurate near the centreline where $\partial\lambda_0/\partial r$ and λ_1 diverge. We would expect less accuracy near the centreline because pathological centreline behaviour is a known pitfall of the power-law model.

6.4 Simulation tests

In this section, we test the implementation of the problem in COMSOL by studying the effect of varying various controllable factors which affect the accuracy of the numerical solution for the streamwise velocity perturbation. The aim of these tests is to reduce the error in the numerical solutions $w_{1,\mathrm{N}}$ and $\lambda_{1,\mathrm{N}}$ near the centreline. As we are considering a time-dependent problem, we must allow the simulation to settle over a sufficient time so that the initial state of the fluid structure no longer affects the flow, which we discuss in Section 6.4.1. In an analogous way, we must ensure the pipe is long enough so that thixotropic flow downstream is no longer affected by the boundary conditions at the inlet, which we discuss in Section 6.4.2. Finally, we study the effect of varying the strength of thixotropy and δ in Section 6.4.3. In these sections, for brevity, we consider only steady non-uniform flow, unless stated otherwise; similar results and problems presented here also arise in unsteady uniform flow.

We must perform these tests to ensure that we are obtaining the most accurate numerical results feasible, and that the low accuracy near the centreline shown in Figure 6.2 cannot be reduced. The results of these tests determine whether we may continue to study this problem using COMSOL, i.e. whether we have achieved the first of the three goals, which is to verify the asymptotic solutions. In this section, we show that we are not able to eliminate the disagreement near the centreline for the streamwise velocity perturbation and hence we cannot verify the asymptotic solutions. Consequently, the numerical solutions we obtain from

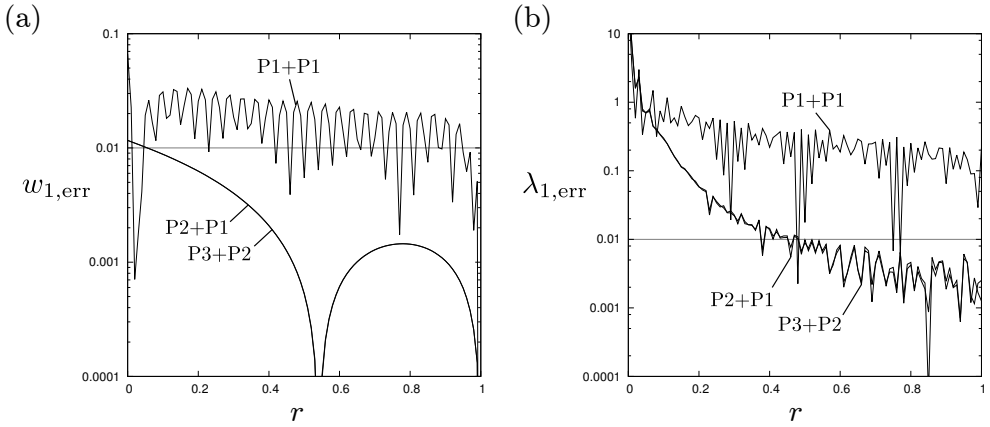

Figure 6.3: The errors (a) $w_{1,\mathrm{err}}$ and (b) $\lambda_{1,\mathrm{err}}$ (shown on a log scale), for three discretisation methods: P1+P1, P2+P1, and P3+P2, with $\delta = 0.01$ indicated for reference. The model parameters are $a = 1$, $b = 1$, $c = 1.5$, $\kappa = 1$, $Q(t) = 1$, $\alpha(z) = 1$, $\mathcal{D}_{\mathrm{t}}Q'(t) = 0$, $\mathcal{D}_{\mathrm{a}}\alpha'(z) = 0.01$ ($\delta = 0.01$).

COMSOL are not grounded well enough to allow us to progress to the second and third of the three goals.

Figures 6.3(a) and (b) show the error in the streamwise velocity perturbation $w_{1,\mathrm{err}}$ and in the structure parameter perturbation $\lambda_{1,\mathrm{err}}$, respectively, in steady non-uniform flow ($\mathcal{D}_{\mathrm{a}}\alpha' \neq 0$) for three discretisation methods. Using P1+P1, both $w_{1,\mathrm{err}}$ and $\lambda_{1,\mathrm{err}}$ are jagged at an $\mathcal{O}(\delta)$ scale, and are larger in magnitude than $\mathcal{O}(\delta)$. Clearly the discretisation method P1+P1 is not sufficient for this problem requirements. Discretising using either of the methods P2+P1 or P3+P2 makes the numerical solution smoother and more accurate than using P1+P1, as shown in Figures 6.3(a) and (b). For both perturbations, the errors using P2+P1 and P3+P2 are very similar, though for $\lambda_{1,\mathrm{N}}$, the error is very slightly reduced. The benefit of this minor increase in accuracy is offset by a substantial increase in computational running time (e.g. 404 seconds of machine time for P2+P1 and 611 seconds for P3+P2, for the examples shown in Figure 6.3, i.e. a roughly 50% increase in running time).

We conclude that, despite the increase in computational running time, the most

appropriate discretisation method is P3+P2, which we use for all numerical solutions for the subsequent examples in this chapter. We note that by default COMSOL includes consistent stabilisation (streamline and crosswind diffusion), but this stabilisation is only designed to be used with P1+P1. We therefore switch off consistent stabilisation methods when using P3+P2, as the flow is sufficiently resolved by the mesh and stabilisation has a negligible effect on the numerical solutions.

6.4.1 Simulation settling in time

In weakly thixotropic flow, thixotropy affects the flow over a short timescale, so the shear history of the fluid is quickly forgotten. Consequently, the initial conditions in the present problem do not have a lasting effect on the flow, and serve only to establish the flow in COMSOL. In this section, we determine the range of t that is required for the numerical solutions to settle, i.e. for the initial conditions to no longer affect the flow. By performing this test, we ensure that the error at the centreline of the numerical solutions is not a remnant of the initial conditions.

Figures 6.4(a) and (b) show the error in the streamwise velocity perturbation $w_{1,\mathrm{err}}$ and in the structure parameter perturbation $\lambda_{1,\mathrm{err}}$, respectively, in steady non-uniform flow ($\mathcal{D}_{\mathrm{a}}\alpha' \neq 0$) at $t = 0.1, 0.5, 1, 2$. When $t = 0.1$, both $w_{1,\mathrm{N}}$ and $\lambda_{1,\mathrm{N}}$ are still settling, but for $t \gtrsim 0.5$, both $w_{1,\mathrm{N}}$ and $\lambda_{1,\mathrm{N}}$ no longer vary, indicating that the fluid has 'forgotten' the initial conditions. Once the flow has settled, the error in both $w_{1,\mathrm{N}}$ and $\lambda_{1,\mathrm{N}}$ near the centreline remains too large, since we require $w_{1,\mathrm{err}} \lesssim \mathcal{O}(\delta)$ and $\lambda_{1,\mathrm{err}} \lesssim \mathcal{O}(\delta)$ ($\delta = 0.01$ is indicated in each plot).

We must also ensure that in unsteady uniform flow ($\mathcal{D}_{\mathrm{t}}Q' \neq 0$) the initial conditions do not affect the flow after a certain time. Unlike in the steady case, we cannot directly compare the numerical solutions at various times because $Q(t)$ continuously changes, but we may compare the errors of the numerical solutions for the perturbations.

Figures 6.5(a) and (b) show the error in the streamwise velocity perturbation $w_{1,\mathrm{err}}$ and in the structure parameter perturbation $\lambda_{1,\mathrm{err}}$, respectively, in unsteady

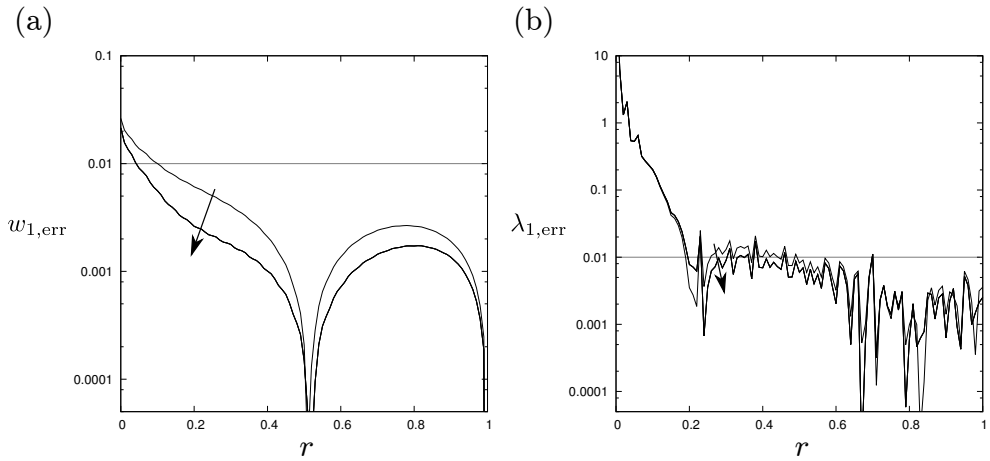

Figure 6.4: Plots of the errors (a) $w_{1,\mathrm{err}}$ and (b) $\lambda_{1,\mathrm{err}}$ at $t = 0.1, 0.5, 1, 2$ in steady non-uniform flow. The model parameters are $a = 1$, $b = 1$, $c = 1.5$, $\kappa = 1$, $Q(t) = 1$, $\alpha(z) = 1$, $\mathcal{D}_{\mathrm{t}}Q'(t) = 0$, and $\mathcal{D}_{\mathrm{a}}\alpha'(z) = 0.01$ ($\delta = 0.01$, indicated). The arrows show the direction of increasing t.

uniform flow at $t = 1, 2, 3, 4$. When $t = 1$, $w_{1,\mathrm{N}}$ is still settling, but for $t \gtrsim 2$, $w_{1,\mathrm{N}}$ settles, in the sense that the error no longer varies significantly. The error in $\lambda_{1,\mathrm{N}}$ settles more slowly than $w_{1,\mathrm{N}}$. As in the steady non-uniform example Figure 6.4, once the flow has settled, the error in both $w_{1,\mathrm{N}}$ and $\lambda_{1,\mathrm{N}}$ remains too large, since we require $w_{1,\mathrm{err}} \lesssim \mathcal{O}(\delta)$ and $\lambda_{1,\mathrm{err}} \lesssim \mathcal{O}(\delta)$ ($\delta = 0.01$ is indicated in each plot).

For both steady flow and unsteady flow we have shown that for $t > 4$ the flow has established and the initial conditions no longer affect the flow. In particular, the error at the centreline of $w_{1,\mathrm{N}}$ is not the result of a long-lasting effect of the initial conditions on the flow. The subsequent numerical solutions presented in this chapter are obtained by sampling the behaviour when $t = 10$.

6.4.2 Simulation settling in space

As mentioned in Section 6.4.1, weak thixotropy affects the flow over a short timescale, so the shear history and the initial state of the fluid structure are quickly forgotten. In weakly advective thixotropy, the boundary conditions at the inlet in the present problem should not have a lasting effect on the effect on the flow. In this section, we determine the distance along the pipe from the inlet z

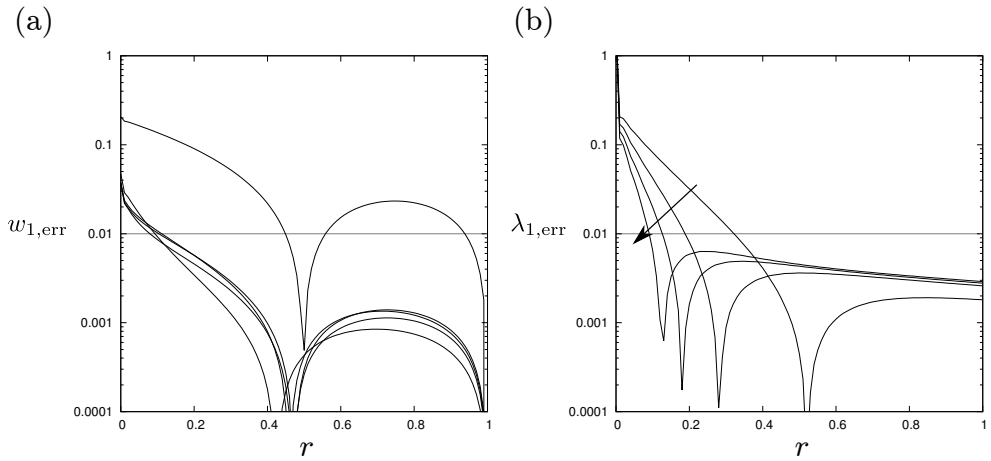

Figure 6.5: Plots of the errors (a) $w_{1,\mathrm{err}}$ and (b) $\lambda_{1,\mathrm{err}}$ at $t = 1, 2, 3, 4$ in unsteady uniform flow. The model parameters are $a = 1$, $b = 1$, $c = 1.5$, $\kappa = 1$, $Q(t) = 1$, $\alpha(z) = 1$, $\mathcal{D}_{\mathrm{t}}Q'(t) = -0.01$, and $\mathcal{D}_{\mathrm{a}}\alpha'(z) = 0$ ($\delta = 0.01$, indicated). The arrow in (b) shows the direction of increasing t; no arrow is given for (a), but we note that the error is largest when $t = 1$.

that is required for the flow to fully establish from the inlet boundary conditions. This is important to determine the most appropriate position along the pipe at which to sample the quantities, to ensure that the inlet conditions do not affect the accuracy of the solution.

Figures 6.4(a) and (b) show the error in the streamwise velocity perturbation $w_{1,\mathrm{err}}$ and in the structure parameter perturbation $\lambda_{1,\mathrm{err}}$, respectively, in steady non-uniform flow ($\mathcal{D}_{\mathrm{a}}\alpha' = 0.01$) at $z = 1, 2, 3, 4, 5$ (where the outlet is at $z = 10$). Note that we scale r by the radius $\alpha(z)$ so that we may compare the error plots. The error plots for both $w_{1,\mathrm{N}}$ and $\lambda_{1,\mathrm{N}}$ vary very little between $z = 1$ and $z = 5$, showing that the flow adjusts from the boundary conditions close to the inlet. It is clear that the error in $w_{1,\mathrm{N}}$ near the centreline is not a result of a slow adjustment from the boundary conditions.

By sampling the flow quantities at $z = 5$, at the middle of the pipe, we can be sure that errors in the perturbation quantities are not a result of sample too close to the inlet (and hence the boundary conditions).

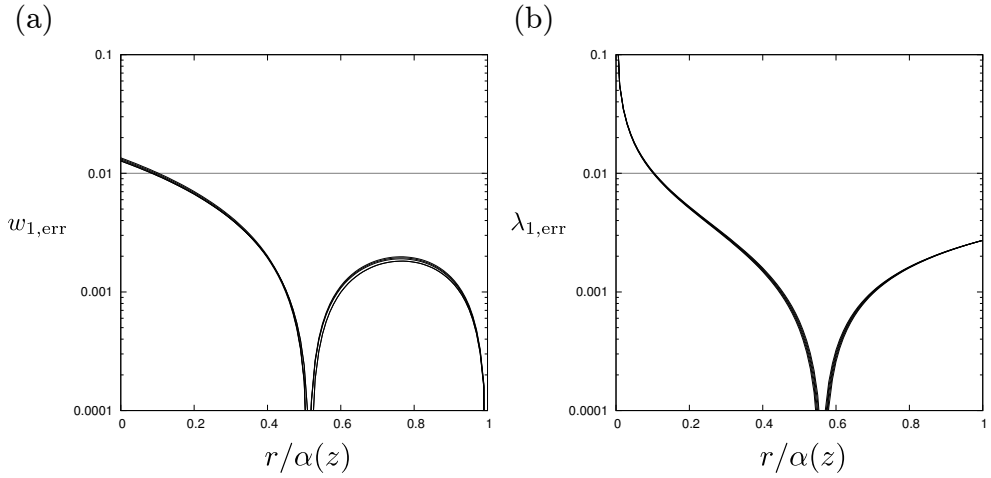

Figure 6.6: Plots of the errors (a) $w_{1,\mathrm{err}}$ and (b) $\lambda_{1,\mathrm{err}}$ at $z = 1, 2, 3, 4, 5$ in steady non-uniform flow. The model parameters are $a = 1$, $b = 1$, $c = 1.5$, $\kappa = 1$, $Q(t) = 1$, $\alpha(z) = 1$, $\mathcal{D}_{\mathrm{t}}Q'(t) = 0$, and $\mathcal{D}_{\mathrm{a}}\alpha'(z) = 0.01$ ($\delta = 0.01$, indicated).

6.4.3 The effect of varying δ

The asymptotic solutions for thixotropic pipe flow presented in Chapter 3 are formally valid only in the asymptotic limit $\delta \to 0$. We cannot consider this limit directly in COMSOL, but we may study the effect of varying δ (by varying α') on the numerical solutions. We require δ to be sufficiently small so that the behaviour at $\mathcal{O}(\delta^2)$ is too small to affect the accuracy of the behaviour at $\mathcal{O}(\delta)$ significantly. For example, if we choose $\delta = 0.1$ then $\delta^2 = 0.01$, so the behaviour at $\mathcal{O}(\delta^2)$ will make it difficult to obtain the $\mathcal{O}(\delta)$ behaviour; if $\delta = 0.001$ then $\delta^2 = 0.000001$, so the $\mathcal{O}(\delta^2)$ behaviour will be much smaller and the $\mathcal{O}(\delta)$ solutions we be clearer. However, we cannot simply decrease δ as much as we wish because eventually numerical noise will affect the accuracy of the $\mathcal{O}(\delta)$ solutions.

Figure 6.7(a) shows the effect of varying δ on the numerical solution for the streamwise velocity perturbation $w_{1,\mathrm{N}}$ (solid lines), along with the corresponding asymptotic solution w_1 (dotted line). For $\delta = 0.00001$, the smallest value of δ shown here, the profile is jagged across the width of the pipe and has a large spike near the centreline. For the larger values of $\delta = 0.001, 0.0001$ the jaggedness is reduced, but the spike near the centreline is still present. It is not until δ is increased further that there is a significant reduction in the size of the spike, as

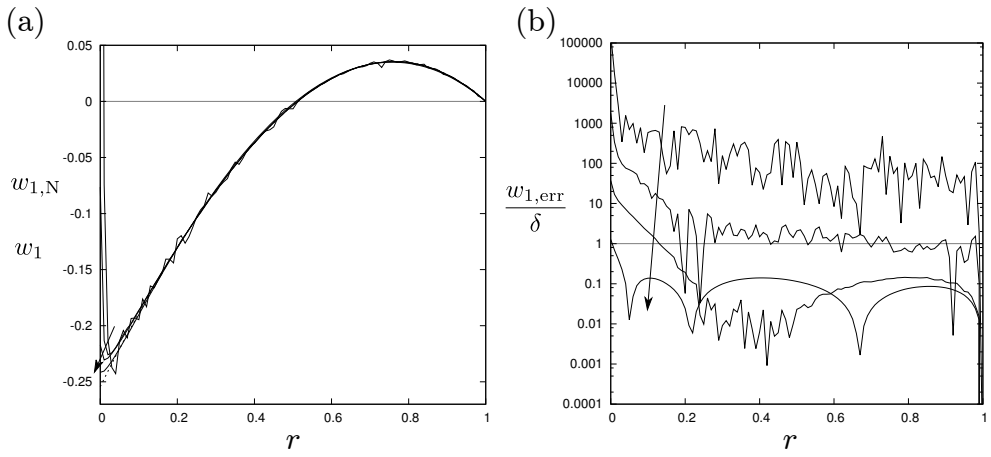

Figure 6.7: (a) Numerical solutions $w_{1,\mathrm{N}}$ (solid) and the corresponding asymptotic solution w_1 (dotted, visible only near the centreline), and (b) the absolute error divided by δ, for $\delta = 0.01, 0.001, 0.0001, 0.00001$. We require $w_{1,\mathrm{err}}/\delta < 1$ for the absolute error to be $w_{1,\mathrm{err}} < \delta$. The arrows show the direction of increasing δ.

shown for $\delta = 0.01$.

Figure 6.7(b) shows how the error in the numerical solutions shown in Figure 6.7(a) decreases as δ increases. In Figure 6.7(b) we require the error to be much less than unity, which is almost the case when $\delta = 0.01$, except that the error near the centreline remains too large. Besides this error, it is clear that $\delta = 0.01$ yields the most accurate solutions.

6.4.4 Numerical results for the Houška model

In the previous sections we showed that we could not eliminate the error at the centreline for the sMMW model. We may instead use the Houška model, for which there is no pathological behaviour at leading order, to verify the asymptotic solutions. (However, the magnitude of $\partial\lambda_1/\partial r$ may be large at the edge of the pseudo-plug, particularly with large values of the regularisation parameter k: see, for example, the troughs in the profiles of λ_1 in Figures 5.1(d) and (f).) As for the sMMW model, we begin by trying to verify the asymptotic solutions and achieve the first goal.

We study the Houška model in steady uniform flow, without thixotropy ($\mathcal{D}_\mathrm{a} = \mathcal{D}_\mathrm{t} = 0$). Figures 6.8(a) and (c) show the leading-order asymptotic solutions w_0 and λ_0 (dotted with diamonds) and the corresponding numerical solutions $w_{0,\mathrm{N}}$ and $\lambda_{0,\mathrm{N}}$ (solid) for an illustrative example of the Houška model in a uniform pipe. The corresponding absolute errors $w_{0,\mathrm{err}}$ or $\lambda_{0,\mathrm{err}}$ are shown in Figures 6.8(b) and (d). We expect the errors in this example to be very small because we are considering steady uniform flow, so there are no geometrical corrections. However, the errors shown in Figures 6.8(b) and (d), at around the order of 10^{-5}– 10^{-4} are too large. Whilst we were not able to obtain numerical solutions for the perturbations (due to the sensitivity of the simulation to the initial and boundary conditions), the error shown here would be similar in magnitude to the perturbation quantities, so extracting the perturbation quantities would be difficult.

The absolute error near the centreline is not larger than away from the centreline for either $w_{0,\mathrm{err}}$ or $\lambda_{0,\mathrm{err}}$, so the numerical solutions for the Houška model do not have a large centreline error similar to the sMMW model. We note that for $\lambda_{0,\mathrm{err}}$ the error is largest near the edge of the pseudo-plug ($r \approx 0.15$), which is also arises for other parameters of the Houška model. It is possible that the pathological behaviour near the edge of the pseudo-plug would be difficult to capture numerically.

From Figure 6.8 it is clear that the numerical solutions for the Houška model are not sufficiently accurate to verify the asymptotic solutions. We would require a significantly higher accuracy across the width of the pipe to study the perturbations and strong thixotropy for the Houška model. In general we found simulating the flow of a Houška fluid is highly sensitive to the initial and boundary conditions. We obtain these conditions from the asymptotic solutions, so setting up a simulation is often time-consuming because each simulation must be tailored for each parameter set of the Houška model (unlike for the sMMW model where the closed-form solutions allow us to study various parameter sets quickly).

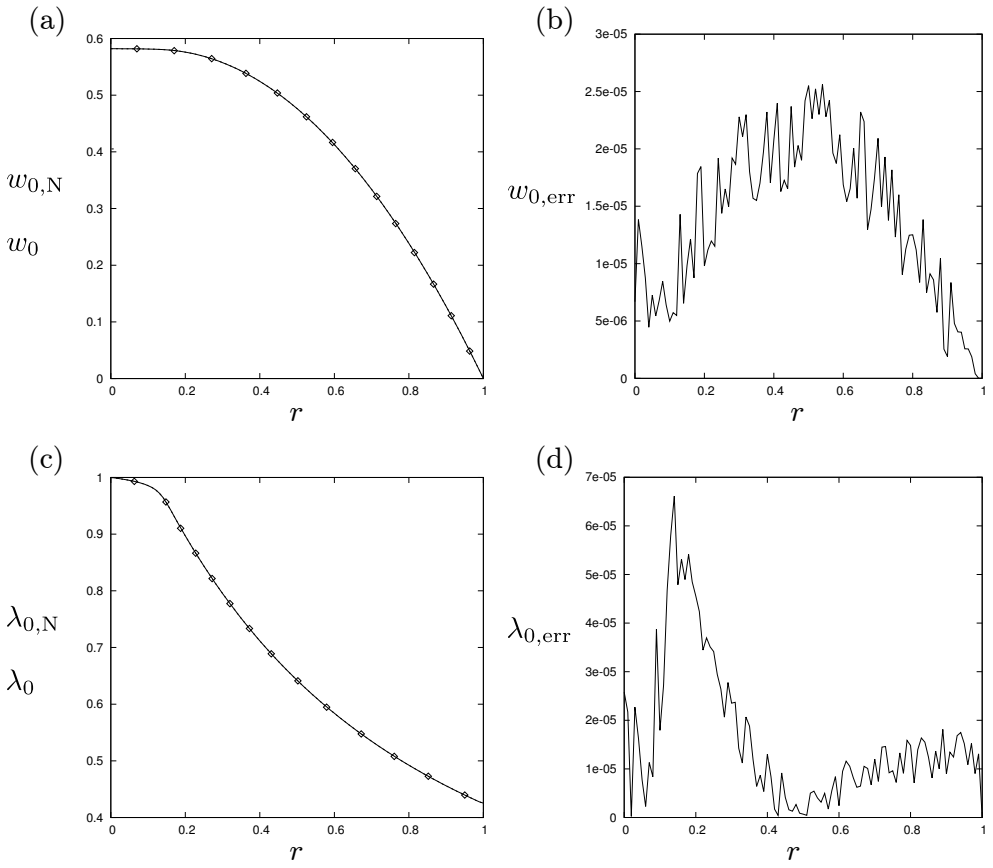

Figure 6.8: Numerical (solid) and asymptotic (dotted with diamonds) solutions for (a) w_0 and (c) λ_0 in steady and uniform flow ($\delta = 0$), with the corresponding absolute errors (b) $w_{0,\mathrm{err}}$ and (d) $\lambda_{0,\mathrm{err}}$. The parameters are $\tau_{\mathrm{y}0} = 0$, $\tau_{\mathrm{y}1} = 0.5$, $\eta_{\mathrm{H}0} = 1$, $\eta_{\mathrm{H}1} = 0.2$, and $k = 100$.

6.5 Partial results

Whilst the numerical results are not accurate enough to allow us to continue to use COMSOL to validate the asymptotic solutions (and achieve the first goal), the results we have obtained offer some insight into the validity of the asymptotic solutions. In this section, we present some numerical solutions for the sMMW model which provide such insights. We present the numerical solution for the anomalous behaviour of Region $\bar{\mathrm{A}}_{\mathrm{I}}^{1,2}$ of the regime diagram. We also present examples of numerical solutions which agree with the asymptotic solutions across the width of the pipe, and which show how we may expect the numerical and asymptotic solutions to disagree more as the strength of thixotropy increases.

The first example is for the anomalous behaviour of w_1 in Region $\bar{\mathrm{A}}_{\mathrm{I}}^{1,2}$ of the regime diagram, first presented in Section 4.1.4 and discussed in detail in Section 4.1.6. We recall that in this region, which only applies to the case of temporal thixotropy ($\mathfrak{R}_{1,2}$), the profile of w_1 is the opposite of that described by the TRC. In particular, w_1 in Region $\bar{\mathrm{A}}_{\mathrm{I}}^{1,2}$ is positive at the centre of the pipe and negative near the wall (see, for example, the profile labelled $\mathfrak{R}_{1,2}$ in Figure 4.3(a)).

Figure 6.9 shows $w_{1,\mathrm{N}}$ (solid) and w_1 (dotted with diamonds) for a fluid in Region $\bar{\mathrm{A}}_{\mathrm{I}}^{1,2}$ (specifically $a = 0.2$, $b = 0.8$, and $c = 4$). We note that the dotted line is only visible for $r \lesssim 0.2$; further away from the centreline the numerical and asymptotic solutions overlap. Aside from the disagreement near the centreline, the numerical solution presented in Figure 6.9 strongly agrees with the corresponding asymptotic solution. Most importantly, the numerical solutions predict the anomalous reversal in the behaviour of w_1 in this region of the regime diagram, which provides strong support for the asymptotic solutions in this anomalous case.

However, we were not able to obtain similarly accurate numerical solutions for the anomalous behaviour in the equivalent region for advective thixotropy $\bar{\mathrm{A}}_{\mathrm{I}}^{2,1}$. In this region, the radial derivative of w_1 has an additional change of sign, as illustrated by the profile labelled $\mathfrak{R}_{2,1}$ in Figure 4.3(a). This feature is much more subtle than the reversal of w_1 in Region $\bar{\mathrm{A}}_{\mathrm{I}}^{1,2}$, so it is much more difficult to capture numerically.

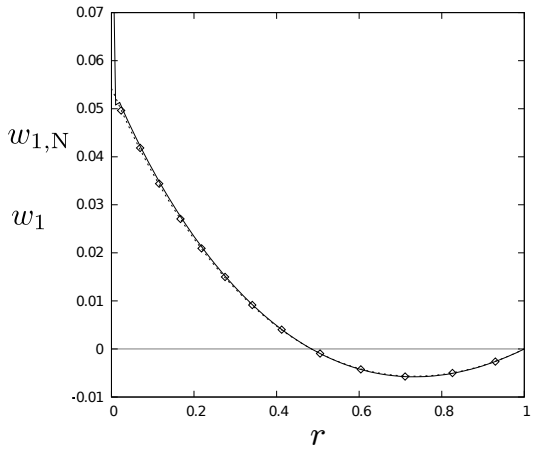

Figure 6.9: Numerical solution $w_{1,\mathrm{N}}$ (solid) and asymptotic solution w_1 (dotted with diamonds) in uniform flow. The parameters are $a = 0.2$, $b = 0.8$, $c = 4$ in Region $\bar{\mathrm{A}}_{\mathrm{I}}^{1,2}$ of the regime diagram, $Q(t) = 1$, $\mathcal{D}_{\mathrm{t}}Q'(t) = -0.001$, $\alpha(z) = 1$, and $\mathcal{D}_{\mathrm{a}}\alpha'(z) = 0$. The solutions are in excellent agreement except at the centreline, where the numerical solution has a large spike not described by the asymptotic solution.

We can also gain insight into the effect of increasing the strength of thixotropy, which we achieve by increasing $\mathcal{D}_{\mathrm{t}}Q'(t)$. Figure 6.10 shows, for a fluid in Region $\bar{\mathrm{A}}_{\mathrm{III}}$, numerical (solid) and asymptotic (dotted with diamonds) solutions for the streamwise velocity perturbation, for two values of $\mathcal{D}_{\mathrm{t}}Q'(t)$. We note that in Figure 6.10 the dotted line is only visible near the centreline near $w_1 = -0.23$. Away from the centreline the numerical and asymptotic solutions cannot be distinguished in this plot.

There is good agreement between the asymptotic and numerical solutions away from the centreline when $\mathcal{D}_{\mathrm{t}}Q'(t) = -0.001$. Near the centreline, the numerical solution has a large spike not described by the asymptotic solution. For stronger thixotropy, such as when $\mathcal{D}_{\mathrm{t}}Q'(t) = -0.1$, the numerical and asymptotic solutions differ significantly across the width of the pipe, suggesting that $\mathcal{D}_{\mathrm{t}}Q'(t) = -0.1$ is out of the range of weak thixotropy.

For some parameters of the sMMW model we are able to obtain accurate numerical solutions across the width of the pipe. One of the best numerical solutions $w_{1,\mathrm{N}}$ we obtained is shown by the solid line in Figure 6.11. The corresponding

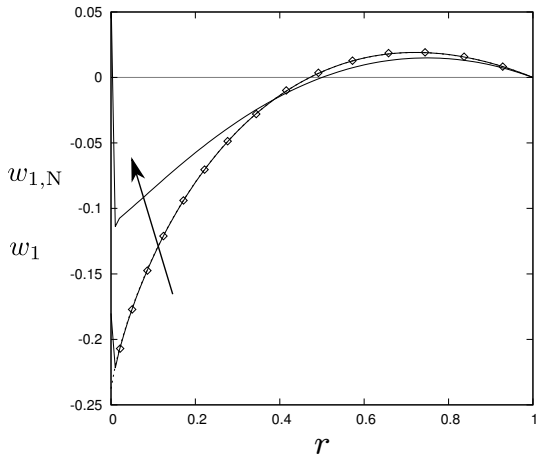

Figure 6.10: Numerical solution $w_{1,\mathrm{N}}$ (solid) and asymptotic solution w_1 (dotted with diamonds) in uniform flow. The parameters are $a = 2$, $b = 0.8$, $c = 4$ (Region $\bar{\mathrm{A}}_{\mathrm{III}}$ of the regime diagram), $Q(t) = 1$, $\mathcal{D}_{\mathrm{t}}Q'(t) = -0.001, -0.1$, $\alpha(z) = 1$, $\mathcal{D}_{\mathrm{a}}\alpha'(z) = 0$. The arrow shows the direction of increasing $\mathcal{D}_{\mathrm{t}}Q'(t)$.

asymptotic solution is shown as a dotted line with diamonds, but is not visible because it lies on top of the numerical solution. The numerical and asymptotic solutions agree across the pipe including the region near the centreline, where numerical solutions for other parameters are much less accurate. Figure 6.11 shows an example of a numerical solution that is of the required accuracy, which implies that obtaining solutions of such an accuracy using COMSOL is possible.

We also obtained similar partial results for steady flow. Figure 6.12 shows an example of the numerical solution $w_{1,\mathrm{N}}$ for an antithixotropic fluid in the weakly advective regime. As in Figures 6.9 and 6.10, the numerical solution (solid) shown in Figure 6.12 agrees with the corresponding asymptotic solution (dotted with diamonds), except near the centreline.

6.6 Summary

In this chapter, we aimed to use COMSOL to achieve three goals: to verify the asymptotic solutions presented in Chapters 3–5; to study the robustness of the asymptotic approach, i.e. to find for what range of the aspect ratio δ the

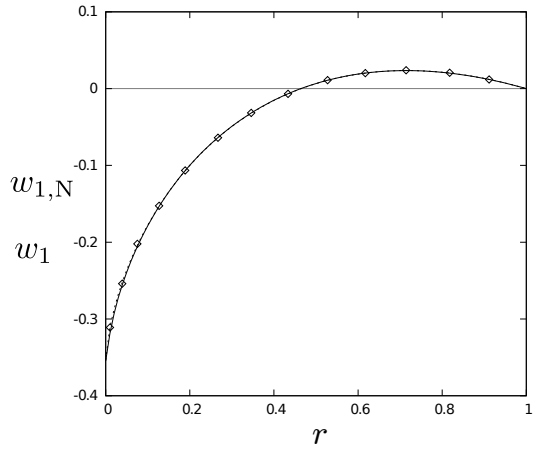

Figure 6.11: Numerical solution $w_{1,\mathrm{N}}$ (solid) and asymptotic solution w_1 (dotted with diamonds) in uniform flow. The parameters are $a = 2$, $b = 1$, $c = 4$, $Q(t) = 1$, $\mathcal{D}_\mathrm{t} Q'(t) = -0.001, -0.1$, $\alpha(z) = 1$, and $\mathcal{D}_\mathrm{a}\alpha'(z) = 0$.

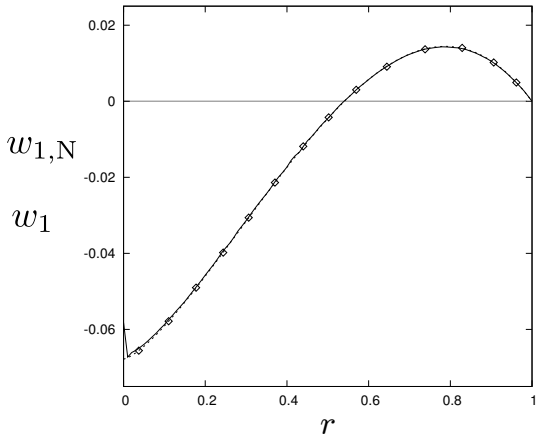

Figure 6.12: Numerical solution $w_{1,\mathrm{N}}$ (solid) and asymptotic solution w_1 (dotted with diamonds) in steady flow. The parameters are $a = 1$, $b = 1$, $c = 1.1$, $Q(t) = 1$, $\mathcal{D}_\mathrm{t} Q'(t) = 0$, $\alpha(z) = 1$, and $\mathcal{D}_\mathrm{a}\alpha'(z) = 0.01$.

perturbation solutions are accurate; and to study regimes of strong thixotropy out of the reach of the asymptotic methods developed for weak thixotropy. We had to progress through these goals in this order, as each goal depended on the success of the previous. As discussed in this chapter, we were not able to verify the asymptotic solutions using COMSOL, so we did not achieve the first of these goals.

We studied two models in this chapter. For the sMMW model, a significant disagreement near the centreline between the numerical and asymptotic solutions for the streamwise velocity perturbation, such as that shown in Figure 6.2(b), is the main reason we are not able to verify the asymptotic solutions. For the Houška model, the numerical and asymptotic solutions for the streamwise velocity disagree across the width of the pipe, as shown in Figure 6.8(b).

We obtained some partial results, presented in Section 6.5, which provide some support for the asymptotic solutions. In particular for the sMMW model, the numerical and asymptotic solutions agree away from the centre of the pipe for a large range of the parameters a, b, and c, including the anomalous behaviour of w_1 in Region $\bar{\mathrm{A}}_{\mathrm{I}}^{1,2}$ of the regime diagram, as shown in Figure 6.10. In some cases, the numerical and asymptotic solutions agree across the width of the pipe, as shown in Figure 6.11, which is an example of the accuracy we require in general to verify the asymptotic solutions.

It may be possible to obtain accurate results across the width of the pipe for different rheological models from the ones used here. In particular, a rheological model which is well-behaved across the width of the pipe, and for which closed-form asymptotic solutions are available, would presumably be easier to calculate numerically. For such a model, initial conditions would be defined analytically and there would be no difficult-to-capture pathological behaviour. The results presented in this chapter suggest that a quantitative improvement in the numerical results would allow us to explore regimes of stronger thixotropy, as originally planned.

One may also consider an approach using adaptive mesh refinement [97] to tackle the steep spatial gradients near the centreline. Adaptive mesh refinements may also improve the numerical solutions for the Houška model, where steep profile

gradients often arise between the centreline and the pipe wall.

Chapter 7

Oscillating Thixotropic Pipe Flow

In this chapter, we formulate and investigate the problem of unsteady thixotropic flow in a uniform cylindrical pipe, driven by an oscillating pressure gradient. There are two key differences between the problem in this chapter and the problem considered in Chapters 2–6. In this problem, we consider a uniform pipe and uniform flow, so the advective effect of thixotropy is absent. Consequently, we only consider regimes of temporal thixotropy. In addition, we specify the pressure gradient in this problem, rather than the volume flux, so the volume flux will be perturbed by thixotropy instead of the pressure gradient. This second difference means that the shape of the profiles of the perturbation quantities will be qualitatively different in this problem from the profiles in the previous set-up. We also consider the slowly adjusting regime, in which the fluid adjusts to changes in the shear rate over a much longer timescale than the pressure gradient oscillation.

We begin by deriving the governing equations for the flow of an incompressible thixotropic fluid in an axisymmetric geometry in Section 7.1. We then rescale and non-dimensionalise these equations, and obtain an appropriate temporal Deborah number $\mathcal{D}_\mathrm{t}$ in Section 7.2. We consider the quickly adjusting regime, in which the typical timescale of the structure evolution is much smaller than the timescale of the pressure gradient, i.e. when $0 < \mathcal{D}_\mathrm{t} \ll 1$. We also consider the slowly adjusting regime in which the structure evolves over a smaller timescale than

the timescale of the pressure gradient, i.e. when $\mathcal{D}_\mathrm{t} \gg 1$. We did not consider the slowly adjusting regime in Chapters 2–6, but we are able to make analytical progess in the present set-up.

In the quickly adjusting regime, we do not choose a particular pressure gradient from the outset because we can obtain general solutions. When we present illustrative examples for particular rheological models, we specialise to an sinusoidally oscillating pressure gradient. In Section 7.3, we asymptotically expand the governing equations in powers of small $\mathcal{D}_\mathrm{t}$, and obtain the governing equations at leading order and first order. We obtain the general solutions for the quickly adjusting regime in Section 7.4, then consider the MMW model in Section 7.5 and the Houška model in Section 7.6.

In the slowly adjusting regime, we can only make limited progress towards general solutions, so we specify a sinusoidal pressure gradient and a rheology from the outset. In Section 7.7, we asymptotically expand the governing equations in powers of small $\mathcal{D}_\mathrm{t}^{-1}$ and obtain the governing equations, and in Section 7.8 we study the behaviour of the MMW model in the slowly adjusting regime.

A substantial benefit of the geometry of this problem is that the flow is in the streamwise direction only, making it a much simpler problem to study numerically. We study this problem numerically using COMSOL in Section 7.9. The method of obtaining asymptotic solutions for this problem in the quickly adjusting regime is similar to that for the previous set-up. We present the full derivation of this problem here, noting the differences where appropriate. After verifying the asymptotic solutions in the quickly adjusting and slowly adjusting regimes using COMSOL, we explore the full range of thixotropic behaviours in Section 7.9.4.

7.1 Governing equations

We consider the flow of an incompressible thixotropic or antithixotropic fluid along a cylindrical pipe of uniform radius, with no swirl and driven by an unsteady pressure gradient, $\hat{G}(\hat{t}) = -\partial\hat{p}/\partial\hat{z}$. Throughout this chapter we refer to $\hat{G}(\hat{t})$ (and

subsequently $G(t)$) as the pressure gradient for convenience, where we note that we are refering to the sign-reverse of the pressure gradient. The velocity is $\hat{\mathbf{u}} = (0, 0, \hat{w}(\hat{r}, \hat{t}))$, where $\hat{w}$ is the streamwise velocity. Here and throughout, a caret denotes a dimensional quantity, whereas dimensionless quantities are unadorned.

The derivation of the governing equations for this problem follows that of the previous set-up, detailed in Chapter 2, except that all quantities in the transverse direction are zero. In particular, the constitutive relation (2.1.2) is unchanged, the shear-rate tensor (2.1.3) reduces to

$$\hat{e}_{ij} = \begin{pmatrix} 0 & 0 & \dfrac{\partial \hat{w}}{\partial \hat{r}} \\ 0 & 0 & 0 \\ \dfrac{\partial \hat{w}}{\partial \hat{r}} & 0 & 0 \end{pmatrix}, \tag{7.1.1}$$

and as before we define $\hat{\Gamma} = \dot{\gamma}^2 = (\partial \hat{w}/\partial \hat{r})^2$.

Using the constitutive relation (2.1.2) and the shear-rate tensor (7.1.1), the hydrodynamic equations are

$$\frac{\partial \hat{p}}{\partial \hat{r}} = 0, \tag{7.1.2}$$

$$\frac{\partial \hat{p}}{\partial \hat{z}} = \frac{1}{\hat{r}} \frac{\partial}{\partial \hat{r}} \left(\hat{r} \hat{\eta} \frac{\partial \hat{w}}{\partial \hat{r}} \right) = -\hat{G}(\hat{t}). \tag{7.1.3}$$

The mass conservation equations (2.1.4) reduces to

$$\frac{\partial \hat{w}}{\partial \hat{z}} = 0, \tag{7.1.4}$$

which is automatically satisfied in uniform flow. We assume the usual no-slip and no-penetration boundary conditions apply at the wall of the pipe, along with the symmetry condition at the centre, given by

$$\hat{\mathbf{u}} = \mathbf{0} \quad \text{at} \quad \hat{r} = \hat{R} \quad \text{and} \quad \hat{\tau}_{rz} = 0 = \hat{u} \quad \text{at} \quad \hat{r} = 0, \tag{7.1.5}$$

respectively, where $\hat{R}$ is the radius of the pipe. The unsteady volume flux $\hat{Q}(\hat{t})$ is

given by

$$\hat{Q}(\hat{t}) = 2\pi \int_0^{\hat{R}} \hat{r}\hat{w}(\hat{r},\hat{t})\,\mathrm{d}\hat{r}. \tag{7.1.6}$$

We have the option to prescribe either the pressure gradient or the volume flux. In this chapter, in contrast to the problem considered in Chapters 2–6, we choose to impose an unsteady pressure gradient $\hat{G}(\hat{t}) = -\partial\hat{p}/\partial\hat{z}$.

The structure evolves according to a kinetic equation of the form

$$\frac{\partial\lambda}{\partial\hat{t}} = \hat{f}(\hat{\Gamma},\lambda), \tag{7.1.7}$$

where $\hat{f}$ is the structure evolution rate, which describes the shear-driven build-up and breakdown of the structure. This structure evolution equation differs from the equation for the previous set-up, given by (2.1.12), because it only has $\partial\lambda/\partial\hat{t}$ on the left-hand-side rather than the material derivative. As for the previous set-up, the structure evolution rate $\hat{f}(\hat{\Gamma},\lambda)$ and the viscosity $\hat{\eta}(\hat{\Gamma},\lambda)$ describe the rheological properties of the fluid, and together form a rheological model. We do not specify a particular rheological model from the outset as we are able to obtain general solutions in closed form (containing integrals) for the velocity and the structure parameter in the quickly adjusting regime.

7.2 Non-dimensionalisation

We now rescale and non-dimensionalise the governing equations introduced in Section 7.1, to which end we define dimensionless quantities via

$$\begin{gathered}\hat{r} = \hat{R}r, \quad \hat{w} = \frac{\hat{G}_0\hat{R}^2 w}{\hat{\mu}_0}, \quad \hat{G} = \hat{G}_0 G, \quad \hat{\eta} = \hat{\mu}_0\eta, \\ \hat{f}(\hat{\Gamma},\lambda) = \hat{f}_0 f(\Gamma,\lambda), \quad \hat{t} = \frac{1}{\hat{\omega}}t, \quad \hat{Q} = \frac{\hat{G}_0\hat{R}^4}{\hat{\mu}_0}Q,\end{gathered} \tag{7.2.1}$$

where $\hat{G}_0$ is the amplitude of the pressure gradient, $\hat{f}_0$ is the structure response timescale, $\hat{\mu}_0$ is the typical viscosity, $\hat{\omega}$ is the frequency of the pressure-gradient oscillation. We note that there are fewer dimensionless quantities here than in

the previous set-up because there are no quantities for the transverse direction.

Using the quantities in (7.2.1) to non-dimensionalise the momentum equation (7.1.3), we obtain

$$\frac{1}{r}\frac{\partial}{\partial r}\left(r\eta\frac{\partial w}{\partial r}\right) = -G. \tag{7.2.2}$$

We non-dimensionalise the boundary conditions (7.1.5) to obtain

$$u = 0 = w \quad \text{at} \quad r = 1 \quad \text{and} \quad \eta(\dot{\gamma}, \lambda)\frac{\partial w}{\partial r} = 0 = u \quad \text{at} \quad r = 0, \tag{7.2.3}$$

and the volume flux (7.1.6) to obtain

$$Q(t) = 2\pi \int_0^1 rw(r,t)\,\mathrm{d}r. \tag{7.2.4}$$

Finally, we non-dimensionalise the structure evolution equation (7.1.7) to obtain

$$\mathcal{D}_\mathrm{t}\frac{\partial \lambda}{\partial t} = f(\Gamma, \lambda), \quad \text{where} \quad \mathcal{D}_\mathrm{t} = \frac{\hat{\omega}}{\hat{f}_0}, \tag{7.2.5}$$

i.e. $\mathcal{D}_\mathrm{t}$ is the temporal Deborah number, which is the ratio of the structure response timescale to the timescale of the unsteady pressure gradient.

7.3 Expansion in the quickly adjusting regime: $0 < \mathcal{D}_\mathbf{t} \ll 1$

For the quickly adjusting regime, we expand the velocity, structure parameter, and volume flux in powers of the small temporal Deborah number $\mathcal{D}_\mathrm{t}$:

$$(w, \lambda, Q) = \sum_{i=0}^{\infty} \mathcal{D}_\mathrm{t}^i (w_i, \lambda_i, Q_i). \tag{7.3.1}$$

We note that $G(t)$ is prescribed so we do not expand it. At leading order ($\mathcal{O}(1)$) and first order ($\mathcal{O}(\mathcal{D}_\mathrm{t})$), terms of $\Gamma = (\partial w/\partial r)^2$, the viscosity $\eta(\Gamma, \lambda)$, and the

structure evolution rate $f(\Gamma, \lambda)$ are

$$\Gamma_0 = \left(\frac{\partial w_0}{\partial r}\right)^2, \quad \text{and} \quad \Gamma_1 = 2\frac{\partial w_0}{\partial r}\frac{\partial w_1}{\partial r}, \tag{7.3.2}$$

$$\eta_0 = \eta(\Gamma_0, \lambda_0), \quad \text{and} \quad \eta_1 = \eta_\Gamma \Gamma_1 + \eta_\lambda \lambda_1, \tag{7.3.3}$$

$$f_0 = f(\Gamma_0, \lambda_0), \quad \text{and} \quad f_1 = f_\Gamma \Gamma_1 + f_\lambda \lambda_1, \tag{7.3.4}$$

where for convenience, as for the previous set-up, we define

$$\eta_\Gamma = \left.\frac{\partial \eta}{\partial \Gamma}\right|_{(\Gamma_0,\lambda_0)}, \quad \text{and} \quad \eta_\lambda = \left.\frac{\partial \eta}{\partial \lambda}\right|_{(\Gamma_0,\lambda_0)}, \tag{7.3.5}$$

$$f_\Gamma = \left.\frac{\partial f}{\partial \Gamma}\right|_{(\Gamma_0,\lambda_0)}, \quad \text{and} \quad f_\lambda = \left.\frac{\partial f}{\partial \lambda}\right|_{(\Gamma_0,\lambda_0)}. \tag{7.3.6}$$

We now substitute the expanded quantities (7.3.1)–(7.3.4), into the momentum equation (7.2.2), the boundary conditions (7.2.3), the volume flux (7.2.4), and the structure evolution equation (7.2.5).

The momentum equation (7.2.2) becomes

$$\frac{1}{r}\frac{\partial}{\partial r}\left(r\eta_0 \frac{\partial w_0}{\partial r}\right) = -G(t), \tag{7.3.7}$$

$$\frac{1}{r}\frac{\partial}{\partial r}\left(r\eta_0 \frac{\partial w_1}{\partial r} + r\left(2\eta_\Gamma \frac{\partial w_0}{\partial r}\frac{\partial w_1}{\partial r} + \eta_\lambda \lambda_1\right)\frac{\partial w_0}{\partial r}\right) = 0, \tag{7.3.8}$$

at leading order and first order, respectively. The boundary conditions (7.2.3) become

$$w_0 = 0 \quad \text{at} \quad r = 1 \quad \text{and} \quad \eta_0 \frac{\partial w_0}{\partial r} = 0 \quad \text{at} \quad r = 0, \tag{7.3.9}$$

$$w_1 = 0 \quad \text{at} \quad r = 1 \quad \text{and} \quad \eta_0 \frac{\partial w_1}{\partial r} + \left(2\eta_\Gamma \frac{\partial w_0}{\partial r}\frac{\partial w_1}{\partial r} + \eta_\lambda \lambda_1\right)\frac{\partial w_0}{\partial r} = 0 \quad \text{at} \quad r = 0, \tag{7.3.10}$$

at leading order and first order, respectively.

The volume flux (7.2.4) becomes

$$Q_0(t) = 2\pi \int_0^1 r w_0(r,t)\,\mathrm{d}r, \quad \text{and} \quad Q_1(t) = 2\pi \int_0^1 r w_1(r,t)\,\mathrm{d}r, \tag{7.3.11}$$

at leading order and first order, respectively.

After expansion, the structure evolution equation (7.2.5) becomes

$$\mathcal{D}_\mathrm{t}\left(\frac{\partial \lambda_0}{\partial t} + \mathcal{D}_\mathrm{t}\frac{\partial \lambda_1}{\partial t} + \mathcal{O}(\mathcal{D}_\mathrm{t}^2)\right) = f_0 + \mathcal{D}_\mathrm{t}\left(2f_\Gamma \frac{\partial w_0}{\partial r}\frac{\partial w_1}{\partial r} + f_\lambda \lambda_1\right) + \mathcal{O}(\mathcal{D}_\mathrm{t}^2). \tag{7.3.12}$$

In the quickly adjusting regime $0 < \mathcal{D}_\mathrm{t} \ll 1$, so the structure evolution equation (7.2.5) is

$$f_0 = 0, \tag{7.3.13}$$

$$2f_\Gamma \frac{\partial w_0}{\partial r}\frac{\partial w_1}{\partial r} + f_\lambda \lambda_1 = \frac{\partial \lambda_0}{\partial t}, \tag{7.3.14}$$

at leading order and first order, respectively.

7.4 Solutions in the quickly adjusting regime

In this section, we consider the quickly adjusting regime, in which the temporal Deborah number is small, i.e. $0 < \mathcal{D}_\mathrm{t} \ll 1$, so the structure response timescale is much smaller than the typical timescale of the pressure gradient. When we consider the specific case of a sinusoidally oscillating pressure gradient, the typical timescale is the period of the oscillation. The leading-order governing equations in the quickly adjusting regime are the momentum equation (7.3.7) and the structure evolution equation (7.3.13):

$$\frac{1}{r}\frac{\partial}{\partial r}\left(r\eta_0 \frac{\partial w_0}{\partial r}\right) = -G(t) \tag{7.4.1}$$

$$f_0 = 0, \tag{7.4.2}$$

subject to the boundary conditions (7.3.9):

$$w_0 = 0 \quad \text{at} \quad r = 1 \quad \text{and} \quad \eta_0 \frac{\partial w_0}{\partial r} = 0 \quad \text{at} \quad r = 0. \tag{7.4.3}$$

The first-order governing equations in the quickly adjusting regime are the momentum equation (7.3.8) and the structure evolution equation (7.3.14):

$$\frac{1}{r}\frac{\partial}{\partial r}\left(r\eta_0 \frac{\partial w_1}{\partial r} + r\left(2\eta_\Gamma \frac{\partial w_0}{\partial r}\frac{\partial w_1}{\partial r} + \eta_\lambda \lambda_1\right)\frac{\partial w_0}{\partial r}\right) = 0 \tag{7.4.4}$$

$$2f_\Gamma \frac{\partial w_0}{\partial r}\frac{\partial w_1}{\partial r} + f_\lambda \lambda_1 = \frac{\partial \lambda_0}{\partial t}, \tag{7.4.5}$$

subject to the boundary conditions (7.3.10):

$$w_1 = 0 \quad \text{at} \quad r = 1 \quad \text{and} \quad \eta_0 \frac{\partial w_1}{\partial r} + \left(2\eta_\Gamma \frac{\partial w_0}{\partial r}\frac{\partial w_1}{\partial r} + \eta_\lambda \lambda_1\right)\frac{\partial w_0}{\partial r} = 0 \quad \text{at} \quad r = 0. \tag{7.4.6}$$

We may now solve the governing equations to obtain general leading-order and first-order solutions for the velocity and structure parameter. We solve the leading-order equations in Section 7.4.1 and the first-order equations in Section 7.4.2.

7.4.1 General solutions at $\mathcal{O}(1)$

In this section, we solve the leading-order governing equations (7.4.1) and (7.4.2) subject to the no-slip and symmetry conditions (7.4.3) for general $\eta(\dot{\gamma}, \lambda)$ and $f(\dot{\gamma}, \lambda)$ to obtain asymptotic solutions in terms of integrals. We follow the method presented in Section 3.2, except that here we prescribe the pressure gradient $G(t)$, rather than the volume flux $Q(t)$. A result of prescribing the pressure gradient is that the perturbation to the volume flux, $Q_1(t)$, will not be zero in general. We can solve the leading-order governing equations to obtain general solutions for the leading-order velocity $w_0(r,t)$, the leading-order structure parameter $\lambda_0(r,t)$, and the leading-order flux $Q_0(t)$.

We begin by defining a variable q equal to the leading-order shear rate, so at

equilibrium ($f(\Gamma, \lambda) = 0$) we may write the stress τ as

$$\tau(q) = \eta(q^2, \lambda)q, \quad \text{subject to} \quad f(q^2, \lambda) = 0, \quad \text{where} \quad q = \frac{\partial w_0}{\partial r}. \tag{7.4.7}$$

We rewrite the leading-order momentum equation (7.4.1) using (7.4.7), which yields

$$\frac{1}{r}\frac{\partial}{\partial r}\left[r\tau(q)\right] = -G(t). \tag{7.4.8}$$

Rearranging and integrating (7.4.8) with respect to r, and applying the symmetry condition at $r = 0$ (7.4.3), yields

$$\tau(q) = -\frac{G(t)r}{2} \quad \text{or} \quad q = \tau^{-1}\left(-\frac{G(t)r}{2}\right), \tag{7.4.9}$$

where we have . We note that for (7.4.9) to hold, $\tau(q)$ must be invertible. To obtain the general solution for w_0, we integrate the second of (7.4.9) with respect to r, to find

$$w_0(r,t) = -\int_r^1 \tau^{-1}\left(-\frac{G(t)r'}{2}\right)\,\mathrm{d}r'. \tag{7.4.10}$$

Using the substitution $\xi = -G(t)r'/2$, so $\mathrm{d}r' = -(2/G(t))\mathrm{d}\xi$, we obtain

$$w_0(r,t) = \frac{2}{G(t)}\int_{-G(t)r/2}^{-G(t)/2} \tau^{-1}(\xi)\,\mathrm{d}\xi. \tag{7.4.11}$$

We are able to obtain a general solution for λ_0, which is defined implicitly by

$$f(q^2(r,t), \lambda_0(r,t)) = 0. \tag{7.4.12}$$

We also require $\partial\lambda_0/\partial t$ to solve the general solutions at first order (presented in Section 7.4). We find this derivative by implicitly differentiating (7.4.12) with respect to t, which yields

$$\frac{\partial f}{\partial t} = 2qf_\Gamma(q^2, \lambda_0)\frac{\partial q}{\partial t} + f_\lambda(q^2, \lambda_0)\frac{\partial \lambda_0}{\partial t} = 0. \tag{7.4.13}$$

By rearranging (7.4.13) we obtain

$$\frac{\partial \lambda_0}{\partial t} = -\frac{2q f_\Gamma(q^2, \lambda_0)}{f_\lambda(q^2, \lambda_0)} \frac{\partial q}{\partial t}. \tag{7.4.14}$$

Using the first of (7.4.9), we find the derivative of q with respect to t:

$$\frac{\partial q}{\partial t} = -\frac{G'(t) r}{2\tau'(q)}. \tag{7.4.15}$$

We have now obtained general solutions for w_0 and λ_0, and the required derivatives. After we select a rheological model and define f and η, we use the computer algebra package Maple to evaluate the integral in (7.4.11) using quadrature.

7.4.2 General solutions at $\mathcal{O}(\mathcal{D}_\mathbf{t})$

In this section, we solve the first-order governing equations (7.4.4) and (7.4.5) subject to the no-slip and symmetry conditions (7.4.6) for general $\eta(\dot{\gamma}, \lambda)$ and $f(\dot{\gamma}, \lambda)$ to obtain asymptotic solutions in terms of integrals.

We begin by rearranging (7.4.5) for λ_1, which yields

$$\lambda_1 = \frac{1}{f_\lambda} \left(\frac{\partial \lambda_0}{\partial t} - 2 f_\Gamma \frac{\partial w_0}{\partial r} \frac{\partial w_1}{\partial r} \right). \tag{7.4.16}$$

By replacing λ_1 in (7.4.4) using (7.4.16), we obtain

$$\frac{1}{r} \frac{\partial}{\partial r} \left[r A(r,t) \frac{\partial w_1}{\partial r} + r B(r,t) \right] = 0, \tag{7.4.17}$$

where

$$A(r,t) = \eta_0 + 2 \left(\eta_\Gamma - f_\Gamma \frac{\eta_\lambda}{f_\lambda} \right) \left(\frac{\partial w_0}{\partial r} \right)^2, \tag{7.4.18}$$

$$B(r,t) = \frac{\eta_\lambda}{f_\lambda} \frac{\partial \lambda_0}{\partial t} \frac{\partial w_0}{\partial r}. \tag{7.4.19}$$

By rearranging and integrating (7.4.17) with respect to r, we obtain

$$A(r,t)\frac{\partial w_1}{\partial r} + B(r,t) = \frac{C}{r}. \tag{7.4.20}$$

By using the symmetry condition at the centreline in (7.4.6) and rearranging, we obtain

$$\frac{\partial w_1}{\partial r} = -\frac{B(r,t)}{A(r,t)}. \tag{7.4.21}$$

By integrating (7.4.21) with respect to r, we obtain the general solution for the streamwise velocity perturbation:

$$w_1(r,t) = \int_r^1 \frac{B(r',t)}{A(r',t)}\,\mathrm{d}r'. \tag{7.4.22}$$

Using (7.4.16), the general solution for the structure parameter perturbation is

$$\lambda_1(r,t) = \frac{1}{f_\lambda}\left(\frac{\partial \lambda_0}{\partial t} + 2f_\Gamma \frac{\partial w_0}{\partial r}\frac{B(r,t)}{A(r,t)}\right). \tag{7.4.23}$$

Finally, using (7.3.11), we can obtain the solution for the volume flux perturbation:

$$Q_1(t) = 2\pi \int_0^1 r \int_r^1 \frac{B(r',t)}{A(r',t)}\,\mathrm{d}r'\,\mathrm{d}r. \tag{7.4.24}$$

Having obtained the general solutions at leading order and first order, we now consider the purely viscous MMW model in Section 7.5.

7.5 Quickly adjusting regime: results for the MMW model

We consider purely viscous fluids described by the MMW model, discussed in detail in Section 2.5.1. We present the MMW model again here for reference. The constitutive relation is

$$\hat{\eta} = \hat{\mu}_0 \lambda, \tag{7.5.1}$$

and the structure evolution rate is

$$\hat{f}(\hat{\Gamma}, \lambda) = -\hat{k}_1 \hat{\Gamma}^{a/2} \lambda^b + \hat{k}_2 \hat{\Gamma}^{c/2} (1-\lambda)^d, \tag{7.5.2}$$

where the parameters a, b, c, and d are non-negative.

We non-dimensionalise the constitutive relation (7.5.1) and the structure evolution rate (7.5.2) using the quantities defined in (7.2.1) and

$$\hat{f}_0 = \hat{k}_1 \left(\frac{\hat{G}_0 \hat{R}}{\hat{\mu}_0} \right)^a \quad \text{and} \quad \kappa = \frac{\hat{k}_2}{\hat{k}_1} \left(\frac{\hat{G}_0 \hat{R}}{\hat{\mu}_0} \right)^{c-a}, \tag{7.5.3}$$

to obtain

$$\eta = \lambda, \tag{7.5.4}$$

and

$$f(\Gamma, \lambda) = -\Gamma^{a/2} \lambda^b + \kappa \Gamma^{c/2} (1-\lambda)^d. \tag{7.5.5}$$

At equilibrium, when $\lambda = \lambda_{\text{eq}}$, the structure evolution rate is zero, i.e. $f(\Gamma, \lambda_{\text{eq}}) = 0$, so from (7.5.5) we obtain

$$\frac{\lambda_{\text{eq}}^b}{(1-\lambda_{\text{eq}})^d} = \kappa \Gamma^{(c-a)/2}. \tag{7.5.6}$$

We are not able to isolate λ_{eq} in (7.5.6) for general a, b, c, and d. However, in the special case of $d = 0$ (7.5.6) yields

$$\eta = \lambda_{\text{eq}} = \kappa^{1/b} \Gamma^{(n-1)/2}, \quad \text{where} \quad n = \frac{c-a}{b} + 1. \tag{7.5.7}$$

So at equilibrium, the constitutive relation (7.5.7) is that of a power-law fluid at leading order, where n is the familiar power-law exponent (for which we require $n > 0$ for physical behaviour) and $\kappa^{1/b}$ is a dimensionless consistency parameter. We study both the simplified MMW model (sMMW, with $d = 0$) and the full MMW model. We are able to obtain explicit solutions for the leading-order and first-order quantities for the sMMW model, which we present in the following section.

7.5.1 Leading-order solutions for the sMMW model

In this section, we obtain solutions for the leading-order quantities w_0, λ_0, and Q_0. Recalling that $\Gamma = (\partial w_0/\partial r)^2$ and using (7.5.7), at leading order we obtain

$$\eta_0 = \lambda_0 = \kappa^{1/b} \left| \frac{\partial w_0}{\partial r} \right|^{n-1}. \tag{7.5.8}$$

By rearranging and integrating the leading-order momentum equation (7.4.1) with respect to r, and applying the symmetry condition at the centreline (7.4.3) we obtain

$$\eta_0 \frac{\partial w_0}{\partial r} = -\frac{1}{2} G(t) r. \tag{7.5.9}$$

Substituting (7.5.8) into (7.5.9) yields

$$\left| \frac{\partial w_0}{\partial r} \right|^{n-1} \frac{\partial w_0}{\partial r} = -\frac{1}{2} \kappa^{-1/b} G(t) r. \tag{7.5.10}$$

Given that $\kappa, r \geq 0$, we may write

$$\left| \frac{\partial w_0}{\partial r} \right|^{n} = \frac{1}{2} \kappa^{-1/b} |G(t)| r, \tag{7.5.11}$$

which yields

$$\left| \frac{\partial w_0}{\partial r} \right| = \left(\frac{1}{2} \kappa^{-1/b} |G(t)| r \right)^{1/n}. \tag{7.5.12}$$

When the pressure gradient $G(t) > 0$, the velocity is positive and largest at the centreline and zero at the wall, and when $G(t) < 0$, the velocity is negative and largest at the centreline and zero at the wall. In addition, the velocity will be monotonically increasing or decreasing in the radial direction, so $\mathrm{sgn}(\partial w_0/\partial r) = -\mathrm{sgn}(G(t))$. So from (7.5.12) we may write

$$\frac{\partial w_0}{\partial r} = -\kappa^{-1/(bn)} \left(\frac{1}{2} |G(t)| r \right)^{1/n} \frac{G(t)}{|G(t)|}. \tag{7.5.13}$$

By rearranging and integrating (7.5.13) with respect to r we obtain the solution for w_0:

$$w_0(r,t) = \kappa^{-1/(bn)} \frac{n}{n+1} \left(\frac{1}{2}|G(t)|\right)^{1/n} \frac{G(t)}{|G(t)|} \left(1 - r^{(n+1)/n}\right), \tag{7.5.14}$$

using the no-slip boundary condition (7.4.3).

We obtain the solution for the leading-order structure λ_0 using (7.5.8) and (7.5.12):

$$\lambda_0(r,t) = \kappa^{1/(bn)} \left(\frac{1}{2}|G(t)|\right)^{(n-1)/n} r^{(n-1)/n}. \tag{7.5.15}$$

Finally, we obtain the leading-order volume flux using (7.3.11) and (7.5.14):

$$Q_0(t) = \kappa^{-1/(bn)} \frac{n\pi}{3n+1} \left(\frac{1}{2}|G(t)|\right)^{1/n} \frac{G(t)}{|G(t)|}. \tag{7.5.16}$$

7.5.2 First-order solutions for the sMMW model

In this section, we obtain solutions for the first-order quantities w_1, λ_1, and Q_1. To find $A(r,t)$ and $B(r,t)$, given by (7.4.18) and (7.4.19), respectively, we require

$$\eta_\Gamma = 0, \qquad f_\Gamma = -\frac{a}{2}\Gamma_0^{a/2-1}\lambda_0^b + \frac{c}{2}\kappa\Gamma_0^{c/2-1}, \tag{7.5.17}$$

$$\eta_\lambda = 1, \qquad f_\lambda = -b\Gamma_0^{a/2}\lambda_0^{b-1}, \tag{7.5.18}$$

where f is given by (7.5.5) with $d = 0$. So $A(r,t)$ and $B(r,t)$ are

$$A(r,t) = n\kappa^{1/(bn)} \left(\frac{1}{2}|G|r\right)^{(n-1)/n} = n\lambda_0, \tag{7.5.19}$$

$$B(r,t) = \kappa^{(a-b+1)/(bn)} \frac{n-1}{bn} \frac{G'}{|G|} \left(\frac{1}{2}|G|r\right)^{(2n-c-1)/n}. \tag{7.5.20}$$

Using the general solution for w_1, given by (7.4.22), with (7.5.19) and (7.5.20), we obtain

$$w_1(r,t) = \kappa^{(a-b)/(bn)} \frac{n-1}{bn^2} \frac{G'}{|G|} \left(\frac{1}{2}|G|\right)^{(n-c)/n} \int_r^1 r'^{(n-c)/n} \, \mathrm{d}r', \tag{7.5.21}$$

from which we obtain the solution for w_1:

$$w_1(r,t) = \kappa^{(a-b)/(bn)} \frac{n-1}{bn(2n-c)} \frac{G'}{|G|} \left(\frac{1}{2}|G|\right)^{(n-c)/n} \left(1 - r^{(2n-c)/n}\right). \tag{7.5.22}$$

We can now obtain the solution for the structure parameter perturbation λ_1 using (7.4.23):

$$\lambda_1(r,t) = -\kappa^{(a-b+2)/(bn)} \frac{n-1}{bn^2} \frac{GG'}{|G|^2} \left(\frac{1}{2}|G|\right)^{(2n-c-2)/n} r^{(2n-c-2)/n}. \tag{7.5.23}$$

Finally, we obtain the first-order volume flux using (7.3.11):

$$Q_1(t) = \kappa^{(a-b)/(bn)} \frac{(n-1)\pi}{bn(4n-c)} \frac{G'}{|G|} \left(\frac{1}{2}|G|\right)^{(n-c)/n}. \tag{7.5.24}$$

Now we have obtained leading-order and first-order solutions for the sMMW model. In the following section we present some illustrative examples of the behaviour of the sMMW model.

7.5.3 Illustrative results

In order to present illustrative examples of the leading-order and first-order behaviour, we consider a sinusoidal pressure gradient of the form $\hat{G}(\hat{t}) = \hat{G}_0 \sin(\hat{\omega}\hat{t})$, which is

$$G(t) = \sin(t) \tag{7.5.25}$$

in dimensionless form. By selecting a sinusoidal pressure gradient, we will be able to analytical solutions in closed form, and hence allow an in-depth analysis of the flow behaviour. We note the solutions for w_0, λ_0, w_1, and λ_1, given by (7.5.14),

(7.5.15), (7.5.22), and (7.5.23), respectively, are composed of the product of a function of t and a function of r. For a given set of parameters (a, b, c), the oscillating pressure gradient only has the effect of scaling w_0, λ_0, w_1, and λ_1.

7.5.3.1 Leading-order behaviour

We present illustrative examples of w_0 and λ_0 for the sMMW model in Figure 7.1, given by (7.5.14) and (7.5.15) respectively, at various times and for various values of n. Each subfigure shows w_0 and λ_0 at $t/(2\pi) = 0.15, 0.2, 0.25$. At these times, $G(t)(= -\partial p/\partial z)$ is positive, so the velocity is positive. (We note that whether or not the flow is accelerating or decelerating does not affect the velocity or structure at leading order.) In Figures 7.1(a) and (b), $n = 0.8$; in Figures 7.1(c) and (d); $n = 1$, and in Figures 7.1(e) and (f), $n = 1.2$. For all of the fluids, the velocity w_0 increases as $G(t)$ increases, as expected. For thixotropic fluids, for example when $n = 0.8$, the structure breaks down as the pressure gradient increases, as shown in Figure 7.1(b). For thixotropic fluids, for example when $n = 1$, the structure is constant across the width of the pipe regardless of the pressure gradient, as shown in Figure 7.1(d). For antithixotropic fluids, for example when $n = 1.2$, the structure builds up as the pressure gradient increases, as shown in Figure 7.1(f).

When the pressure gradient is negative, w_0 will be the opposite of those shown in Figure 7.1, but λ_0, which depends on the magnitude of the shear rate $|\partial w_0/\partial r|$, will be the same as those shown in Figure 7.1.

Figure 7.2 shows examples of the leading-order volume flux Q_0, given by (7.5.16), over one period of the pressure gradient, with $n = 0.4, 0.7, 1, 1.3, 1.6$ increasing following the arrow. For thixotropic fluids, as the pressure gradient begins to increase, the volume flux increases slowly at first because the viscosity is high. As the pressure gradient increases further the structure breaks down and the fluid flows more easily, allowing the volume flux to increase more rapidly. Conversely, the volume flux for antithixotropic fluids increases rapidly at first because the viscosity is low. As the pressure gradient increases, the structure builds up and the fluid flows less easily.

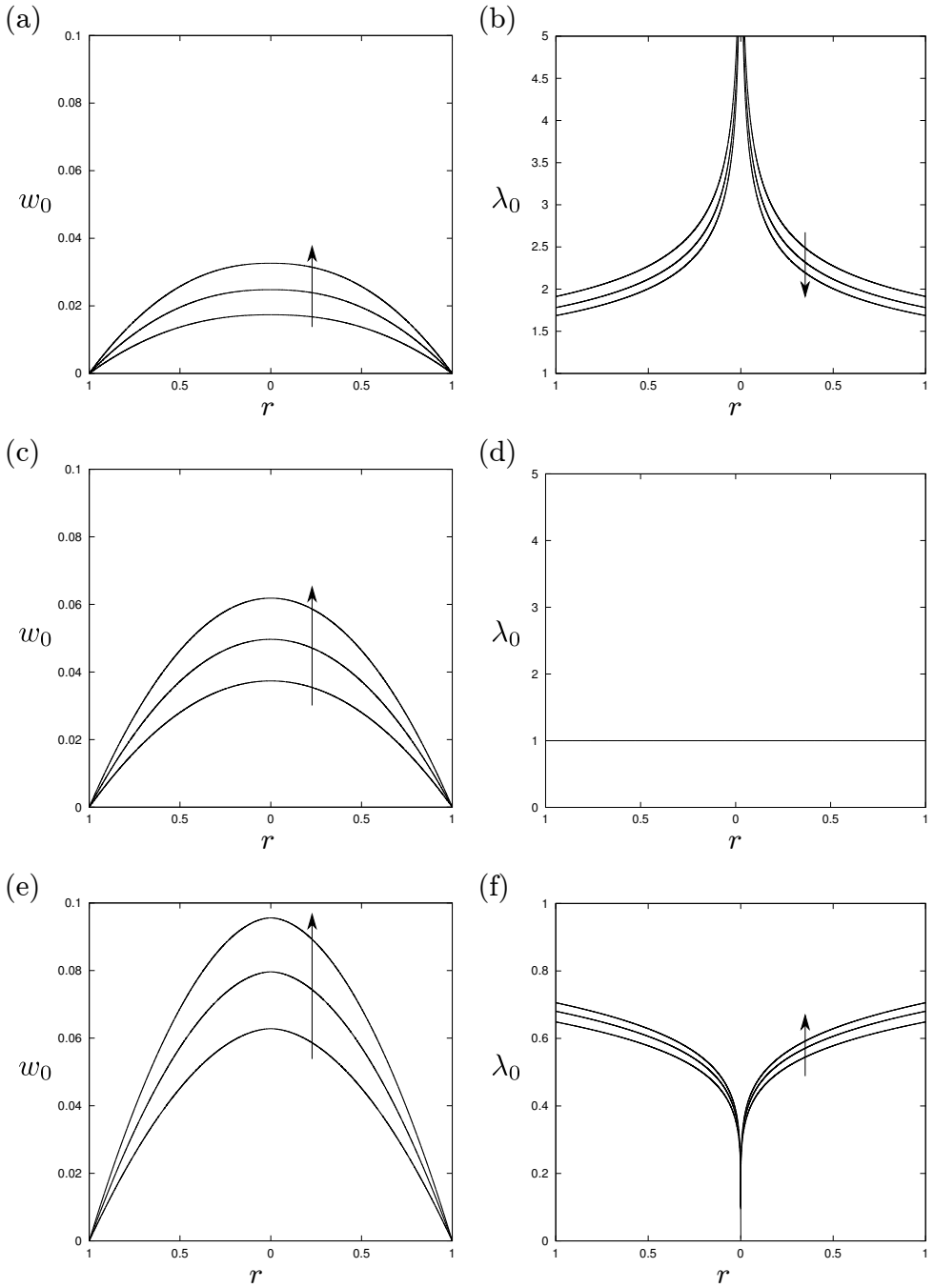

Figure 7.1: Profiles of (a,c,e) w_0 and (b,d,f) λ_0 for (a,b) $n = 0.8$, (c,d) $n = 1$, and (e,f) $n = 1.2$. The parameters in common are $\kappa = 1$ and $b = 1$, at $t/(2\pi) = 0.15, 0.2, 0.25$, for the pressure gradient $G(t) = \sin(t)$. The arrows show the direction of increasing t.

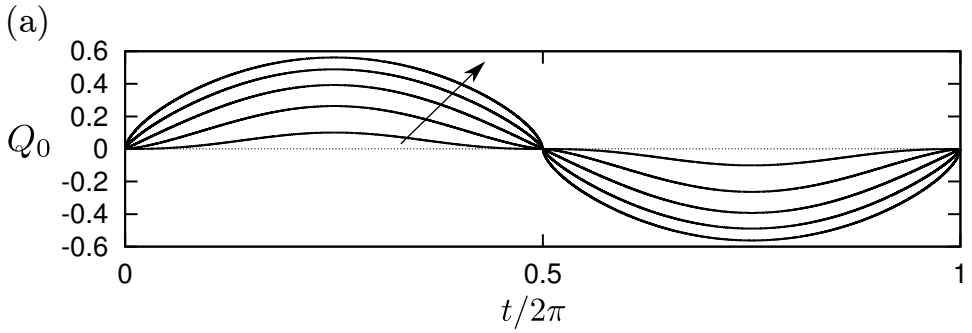

Figure 7.2: Plots of the leading order volume flux Q_0 for $n = 0.4, 0.7, 1, 1.3, 1.6$, for the pressure gradient $G(t) = \sin(t)$. The other parameters are $\kappa = 1$ and $b = 1$. The arrows show the direction of increasing n.

7.5.3.2 First-order behaviour

We present illustrative examples of w_1 and λ_1 for the sMMW model in Figure 7.3, given by (7.5.22) and (7.5.23) respectively, at various times and for various values of n. Each subfigure shows w_1 and λ_1 at $t/(2\pi) = 0.15, 0.2, 0.25, 0.3, 0.35$. We note that when $t/(2\pi) = 0.15, 0.2$ the pressure gradient is increasing, so the flow is accelerating, and when $t/(2\pi) = 0.3, 0.35$ the pressure gradient is decreasing, so the flow is decelerating.

For thixotropic fluids, for example $n = 0.8$ as shown in Figure 7.3(a), w_1 is negative when the flow is accelerating, and is positive when the flow is decelerating. In addition, λ_1, shown in Figure 7.3(b), is positive across the pipe when the flow is accelerating and negative when the flow is decelerating. For antithixotropic fluids, for example $n = 1.2$ as shown in Figure 7.3(c), w_1 is positive when the flow is accelerating, and is negative when the flow is decelerating. In addition, λ_1, shown in Figure 7.3(d), is negative across the pipe when the flow is accelerating and positive when the flow is decelerating. At $t/(2\pi) = 0.25$ in Figure 7.3, the magnitude of the pressure gradient is at its maximum. At these times, the derivative of the pressure gradient $G'(t) = \cos(t) = 0$ and the flow is neither accelerating nor decelerating, so $w_1 = 0$ and $\lambda_1 = 0$.

The behaviour of w_1 and λ_1 shown in Figure 7.3 is what we would expect. For

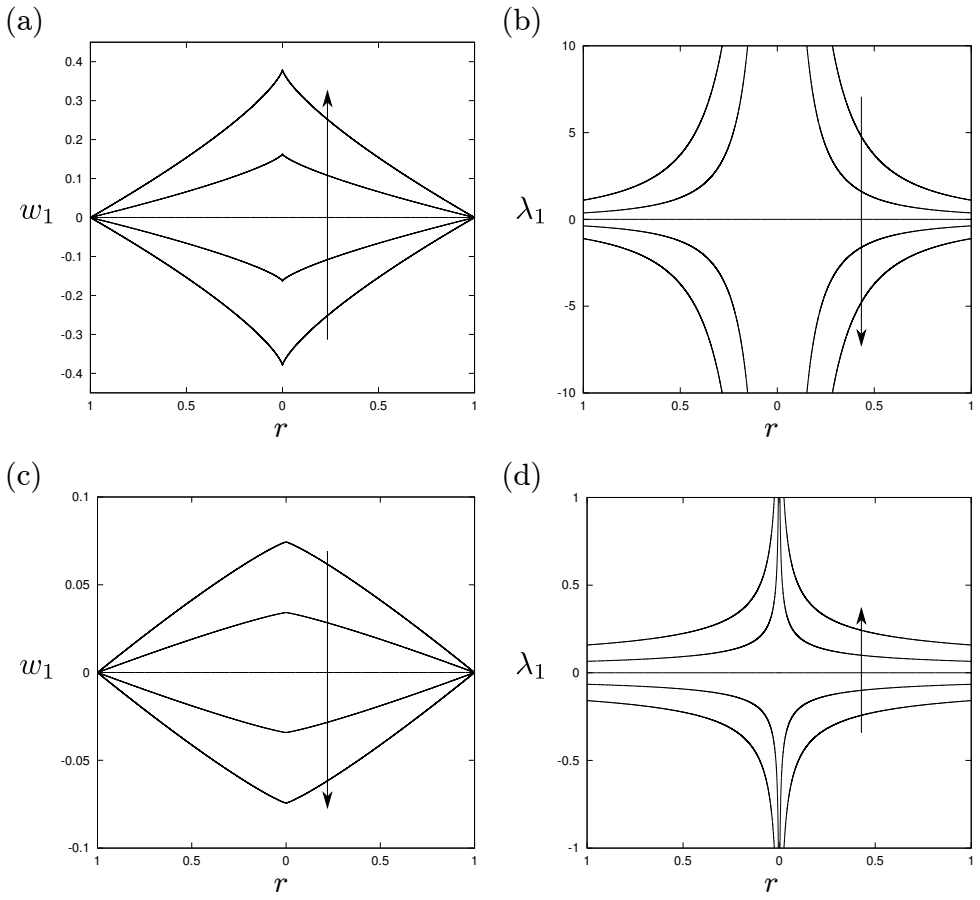

Figure 7.3: Profiles of (a,c) w_1 and (b,d) λ_1 for (a,b) $n = 0.8$ ($a = 1.2$) and (c,d) $n = 1.2$ ($a = 0.8$). The other parameters are $\kappa = 1$, $b = 1$, and $c = 1$, at $t/(2\pi) = 0.15, 0.2, 0.25, 0.3, 0.35$, for the pressure gradient $G(t) = \sin(t)$. The arrows show the direction of increasing t.

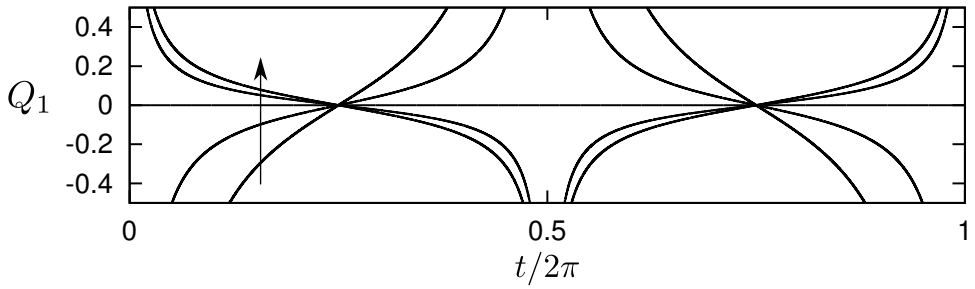

Figure 7.4: Plots of Q_1 for $n = 0.8$ ($a = 1.2$), $n = 0.9$ ($a = 1.1$), $n = 1$ ($a = 1$), $n = 1.1$ ($a = 0.9$), and $n = 1.2$ ($a = 0.8$). The other parameters are $\kappa = 1$, $b = 1$, and $c = 1$, for the pressure gradient $G(t) = \sin(t)$. The arrows show the direction of increasing n.

thixotropic fluids in increasing pressure gradients, the effect of thixotropy is to slow the breakdown of the structure, so the fluid is more structured than it would be in the absence of thixotropy, so λ_1 is positive. A more structured, and hence more viscous, fluid is less readily sheared, so the velocity is negatively perturbed. Conversely for antithixotropic fluids in increasing pressure gradients, the effect of antithixotropy is to slow the build up of structure, so the structure is more broken down, so λ_1 is negative. A less structured fluid is more readily sheared, so the velocity is positively perturbed.

Figure 7.4 shows plots of the volume flux perturbation Q_1, given by (7.5.24), over one period of the pressure-gradient oscillation, for $n = 0.8, 0.9, 1, 1.1, 1.2$. At times of flow reversal, at $t/(2\pi) = 0, 0.5, 1$ in Figure 7.4, the pressure gradient is zero and the volume flux perturbation diverges for both thixotropic and antithixotropic fluids. This divergence indicates that the small-$\mathcal{D}_\mathrm{t}$ asymptotic expansion breaks down when the pressure gradient is small, i.e. when the leading-order shear rate is low. In Figure 7.4, the magnitude of the pressure gradient is at its maximum at $t/(2\pi) = 0.25, 0.75$, and the derivative of the pressure gradient $G'(t) = \cos(t) = 0$, so the flow is neither accelerating nor decelerating, so $Q_1 = 0$.

Figure 7.5 shows an example of the first-order-accurate volume flux $Q_0 + \mathcal{D}_\mathrm{t} Q_1$ (solid line, $\mathcal{D}_\mathrm{t} = 0.05$) and Q_0 (dotted line) over one period of the pressure-

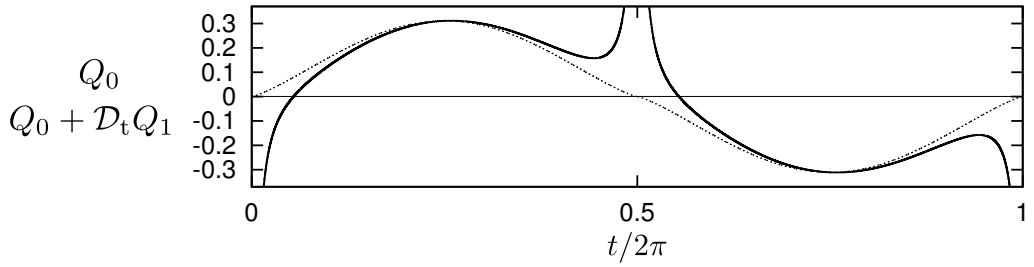

Figure 7.5: Plot of the first-order-accurate volume flux $Q_0 + \mathcal{D}_\mathrm{t} Q_1$ (solid) and Q_0 (dotted) for $n = 0.8$ ($a = 1.2$), for the pressure gradient $G(t) = \sin(t)$. The other parameters are $\mathcal{D}_\mathrm{t} = 0.05$, $\kappa = 1$, $b = 1$, and $c = 1$. Note the breakdown of the perturbation approach when $t = k\pi$ for $k \in \mathbb{Z}$.

gradient oscillation for a thixotropic fluid ($n = 0.8$). In the case of a thixotropic fluid, the effect of thixotropy is to decrease the volume flux when the flow is accelerating and to increase it when the flow is decelerating. Away from times of maximum or minimum pressure gradient ($t/(2\pi) = 0.25, 0.75$), the flux with thixotropy ($Q_0 + \mathcal{D}_\mathrm{t} Q_1$) lags behind the flux without thixotropy (Q_0) and the pressure gradient (G).

7.6 Quickly adjusting regime: results for the Houška model

We also consider fluids with yield-stress behaviour described by the Houška model, discussed in detail in Section 2.5.2. We present the Papanastasiou-regularised Houška model again here for reference. The constitutive relation is

$$\hat{\eta}(\dot{\gamma}, \lambda) = \frac{\hat{\tau}_\mathrm{y}(\lambda)(1 - \mathrm{e}^{-\hat{k}\dot{\gamma}})}{\dot{\gamma}} + \hat{\eta}_\mathrm{H}(\lambda), \tag{7.6.1}$$

where $\dot{\gamma}$ is the shear rate, $\hat{\eta}$ is the effective viscosity, and the yield stress $\hat{\tau}_\mathrm{y}$ and the viscosity parameter $\hat{\eta}_\mathrm{H}$ are linear functions of λ:

$$\hat{\tau}_\mathrm{y}(\lambda) = \hat{\tau}_{\mathrm{y}0} + \lambda \hat{\tau}_{\mathrm{y}1} \quad \text{and} \quad \hat{\eta}_\mathrm{H}(\lambda) = \hat{\eta}_{\mathrm{H}0} + \lambda \hat{\eta}_{\mathrm{H}1}, \tag{7.6.2}$$

where $\lambda \in [0,1]$. The form of $\hat{f}(\hat{\Gamma},\lambda)$ is that of the MMW model with $b=1$, $c=0$, and $d=1$:

$$\hat{f}(\hat{\Gamma},\lambda) = -\hat{k}_1\hat{\Gamma}^{a/2}\lambda + \hat{k}_2(1-\lambda). \tag{7.6.3}$$

We non-dimensionalise (7.6.3) and (7.6.1) using the quantities defined in (7.2.1) and (7.5.3), together with the scale $\hat{\mu}_0 = \hat{\eta}_{\mathrm{H0}}$ and

$$\eta_{\mathrm{H1}} = \frac{\hat{\eta}_{\mathrm{H1}}}{\hat{\eta}_{\mathrm{H0}}}, \quad k = \frac{\hat{k}\hat{G}_0\hat{R}}{\hat{\eta}_{\mathrm{H0}}}, \quad \tau_{\mathrm{y0}} = \frac{\hat{\tau}_{\mathrm{y0}}}{\hat{G}_0\hat{R}}, \quad \text{and} \quad \tau_{\mathrm{y1}} = \frac{\hat{\tau}_{\mathrm{y1}}}{\hat{G}_0\hat{R}}, \tag{7.6.4}$$

which yields

$$f(\Gamma,\lambda) = -\Gamma^{a/2}\lambda + \kappa(1-\lambda), \tag{7.6.5}$$

and

$$\eta(\dot{\gamma},\lambda) = \frac{(\tau_{\mathrm{y0}} + \lambda\tau_{\mathrm{y1}})(1-\mathrm{e}^{-k\dot{\gamma}})}{\dot{\gamma}} + 1 + \lambda\eta_{\mathrm{H1}}, \tag{7.6.6}$$

respectively.

7.6.1 Illustrative results

In this section, we present illustrative examples of the leading-order behaviour for the Houška model. To obtain these solutions, we evaluate the general solutions obtained in Sections 7.4.1 and 7.4.2, evaluating the integrals using quadrature in the computer algebra package Maple.

As we are using a regularised Houška model, we cannot observe true yield-stress behaviour, as in the case of the unregularised model. As before, we refer to aspects of this 'regularised yield-stress' behaviour as follows. When the stress in the fluid is above and below the yield stress τ_{y}, we say it is 'yielded' and 'unyielded', respectively. For plug-like flow, in which the fluid is unyielded near the centre of the pipe and yielded near the wall, we refer to the unyielded region as a 'pseudo-plug', which is bounded by a 'yield surface'. We use this terminology throughout this section.

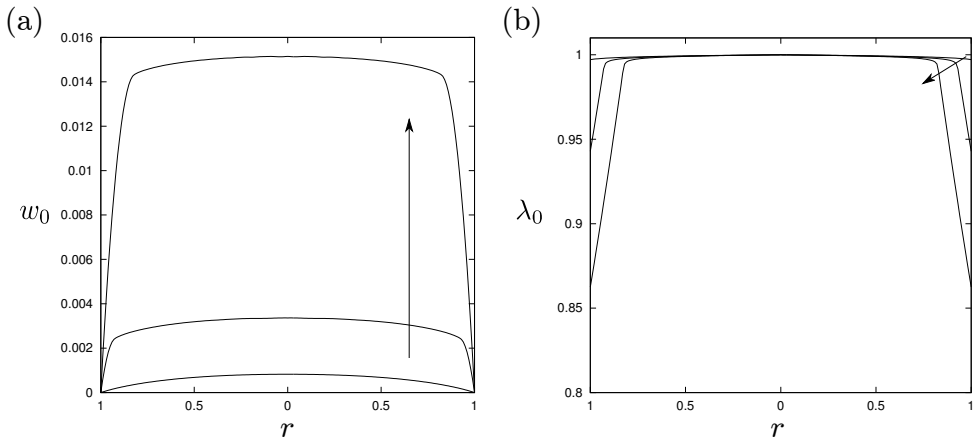

Figure 7.6: Profiles of (a) w_0, (b) λ_0 at $t/(2\pi) = 0.06, 0.07, 0.08$. The parameters are $\kappa = 1$, $\tau_{y0} = 1$, $\tau_{y1} = 0.2$, $\eta_0 = 1$, and $\eta_1 = 1$. The arrows show the direction of increasing t.

7.6.1.1 Leading-order solutions

At low shear rates, the fluid is in an unyielded state in which it is highly structured across the width of the pipe. As the pressure gradient increases the shear rate increases, and the fluid near the wall, where the shear rate is largest, eventually yields. Following yielding, the velocity increases rapidly, further destructuring the fluid near the wall, and reducing the width of the pseudo-plug. Figures 7.6(a) and (b) show w_0 and λ_0, respectively, just before and just after yielding, with the arrow indicating the direction of increasing t (and increasing pressure gradient). We note that in a true yield-stress fluid prior to yielding $w_0 = 0$ and $\lambda_0 = 1$; in the present case, an effect of regularisation is that w_0 and λ_0 deviate from true yield-stress behaviour when the fluid is unyielded. As the pressure gradient increases, λ_0 decreases near the wall, as shown in Figure 7.6(b), which decreases the width of the pseudo-plug and allows w_0 to increase, as shown in Figure 7.6(a).

Figure 7.7 shows the leading-order volume flux Q_0 over one period of the pressure gradient, illustrating clearly the process of yielding and unyielding. When the pressure gradient is sufficiently small, the fluid does not yield anywhere, as shown by the flat sections in Figure 7.7.

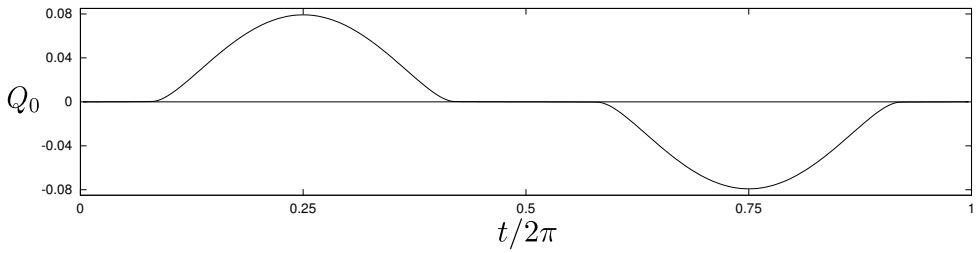

Figure 7.7: Plot of Q_0 over one period of the pressure-gradient oscillation. The parameters are $\kappa = 1$, $\tau_{y0} = 1$, $\tau_{y1} = 0.2$, $\eta_0 = 1$, and $\eta_1 = 1$.

7.6.1.2 First-order solutions

Figures 7.8(a) and (b) show w_1 and λ_1, respectively, just before and just after yielding, with the arrow indicating the direction of increasing t (and increasing pressure gradient). When the fluid is unyielded, the velocity and structure perturbations are zero. After yielding, the velocity perturbation grows in magnitude as the pressure gradient increases and the structure perturbation increases near the wall where the fluid is yielded. The effect of thixotropy is to slow the breakdown of fluid under shearing, so the structure remains more built up and so the structure perturbation is positive. The increase in structure means that the fluid is less readily sheared than in the absence of thixotropy, so the velocity is negatively perturbed.

Figure 7.9 shows the volume flux perturbation over one period of the pressure gradient. As for Q_0, $Q_1 = 0$ when the fluid is unyielded. In addition, $Q_1 = 0$ at $t/2\pi = 0.25, 0.75$, when the magnitude of the pressure gradient is largest. As the pressure gradient increases, the fluid yields at $t/2\pi \approx 0.1$ and Q_1 decreases to a minimum at $t/(2\pi) \approx 0.15$, then increases. When the time-derivative of the pressure gradient $G'(t) > 0$, $Q_1 > 0$, and when $G'(t) < 0$, $Q_1 < 0$.

Thixotropy has the effect of delaying the peaks in the volume flux. Figure 7.10, which shows $Q_0 + \mathcal{D}_t Q_1$ (solid) and Q_0 (dashed), illustrates this effect clearly. Comparing the leading-order flux with the combination of the leading-order and

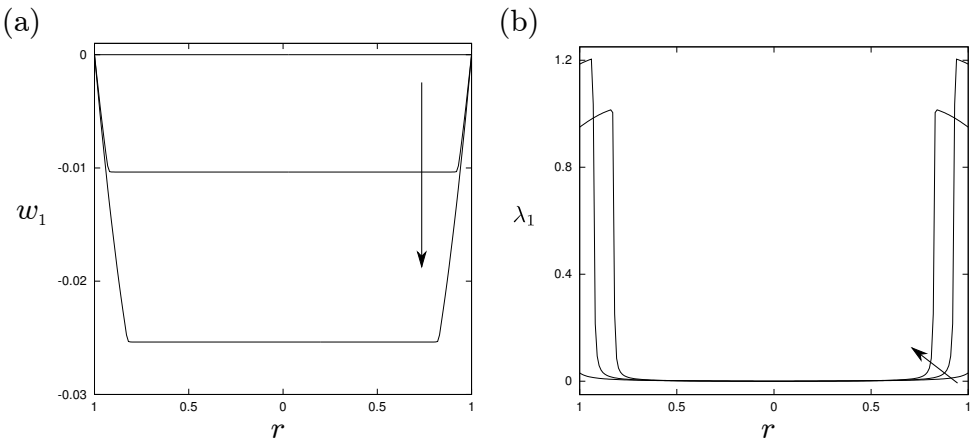

Figure 7.8: Profiles of (a) w_1, (b) λ_1 at $t/(2\pi) = 0.06, 0.07, 0.08$. The parameters are $\mathcal{D}_\mathrm{t} = 1$, $\kappa = 1$, $\tau_{\mathrm{y}0} = 1$, $\tau_{\mathrm{y}1} = 0.2$, $\eta_0 = 1$, and $\eta_1 = 1$. The arrows show the direction of increasing t.

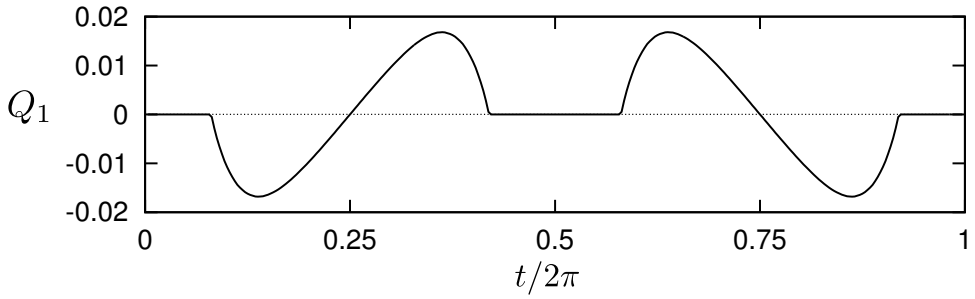

Figure 7.9: Plot of Q_1 when $\mathcal{D}_\mathrm{t} = 1$, $\kappa = 1$, $\tau_{\mathrm{y}0} = 1$, $\tau_{\mathrm{y}1} = 0.2$, $\eta_0 = 1$, and $\eta_1 = 1$.

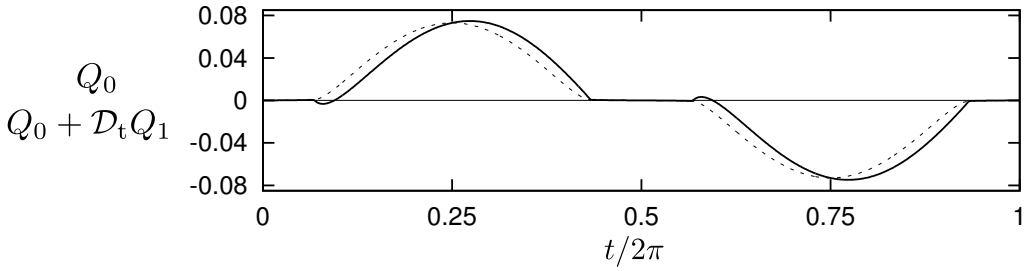

Figure 7.10: Plot of $Q_0 + \mathcal{D}_t Q_1$ (solid) and Q_0 (dashed) when $\mathcal{D}_t = 1$, $\kappa = 1$, $\tau_{y0} = 1$, $\tau_{y1} = 0.2$, $\eta_0 = 1$, and $\eta_1 = 1$.

first-order fluxes shows that thixotropy has the effect of moving the peak of the flux to the right, i.e. to a later time. So when thixotropy is present, the flux lags slightly behind the pressure gradient.

We note that just after yielding at $t/2\pi \approx 0.1$, Figure 7.10 shows Q to be negative, which implies that the fluid flows against the pressure gradient immediately after yielding. This behaviour is not physically meaningful and arises simply because we set $\mathcal{D}_t = 1$ in Figure 7.10 to clearly illustrate the lag in the volume flux. This feature indicates a local-in-time breakdown of the perturbation approach since $Q_0 \sim \mathcal{D}_t Q_1$ when Q_0 is small. When $\mathcal{D}_t$ is made appropriately small, as shown in Figure 7.11, this feature vanishes as expected.

7.7 Expansion and solutions in the slowly adjusting regime: $\mathcal{D}_t \gg 1$

In this section, we study flow in the slowly adjusting regime. It is difficult to make significant progress towards solutions for general rheologies, unlike in the quickly adjusting regime (shown in Section 7.4). We make a small amount of progress before specialising to the sMMW model, for which explicit solutions are available.

In this regime, we expand the velocity, structure parameter, and volume flux in

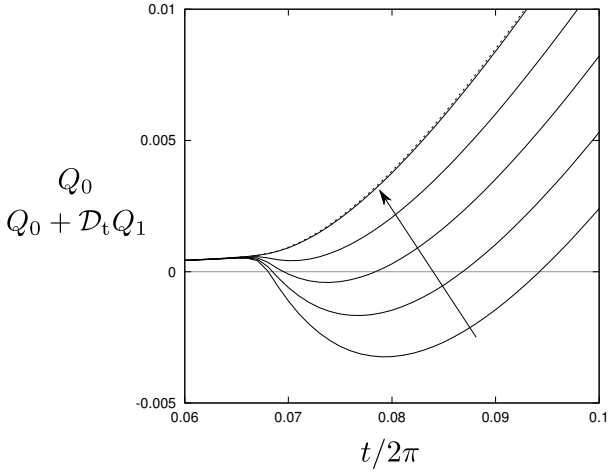

Figure 7.11: Plot of $Q_0 + \mathcal{D}_\mathrm{t} Q_1$ (solid) and Q_0 (dotted) when $\mathcal{D}_\mathrm{t} = 0.01, 0.25, 0.5, 0.75, 1$, and $\kappa = 1$, $\tau_{\mathrm{y}0} = 1$, $\tau_{\mathrm{y}1} = 0.2$, $\eta_0 = 1$, and $\eta_1 = 1$. The arrow shows the direction of decreasing $\mathcal{D}_\mathrm{t}$.

powers of the reciprocal of the large temporal Deborah number $\mathcal{D}_\mathrm{t}$:

$$(w, \lambda, Q) = \sum_{i=0}^{\infty} \frac{1}{\mathcal{D}_\mathrm{t}^i} (w_i, \lambda_i, Q_i). \tag{7.7.1}$$

We note that $G(t)$ is prescribed so we do not expand it.

At leading order and first order, excluding the structure evolution equation, we obtain the same governing equations as in the quickly adjusting regime, given by (7.3.7)–(7.3.11), where we note that the quantities w_0, λ_0, etc. are now from the expansion (7.7.1). In the slowly adjusting regime, after the expansion (7.7.1), the structure evolution equation (7.2.5) becomes

$$\mathcal{D}_\mathrm{t} \left(\frac{\partial \lambda_0}{\partial t} + \frac{1}{\mathcal{D}_\mathrm{t}} \frac{\partial \lambda_1}{\partial t} + \mathcal{O}\left(\frac{1}{\mathcal{D}_\mathrm{t}^2} \right) \right) = f_0 + \frac{1}{\mathcal{D}_\mathrm{t}} f_1 + \mathcal{O}\left(\frac{1}{\mathcal{D}_\mathrm{t}^2} \right), \tag{7.7.2}$$

so at $\mathcal{O}(\mathcal{D}_\mathrm{t})$ and $\mathcal{O}(1)$ we obtain

$$\frac{\partial \lambda_0}{\partial t} = 0 \quad \text{and} \quad \frac{\partial \lambda_1}{\partial t} = f_0, \tag{7.7.3}$$

respectively, where $f_0 = f(\dot{\gamma}_0, \lambda_0)$.

From (7.7.3), we see that λ_0 does not depend on t, so λ depends only on r at leading order: $\lambda \simeq \lambda_0(r) + \text{h.o.t.}$ We expect to obtain this result, because when the structure adjusts much more slowly than the characteristic timescale of the pressure gradient oscillation, the structure must be almost constant in time.

Following McArdle et al. [94], we assume the pressure gradient has been oscillating infinitely long so that the initial state of the fluid has been 'forgotten' and the flow is periodic. While the structure will not be in equilibrium, in general, with the shear rate, there will be no net build-up or breakdown over one period of the oscillation. Integrating the first-order structure evolution equation in (7.7.3) over one period of the pressure gradient yields

$$\int_0^{2\pi} \frac{\partial \lambda_1}{\partial t}\,\mathrm{d}t = \int_0^{2\pi} f_0\,\mathrm{d}t. \tag{7.7.4}$$

Since λ_1 is periodic, we obtain

$$0 = \int_0^{2\pi} f_0\,\mathrm{d}t, \tag{7.7.5}$$

so there is no net build-up or breakdown over one period of the pressure gradient, as expected. In the following section we obtain solutions for the sMMW model by first specialising to the MMW model, then specialising further to the sMMW model.

7.8 Slowly adjusting regime: results for the MMW model

In this section, we make some progress towards solutions for the full MMW model, though to obtain explicit solutions, we must specialise further to the sMMW model, which we present in the following section.

We begin by rearranging and integrating (7.4.1) with respect to r, and applying

the symmetry condition at the centreline to obtain

$$\frac{\partial w_0}{\partial r} = -\frac{r}{2\eta_0}\sin(t), \tag{7.8.1}$$

where we have chosen a sinusoidal pressure gradient $G(t) = \sin(t)$.

Now we use (7.7.5) with the MMW structure evolution rate, which yields

$$0 = \int_0^{2\pi} -\left|\frac{\partial w_0}{\partial r}\right|^a \lambda_0^b + \kappa\left|\frac{\partial w_0}{\partial r}\right|^c (1-\lambda_0)^d \,\mathrm{d}t. \tag{7.8.2}$$

Following some rearrangement, and since λ_0 does not depend on t, we obtain

$$\frac{\lambda_0^b}{(1-\lambda_0)^d} = \frac{\kappa\displaystyle\int_0^{2\pi}\left|\frac{\partial w_0}{\partial r}\right|^c \mathrm{d}t}{\displaystyle\int_0^{2\pi}\left|\frac{\partial w_0}{\partial r}\right|^a \mathrm{d}t}. \tag{7.8.3}$$

Replacing the shear-rate terms in (7.8.3) using (7.8.1), recalling that in the MMW model $\eta_0 = \eta_0(\lambda_0)$, we obtain

$$\frac{\lambda_0^b}{(1-\lambda_0)^d} = \kappa\left(\frac{r}{2\eta_0}\right)^{c-a} \frac{\displaystyle\int_0^{2\pi}|\sin(t)|^c \,\mathrm{d}t}{\displaystyle\int_0^{2\pi}|\sin(t)|^a \,\mathrm{d}t}. \tag{7.8.4}$$

For convenience, we rewrite this as

$$\frac{\lambda_0^b}{(1-\lambda_0)^d} = \kappa\left(\frac{r}{2\eta_0}\right)^{c-a}\beta(a,c), \tag{7.8.5}$$

where

$$\beta(a,c) = \frac{B\left(\frac{1+c}{2},\frac{1}{2}\right)}{B\left(\frac{1+a}{2},\frac{1}{2}\right)}, \tag{7.8.6}$$

and $B(x,y)$ is the Beta function:

$$B(x,y) = 2\int_0^{\frac{\pi}{2}} (\sin(\theta))^{2x-1}(\cos(\theta))^{2y-1}\,\mathrm{d}\theta. \tag{7.8.7}$$

To make further analytical progress, we must be able to solve (7.8.5) for λ_0, which is not possible for general b and d. As discussed in Appendix B, there are various specific choices for b and d that we may use. We choose to specialise to the sMMW model, in which $d = 0$.

7.8.1 Results for the sMMW model

Upon specialising to the sMMW model, where $\eta_0 = \lambda_0$ and $d = 0$, (7.8.5) becomes

$$\lambda_0^b = \kappa \left(\frac{r}{2\lambda_0}\right)^{c-a} \beta(a, c), \tag{7.8.8}$$

which we rearrange to obtain the solution for λ:

$$\lambda_0(r) = \left(\frac{(\kappa\beta)^{1/b}}{2^{n-1}}\right)^{1/n} r^{(n-1)/n}, \tag{7.8.9}$$

where $n = (c - a + b)/b$, and we have written $\beta \equiv \beta(a, c)$ for convenience.

We may now obtain the solution for w_0 using (7.8.1), together with the no-slip boundary condition (7.4.3):

$$w_0(r, t) = \left(\frac{(\kappa\beta)^{-1/b}}{2}\right)^{1/n} \frac{n}{n+1} \sin(t)(1 - r^{(n+1)/n}). \tag{7.8.10}$$

The volume flux is

$$Q_0(t) = 2\pi \int_0^1 r w_0 \, \mathrm{d}r, \tag{7.8.11}$$

so using (7.8.10), we obtain the solution for the volume flux:

$$Q_0(t) = \pi \left(\frac{(\kappa\beta)^{-1/b}}{2}\right)^{1/n} \frac{n}{3n+1} \sin(t). \tag{7.8.12}$$

There are similarities between the solutions in the slowly adjusting regime, given by (7.8.10), (7.8.9), and (7.8.12), and the leading-order solutions in the quickly adjusting regime, given by (7.5.14), (7.5.15), and (7.5.16), respectively (we note that these solutions are also the solutions for the case when $\mathcal{D}_\mathrm{t} = 0$, i.e. with no

thixotropy). In particular, the solutions when $\mathcal{D}_\mathrm{t} \gg 1$ and when $\mathcal{D}_\mathrm{t} = 0$ only differ by a factor $\alpha(t)$:

$$w_{\mathcal{D}_\mathrm{t}\gg 1} = \alpha(t) w_{\mathcal{D}_\mathrm{t}=0}, \quad \lambda_{\mathcal{D}_\mathrm{t}\gg 1} = \frac{1}{\alpha(t)} \lambda_{\mathcal{D}_\mathrm{t}=0}, \quad \text{and} \quad Q_{\mathcal{D}_\mathrm{t}\gg 1} = \alpha(t) Q_{\mathcal{D}_\mathrm{t}=0}, \tag{7.8.13}$$

where

$$\alpha(t) = \left(\frac{|\sin(t)|^{n-1}}{\beta^{1/b}} \right)^{1/n}. \tag{7.8.14}$$

7.9 Numerical solutions using COMSOL

Having obtained asymptotic solutions for the unsteady flow of thixotropic fluid along a uniform cylindrical pipe in Sections 7.1–7.5, 7.7, and 7.8, we now study this problem numerically using the finite element analysis software package COMSOL Multiphysics ® [54]. (Due to time constraints, we were not able to explore the behaviour of the Houška model numerically in this thesis. Asymptotic solutions for the Houška model are presented in Section 7.6.) In particular, we wish to verify the results of the asymptotic approach used for the quickly adjusting regime in Sections 7.4–7.6, and the slowly adjusting regime in Sections 7.7 and 7.8. We also wish to use the asymptotic solutions with COMSOL to extend our understanding of thixotropic pipe flow and build a full picture of thixotropic behaviour, from the quickly adjusting regime, through the regime of balanced thixotropy, to the slowly adjusting regime, i.e. for $\mathcal{D}_\mathrm{t}$ in the range $[0, \infty)$.

We formalise these aims in a similar way to Chapter 6 for the first goal: (i) to verify the solutions presented in Sections 7.1–7.8. Since we have solutions for both the quickly and the slowly adjusting regimes, we tackle a different second goal here: (ii) to use COMSOL to obtain the behaviour when $\mathcal{D}_\mathrm{t} = \mathcal{O}(1)$, and therefore obtain the full range of possible thixotropic behaviours in this problem.

7.9.1 Implementation

In this section, we present the implementation of this problem in COMSOL, which differs from the implementation for the previous set-up in a few ways. The most notable is that we consider a uniform pipe, which means that we may study the flow in COMSOL in a 1D axisymmetric geometry, rather than a 2D axisymmetric geometry. This difference considerably simplifies the numerical problem, which allows for the use of higher-order discretisations and more refined meshes compared to the previous set-up.

We implement the geometry for this problem as a 1D axisymmetric interval, with a radius equal to unity. As we are considering a 1D geometry, there are no inlet or outlet conditions like those in the previous set-up. The governing equations for this problem are the momentum equation (7.2.2) and the structure evolution equation (7.2.5), which are subject to the no-slip boundary condition, and, as we are considering a time-dependent flow, initial conditions.

We rearrange (7.2.2) to obtain

$$\frac{\partial}{\partial r}\left(r\eta\frac{\partial w}{\partial r}\right) = -Gr, \tag{7.9.1}$$

which we implement, as termed in COMSOL, as a general form PDE. We apply the no-slip boundary condition as a Dirichlet boundary condition. We also implement the structure evolution equation (7.2.5) using the same general equation in COMSOL. We note that as in the previous set-up, we do not need to manually adjust the equations for the axisymmetric geometry in the present set-up.

The flow is driven by a sinusoidal pressure gradient $G(t) = \sin(t)$, and for the initial conditions we use the solutions in the slowly adjusting regime, given by (7.8.10) and (7.8.9), which are suitable for both quickly adjusting and slowly adjusting flow. When $\mathcal{D}_\mathrm{t}$ is small, the fluid will quickly adjust from the initial conditions to periodic flow, 'forgetting' the initial conditions in the process. When $\mathcal{D}_\mathrm{t}$ is large, the initial conditions are close to the periodic solutions to which the flow gradually converges.

Following some initial tests for the sMMW model, it is clear that this set-up

is much less computationally expensive than for the set-up in Chapter 6; the running times are roughly 500 times smaller in the former case, for a single value of t, with similar mesh refinements and discretisation orders. This shorter running time means we are able to use a high mesh resolution and discretisation order, which will yield more accurate numerical solutions. In general, for the numerical solutions in this Chapter, we use 10 000 uniformly distributed mesh points, and we discretise the problem using seventh-order polynomials, the highest order available in COMSOL. In a typical simulation of slowly adjusting flow, for 50 periods of the pressure gradient, which is sufficient for periodic flow to be established from the initial conditions. Quickly adjusting flow converges to a periodic solution more quickly than slowly adjusting flow, so running times are shorter.

In Sections 7.9.2 and 7.9.3 we verify the asymptotic solutions in the quickly adjusting and slowly adjusting regimes, respectively. To distinguish the asymptotic solutions in these regimes, we denote the structure parameter λ_{q} or λ_{s} and the volume flux Q_{q} or Q_{s}, respectively. We also denote corresponding numerical solutions λ_{N} and Q_{N}, and when referring to a quantity in general, we use λ and Q. We also indicate whether a solution is leading order or first order where appropriate, e.g. $\lambda_{\mathrm{q},0}$. We continue to use this notation when presenting results for the full range of thixotropic behaviour in Section 7.9.4.

7.9.2 Verification and solutions for the quickly adjusting regime $0 < \mathcal{D}_{\mathbf{t}} \ll 1$

Having implemented the problem in COMSOL, we begin with goal (i): to verify the asymptotic solutions, which will provide support for the asymptotic approach in the quickly adjusting regime. As expected, we are able to obtain significantly more accurate results for the present set-up than for the problem in Chapter 6. For brevity, we focus on numerical solutions for the perturbation quantities. Sufficient accuracy of the leading-order numerical solutions is implied by a high accuracy in the numerical solutions for the perturbations. We use the same notation and terminology as introduced in Section 6.2.2.

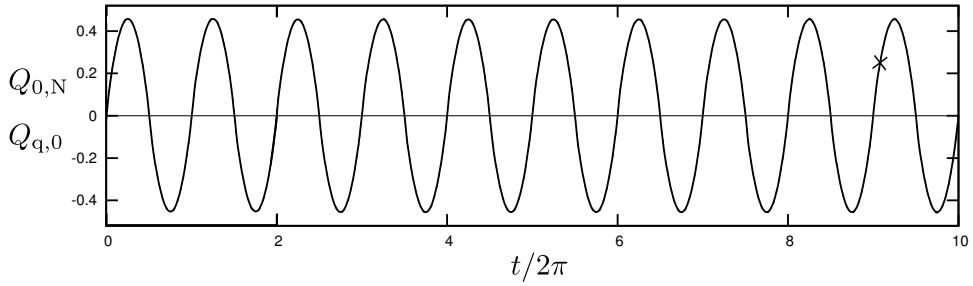

Figure 7.12: Plots of $Q_{0,\mathrm{N}}$ (solid) and $Q_{\mathrm{q},0}$ (dotted, not visible) over 10 periods of the pressure gradient. The parameters are $\mathcal{D}_{\mathrm{t}} = 10^{-3}$, $\kappa = 1$, $a = 1$, $b = 1$, and $c = 1.2$ ($n = 1.2$). The cross indicates the time for which an example of $w_{1,\mathrm{N}}$ and $\lambda_{1,\mathrm{N}}$ is shown later in this section.

In this section, we present illustrative examples of numerical solutions for the perturbation quantities for the sMMW model, showing that they are in good agreement with the asymptotic solutions (presented in Section 7.5.2). Figure 7.12 shows the numerical solution for the leading-order flux $Q_{0,\mathrm{N}}$ (solid), and the corresponding asymptotic solution $Q_{\mathrm{q},0}$ (dotted), which lies on top of the solid line and so is not visible.

Figures 7.13(a) and (c) show numerical solutions for the velocity $w_{1,\mathrm{N}}$ and the structure parameter $\lambda_{1,\mathrm{N}}$ (solid lines), respectively, for an antithixotropic fluid ($n = 1.2$). The plots are taken at the time indicated by the cross in Figure 7.12, where $t/2\pi = 9.125$, $G(t) \approx 0.707$ and $G'(t) \approx 0.707$. These figures also include the corresponding asymptotic solutions $w_{\mathrm{q},1}$ and $\lambda_{\mathrm{q},1}$ (dotted with diamonds). Note that in Figure 7.13(a), $w_{\mathrm{q},1}$ cannot be distinguished from $w_{1,\mathrm{N}}$. In Figure 7.13(c), $\lambda_{\mathrm{q},1}$ is visible at $r \lesssim 0.01$, but not further away from the centreline. Figures 7.13(b) and (d) show the corresponding absolute errors $w_{\mathrm{q},1,\mathrm{err}}$ and $\lambda_{\mathrm{q},1,\mathrm{err}}$, respectively.

Figure 7.14 shows the equivalent plots to those in Figure 7.13 for a thixotropic fluid ($n = 0.9$). In particular, Figures 7.14(a) and (c) show the numerical solutions $w_{1,\mathrm{N}}$ and $\lambda_{1,\mathrm{N}}$ (solid lines), respectively. These figures also include the corresponding asymptotic solutions $w_{\mathrm{q},1}$ and $\lambda_{\mathrm{q},1}$ (dotted with diamonds). Note that in Figure 7.14(c), $\lambda_{\mathrm{q},1}$ cannot be distinguished from $\lambda_{1,\mathrm{N}}$. Figures 7.14(b) and (d) show the corresponding absolute errors $w_{\mathrm{q},1,\mathrm{err}}$ and $\lambda_{\mathrm{q},1,\mathrm{err}}$, respectively.

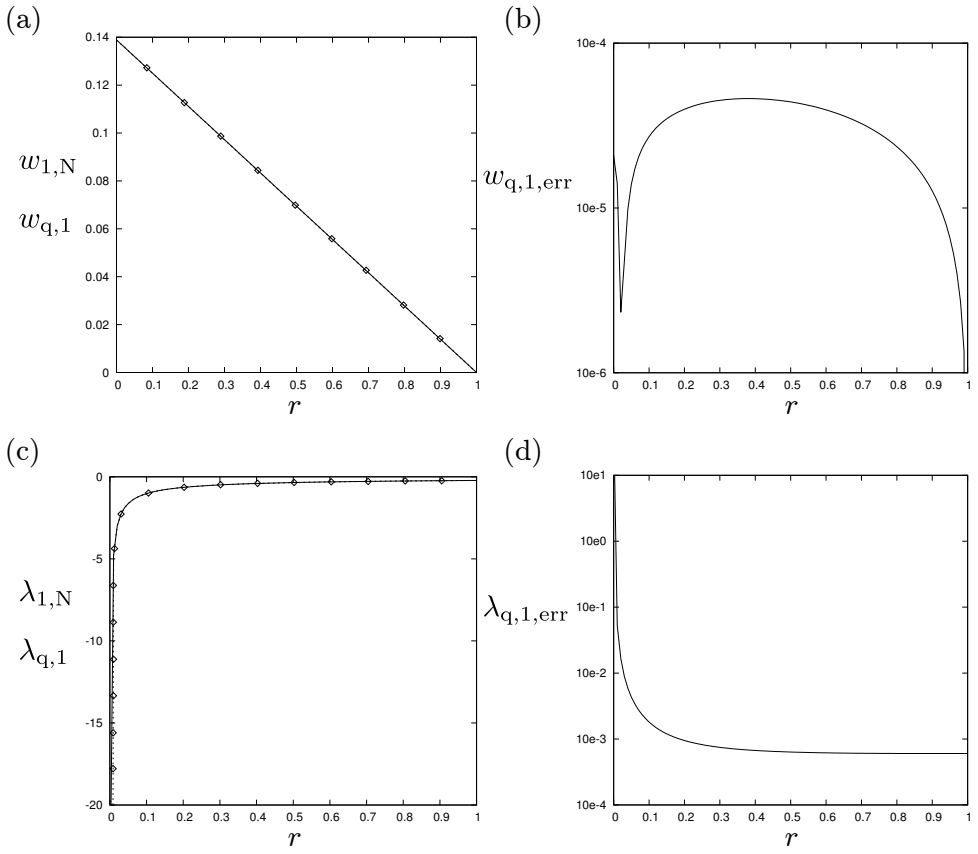

Figure 7.13: Profiles of (a) $w_{1,\mathrm{N}}$ (solid) and $w_{\mathrm{q},1}$ (dotted with diamonds), (b) $w_{\mathrm{q},1,\mathrm{err}}$, (c) $\lambda_{1,\mathrm{N}}$ (solid) and $\lambda_{\mathrm{q},1}$ (dotted with diamonds), and (d) $\lambda_{\mathrm{q},1,\mathrm{err}}$, at $t/2\pi = 9.125$, when $G(t) \approx 0.707$ and $G'(t) \approx 0.707$. The parameters are $\mathcal{D}_{\mathrm{t}} = 10^{-3}$, $\kappa = 1$, $a = 1$, $b = 1$, and $c = 1.2$ ($n = 1.2$).

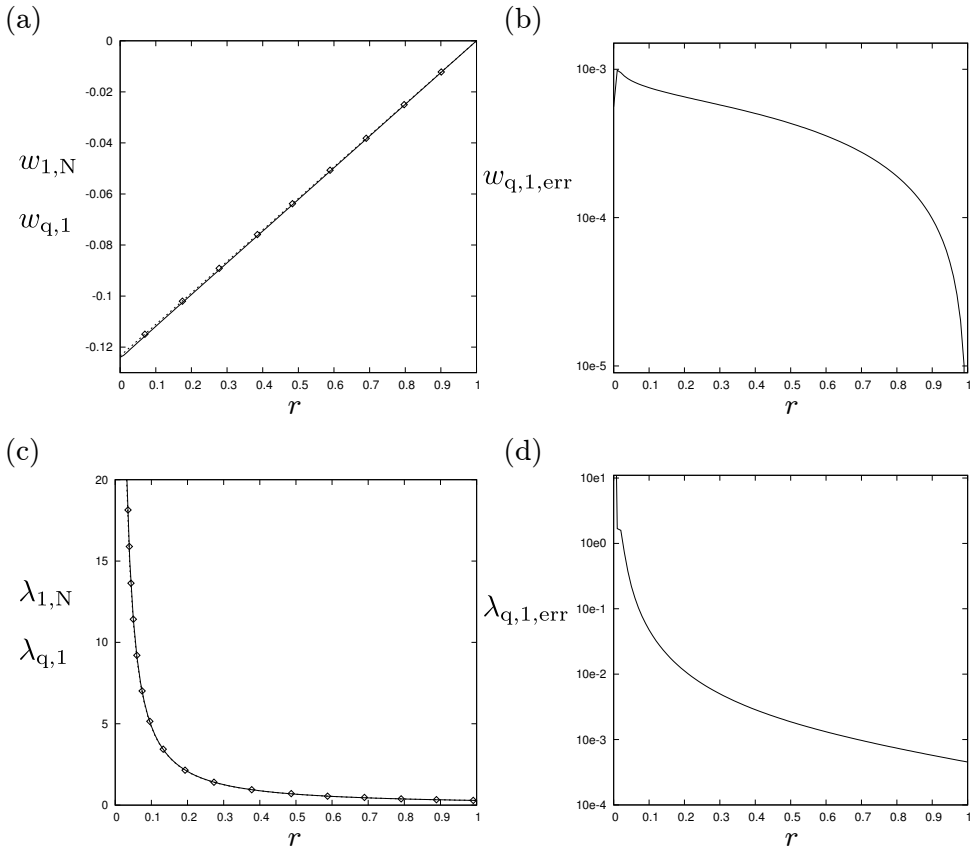

Figure 7.14: Profiles of (a) $w_{1,\mathrm{N}}$ (solid) and $w_{\mathrm{q},1}$ (dotted with diamonds), (b) $w_{\mathrm{q},1,\mathrm{err}}$, (c) $\lambda_{1,\mathrm{N}}$ (solid) and $\lambda_{\mathrm{q},1}$ (dotted with diamonds), and (d) $\lambda_{\mathrm{q},1,\mathrm{err}}$, at $t/2\pi = 9.125$, when $G(t) \approx 0.707$ and $G'(t) \approx 0.707$. The parameters are $\mathcal{D}_{\mathrm{t}} = 10^{-3}$, $\kappa = 1$, $a = 1$, $b = 1$, and $c = 0.9$ ($n = 0.9$).

Figures 7.13(a) and 7.14(a) show that the numerical and asymptotic solutions for the velocity perturbation are in excellent agreement, which is confirmed by the corresponding error plots in Figures 7.13(b) and 7.14(b). In the antithixotropic case $w_{\mathrm{q},1,\mathrm{err}} < 10^{-4}$ everywhere (where we require $w_{\mathrm{q},1,\mathrm{err}} < \mathcal{D}_{\mathrm{t}} = 10^{-3}$), and in the thixotropic case the maximum error is $w_{\mathrm{q},1,\mathrm{err}} \approx 10^{-3}$ near the centreline, but still sufficiently small everywhere. In both cases the error is sufficiently small to describe the numerical solutions as accurate.

Figures 7.13(c) and 7.14(c) show that the numerical and asymptotic solutions for the structure parameter perturbation also appear to be in excellent agreement. However, the respective error plots, Figures 7.13(d) and 7.14(d), show that the numerical solutions are only accurate away from the centreline, and that the accuracy decreases approaching the centreline. This is as expected, because the asymptotic solution for the structure parameter perturbation $\lambda_{\mathrm{q},1}$ exhibits pathological behaviour at the centreline, as shown in Figures 7.3(b) and (d). In particular, $\lambda_{\mathrm{q},1}$ diverges as $r \to 0$ in both cases. This pathological behaviour indicates a local breakdown of the asymptotic expansion, and the divergent gradients in $\lambda_{\mathrm{q},1}$ are impossible to fully capture numerically, so we expect some disagreement between the numerical and asymptotic solutions near the centreline.

7.9.3 Verification and solutions for the slowly adjusting regime $\mathcal{D}_{\mathbf{t}} \gg 1$

In this section, we present illustrative examples of numerical solutions for the sMMW model in the slowly adjusting regime, showing that they are in good agreement with the analytical solutions (presented in Section 7.8.1). In the following examples of numerical solutions, we set $\mathcal{D}_{\mathrm{t}} = 10^5$ unless stated otherwise. To ensure the flow is periodic, after adjusting from the initial conditions, we simulate the flow over 50 periods of the pressure gradient oscillation.

Figure 7.15(a) shows an antithixotropic ($n = 2$) example of the numerical solution for the volume flux Q_{N} (solid), and the corresponding analytical solution Q_{s} (dotted with diamonds). Figure 7.15(b) shows an equivalent thixotropic ($n = 0.8$) example of the numerical solution for the volume flux Q_{N} (solid), and the

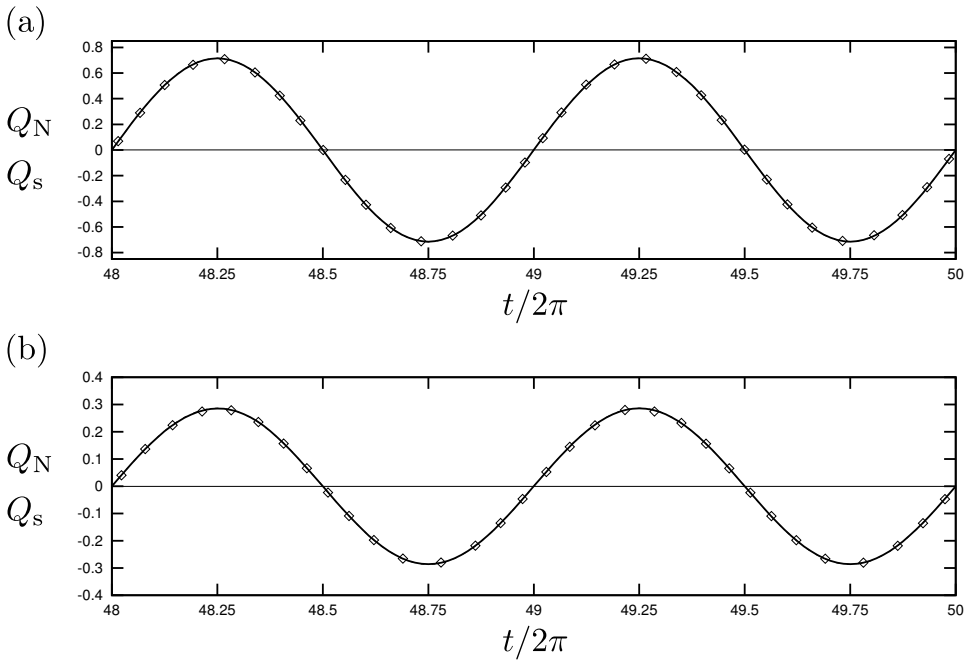

Figure 7.15: Plots of $Q_{\rm N}$ (solid) and $Q_{\rm s}$ (dotted with diamonds), for (a) an antithixotropic fluid ($n = 2$) and (b) a thixotropic fluid ($n = 0.8$), over two periods of the pressure gradient. The parameters are $\mathcal{D}_{\rm t} = 10^5$, $\kappa = 1$, $a = 1$, $b = 1$, and (a) $c = 2$ ($n = 2$) and (b) $c = 0.8$ ($n = 0.8$).

corresponding analytical solution Q (dotted with diamonds). It is clear that in both cases the numerical and analytical solutions are in good agreement.

Figure 7.16 shows an antithixotropic example of the numerical solutions for the velocity and structure parameter in the slowly adjusting regime, and the corresponding error plots, when $t/2\pi = 49.25$ ($G = 1$ and $G' = 0$). Figure 7.16(a) shows an example of the numerical solution w_{N} (solid) and the analytical solution w_{s} (dotted with diamonds) when $n = 2$. These solutions are in good agreement across the width of the pipe. As the plot for $w_{\mathrm{s,err}}$ in Figure 7.16(b) shows, the error is largest at the centreline, where $w_{\mathrm{s,err}} \approx 0.00017$, and decreases monotonically to the wall.

An example of the numerical and analytical solutions λ_{N} (solid) and λ_{s} (dotted with diamonds), respectively, when $n = 2$ is shown in Figure 7.16(c). Again, these solutions are in good agreement across the width of the pipe. As the plot for $\lambda_{\mathrm{s,err}}$ in Figure 7.16(d) shows, the error is smallest at the centreline and increases monotonically to the wall, where $\lambda_{\mathrm{s,err}} \approx 0.00005$.

Figure 7.17 shows a thixotropic example of the numerical solutions for the velocity and structure parameter in the slowly adjusting regime, and the corresponding error plots, when $t/2\pi = 49.25$ ($G = 1$ and $G' = 0$). Figure 7.17(a) shows an example of the numerical solution w_{N} (solid) and the analytical solution w_{s} (dotted with diamonds) when $n = 0.8$. These solutions are in good agreement across the width of the pipe. As the plot for $w_{\mathrm{s,err}}$ in Figure 7.17(b) shows, the error is largest at the centreline, where $w_{\mathrm{s,err}} \approx 0.0005$, and decreases monotonically to the wall.

Figure 7.17(c) illustrates good agreement between the numerical and analytical solutions λ_{N} (solid) and λ_{s} (dotted with diamonds), respectively, when $n = 0.8$. As shown in Figure 7.17(d), the error is smallest just outside the centreline, and, apart from a spike at the centreline, increases to the wall, where $\lambda_{\mathrm{s,err}} \approx 0.00011$.

In the slowly adjusting regime, the typical timescale of the variation of the structure parameter is much larger than the timescale of the pressure gradient oscillation. Consequently, we do not expect the structure parameter to vary significantly with time as the pressure gradient oscillates, once periodic behaviour is established. We formalised this expectation in Section 7.7, where we took

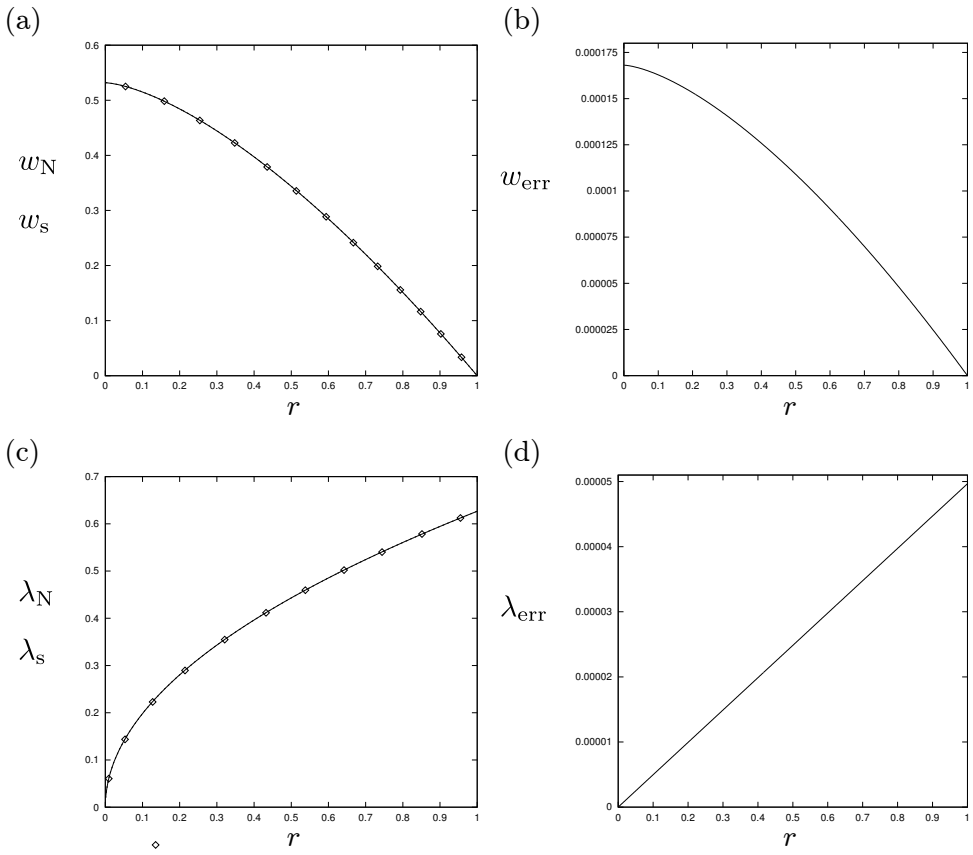

Figure 7.16: Profiles of (a) w_{N} (solid) and w_{s} (dotted with diamonds), (b) $w_{\mathrm{s,err}}$, (c) λ_{N} (solid) and λ_{s} (dotted with diamonds), and (d) $\lambda_{\mathrm{s,err}}$. The parameters are $\mathcal{D}_{\mathrm{t}} = 10^5$, $\kappa = 1$, $a = 1$, $b = 1$, and $c = 2$ ($n = 2$).

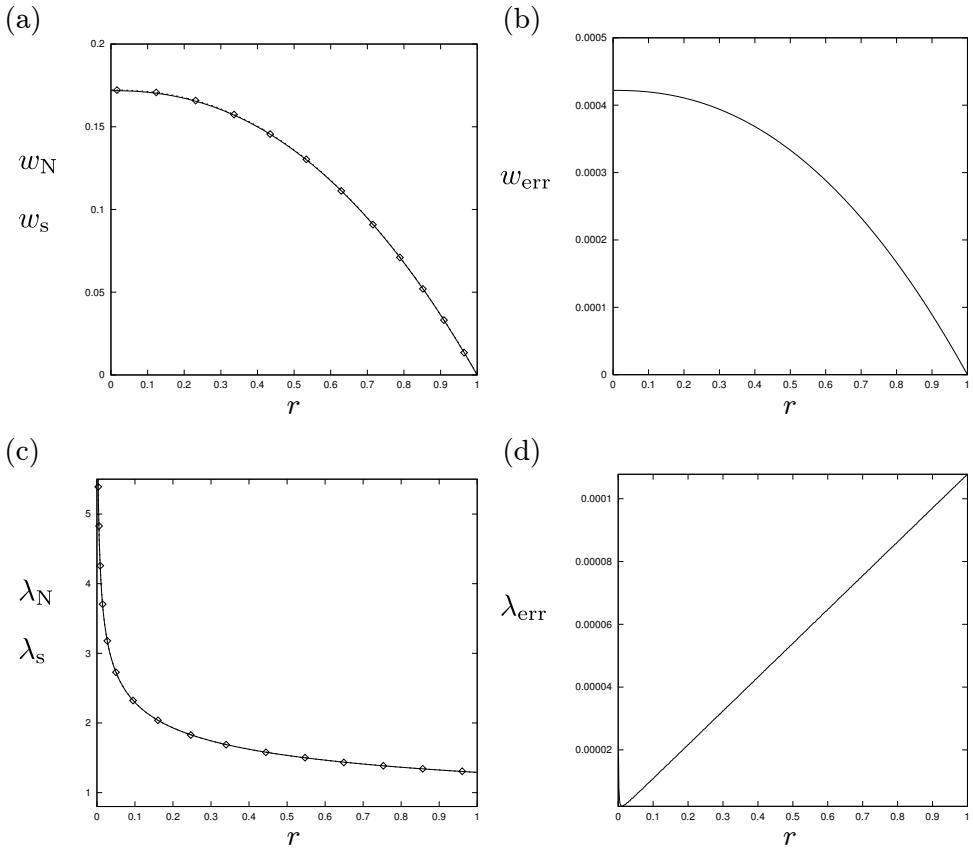

Figure 7.17: Profiles of (a) w_{N} (solid) and w_{s} (dotted with diamonds), (b) $w_{\mathrm{s,err}}$, (c) λ_{N} (solid) and λ_{s} (dotted with diamonds), and (d) $\lambda_{\mathrm{s,err}}$. The parameters are $\mathcal{D}_{\mathrm{t}} = 10^5$, $\kappa = 1$, $a = 1$, $b = 1$, and $c = 0.8$ ($n = 0.8$).

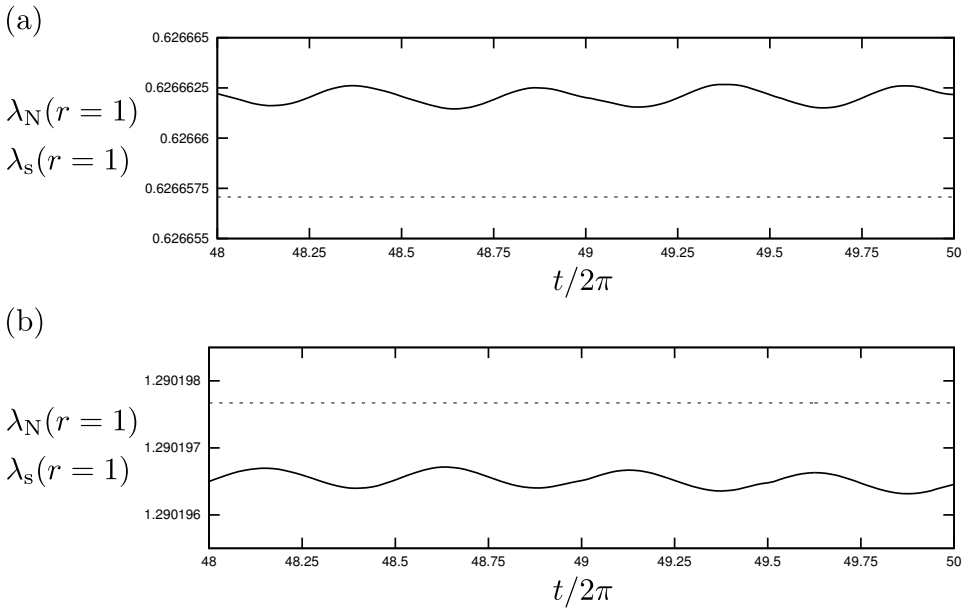

Figure 7.18: Plots of $\lambda_N(r=1)$ (solid) and $\lambda_s(r=1)$ (dotted with diamonds) over two periods of the pressure gradient, for (a) an antithixotropic fluid and (b) a thixotropic fluid. The parameters are $\mathcal{D}_t = 10^5$, $\kappa = 1$, $a = 1$, $b = 1$, and (a) $c = 2$ ($n = 2$) and (b) $c = 0.8$ ($n = 0.8$).

$\lambda = \lambda_s(r) + \text{h.o.t.}$, which assumes there is some higher-order, i.e. small, variation in time. We can confirm this assumption is correct by studying how λ_N varies with time.

Figure 7.18(a) shows λ_N (solid) and λ_s (dotted with diamonds) at the wall of the pipe, for an antithixotropic fluid ($n = 2$). Figure 7.18(b) shows the equivalent plot for a thixotropic fluid ($n = 0.8$). The value of λ_N at the wall oscillates, with a magnitude of roughly 10^{-6} in both cases, at twice the frequency of the pressure gradient. This oscillation arises from oscillations in higher-order terms not obtained in our asymptotic expansion. Aside from this oscillation, λ_N does not vary significantly as the pressure gradient oscillates, indicating that the initial assumption that $\lambda_s = \lambda_s(r) + \text{h.o.t.}$ is accurate, with the higher-order terms depending on time. The absolute error between the numerical and asymptotic solutions in the antithixotropic case is roughly 0.000005, and in the thixotropic case is roughly 0.000001.

7.9.4 Full range of thixotropic behaviour

In this section, we study the full range of thixotropic behaviour, from the quickly adjusting regime through the balanced regime, in which $\mathcal{D}_\mathrm{t} = \mathcal{O}(1)$, to the slowly adjusting regime. In the balanced regime the typical timescale of the structure is similar to the timescale of the pressure gradient oscillation. We are not able to explore this regime analytically, but we may use the solutions already obtained for the sMMW model in the quickly adjusting regime in Section 7.5.1 and in the slowly adjusting regime in Section 7.8.1 to make progress. In Sections 7.9.2 and 7.9.3, we showed that we can obtain accurate numerical solutions using COMSOL in both of these regimes, so we are confident that we may use COMSOL to obtain accurate numerical solutions for the regime of balanced thixotropy.

7.9.4.1 Variation of λ in time

In this section, we study how λ varies in time at a given radial position as $\mathcal{D}_\mathrm{t}$ varies. In particular, we show an example for a thixotropic and antithixotropic fluid at two locations in the pipe: at the wall ($r = 1$) and between the wall and the centre of the pipe ($r = 0.5$). Figures 7.19(a) and (b) show λ at $r = 0.5$ and $r = 1$, respectively, for an antithixotropic fluid ($n = 2$), for various values of $\mathcal{D}_\mathrm{t}$. The dotted line with diamonds is the asymptotic solution λ_q, given by (7.5.15). The other dotted line, which is not visible, at $\lambda_\mathrm{s} \approx 0.45$ in (a) and $\lambda_\mathrm{s} \approx 0.62$ in (b), is the asymptotic solution λ_s, given by (7.8.9). The solid lines are the numerical solutions λ_N for $\mathcal{D}_\mathrm{t} = 10^{-3}, 10^{-1/2}, 1, 10^{1/2}, 10^{3}$, where the arrows show the direction of increasing $\mathcal{D}_\mathrm{t}$, i.e. from λ_q, through λ_N, to λ_s.

When $\mathcal{D}_\mathrm{t} = 10^{-3}$, the numerical and asymptotic solutions are in good agreement, and are in phase with the pressure gradient oscillation (not shown). The structure is the most broken down when $G = 0$ (at $t/2\pi = 0, 0.5, 1, 1.5, 2$ in Figure 7.19), and the most built up when $|G|$ is largest (at $t/2\pi = 0.25, 0.75, 1.25, 1.75$ in Figure 7.19). As $\mathcal{D}_\mathrm{t}$ increases, the peaks and troughs in the structure move to larger t, so the structure lags behind the pressure gradient. As $\mathcal{D}_\mathrm{t}$ continues to increase, the lag increases and λ varies less with time. The effect of the lag is that the structure is the most broken down just after when $G = 0$ and is the most built up

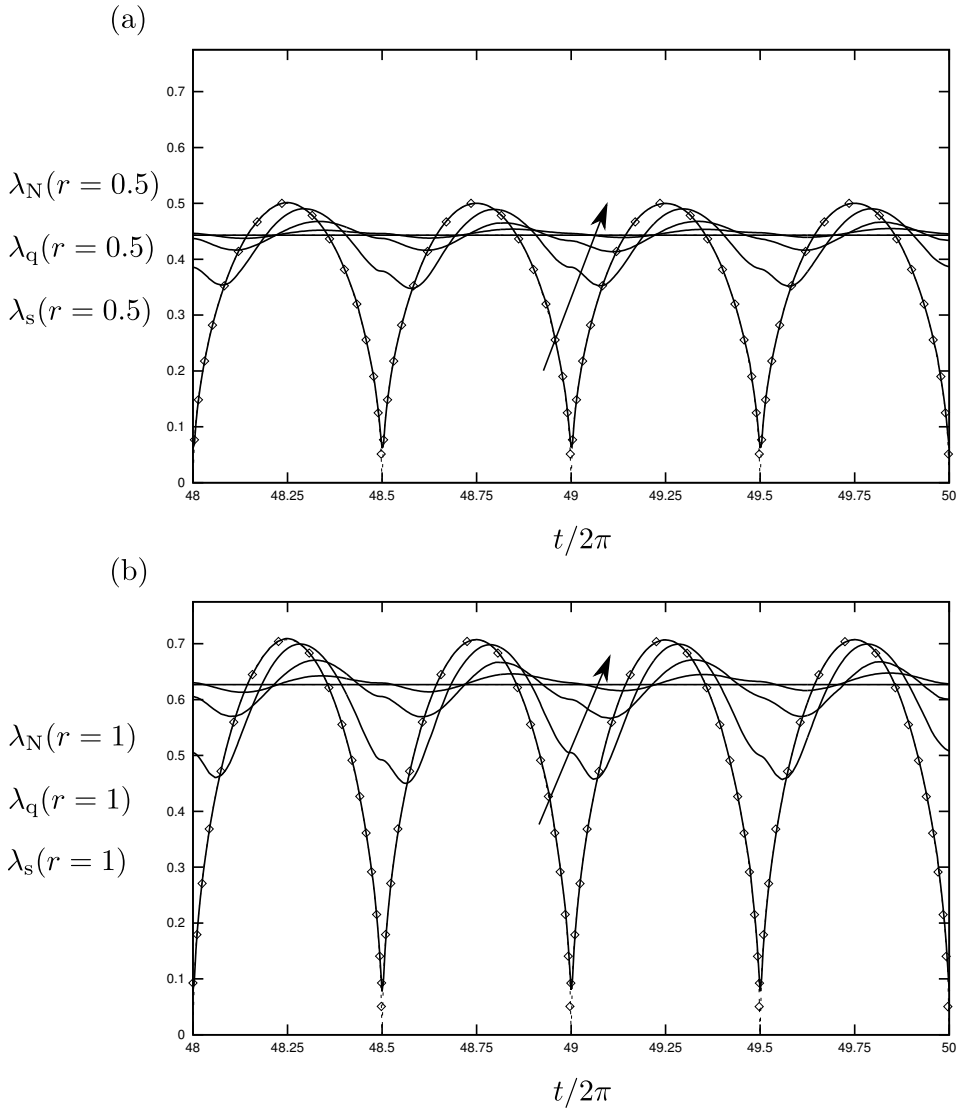

Figure 7.19: Plots of λ_N (solid) and λ_q and λ_s (dotted with diamonds) with respect to time for various values of $\mathcal{D}_t$ for an antithixotropic fluid, at (a) $r = 0.5$ and (b) $r = 1$. For λ_N, $\mathcal{D}_t = 10^{-3}, 10^{-1/2}, 1, 10^{1/2}, 10^3$. The arrows show the direction of increasing $\mathcal{D}_t$. The parameters are $\kappa = 1$, $a = 1$, $b = 1$, and $c = 2$ ($n = 2$).

just after when $|G|$ is largest. As $\mathcal{D}_\mathrm{t}$ becomes large, λ tends towards a constant value.

For the antithixotropic fluid shown in Figure 7.19, λ increases monotonically with r, so λ is smaller near the centreline (cf. corresponding values of λ in Figures 7.19 (a) and (b)). Since the shear rate is higher near the wall than near the centreline, λ is larger near the wall. In addition, λ varies more strongly near the wall, which yields a larger variation in λ in time at $r = 1$ than at $r = 0.5$.

Figures 7.20(a) and (b) show the equivalent plots of λ at $r = 0.5$ and $r = 1$, respectively, for a thixotropic fluid ($n = 0.8$), for various values of $\mathcal{D}_\mathrm{t}$. In this plot, the asymptotic solutions λ_q and λ_s (≈ 1.55) in (a) and $\lambda_\mathrm{s} \approx 1.3$ in (b), are not visible. The solid lines are the numerical solutions λ_N for $\mathcal{D}_\mathrm{t} = 10^{-3}, 10^{-3/2}, 10^{-1}, 1, 10^{3}$, where the arrows show the direction of increasing $\mathcal{D}_\mathrm{t}$. Note that the values of $\mathcal{D}_\mathrm{t}$ used in Figure 7.20 differ from those in Figure 7.19. In each figure, we use values of $\mathcal{D}_\mathrm{t}$ which clearly show how λ varies.

As in the antithixotropic case, when $\mathcal{D}_\mathrm{t} = 10^{-3}$, the numerical and asymptotic solutions are in good agreement, and are in phase with the pressure gradient oscillation (not shown). As $\mathcal{D}_\mathrm{t}$ increases, λ varies less significantly with time, and begins to lag behind the pressure gradient. In contrast to the antithixotropic case, when $\mathcal{D}_\mathrm{t}$ is small, the structure is the most built up when $G = 0$ (at $t/2\pi = 0, 0.5, 1, 1.5, 2$ in Figure 7.20), and most broken down when $|G|$ is largest (at $t/2\pi = 0.25, 0.75, 1.25, 1.75$ in Figure 7.20). As in the antithixotropic case, as $\mathcal{D}_\mathrm{t}$ increases, λ lags increasingly behind the pressure gradient and varies less with time. The result is that the structure is the most built up just after when $G = 0$ and is the most broken down just after when $|G|$ is largest. As $\mathcal{D}_\mathrm{t}$ becomes large, λ tends towards a constant value.

For the thixotropic fluid shown in Figure 7.20, λ decreases monotonically with r, so λ is larger near the centreline (cf. corresponding values of λ in Figures 7.20 (a) and (b)). Since the shear rate is higher near the wall than near the centreline, λ is smaller near the wall. In addition, as in the antithixotropic case, λ varies more strongly near the wall, which yields a larger variation in λ in time at $r = 1$ than at $r = 0.5$.

It is clear that when $\mathcal{D}_\mathrm{t} = \mathcal{O}(1)$, for both thixotropic and antithixotropic fluids,

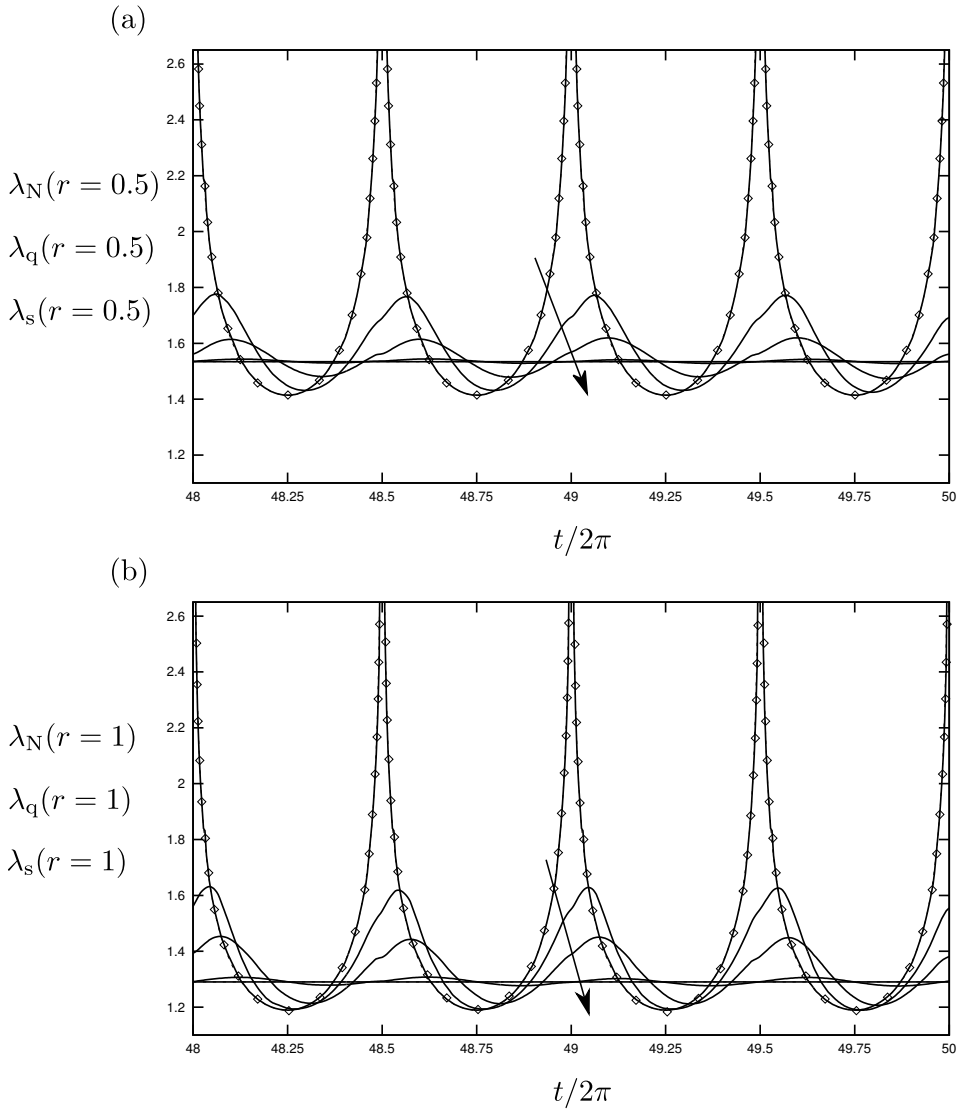

Figure 7.20: Plots of λ_N (solid) and λ_q and λ_s (dotted with diamonds) with respect to time for various values of $\mathcal{D}_t$ for a thixotropic fluid, at (a) $r = 0.5$ and (b) $r = 1$. For λ_N, $\mathcal{D}_t = 10^{-3}, 10^{-3/2}, 10^{-1}, 1, 10^3$. The arrows show the direction of increasing $\mathcal{D}_t$. The parameters are $\kappa = 1$, $a = 1$, $b = 1$, and $c = 0.8$ ($n = 0.8$).

the structure lags behind the pressure gradient oscillation. The lag increases as $\mathcal{D}_\mathrm{t}$ increases, but this will have a decreasing effect on the flow because λ also varies less as $\mathcal{D}_\mathrm{t}$ increases.

We note in Figures 7.19 and 7.20 that some plots of λ_N have a small wobble when the pressure gradient changes direction, i.e. at $t/2\pi = 48.5, 49, 49.5$. These wobbles are most noticeable in Figure 7.19 when $\mathcal{D}_\mathrm{t} = 10^{-1/2}, 1$, and in Figure 7.19 when $\mathcal{D}_\mathrm{t} = 10^{-3/2}, 10^{-1}$. When the pressure gradient changes direction, the shear rate drops to zero, which briefly slows the evolution of λ. This feature is only apparent when $\mathcal{D}_\mathrm{t} = \mathcal{O}(1)$ because it arises from a balance between sufficient variation in λ with time, which is not present when $\mathcal{D}_\mathrm{t} \gg 1$, and a lag in the evolution of λ, which is not present when $0 < \mathcal{D}_\mathrm{t} \ll 1$.

7.9.4.2 Variation of Q in time

In this section, we present examples of how Q varies as $\mathcal{D}_\mathrm{t}$ varies, and how the behaviour of λ affects Q as $\mathcal{D}_\mathrm{t}$ varies. We show an example for a thixotropic and antithixotropic fluid over two periods of the pressure gradient. We use the same parameters in the examples in this section as in Figures 7.19 and 7.20, so the plots are directly comparable.

Figure 7.21(a) shows Q_N, Q_q, and Q_s for an antithixotropic fluid ($n = 2$), for various values of $\mathcal{D}_\mathrm{t}$. Figure 7.21(b) shows a zoom of half of a period, in which $G > 0$. The asymptotic solutions Q_q and Q_s are given by (7.5.16) and (7.8.12) respectively. The solid lines in Figures 7.21(a) and (b) are the numerical solutions Q_N for $\mathcal{D}_\mathrm{t} = 10^{-3}, 10^{-1/2}, 1, 10^{1/2}, 10^{3}$, where the arrows show the direction of increasing $\mathcal{D}_\mathrm{t}$, i.e. from Q_q, through Q_N, to Q_s.

As $\mathcal{D}_\mathrm{t}$ increases, the peaks and troughs of the flux increase in magnitude near when G is largest, either positive or neagtive, i.e. when $|G|$ is largest ($t/2\pi = 0.25, 0.75, 1.25, 1.75$, when forcing in either direction is largest), which is particularly noticeable when $\mathcal{D}_\mathrm{t} = 10^{-1/2}, 1, 10^{1/2}$ in Figure 7.21(b). As shown in Figure 7.19, the structure lags behind G. The structure is thus broken down relative to its equilibrium state just before the peak in $|G|$, and so the fluid flows more easily, yielding a larger flux just before these maxima. We note that the flux is

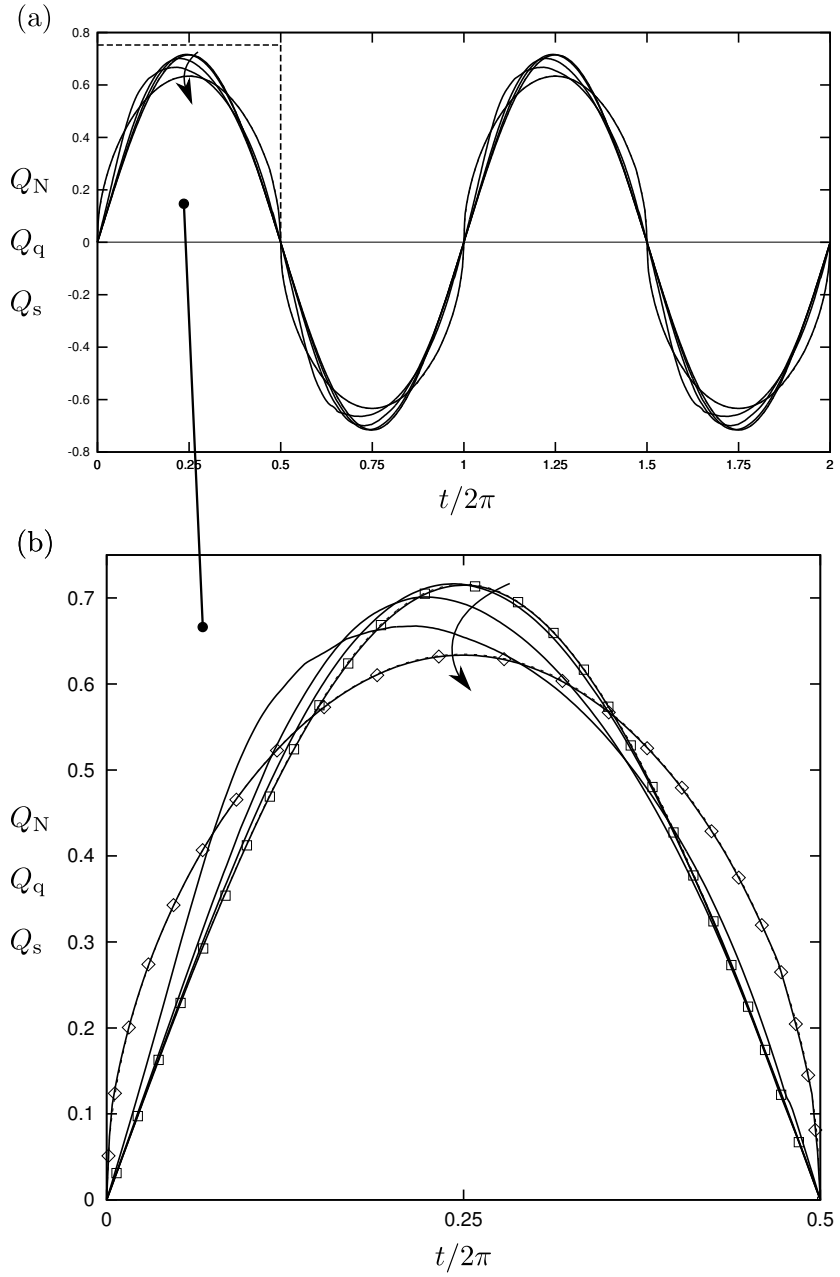

Figure 7.21: Plots of Q_{N} (solid) and Q_{q} (dotted with boxes) and Q_{s} (dotted with diamonds) with respect to time for various values of $\mathcal{D}_{\mathrm{t}}$ for an antithixotropic fluid ($n = 2$), where $\mathcal{D}_{\mathrm{t}} = 10^{-3}, 10^{-1/2}, 1, 10^{1/2}, 10^{3}$. The arrows show the direction of increasing $\mathcal{D}_{\mathrm{t}}$. The parameters are $\kappa = 1$, $a = 1$, $b = 1$, and $c = 2$ ($n = 2$).

not largest when λ is smallest, rather it is largest at a time when the reduced structure is balanced with a sufficiently large pressure gradient.

Figure 7.22(a) shows Q_{N}, Q_{q}, and Q_{s} for a thixotropic fluid ($n = 2$), for various values of $\mathcal{D}_{\mathrm{t}}$. Figure 7.22(b) shows a zoom of half of a period, in which $G > 0$. As in Figure 7.21, the asymptotic solutions Q_{q} and Q_{s} are given by (7.5.16) and (7.8.12) respectively. The solid lines in Figures 7.22(a) and (b) are the numerical solutions Q_{N} for $\mathcal{D}_{\mathrm{t}} = 10^{-3}, 10^{-1/2}, 1, 10^{1/2}, 10^{3}$, where the arrows show the direction of increasing $\mathcal{D}_{\mathrm{t}}$, i.e. from Q_{q}, through Q_{N}, to Q_{s}.

In contrast to the antithixotropic case, as $\mathcal{D}_{\mathrm{t}}$ increases in the thixotropic case, the flux decreases in magnitude near when the magnitude of the pressure gradient is largest ($t/2\pi = 0.25, 0.75, 1.25, 1.75$). The peaks and troughs in the flux lag slightly behind G, which is particularly noticeable when $\mathcal{D}_{\mathrm{t}} = 10^{-1/2}, 1$ in Figure 7.22(b). As shown in Figure 7.20, and as in the antithixotropic case, the structure lags behind G. The structure is thus broken down relative to its equilibrium state just after the peak in $|G|$, and so the fluid flows more easily, yielding a larger flux just after these maxima.

The difference between the antithixotropic and thixotropic case is that in the thixotropic case the structure is the most broken down just after the peak in the pressure gradient, and so the fluid flows most easily, yielding a larger flux.

7.10 Summary

In this chapter, we studied the oscillating flow of thixotropic and antithixotropic fluids in a uniform pipe. This flow set-up bore similarities to the previous set-up, studied in Chapters 2–6. The set-up studied in this chapter is simpler than the previous set-up: we consider a uniform pipe, so the advective effect of thixotropy is absent. So only the temporal change in the pressure gradient drives structure evolution, which yields the temporal effect of thixotropy. A result of this simplification is that we are able to obtain explicit asymptotic solutions for the sMMW model in the quickly adjusting regime, as in the previous set-up, and in the slowly adjusting regime, which we were not able to explore in the previous set-up. A

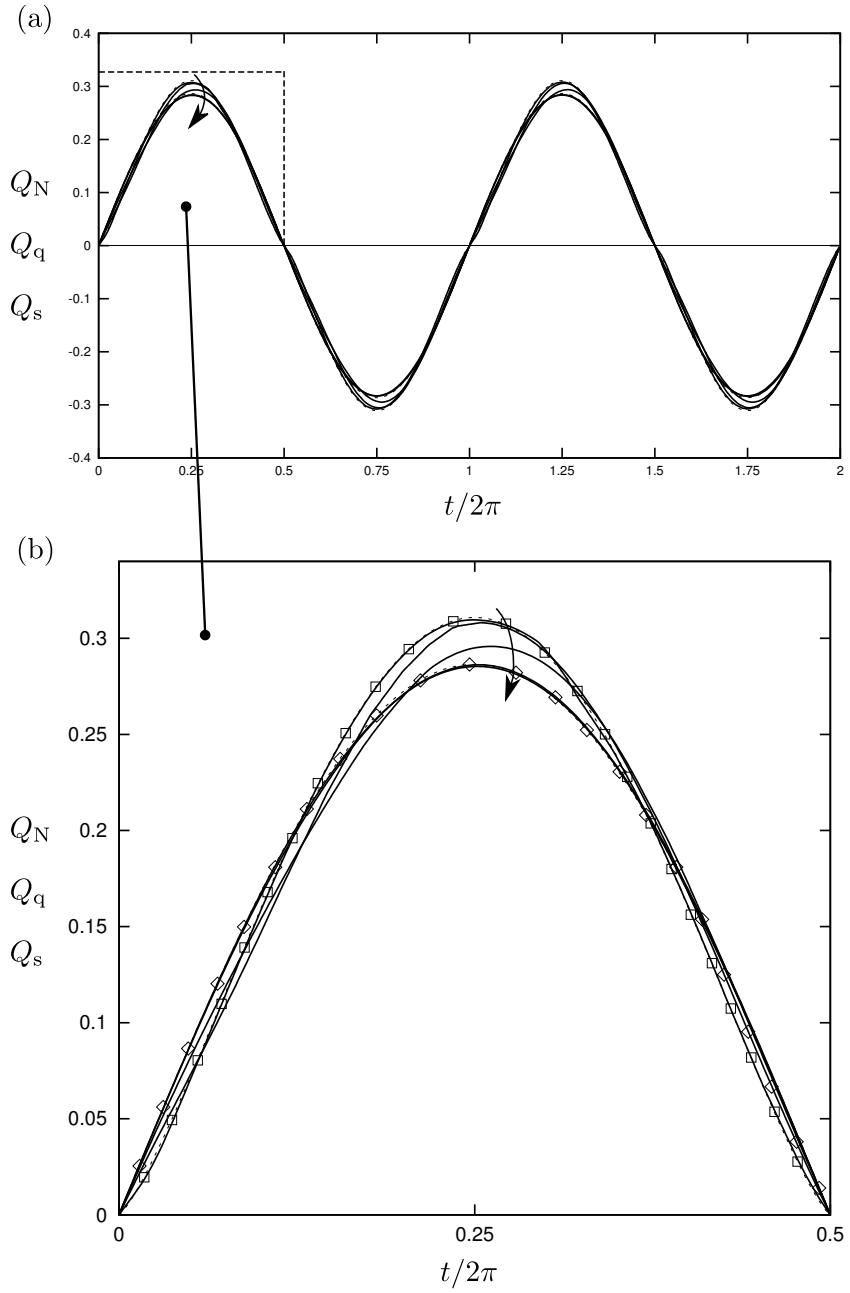

Figure 7.22: Plots of Q_{N} (solid) and Q_{q} (dotted with solid) and Q_{s} (dotted with diamonds) with respect to time for various values of $\mathcal{D}_{\mathrm{t}}$ for a thixotropic fluid ($n = 0.8$), where $\mathcal{D}_{\mathrm{t}} = 10^{-3}, 10^{-3/2}, 10^{-1}, 1, 10^{3}$. The arrows show the direction of increasing $\mathcal{D}_{\mathrm{t}}$. The parameters are $\kappa = 1$, $a = 1$, $b = 1$, and $c = 0.8$ ($n = 0.8$).

further benefit of this simplification is that we were able to successfully study this problem numerically using the finite element analysis software COMSOL. Through asymptotic and numerical methods, we were able to build a complete picture of the range of thixotropic behaviours.

In the quickly adjusting regime we followed a similar approach to obtain general asymptotic solutions used for the previous set-up in Chapters 3–5, with one important difference. In this chapter, we chose to prescribe a time-dependent pressure gradient, whereas in the previous set-up we specified the volume flux. In the previous set-up, the prescribed volume flux constrained the streamwise velocity perturbation to take a particular shape, such as that shown in Figure 3.1. In the present set-up, the streamwise velocity perturbation was not constrained by a flux condition, so in general it took a shape like those shown in Figure 7.3, which is largest in magnitude at the centreline and decreases in magnitude towards the wall.

In the previous set-up, the balance of the pressure gradient perturbation and the thixotropic stress term which enforces the flux condition (discussed in detail in Sections 4.1.6, 4.2.4, and 5.5) meant that the shape of the streamwise velocity perturbation was finely tuned, and could yield unexpected behaviour. In the present set-up there was no such subtle balance, and the shape of the perturbations may be described in general.

In the slowly adjusting regime we were able to obtain explicit solutions for the sMMW model, which corresponded with the explicit solutions in the quickly adjusting regime. We were not able to obtain equivalent solutions in the previous set-up. These solutions allowed us to explore strongly thixotropic behaviour in which the structure remains constant in time at leading order.

Having obtained explicit solutions in the quickly adjusting regime and slowly adjusting regime, we were able to study the regime of balanced thixotropy numerically, in which the timescale of structure evolution is similar to the timescale of the pressure gradient oscillation. As in the previous set-up, we used COMSOL for this. After implementing the problem in COMSOL, we first verified the asymptotic solutions in both the quickly adjusting and slowly adjusting regimes. Then after confirming the asymptotic and numerical solutions were in good agreement

in both regimes, we studied the effect of varying $\mathcal{D}_\mathrm{t}$ to build a full picture of the thixotropic behaviour: from the asymptotic solutions for $0 < \mathcal{D}_\mathrm{t} \ll 1$, through numerical solutions, including when $\mathcal{D}_\mathrm{t} = \mathcal{O}(1)$, to the asymptotic solutions for $\mathcal{D}_\mathrm{t} \gg 1$.

The full range of behaviour for a thixotropic fluid can be summarised as follows. When $\mathcal{D}_\mathrm{t}$ is small, the structure adjusts quickly to changes in the shear rate. At times of flow reversal, when the pressure gradient is small, the structure is at a maximum, as shown by the divergent peaks of λ_q at these times in Figure 7.20. When the magnitude of the pressure gradient is largest, the structure is at a minimum, as shown by the troughs in Figure 7.20. As $\mathcal{D}_\mathrm{t}$ increases, the behaviour of the structure is affected in two ways. The first is that the structure varies less, tending towards a constant value as $\mathcal{D}_\mathrm{t}$ diverges. The second is that the peaks and troughs begin to lag behind the pressure gradient. The lag is particularly noticeable when $\mathcal{D}_\mathrm{t} = \mathcal{O}(1)$. When the pressure gradient is largest in magnitude, the structure gradually breaks down, tending towards a minimum over an $\mathcal{O}(1)$ timescale. Before the structure reaches this minimum, the pressure gradient begins to decrease in magnitude, which cuts off the structure breakdown. The result is that the structure is most broken down just after the maximum magnitude of the pressure gradient. A similar process takes place for antithixotropic fluids, except that the structure is the most built up just after the pressure gradient maximum.

The behaviour of the structure when $\mathcal{D}_\mathrm{t} = \mathcal{O}(1)$ has a clear effect on the volume flux (and the streamwise velocity). The volume flux depends on the pressure gradient and the structure parameter. In particular, the flux will be large when the pressure gradient is large and when the structure is broken down. When $0 < \mathcal{D}_\mathrm{t} \ll 1$, for thixotropic fluids, the structure is always smallest when the pressure gradient is largest, so the volume flux is in phase with the pressure gradient. For larger values of $\mathcal{D}_\mathrm{t}$, the structure is the most broken down just after the maxima of the pressure gradient, so the flux is largest at a compromise between large pressure gradient and broken down structure. As shown in Figure 7.22, this compromise causes the flux to lag slightly behind the pressure gradient. A similar process takes place for antithixotropic fluids, except that the structure is the most broken down just before the pressure gradient maximum, so the volume

flux leads the pressure gradient.

A clear direction for further work on this flow set-up would be to explore the parameter space of the full MMW model, in particular to see how the value of the parameters a, b, c, and d affect the lags and leads in the flow. In addition, a study of a viscoplastic model, such as the regularised Houška model used in previous sections, would be insightful, particularly regarding the yielding and unyielding of the fluid and how it affects the volume flux.

Chapter 8

Conclusions and Future Work

The focus of this thesis was on slowly varying flows of complex fluids. We obtained asymptotic solutions for two closely related pipe-flow problems in order to determine the characteristic behaviour and underlying mechanisms of thixotropic flow in slowly varying geometries, and whether thixotropic and antithixotropic fluid flow could be described in general, in the sense that their qualitative features could be predicted without a detailed analysis. In addition, we investigated the application of the standard FEM software COMSOL to these problems in order to explore the strengths and weaknesses of 'off-the-shelf' numerical packages for such flows.

8.1 Conclusions

In Chapters 2–5 we studied the unsteady flow of thixotropic fluids in a slowly varying pipe. We analysed the behaviour of thixotropic fluids in detail using three rheological models, the simplified and full Moore–Mewis–Wagner viscous models (the sMMW and MMW models, respectively), and the Houška viscoplastic model, and obtained a complete description of their behaviours. Work on the simpler set-up of steady flow in a slowly varying 2D channel done by Pritchard et al. [29] (PWM) had suggested that the behaviour of thixotropic fluids in these problems could be described in general. Specifically, PWM suggested that it could be

described by the thixotropic reference case (TRC), in which in a widening channel the streamwise velocity perturbation is positive near the centre of the pipe and negative near the walls, and the structure parameter perturbation is negative everywhere and largest at the centreline (see Section 3.3.1 and Figure 3.1 for details).

In the process of exploring the behaviour of the three rheological models, we found that the TRC fails to capture the full range of behaviour that each rheological model is capable of displaying, and so the corresponding description of the mechanisms presented by PWM is not complete. While the description presented by PWM is in accord with physical intuition, it does not account for the subtle interaction between two aspects of the dynamics. In our analysis, we found that the behaviour of the fluid depends on a combination of the effects of the pressure gradient perturbation and a thixotropic stress term. In some cases a fine balance between these two terms emerges and so a small change in either can yield behaviour which is not described by the TRC. For example, the streamwise velocity perturbation is the opposite of what is predicted by the TRC for some particularly strongly antithixotropic sMMW and MMW fluids, and some low-yield-stress Houška fluids. Consequently, we had to refine the description of the mechanisms presented by PWM to include the more subtle effects of the pressure gradient perturbation and the thixotropic stress term.

The important consequence of this work is that those studying thixotropic fluids in slowly varying geometries should be aware that commonly used rheological models, such as the MMW and Houška models, may exhibit behaviour that is inconsistent with the TRC. In particular, the behaviour of these models for one set of parameters may be qualitatively different from the behaviour for another set, so one cannot assume that any particular set of results represents the general description of the problem. This discovery complicates the use of thixotropic models in slowly varying geometries, and a detailed analysis similar to that presented in Chapters 4 and 5 may be necessary to determine whether any particular behaviour is generic.

In Chapter 6, we investigated the application of the off-the-shelf FEM package COMSOL to the set-up in Chapters 2–5. It is clear that the numerical solutions

obtained are least accurate when the shear rate is low, which occurs near the centre of the pipe for the sMMW and MMW models, and in or at the edges of the pseudo-plug in the Houška model. Various attempts to resolve this issue were not entirely successful, which suggests that off-the-shelf FEM software is not suitable for this kind of problem, or was not implemented correctly.

Despite the drawbacks of the numerical results in Chapter 6, some numerical results provided support for the asymptotic results in Chapter 4. For example, as shown in Section 6.5, we obtained numerical results that were accurate away from the centreline, including for an illustrative case where the behaviour is inconsistent with the TRC (see Figure 6.9).

In Chapter 7, we investigated the oscillating flow of a thixotropic fluid in a uniform pipe. This set-up is simpler than that studied in Chapters 2–6, and as a consequence we were able to make more analytical and numerical progress. In Chapters 2–5 we specified the volume flux, which gave the streamwise velocity profiles (including the TRC) their characteristic shape. Conversely in Chapter 7, we specified the pressure gradient, which meant there was no fine balance between the pressure gradient and the thixotropic stress term, so the streamwise velocity perturbation profiles were always positive everywhere or negative everywhere. Consequently, we were able to qualitatively describe the behaviour of a fluid based on whether it was thixotropic or antithixotropic.

Unlike in Chapters 2–5, we obtained asymptotic solutions for this set-up for both small and large $\mathcal{D}_\mathrm{t}$. The large-$\mathcal{D}_\mathrm{t}$ solutions revealed that the structure parameter for strongly thixotropic fluids is constant in time, though not in space, at leading order. We would expect this behaviour because the structure of a thixotropic fluid which evolves over a long timescale adjusts too slowly to changes in the pressure gradient to affect the leading-order behaviour.

The application of COMSOL to the set-up in Chapter 7 was more successful than for the set-up studied in Chapters 2–5, because only one spatial dimension was involved and so we could use a much higher resolution. We obtained numerical solutions that were sufficiently accurate to allow an exploration of thixotropic behaviour for all values of $\mathcal{D}_\mathrm{t}$, including that out of the scope of the asymptotic approach, when $\mathcal{D}_\mathrm{t} = \mathcal{O}(1)$. We showed the changing effect of thixotropy on the

flow as $\mathcal{D}_\mathrm{t}$ is varied.

The most interesting behaviour occurs when $\mathcal{D}_\mathrm{t} = \mathcal{O}(1)$, when thixotropic effects yield a noticeable lag in the flow quantities. For both thixotropic and antithixotropic fluids, the structure lags behind the pressure gradient, as expected, but the effect of this lag on the velocity, and therefore the volume flux, differs for thixotropic and antithixotropic fluids. In thixotropic fluids, the velocity and flux lag behind the pressure gradient, but in antithixotropic fluids, they lead the pressure gradient. This behaviour occurs because the peaks in the velocity and structure are controlled by a balance between low structure and high pressure gradient. A high velocity and volume flux requires a low structure and a high pressure gradient, which when $\mathcal{D}_\mathrm{t} = \mathcal{O}(1)$ occurs just after the peak in the pressure gradient for thixotropic fluids and just before the peak for antithixotropic fluids.

8.2 Future work

A continuation of the work in Chapters 2–6 is an obvious direction in which to build on the work described in this thesis. Interesting unexpected behaviour arose in the weakly thixotropic regimes, and whether this persists into regimes of strong thixotropy is an important open question. It is important to use the results of Chapter 6 to build an appropriate numerical solver to fully verify the results of Chapters 4 and 5. Following the verification, one could study the strongly thixotropic regimes as done in Chapter 7, which would allow a full analysis for the problem to be completed, and to determine whether and how the behaviour inconsistent with the TRC arises in more strongly thixotropic flow.

A clear direction for extending the work in Chapter 7 is to study the Houška model for the full range of the Deborah number $\mathcal{D}_\mathrm{t}$. In the analysis of the quickly adjusting regime in Section 7.4, the absence of pathological behaviour meant that Houška fluid flow provided a useful insight into slowly varying thixotropic flow, and we expect it to do the same for the balanced regime and the slowly adjusting regime.

In addition to these directions, one may also consider applying the asymptotic approach employed in this thesis to other lubrication set-ups. Such set-ups include free-surface thin-film and rivulet flows, which have been studied in the context of non-Newtonian fluids by Hewitt and Balmforth [22] and by Wilson and co-workers [44, 81, 82].

It is clear from the work presented in this thesis that thixotropic fluids continue to be an interesting and sometimes unpredictable area of research. Much work remains to be done to fully understand the behaviour and role of thixotropic fluids in industrial and everyday settings.

Appendix A

sMMW model

In this appendix, we obtain the centreline behaviour (flat, cusp or singularity) of w_1 (Section A.1) and λ_1 (Section A.2) from the explicit solutions presented in Section 4.1.3.

A.1 Behaviour of w_1 near the centreline

In this section, we analyse the behaviour of w_1, given by (4.1.39), near the centreline. In particular, we first determine the dominant terms of w_1 and $\partial w_1/\partial r$ as $r \to 0$, and determine the nature of w_1 at the centreline, then we find the sign of w_1 at the centreline. We use this information to determine when w_1 agrees with the TRC and when it does not.

The behaviour of w_1 near the centreline depends on which term in r in (4.1.39) dominates as $r \to 0$, i.e. which exponent of r has the lowest value. The exponents of r in (4.1.39) are

$$r^0, \quad r^{(n+1)/n}, \quad r^{(2n-c)/n}, \quad \text{and} \quad r^{(3n-c+1)/n}. \tag{A.1.1}$$

As $n > 0$, the constant term in w_1 is always larger than the term in $r^{(n+1)/n}$ as $r \to 0$, so the term in $r^{(n+1)/n}$ never dominates as $r \to 0$. In addition, the term in $r^{(2n-c)/n}$ is always larger than the term in $r^{(3n-c+1)/n}$ as $r \to 0$, which becomes

clear by rewriting the exponent $(3n-c+1)/n$ as $(2n-c)/n+(n+1)/n$. So either the constant term or the term in $r^{(2n-c)/n}$ dominates as $r \to 0$, so the centreline behaviour of w_1 is determined by whether $(2n-c)/n$ is greater than or less than zero. When $(2n-c)/n > 0$, $r^{(2n-c)/n} \to 0$ as $r \to 0$ and so the constant term in w_1 dominates. When $(2n-c)/n < 0$, $r^{(2n-c)/n}$ grows without bound as $r \to 0$ and so the term in $r^{(2n-c)/n}$ in w_1 dominates. We note that for the expansion scheme to be valid we require the flux condition (3.1.12) to be satisfied, i.e. we require rw_1 to be integrable. The flux condition is satisfied when $r^{(2n-c)/n+1}$ is integrable, i.e. when $(2n-c)/n+1 > -1$, or $4n-c > 0$.

The behaviour of $\partial w_1/\partial r$ at the centreline is dominated by the term in r with the lowest value exponent. The terms of r are the derivatives with respect to r of those in (A.1.1), and are given by

$$r^{1/n}, \quad r^{(n-c)/n}, \quad \text{and} \quad r^{(2n-c+1)/n}. \tag{A.1.2}$$

As $n > 0$, the term in $r^{1/n} \to 0$ as $r \to 0$, so if this term dominates, $\partial w_1/\partial r \to 0$ and w_1 is flat at the centreline. The term in $r^{(n-c)/n}$ is always larger than the term in $r^{(2n-c+1)/n}$ as $r \to 0$, which becomes clear by rewriting the exponent $(2n-c+1)/n$ as $(n-c)/n+(n+1)/n$. So we may determine the centreline behaviour of $\partial w_1/\partial r$ by studying the exponent $(n-c)/n$. When $0 < (n-c)/n$, $\partial w_1/\partial r \to 0$ as $r \to 0$, so w_1 is flat at the centreline. When $-1 < (n-c)/n < 0$, i.e. when $0 < 2n-c < n$, $\partial w_1/\partial r \to \infty$ as $r \to 0$, so w_1 has a cusp at the centreline (when $0 < 2n-c$, the constant term dominates in w_1 as $r \to 0$, so w_1 remains finite). When $(n-c)/n < -1$, i.e. when $2n-c < 0$, $\partial w_1/\partial r \to \infty$ as $r \to 0$, so w_1 is singular at the centreline (when $2n-c < 0$, terms in $r^{(2n-c)/n}$ dominate w_1 as $r \to 0$, so w_1 grows without bound).

To summarise, when $n < 2n-c$, the constant term in w_1 dominates as $r \to 0$ and w_1 is flat and finite at the centreline. When $0 < 2n-c < n$, the constant term in w_1 dominates as $r \to 0$ and w_1 has a cusp and is finite at the centreline. When $2n-c < 0$, terms in $r^{(2n-c)/n}$ in w_1 dominate as $r \to 0$ and w_1 is singular at the centreline. The sign of w_1 at the centreline is the sign of the constant term when $0 < 2n-c$ and of the coefficient of the term in $r^{(2n-c)/n}$ when $2n-c < 0$. We discuss the sign of w_1 at the centreline in the following section.

Sign of w_1 at the centreline

We now discuss the sign of w_1 at the centreline in more detail. For simplicity, we consider the quickly adjusting regime $\mathfrak{R}_{1,2}$ ($\mathcal{D}_{\mathrm{t}}^* \neq 0$, $\mathcal{D}_{\mathrm{a}}^* = 0$) and the weakly advective regime $\mathfrak{R}_{2,1}$ ($\mathcal{D}_{\mathrm{a}}^* \neq 0$, $\mathcal{D}_{\mathrm{t}}^* = 0$) separately.

Sign of w_1 at the centreline in $\mathfrak{R}_{1,2}$

In the quickly adjusting regime ($\mathcal{D}_{\mathrm{a}}^* = 0$), the solution for w_1 (4.1.39) is

$$w_1(r,z,t) = -\mathcal{D}_{\mathrm{t}}^* \kappa^{(1-b)/b} \frac{n-1}{b} \frac{Q'}{Q} \left(\frac{3n+1}{\pi n} Q \alpha^{-(3n+1)/n} \right)^{n-c} \alpha^{(2n-c)/n} \times \left[\frac{3n+1}{(4n-c)(n+1)} \left(1 - \left(\frac{r}{\alpha} \right)^{(n+1)/n} \right) - \frac{1}{2n-c} \left(1 - \left(\frac{r}{\alpha} \right)^{(2n-c)/n} \right) \right]. \tag{A.1.3}$$

We note that $\kappa, b, n, Q, \alpha > 0$ and $r^{(n+1)/n} \to 0$ as $r \to 0$.

When $(2n-c)/n > 0$, w_1 is finite at the centreline, with the sign of the constant term in (A.1.3), i.e.

$$\lim_{r \to 0} \operatorname{sgn}(w_1) = \operatorname{sgn} \left\{ -\mathcal{D}_{\mathrm{t}}^* Q' \left(\frac{3n+1}{(4n-c)(n+1)} - \frac{1}{2n-c} \right) \right\}. \tag{A.1.4}$$

As stated in Section 4.1.3, we only consider decelerating flow and assume that $\mathcal{D}_{\mathrm{t}}^* Q' < 0$, so with some rearrangement (A.1.4) becomes

$$\lim_{r \to 0} \operatorname{sgn}(w_1) = \operatorname{sgn} \left\{ \frac{(n-1)(n-c-1)}{(2n-c)(n+1)(4n-c)} \right\}. \tag{A.1.5}$$

Given that here $2n - c > 0$ and $n + 1 > 0$, and for the flux condition to be satisfied, $4n - c > 0$, (A.1.5) becomes

$$\lim_{r \to 0} \operatorname{sgn}(w_1) = \operatorname{sgn}\{(n-1)(n-c-1)\}. \tag{A.1.6}$$

So for $2n - c > 0$, when $n - 1 < 0$ (and so $n - c - 1 < 0$) and when $n - c - 1 > 0$ (and so $n - 1 > 0$), w_1 is positive and finite at the centreline. When $n - 1 > 0$ and $n - c - 1 < 0$, i.e. when $0 < n - 1 < c$, w_1 is negative and finite at the centreline.

We note then that w_1 is positive for some antithixotropic fluids and is negative for others.

When $(2n-c)/n < 0$, w_1 is unbounded at the centreline, with the sign of the coefficient of the term in $r^{(2n-c)/n}$ in (A.1.3), i.e.

$$\lim_{r\to 0} \operatorname{sgn}(w_1) = \operatorname{sgn}\left\{-(n-1)\right\}, \tag{A.1.7}$$

for $\mathcal{D}_{\mathrm{t}}^{*} Q' < 0$ and $2n - c < 0$. So when $n - 1 < 0$ (for thixotropic fluids) w_1 is positive and unbounded at the centreline, and when $n-1 > 0$ (for antithixotropic fluids) w_1 is negative and unbounded at the centreline.

Sign of w_1 at the centreline in $\mathfrak{R}_{2,1}$

In the weakly advective regime ($\mathcal{D}_{\mathrm{t}}^{*} = 0$), the solution for w_1 (4.1.39) is

$$\begin{aligned} w_1(r,z,t) = \mathcal{D}_{\mathrm{a}}^{*} \kappa^{(1-b)/b} \frac{3(3n+1)(n-1)}{b\pi(n+1)} \frac{Q\alpha'}{\alpha^{(n+c)/n}} \left(\frac{3n+1}{\pi n} Q \alpha^{-(3n+1)/n}\right)^{n-c} \\ \times \left[\frac{3n+1}{(4n-c)(5n-c+1)} \left(1 - \left(\frac{r}{\alpha}\right)^{(n+1)/n}\right)\right. \\ \left. - \frac{1}{2n-c} \left(1 - \left(\frac{r}{\alpha}\right)^{(2n-c)/n}\right) + \frac{1}{3n-c+1} \left(1 - \left(\frac{r}{\alpha}\right)^{(3n-c+1)/n}\right)\right]. \end{aligned} \tag{A.1.8}$$

Again, we note that $\kappa, b, n, Q, \alpha > 0$, $r^{(n+1)/n} \to 0$ as $r \to 0$, and $r^{(3n-c+1)/n} < r^{(2n-c)/n}$ when $0 < r \ll 1$.

When $(2n-c)/n > 0$, w_1 is finite at the centreline, with the sign of the constant term in (A.1.8), i.e.

$$\lim_{r\to 0} \operatorname{sgn}(w_1) = \operatorname{sgn}\left\{\mathcal{D}_{\mathrm{a}}^{*} \alpha'(n-1) \left[\frac{3n+1}{(4n-c)(5n-c+1)} - \frac{1}{2n-c} + \frac{1}{3n-c+1}\right]\right\}. \tag{A.1.9}$$

As stated in Section 4.1.3, we only consider flow in a widening pipe and assume

that $\mathcal{D}_{\mathrm{a}}^{*}\alpha' > 0$, so with some rearrangement (A.1.9) becomes

$$\lim_{r\to 0}\operatorname{sgn}(w_1) = \operatorname{sgn}\left\{-\frac{2n(n-1)(n^2+3(2+c)n-(c^2+c-1))}{(2n-c)(3n-c+1)(4n-c)(5n-c+1)}\right\}. \tag{A.1.10}$$

Given that here $2n-c>0$ (so $3n-c+1>0$) and $n>0$, and for the flux condition to be satisfied $4n-c>0$ (so $5n-c+1>0$), (A.1.10) becomes

$$\lim_{r\to 0}\operatorname{sgn}(w_1) = \operatorname{sgn}\left\{-(n-1)(n^2+3(2+c)n-(c^2+c-1))\right\}. \tag{A.1.11}$$

The sign of $n^2+3n(c+2)-(c^2+c-1)$ in (A.1.11) is not immediately clear, but by setting this term equal to zero and finding its roots, we are able to show that it is positive for all $(2n-c)/n>0$. By setting $n^2+3n(c+2)-(c^2+c-1)=0$ we obtain a concave-up quadratic in n. After solving for n using the quadratic formula, we obtain only one root n which may be positive, which is given by

$$n = -\frac{3}{2}(2+c)+\frac{1}{2}\sqrt{13c^2+40c+32}. \tag{A.1.12}$$

When n is larger than this root, $n^2+3n(c+2)-(c^2+c-1)>0$. For $(2n-c)/n>0$, so $n>c/2$, if

$$\frac{c}{2} > -\frac{3}{2}(2+c)+\frac{1}{2}\sqrt{13c^2+40c+32}, \tag{A.1.13}$$

then n is greater than the root. Following some rearrangement, (A.1.13) becomes

$$3c^2+8c+4>0, \tag{A.1.14}$$

which is always true because $c>0$, so (A.1.13) holds, and so

$$n > -\frac{3}{2}(2+c)+\frac{1}{2}\sqrt{13c^2+40c+32}. \tag{A.1.15}$$

Hence $n^2+3n(c+2)-(c^2+c-1)>0$ when $(2n-c)/n>0$. So we can rewrite (A.1.11) as

$$\lim_{r\to 0}\operatorname{sgn}(w_1) = \operatorname{sgn}\left\{-(n-1)\right\}. \tag{A.1.16}$$

So for $2n-c>0$, when $n-1<0$ (thixotropic fluids), w_1 is positive and finite

at the centreline, and when $n-1>0$ (antithixotropic fluids), w_1 is negative and finite at the centreline.

When $(2n-c)/n<0$, w_1 is finite at the centreline, with the sign of the coefficient of the term in $r^{(2n-c)/n}$ in (A.1.8), i.e.

$$\lim_{r\to 0}\operatorname{sgn}(w_1)=\operatorname{sgn}\left\{-(n-1)\right\}, \tag{A.1.17}$$

for $\mathcal{D}^*_{\mathrm{a}}\alpha'>0$ and $2n-c<0$. When $n-1<0$, w_1 is positive and unbounded at the centreline, and when $n-1>0$, w_1 is negative and unbounded at the centreline. Unlike in the quickly adjusting regime, w_1 is negative at the centreline for all antithixotropic fluids in the weakly advective regime.

We summarise the sign of w_1 at the centreline as follows. In the quickly adjusting regime with $\mathcal{D}^*_{\mathrm{t}}Q'<0$:

- when $n-1<0$ $(a>c)$, i.e. for all thixotropic fluids, w_1 is positive at the centreline;
- when $n-1>0$ $(a<c)$ and $n-c-1<0$ $(a>c(1-b))$, i.e. for antithixotropic fluids satisfying $n-c-1<0$, w_1 is negative at the centreline;
- when $n-1>0$ $(a<c)$ and $n-c-1>0$ $(a<c(1-b))$, i.e. for antithixotropic fluids satisfying $n-c-1>0$, w_1 is positive at the centreline.

In the weakly advective regime with $\mathcal{D}^*_{\mathrm{a}}\alpha'>0$:

- when $n-1<0$ $(a>c)$, i.e. for all thixotropic fluids, w_1 is positive at the centreline;
- when $n-1>0$ $(a<c)$, i.e. for all antithixotropic fluids, w_1 is negative at the centreline.

We note that for thixotropic fluids, w_1 is positive at the centreline in both the quickly adjusting regime and in the weakly advective regime. On the other hand for antithixotropic fluids, w_1 is not always negative at the centreline in the quickly adjusting regime, as it is in the weakly advective regime.

A.2 Behaviour of λ_1 near the centreline

In this section, we analyse the behaviour of λ_1, given by (4.1.40), near the centreline. In particular, we first determine the dominant terms of λ_1 and $\partial\lambda_1/\partial r$ as $r \to 0$, and determine the nature of λ_1 at the centreline, then we find the sign of λ_1 at the centreline. We use this information to determine when λ_1 agrees with the TRC and when it does not.

The behaviour of λ_1 near the centreline depends on which term in r in (4.1.40) dominates as $r \to 0$, i.e. which exponent of r has the lowest value. The exponents of r in (4.1.40) are

$$r^{(n-1)/n}, \quad r^{(2n-c-2)/n}, \quad \text{and} \quad r^{(3n-c-1)/n}. \tag{A.2.1}$$

The term in $r^{(2n-c-2)/n}$ is always larger than the term in $r^{(3n-c-1)/n}$ as $r \to 0$, which becomes clear by rewriting the exponent $(3n-c-1)/n$ as $(2n-c-2)/n + (n+1)/n$, where $n > 0$. So the term in either $r^{(n-1)/n}$ or $r^{(2n-c-2)/n}$ dominates as $r \to 0$, and so the centreline behaviour of λ_1 is determined by the sign of $(2n-c-2)/n - (n-1)/n$, i.e. by the sign of $n-c-1$. When $(n-1)/n < (2n-c-2)/n$ (so $n-c-1 > 0$), which includes only antithixotropic fluids ($n-1 > 0$), the behaviour of λ_1 depends on the term in $r^{(n-1)/n}$, so $\lambda_1 \to 0$ as $r \to 0$. When $(n-1)/n > (2n-c-2)/n$ (so $n-c-1 < 0$), the behaviour of λ_1 depends on the term in $r^{(2n-c-2)/n}$. So when $2n-c-2 > 0$, $\lambda_1 \to 0$ as $r \to 0$, and when $2n-c-2 < 0$, λ_1 grows without bound as $r \to 0$, with the sign determined by the coefficient of the term in $r^{(2n-c-2)/n}$.

The behaviour of $\partial\lambda_1/\partial r$ at the centreline is dominated by the term in r with the lowest value exponent. The terms of r are the derivatives with respect to r of those in (A.2.1), and are given by

$$r^{-1/n}, \quad r^{(n-c-2)/n}, \quad \text{and} \quad r^{(2n-c-1)/n}. \tag{A.2.2}$$

As $n > 0$, the term in $r^{-1/n}$ grows without bound as $r \to 0$ for all values of n, so $\partial\lambda_1/\partial r \to \pm\infty$ as $r \to 0$, and λ_1 is infinitely steep at the centreline.

To summarise, λ_1 is singular at the centreline when $2n-c-2<0$, which includes all thixotropic fluids ($n-1<0$) and some antithixotropic fluids ($0<n-1<c/2$). When $0<2n-c-2$, λ_1 is zero with a cusp at the centreline, which includes only antithixotropic fluids ($c/2<n-1$). The sign of λ_1 at the centreline is the sign of the coefficient of the term in $r^{(2n-c-2)/n}$ when $2n-c-2<0$. We discuss the sign of λ_1 at the centreline in the following section.

Sign of λ_1 at the centreline

We now discuss the sign of λ_1 at the centreline in more detail. For simplicity, we consider the quickly adjusting regime $\mathfrak{R}_{1,2}$ ($\mathcal{D}_{\mathrm{t}}^{*}\neq 0$, $\mathcal{D}_{\mathrm{a}}=0$) and the weakly advective regime $\mathfrak{R}_{2,1}$ ($\mathcal{D}_{\mathrm{a}}^{*}\neq 0$, $\mathcal{D}_{\mathrm{t}}=0$) separately.

Sign of λ_1 at the centreline in $\mathfrak{R}_{1,2}$

In the quickly adjusting regime ($\mathcal{D}_{\mathrm{a}}^{*}=0$), the solution for λ_1 (4.1.40) is

$$\lambda_1=-\mathcal{D}_{\mathrm{t}}^{*}\frac{Q'}{Q}\kappa^{(2-b)/b}\frac{n-1}{bn}\left(\frac{3n+1}{\pi n}Q\alpha^{-(3n+1)/n}\right)^{2n-c-2}\times\left[r^{(2n-c-2)/n}+\frac{(n-1)(3n+1)}{4n-c}\alpha^{(n-c-1)/n}r^{(n-1)/n}\right]. \tag{A.2.3}$$

We note that $\kappa,b,n,Q,\alpha>0$, so the sign of λ_1 at the centreline is

$$\lim_{r\to 0}\operatorname{sgn}(\lambda_1)=\lim_{r\to 0}\operatorname{sgn}\left\{-\mathcal{D}_{\mathrm{t}}^{*}Q'(n-1)\times\left(r^{(2n-c-2)/n}+\frac{(n-1)(3n+1)}{4n-c}\alpha^{(n-c-1)/n}r^{(n-1)/n}\right)\right\}. \tag{A.2.4}$$

When $(n-1)/n<(2n-c-2)/n$, i.e. when $n-c-1>0$ (so $n-1>0$), the sign of λ_1 at the centreline depends on the sign of the coefficient of the term in $r^{(n-1)/n}$ in (A.2.4). Given that $n-1>0$, $r^{(n-1)/n}\to 0$ as $r\to 0$, so $\lambda_1=0$ at the centreline when $n-c-1>0$.

When $(n-1)/n>(2n-c-2)/n$, i.e. when $n-c-1<0$, the sign of λ_1 at the centreline depends on the sign of the coefficient of the term in $r^{(2n-c-2)/n}$ in

(A.2.4), i.e.

$$\lim_{r\to 0}\operatorname{sgn}(\lambda_1)=\lim_{r\to 0}\operatorname{sgn}\left\{(n-1)r^{(2n-c-2)/n}\right\}, \tag{A.2.5}$$

for $\mathcal{D}_{\mathrm{t}}^{*}Q'<0$. When $2n-c-2>0$, $r^{(2n-c-2)/n}\to 0$ as $r\to 0$, so $\lambda_1=0$ at the centreline. When $2n-c-2<0$, the sign of λ_1 at the centreline depends on the sign of the coefficient of the term in $r^{(2n-c-2)/n}$ in (A.2.5):

$$\lim_{r\to 0}\operatorname{sgn}(\lambda_1)=\operatorname{sgn}\left\{n-1\right\}. \tag{A.2.6}$$

So when $n-1<0$ and $2n-c-2<0$, λ_1 is negative at the centreline, and when $n-1>0$ and $2n-c-2<0$, λ_1 is positive at the centreline.

Sign of λ_1 at the centreline in $\mathfrak{R}_{2,1}$

In the weakly advective regime ($\mathcal{D}_{\mathrm{t}}^{*}=0$), the solution for λ_1 (4.1.40) becomes

$$\begin{aligned}\lambda_1=\mathcal{D}_{\mathrm{a}}^{*}\kappa^{(2-b)/b}\frac{3(3n+1)(n-1)}{\pi bn}\frac{Q\alpha'}{\alpha^3}\left(\frac{3n+1}{\pi n}Q\alpha^{-(3n+1)/n}\right)^{2n-c-2}r^{(2n-c-2)/n}\\ \times\left[\frac{1}{n+1}\left(1-\left(\frac{r}{\alpha}\right)^{(n+1)/n}\right)+\frac{(n-1)(3n+1)}{(4n-c)(5n-c+1)}\left(\frac{r}{\alpha}\right)^{(-n+c+1)/n}\right].\end{aligned} \tag{A.2.7}$$

We note that $\kappa,b,n,Q,\alpha>0$, and $r^{(3n-c-1)/n}<r^{(2n-c-2)/n}$ when $0<r\ll 1$, so the sign of λ_1 at the centreline is

$$\begin{aligned}\lim_{r\to 0}\operatorname{sgn}(\lambda_1)=\lim_{r\to 0}\operatorname{sgn}\left\{\mathcal{D}_{\mathrm{a}}^{*}\alpha'(n-1)\left[\frac{1}{n+1}r^{(2n-c-2)/n}\right.\right.\\ \left.\left.+\frac{(n-1)(3n+1)}{(4n-c)(5n-c+1)}r^{(n-1)/n}\alpha^{(n-c-1)/n}\right]\right\}.\end{aligned} \tag{A.2.8}$$

When $(n-1)/n<(2n-c-2)/n$, i.e. when $n-c-1>0$ (so $n-1>0$), the sign of λ_1 at the centreline depends on the sign of the coefficient of the term in $r^{(n-1)/n}$ in (A.2.8). Given that $n-1>0$, $r^{(n-1)/n}\to 0$ as $r\to 0$, so $\lambda_1=0$ at the centreline when $n-c-1>0$.

When $(n-1)/n>(2n-c-2)/n$, i.e. when $n-c-1<0$, the sign of λ_1 at

the centreline depends on the sign of the coefficient of the term in $r^{(2n-c-2)/n}$ in (A.2.8), i.e.

$$\lim_{r\to 0} \operatorname{sgn}(\lambda_1) = \lim_{r\to 0} \operatorname{sgn}\left\{(n-1)r^{(2n-c-2)/n}\right\}, \tag{A.2.9}$$

for $\mathcal{D}^*_{\mathrm{a}}\alpha' > 0$. When $2n-c-2 > 0$, $r^{(2n-c-2)/n} \to 0$ as $r \to 0$, so $\lambda_1 = 0$ at the centreline. When $2n-c-2 < 0$, the sign of λ_1 at the centreline depends on the sign of the coefficient of the term in $r^{(2n-c-2)/n}$ in (A.2.9):

$$\lim_{r\to 0} \operatorname{sgn}(\lambda_1) = \operatorname{sgn}\{n-1\}. \tag{A.2.10}$$

So when $n-1 < 0$ and $2n-c-2 < 0$, λ_1 is negative at the centreline, and when $n-1 > 0$ and $2n-c-2 < 0$, λ_1 is positive at the centreline.

In summary, in decelerating flow in the quickly adjusting regime ($\mathcal{D}^*_{\mathrm{t}}Q' < 0$) and in a widening pipe in the weakly advective regime ($\mathcal{D}^*_{\mathrm{a}}\alpha' > 0$), λ_1 is negative and singular at the centreline for all thixotropic fluids ($n < 1$, $a > c$). In addition, in these regimes λ_1 is positive and singular at the centreline for some antithixotropic fluids ($1 < n < c/2+1$, $c(1-b/2) < a < c$), and zero at the centreline, with a cusp, for the other antithixotropic fluids ($n > c/2+1$, $a < c(1-b/2)$).

Appendix B

MMW model

In this appendix, we present explicit solutions for special cases of the MMW model (Section B.1), and obtain the centreline behaviour (flat, cusp or singularity) of w_1 (Section B.2) and λ_1 (Section B.3) from the centreline asymptotics presented in Sections 4.2.3.1 and 4.2.3.2.

B.1 MMW model with $b = d = 1$

In this section, we obtain solutions for a special case of the MMW model. We are able to find explicit solutions for the leading-order streamwise and transverse velocities, the structure parameter, and the relevant perturbations. From (2.5.6), which we rewrite here for convenience

$$\frac{\lambda_{\mathrm{eq}}^b}{(1-\lambda_{\mathrm{eq}})^d} = \kappa\Gamma^{(c-a)/2}, \tag{B.1.1}$$

we consider the special case in which $b = d = 1$. In this case, (B.1.1), following some rearrangement, becomes

$$\lambda_{\mathrm{eq}} = \frac{\kappa\Gamma^{(c-a)/2}}{1+\kappa\Gamma^{(c-a)/2}} = (\kappa^{-1}\Gamma^{(a-c)/2}+1)^{-1}. \tag{B.1.2}$$

Recalling that the constitutive relation, given by (2.5.4), is

$$\eta = \lambda, \tag{B.1.3}$$

so the leading order momentum equation (3.1.2) becomes

$$\frac{1}{r}\frac{\partial}{\partial r}\left[r\lambda_0\frac{\partial w_0}{\partial r}\right] = -G_0(z,t). \tag{B.1.4}$$

At leading order (B.1.2) is

$$\lambda_0 = \left(\kappa^{-1}\left|\frac{\partial w_0}{\partial r}\right|^{a-c} + 1\right)^{-1}, \tag{B.1.5}$$

so (B.1.4) becomes

$$\frac{1}{r}\frac{\partial}{\partial r}\left[r\left(-\kappa^{-1}\left(\frac{\partial w_0}{\partial r}\right)^{a-c} + 1\right)^{-1}\frac{\partial w_0}{\partial r}\right] = -G_0. \tag{B.1.6}$$

We integrate (B.1.6) with respect to r and rearrange to obtain

$$\left(-\kappa^{-1}\left(\frac{\partial w_0}{\partial r}\right)^{a-c} + 1\right)^{-1}\frac{\partial w_0}{\partial r} = -\frac{G_0 r}{2}, \quad \text{using} \quad \left.\frac{\partial w_0}{\partial r}\right|_{r=0} = 0. \tag{B.1.7}$$

From (B.1.7) we obtain a polynomial equation in terms of $\partial w_0/\partial r$:

$$-\frac{G_0 r}{2\kappa}\left(\frac{\partial w_0}{\partial r}\right)^{a-c} + \frac{\partial w_0}{\partial r} + \frac{G_0 r}{2} = 0. \tag{B.1.8}$$

We can choose a relationship between a and c so that we can solve (B.1.8) to obtain explicit solutions for w_0. We consider $a-c=1$ and $a-c=2$ in Appendices B.1.1 and B.1.3 respectively.

B.1.1 MMW model with $b = d = 1$ and $a - c = 1$

By specialising to $a - c = 1$, (B.1.8) becomes a linear equation in $\partial w_0/\partial r$, the solution of which is

$$\frac{\partial w_0}{\partial r} = \frac{G_0 \kappa r}{G_0 r - 2\kappa}. \tag{B.1.9}$$

Integrating (B.1.9) with respect to r yields the solution for w_0:

$$w_0(r, z, t) = \kappa \left(r - \alpha + \frac{2\kappa}{G_0} \ln \left(\frac{G_0 r - 2\kappa}{G_0 \alpha - 2\kappa} \right) \right), \tag{B.1.10}$$

using the no-slip condition. We note that, as $\kappa > 0$ and $0 \leq r \leq \alpha$, (B.1.10) is only valid for $G_0\alpha - 2\kappa < 0$. Using (B.1.10) with the flux condition (3.1.6) yields

$$Q(t) = 2\pi \int_0^\alpha w_0(r, z, t) r \, \mathrm{d}r = 2\pi \int_0^\alpha \kappa \left(r - \alpha + \frac{2\kappa}{G_0} \ln \left(\frac{G_0 r - 2\kappa}{G_0 \alpha - 2\kappa} \right) \right) r \, \mathrm{d}r. \tag{B.1.11}$$

Evaluating the integral in (B.1.11) yields

$$Q(t) = 2\pi\kappa \left[-\frac{\alpha^3}{6} - \frac{\kappa\alpha^2}{2G_0} - \frac{2\kappa^2\alpha}{G_0^2} + \frac{4\kappa^3}{G_0^3} \ln \left(\frac{2\kappa}{2\kappa - G_0\alpha} \right) \right]. \tag{B.1.12}$$

For a prescribed $Q(t)$, (B.1.12) implicitly defines G_0 in (B.1.10).

Using (B.1.5) and (B.1.9), we find the solution for λ_0:

$$\lambda_0 = 1 - \frac{G_0 r}{2\kappa}. \tag{B.1.13}$$

Using the leading-order mass conservation equation, given by (3.1.1), we obtain the solution for u_0:

$$\begin{aligned} u_0(r, z, t) = \frac{\kappa}{r} \Bigg[& - \left(\frac{G_0 \alpha \alpha_{,z}}{2} + \frac{2\kappa^2 G_{0,z}}{G_0^2} \right) \frac{(\alpha^2 - r^2)}{(G_0\alpha - 2\kappa)} + \frac{6\kappa^2 G_{0,z}}{G_0^3} (\alpha - r) \\ & + \frac{12\kappa^3 G_{0,z}}{G_0^4} \ln \left(\frac{G_0\alpha - 2\kappa}{G_0 r - 2\kappa} \right) - \frac{\kappa G_{0,z}}{G_0^2} \ln \left(\frac{(G_0\alpha - 2\kappa)^{\alpha^2}}{(G_0 r - 2\kappa)^{r^2}} \right) \\ & + \frac{\kappa G_{0,z}}{G_0^2} \left(\frac{1}{2} + \ln(G_0\alpha - 2\kappa) \right) (\alpha^2 - r^2) \Bigg], \end{aligned} \tag{B.1.14}$$

where $G_{0,z}$ is given, via (B.1.12), by

$$G_{0,z} = \frac{\dfrac{G_0^2\alpha^2\alpha'}{2} + \kappa G_0\alpha\alpha' + 2\kappa^2\alpha' - \dfrac{4\kappa^3\alpha'}{2\kappa - G_0\alpha}}{\dfrac{\kappa\alpha^2}{2} + \dfrac{4\kappa^2\alpha}{G_0} + \dfrac{4\kappa^3\alpha}{G_0(2\kappa - G_0\alpha)} - \dfrac{12\kappa^3}{G_0^2}\ln\left(\dfrac{2\kappa}{2\kappa - G_0\alpha}\right)}. \tag{B.1.15}$$

For the solutions for the perturbations, we will also need $G_{0,t}$, which is given, via (B.1.12), by

$$G_{0,t} = \frac{Q'G_0^2}{2\pi\kappa^2}\left[\frac{\alpha^2}{2} + \frac{4\kappa\alpha}{G_0}\left(\frac{3\kappa - G_0\alpha}{2\kappa - G_0\alpha}\right) - \frac{12\kappa^2}{G_0^2}\ln\left(\frac{2\kappa}{2\kappa - G_0\alpha}\right)\right]^{-1}. \tag{B.1.16}$$

We can now find solutions at $\mathcal{O}(\delta)$ in the weakly advective and quickly adjusting regime $\mathfrak{R}_{1,1}$. We require the equations for $A(r,z,t)$ and $B(r,z,t)$, given by (3.3.3) and (3.3.4) respectively, and rewritten here for convenience:

$$A(r,z,t) = \eta_0 + 2\left(\eta_\Gamma - \eta_\lambda\frac{f_\Gamma}{f_\lambda}\right)\left(\frac{\partial w_0}{\partial r}\right)^2, \tag{B.1.17}$$

$$B(r,z,t) = \frac{\eta_\lambda}{f_\lambda}\left[\mathcal{D}_{\mathrm{t}}^*\frac{\partial\lambda_0}{\partial t} + \mathcal{D}_{\mathrm{a}}^*\left(u_0\frac{\partial\lambda_0}{\partial r} + w_0\frac{\partial\lambda_0}{\partial z}\right)\right]\frac{\partial w_0}{\partial r}, \tag{B.1.18}$$

where

$$\eta_\Gamma = 0, \qquad f_\Gamma = -\frac{a}{2}\Gamma_0^{a/2-1}\lambda_0^b + \frac{c}{2}\kappa\Gamma_0^{c/2-1}(1-\lambda_0)^d, \tag{B.1.19}$$

$$\eta_\lambda = 1, \qquad f_\lambda = -b\Gamma_0^{a/2}\lambda_0^{b-1} - d\kappa\Gamma_0^{c/2}(1-\lambda_0)^{d-1}. \tag{B.1.20}$$

Given that $b = d = 1$ and $a - c = 1$, (B.1.19) and (B.1.20) reduce to

$$\eta_\Gamma = 0, \qquad f_\Gamma = -\frac{a}{2}\Gamma_0^{a/2-1}\lambda_0 + \frac{c}{2}\kappa\Gamma_0^{c/2-1}(1-\lambda_0), \tag{B.1.21}$$

$$\eta_\lambda = 1, \qquad f_\lambda = -\Gamma_0^{a/2} - \kappa\Gamma_0^{c/2}. \tag{B.1.22}$$

Using (B.1.21) and (B.1.22) with (B.1.17) we find the equation for $A(r,z,t)$:

$$A(r,z,t) = \left(1 - \frac{G_0 r}{2\kappa}\right)^2. \tag{B.1.23}$$

For $\mathfrak{R}_{1,2}$, using (B.1.21) and (B.1.22) with (B.1.18) we find the equation for $B(r,z,t)$:

$$B(r,z,t) = -\mathcal{D}_{\mathrm{t}}^{*}\frac{G_0 G_{0,t} r^2}{4\kappa^2}\left(\frac{2\kappa - G_0 r}{G_0 \kappa r}\right)^{c}.$$

Using the general solution for w_1, given by (3.3.7), to obtain

$$\begin{aligned} w_1(r,z,t) = {} & \frac{2\kappa^2 G_1}{G_0^2}\left[\ln\left(\frac{G_0\alpha - 2\kappa}{G_0 r - 2\kappa}\right) + \frac{2\kappa G_0(\alpha - r)}{(G_0\alpha - 2\kappa)(G_0 r - 2\kappa)}\right] \\ & - \frac{\mathcal{D}_{\mathrm{t}}^{*} G_0 G_{0,t}}{(\kappa G_0)^c}\int_r^{\alpha(z)}\left(\frac{2\kappa}{r'} - G_0\right)^{c-2}\,\mathrm{d}r'. \end{aligned} \tag{B.1.24}$$

The integral in (B.1.24) can be evaluated for any integer or half-integer $c > 0$.

B.1.2 Comparison with the results of Ahmadpour and Sadeghy

Ahmadpour and Sadeghy [26] (AS) obtained an explicit solution for the streamwise velocity of a Houška fluid in a cylindrical pipe. The structure evolution equation of the Houška model is of the form discussed in Appendix B.1.1, and the constitutive relation of the Houška model can be simplified to that of the MMW model by setting the yield-stress parameters to zero. In this section, we compare AS's model to the full MMW model of the present work, and, upon taking the appropriate asymptotic limits of AS's exact solution for the streamwise velocity (denoted $W(r)$ here), given by (18) in [26], we recover the equivalent solution of the present work, given by (B.1.10).

The solution for the streamwise velocity obtained by AS (18) is given by

$$
\begin{aligned}
W(r) &= \frac{1}{8}(1-r^2) + \frac{1}{2}(r-1)\left(Bn_\infty + \frac{1+S}{Tx}\right) \\
&- \frac{1}{2}\left(\frac{r}{2} - Bn_\infty + \frac{1-S}{Tx}\right) \\
&\times \sqrt{\frac{r^2}{4} + r\left(-Bn_\infty + \frac{1-S}{Tx}\right) + \left[Bn_\infty^2 + \frac{(S+1)^2}{Tx^2} + \frac{2Bn_\infty(1+S) - 4Bn_0}{Tx}\right]} \\
&+ 2\ln\Bigg(- 2Bn_\infty + \frac{2-2S}{Tx} + r \\
&+ 2\sqrt{\frac{r^2}{4} + r\left(-Bn_\infty + \frac{1-S}{Tx}\right) + \left[Bn_\infty^2 + \frac{(S+1)^2}{Tx^2} + \frac{2Bn_\infty(1+S) - 4Bn_0}{Tx}\right]}\Bigg) \\
&\times \left(\frac{Bn_0 - Bn_\infty}{Tx} - \frac{S}{Tx^2}\right) + \frac{1}{2}\left(\frac{1}{2} - Bn_\infty + \frac{1-S}{Tx}\right) \\
&\times \sqrt{\frac{1}{4} + \left(-Bn_\infty + \frac{1-S}{Tx}\right) + \left[Bn_\infty^2 + \frac{(S+1)^2}{Tx^2} + \frac{2Bn_\infty(1+S) - 4Bn_0}{Tx}\right]} \\
&- 2\ln\Bigg(- 2Bn_\infty + \frac{2-2S}{Tx} + 1 \\
&+ 2\sqrt{\frac{1}{4} + \left(-Bn_\infty + \frac{1-S}{Tx}\right) + \left[Bn_\infty^2 + \frac{(S+1)^2}{Tx^2} + \frac{2Bn_\infty(1+S) - 4Bn_0}{Tx}\right]}\Bigg) \\
&\times \left(\frac{Bn_0 - Bn_\infty}{Tx} - \frac{S}{Tx^2}\right),
\end{aligned}
\tag{B.1.25}
$$

where $Bn_0 \propto \tau_{y,0}$ and $Bn_\infty \propto \tau_{y,\infty}$ are Bingham numbers, $S \propto 1/\eta_\infty$ is a viscosity number, and $Tx \propto 1/\eta_\infty$ is the Thixotropy number of Wachs et al. [46].

We simplify the Houška model, as presented by AS, to obtain a special case of the MMW model in the present work. In particular, we set $a = \kappa = 1$, $b = 1$, and $m = 1$ in (3) of AS to obtain the structure evolution equation of the MMW model with $a = b = d = 1$ and $c = 0$ (equation (4.2.1), where $\Gamma = \dot{\gamma}^2$):

$$
\frac{\mathrm{d}\lambda}{\mathrm{d}t} = -\dot{\gamma}\lambda + (1-\lambda). \tag{B.1.26}
$$

We also set the yield stress parameters $\tau_{y,\infty} = \tau_{y,0} = 0$, the high-shear viscosity

$\eta_\infty = 0$, the low-shear viscosity $\eta_0 = 1$, and $n = 1$ in (2) of AS to obtain the constitutive relation of the MMW model:

$$\tau = \lambda\dot{\gamma}. \tag{B.1.27}$$

Following the model simplification, the Bingham numbers become $Bn_0 = Bn_\infty = 0$ and the viscosity parameter $\eta_0 = 1$ in (B.1.25). We note from AS that now $S = 1/\eta_\infty$ and $T = G/\eta_\infty$, where G is the imposed pressure gradient of AS and, for presentational clarity, $T \equiv Tx$, so we set $S = T/G$, where $G = \mathcal{O}(1)$. Now, after simplification, (B.1.25) yields

$$\begin{aligned} W(r) = \frac{1}{8}(1-r^2) + \frac{1}{2}(r-1)\left(\frac{1}{T}+\frac{1}{G}\right) \\ - \frac{1}{2}\left(\frac{r}{2}+\frac{1}{T}-\frac{1}{G}\right) sq(r) + \frac{1}{2}\left(\frac{1}{2}+\frac{1}{T}-\frac{1}{G}\right) sq(1) \\ - 2\ln\left(\frac{\frac{2}{T}-\frac{2}{G}+r+2sq(r)}{\frac{2}{T}-\frac{2}{G}+1+2sq(1)}\right)\frac{1}{GT}, \end{aligned} \tag{B.1.28}$$

where

$$sq(r) = \sqrt{\frac{r^2}{4} + r\left(\frac{1}{T}-\frac{1}{G}\right) + \frac{1}{G^2} + \frac{2}{GT} + \frac{1}{T^2}}. \tag{B.1.29}$$

We consider the limit $\eta_\infty \to 0$, so $T \to \infty$. Following an asymptotic expansion of (B.1.28) in powers of $1/T$, we obtain the terms $\sqrt{(2/G-r)^2}/(2/G-r)$ and $\sqrt{(2/G-1)^2}/(2/G-1)$ (where $0 \le r \le 1$). Taking $2/G - 1 > 0$ (so $G - 2 < 0$, as required in (B.1.10)), we obtain

$$W(r) = \frac{1}{T}\left(r - 1 + \frac{2}{G}\ln\left(\frac{Gr-2}{G-2}\right)\right) + \mathcal{O}\left(\frac{1}{T^2}\right), \tag{B.1.30}$$

where terms at $\mathcal{O}(1)$ cancel to zero. Hence by scaling $W(r)$ via $\hat{W}(r) = W(r)T$ in (B.1.30), we obtain

$$\hat{W}(r) = r - 1 + \frac{2}{G}\ln\left(\frac{Gr-2}{G-2}\right) + \mathcal{O}\left(\frac{1}{T}\right). \tag{B.1.31}$$

Now (B.1.31) agrees with (B.1.10), after setting $\kappa = 1$ and $\alpha = 1$:

$$w_0 = r - 1 + \frac{2}{G_0} \ln\left(\frac{G_0 r - 2}{G_0 - 2}\right), \tag{B.1.32}$$

as required.

B.1.3 MMW model with $b = d = 1$ and $a - c = 2$

By specialising to $a - c = 2$, (B.1.8) becomes a quadratic equation in $\partial w_0/\partial r$, the solutions of which are

$$\frac{\partial w_0}{\partial r} = \frac{1}{G_0 r}\left(\kappa + \sqrt{\kappa(G_0^2 r^2 + \kappa)}\right), \tag{B.1.33}$$

$$\frac{\partial w_0}{\partial r} = \frac{1}{G_0 r}\left(\kappa - \sqrt{\kappa(G_0^2 r^2 + \kappa)}\right). \tag{B.1.34}$$

By integrating these with respect to r we obtain

$$w_0 = \frac{1}{G_0}\sqrt{\kappa\left(G_0^2 r'^2 + \kappa\right)} - \frac{\kappa}{G_0} \ln\left(\frac{2\kappa^2 + 2\kappa\sqrt{\kappa(G_0^2 r'^2 + \kappa)}}{r'^2}\right)\Bigg|_r^\alpha, \tag{B.1.35}$$

$$w_0 = -\frac{1}{G_0}\sqrt{\kappa\left(G_0^2 r'^2 + \kappa\right)} + \frac{\kappa}{G_0} \ln\left(2\kappa^2 + 2\kappa\sqrt{\kappa(G_0^2 r'^2 + \kappa)}\right)\Bigg|_r^\alpha, \tag{B.1.36}$$

respectively.

B.2 Behaviour of w_1 at the centreline

The centreline behaviour of w_1 for thixotropic fluids is determined by the relative sizes of the exponents in the terms in

$$r^2 \quad \text{and} \quad r^{2\zeta - a + 2} \tag{B.2.1}$$

in (4.2.26). When $2 < 2\zeta - a + 2$, the first term in (4.2.26) dominates as $r \to 0$. In this case, $\partial w_1/\partial r$ contains only terms in r with positive exponents, which are r and $r^{2\zeta - a + 1}$, so $\partial w_1/\partial r \to 0$ as $r \to 0$ and w_1 is flat at the centreline. When

$2 > 2\zeta - a + 2$, the second term in (4.2.26) dominates as $r \to 0$. In this case, when $2\zeta - a + 2 > 1$, $\partial w_1/\partial r \to 0$ as $r \to 0$, so w_1 is flat at the centreline. When $0 < 2\zeta - a + 2 < 1$, $\partial w_1/\partial r$ diverges as $r \to 0$ but w_1 remains finite as $r \to 0$, so w_1 has a cusp at the centreline. When $2\zeta - a + 2 < 0$, $\partial w_1/\partial r$ and w_1 diverge as $r \to 0$, so w_1 is singular at the centreline. For the expansion scheme to be valid we require the flux condition (3.1.12) to be satisfied, i.e. we require rw_1 to be integrable. The flux condition is satisfied when $2\zeta - a + 2 > -2$, i.e. when $2\zeta - a + 4 > 0$.

The centreline behaviour of w_1 for antithixotropic fluids is determined by the relative sizes of the exponents in the terms in

$$r^{(n+1)/n} \quad \text{and} \quad r^{(2n-c)/n} \tag{B.2.2}$$

in (4.2.49). When $(n+1)/n < (2n-c)/n$, i.e. when $n > c+1$, the first term in (4.2.49) dominates as $r \to 0$. In this case, $\partial w_1/\partial r$ contains only terms in r with positive exponents, which are $r^{1/n}$ and $r^{(n-c)/n}$, so $\partial w_1/\partial r \to 0$ as $r \to 0$ and w_1 is flat at the centreline. When $(n+1)/n > (2n-c)/n$, i.e. when $n < c+1$, the second term in (4.2.49) dominates as $r \to 0$. In this case, when $(2n-c)/n > 1$, i.e. when $c < n < c+1$, $\partial w_1/\partial r \to 0$ as $r \to 0$, so w_1 is flat at the centreline. When $0 < (2n-c)/n < 1$, i.e. when $c/2 < n < c$, $\partial w_1/\partial r$ diverges as $r \to 0$ but w_1 remains finite as $r \to 0$, so w_1 has a cusp at the centreline. When $(2n-c)/n < 0$, i.e. when $n < c/2$, $\partial w_1/\partial r$ and w_1 diverge as $r \to 0$, so w_1 is singular at the centreline. For the expansion scheme to be valid we require the flux condition (3.1.12) to hold, i.e. we require rw_1 to be integrable. The flux condition is satisfied when $(2n-c)/n > -2$, i.e. when $n > c/4$. We note that these regions of centreline behaviour are identical to those for antithixotropic fluids when $d = 0$.

B.3 Behaviour of λ_1 at the centreline

The centreline behaviour of λ_1 for thixotropic fluids is determined by the size of the exponent in the term in $r^{2\zeta-a}$ in equation (4.2.30). When $2\zeta - a > 1$, $\partial\lambda_1/\partial r \to 0$ as $r \to 0$, so λ_1 is flat at the centreline. When $0 < 2\zeta - a < 1$,

$\partial\lambda_1/\partial r$ diverges as $r \to 0$ but λ_1 remains finite as $r \to 0$, so λ_1 has a cusp at the centreline. When $2\zeta - a < 0$, $\partial\lambda_1/\partial r$ and λ_1 diverge as $r \to 0$, so λ_1 is singular at the centreline.

The centreline behaviour of λ_1 for antithixotropic fluids is determined by the relative sizes of the exponents in the terms in

$$r^{(n-1)/n} \quad \text{and} \quad r^{(2n-c-2)/n} \tag{B.3.1}$$

in (4.2.50). We note that $\partial\lambda_1/\partial r$ contains a term in $r^{-1/n}$ and so $\partial\lambda_1/\partial r$ always diverges as $r \to 0$. When $(n-1)/n < (2n-c-2)/n$, i.e. when $n > c+1$, the first term in (4.2.50) dominates as $r \to 0$. In this case, $\lambda_1 \to 0$ as $r \to 0$ because $n - 1 > 0$ for antithixotropic fluids, and λ_1 has a cusp at the centreline. When $(n-1)/n > (2n-c-2)/n$, i.e. when $n < c+1$, the second term in (4.2.50) dominates as $r \to 0$. In this case, when $(2n-c-2)/n > 0$, λ_1 is singular at the centreline. When $(2n-c-2)/n < 0$, $\lambda_1 \to 0$ as $r \to 0$ and λ_1 has a cusp at the centreline.

Bibliography

[1] R. I. Tanner. *Engineering Rheology*. Oxford University Press, 2nd edition, 1985. ISBN 9780198564737.

[2] H. A. Barnes, J. F. Hutton, and K. Walters. *An Introduction to Rheology*. Elsevier, 1st edition, 1989. ISBN 0444874690.

[3] H. A. Barnes. Thixotropy — a review. *Journal of Non-Newtonian Fluid Mechanics*, 70(1–2):1–33, 1997.

[4] R. G. Larson. *The Structure and Rheology of Complex Fluids*. Oxford University Press, 1st edition, 1999. ISBN 9780195121971.

[5] P. Štern, H. Valentová, and J. Pokorný. Rheological properties and sensory texture of mayonnaise. *European Journal of Lipid Science and Technology*, 103(1):23–28, 2001.

[6] R. Cross. Elastic and viscous properties of silly putty. *American Journal of Physics*, 80:870–875, 2012.

[7] J. Mewis and N. J. Wagner. Thixotropy. *Advances in Colloid and Interface Science*, 147–148:214–227, 2009.

[8] P. Bottiglieri, F. de Sio, G. Fasanaro, G. Mojoli, M. Impembo, and D. Castaldo. Rheological characterization of ketchup. *Journal of Food Quality*, 14:497–512, 1991.

[9] G. Ovarlez, L. Tocquer, F. Bertrand, and P. Coussot. Rheopexy and tunable yield stress of carbon black suspensions. *Soft Matter*, 9(23):5540–5549, 2013.

[10] M. Houška and R. Žitný. Dynamics of Thixotropic Liquids and Time Dependency. In J. Ahmed, P. Ptaszek, and S. Basu, editors, *Advances in Food Rheology and Its Applications*, chapter 3, pages 47–63. Woodhead Publishing, 2017.

[11] R. H. Ewoldt and G. H. McKinley. Mapping thixo-elasto-visco-plastic behavior. *Rheologica Acta*, 56:195–210, 2017.

[12] P. R. de Souza Mendes and R. L. Thompson. A critical overview of elasto-viscoplastic thixotropic modeling. *Journal of Non-Newtonian Fluid Mechanics*, 187–188:8–15, 2012.

[13] J. A. Svendsen. Mathematical modeling of wax deposition in oil pipeline systems. *AIChE Journal*, 39(8):1377–1388, 1993.

[14] A. P. Szilas, E. Bobok, and L. Navratil. Determination of turbulent pressure loss of non-Newtonian oil flow in rough pipes. *Rheologica Acta*, 20(5):487–496, 1981.

[15] Q. D. Nguyen and D. V. Boger. Measuring the flow properties of yield stress fluids. *Annual Review of Fluid Mechanics*, 24:47–88, 1992.

[16] A. Marquez, J. Quijano, and M. Gaulin. A calibration technique to evaluate the power-law parameters of polymer melts using a torque-rheometer. *Polymer Engineering and Science*, 36:2556–2563, 1996.

[17] M. J. Crochet, A. D. Davies, and K. Walters. *Numerical Simulation of Non-Newtonian Flow, Volume 1.* Elsevier, 1984. ISBN 9780444598554.

[18] S. J. Hahn, T. Ree, and H. Eyring. Flow mechanism of thixotropic substances. *Industrial and Engineering Chemistry,*, 51:856–857, 1959.

[19] N. J. Balmforth and R. V. Craster. Geophysical aspects of non-Newtonian fluid mechanics. In N. J. Balmforth and A. Provenzale, editors, *Geomorphological Fluid Mechanics*, chapter 2, pages 34–51. Springer, 2001.

[20] J. Mewis and N. J. Wagner. Current trends in suspension rheology. *Journal of Non-Newtonian Fluid Mechanics*, 3:147–150, 2009.

[21] J. W. Swan, R. N. Zia, and J. F. Brady. Large amplitude oscillatory microrheology. *Journal of Rheology*, 58:1–41, 2014.

[22] D. R. Hewitt and N. J. Balmforth. Thixotropic gravity currents. *Journal of Fluid Mechanics*, 727:56–82, 2013.

[23] A. Ahmadpour, K. Sadeghy, and S.-R. Maddah-Sadatieh. The effect of a variable plastic viscosity on the restart problem of pipelines filled with gelled waxy crude oils. *Journal of Non-Newtonian Fluid Mechanics*, 205:16–27, 2014.

[24] T. G. Myers. Application of non-Newtonian models to thin film flow. *Physical Review E*, 72(6):066302, 2005.

[25] S. Matsuhisa and R. B. Bird. Analytical and numerical solutions for laminar flow of the non-Newtonian Ellis fluid. *AIChE Journal*, 11(4):588–595, 1965.

[26] A. Ahmadpour and K. Sadeghy. An exact solution for laminar, unidirectional flow of Houska thixotropic fluids in a circular pipe. *Journal of Non-Newtonian Fluid Mechanics*, 194:23–31, 2013.

[27] M. Renardy and T. Wang. Development of shear bands for a model of a thixotropic yield stress fluid. *Journal of Non-Newtonian Fluid Mechanics*, 233:5–12, 2016.

[28] A. Ahmadpour and K. Sadeghy. Start-up flows of Dullaert–Mewis viscoplastic-thixoelastic fluids: A two-dimensional analysis. *Journal of Non-Newtonian Fluid Mechanics*, 197:1–17, 2014.

[29] D. Pritchard, S. K. Wilson, and C. R. McArdle. Flow of a thixotropic or antithixotropic fluid in a slowly varying channel: the weakly advective regime. *Journal of Non-Newtonian Fluid Mechanics*, 238:140–157, 2016.

[30] H. A. Ardakani, E. Mitsoulis, and S. G. Hatzikiriakosa. Thixotropic flow of toothpaste through extrusion dies. *Journal of Non-Newtonian Fluid Mechanics*, 166(21–22):1262–1271, 2011.

[31] J. J. Derksen and Prashant. Simulations of complex flow of thixotropic liquids. *Journal of Non-Newtonian Fluid Mechanics*, 160(2–3):65–75, 2009.

[32] E. W. Williams and S. H. Javadpour. The flow of an elasto-viscous liquid in an axisymmetric pipe of slowly varying cross-section. *Journal of Non-Newtonian Fluid Mechanics*, 7:171–188, 1980.

[33] S. Nezamidoost and K. Sadeghy. Peristaltic pumping of thixotropic fluids: a numerical study. *Journal of Society of Rheology, Japan*, 40:1–9, 2012.

[34] S. Nezamidoost, K. Sadeghy, and V. Askari. Pulsatile flow of thixotropic fluids through a partially-constricted tube. *Journal of Society of Rheology, Japan*, 41:45–52, 2013.

[35] A. S. Uppal, R. V. Craster, and O. K. Matar. Dynamics of spreading thixotropic droplets. *Journal of Non-Newtonian Fluid Mechanics*, 240:1–14, 2017.

[36] C. M. Oishi, R. L. Thompson, and F. P. Martins. Transient motions of elasto-viscoplastic thixotropic materials subjected to an imposed stress field and to stress-based free-surface boundary conditions. *International Journal of Engineering Science*, 109:165–201, 2016.

[37] P. Coussot, N. Roussel, and H. Chanson. Continuous or catastrophic solid-liquid transition in jammed systems. *Physics of Fluids*, 17:011704, 2005.

[38] D. J. Acheson. *Elementary Fluid Dynamics*. Clarendon Press, 2nd edition, 1990. ISBN 9780198596790.

[39] O. Reynolds. On the theory of lubrication and its application to Mr. Beauchamp Tower's experiments, including an experimental determination of the viscosity of olive oil. *Philosophical Transactions of the Royal Society of London*, 177:157–234, 1886.

[40] V. A. Gorodstov. Spreading of a film of nonlinearly viscous liquid over a horizontal smooth solid surface. *Journal of Engineering Physics*, 57(2):879–884, 1988.

[41] N. J. Balmforth and R. V. Craster. A consistent thin-layer theory for Bingham plastics. *Journal of Non-Newtonian Fluid Mechanics*, 84(1):65–81, 1999.

[42] A. B. Ross, S. K. Wilson, and B. R. Duffy. Thin-film flow of a viscoplastic material round a large horizontal stationary or rotating cylinder. *Journal of Fluid Mechanics*, 430:309–333, 2001.

[43] I. A. Frigaard and D. P. Ryan. Flow of a visco-plastic fluid in a channel of slowly varying width. *Journal of Non-Newtonian Fluid Mechanics*, 123(1): 67–83, 2004.

[44] S. K. Wilson, B. R. Duffy, and A. B. Ross. On the gravity-driven draining of a rivulet of a viscoplastic material down a slowly varying substrate. *Physics of Fluids*, 14:555–571, 2002.

[45] A Putz, I. A. Frigaard, and D. M. Martinez. On the lubrication paradox and the use of regularisation methods for lubrication flows. *Journal of Non-Newtonian Fluid Mechanics*, 163(1–3):62–77, 2009.

[46] A. Wachs, G. Vinay, and I. Frigaard. A 1.5D numerical model for the start up of weakly compressible flow of a viscoplastic and thixotropic fluid in pipelines. *Journal of Non-Newtonian Fluid Mechanics*, 159(1–3):81–94, 2009.

[47] C. Ancey. Plasticity and geophysical flows: A review. *Journal of Non-Newtonian Fluid Mechanics*, 142(1–3):4–35, 2007.

[48] A. Khaldoun, P. Moller, A. Fall, G. Wegdam, B. Leeuw, Y. Méheust, J. O. Fossum, and D. Bonn. Quick clay and landslides of clayey soils. *Physics of Fluids*, 103:188301, 2009.

[49] A. Oron, S. H. Davis, and S. G. Bankoff. Long-scale evolution of thin liquid films. *Reviews of Modern Physics*, 69(3):931–980, 1997.

[50] R. V. Craster and O. K. Matar. Dynamics and stability of thin liquid films. *Reviews of Modern Physics*, 81(3):1131–1198, 2009.

[51] P. R. de Souza Mendes and E. S. S. Dutra. Viscosity function for yield-stress liquids. *Applied Rheology*, 14(6):296–302, 2004.

[52] E. Tibäck, M. Langton, J. Oliveira, and L. Ahrné. Mathematical modeling of the viscosity of tomato, broccoli and carrot purees under dynamic conditions. *Journal of Food Engineering*, 124:35–42, 2014.

[53] S. Livescu. Mathematical modeling of thixotropic drilling mud and crude oil flow in wells and pipelines — a review. *Journal of Petroleum Science and Engineering*, 98–99:174–184, 2012.

[54] Comsol multiphysics® v. 5.2a. URL `www.comsol.com`.

[55] P. Coussot, Q. D. Nguyen, H. T. Huynh, and D. Bonn. Avalanche behaviour in yield stress fluids. *Physical Review Letters*, 88(17):175501, 2002.

[56] H. A. Barnes and K. Walters. The yield stress myth? *Rheologica Acta*, 24: 323–326, 1985.

[57] M. Renardy. The mathematics of myth: Yield stress behaviour as a limit of non-monotone constitutive theories. *Journal of Non-Newtonian Fluid Mechanics*, 165:519–526, 2010.

[58] T. C. Papanastasiou. Flows of materials with yield. *Journal of Rheology*, 31 (5):385–404, 1987.

[59] D. D. Joseph. *Fluid Dynamics of Viscoelastic Liquids*. Springer, 1st edition, 1990. ISBN 3540971556.

[60] R. G. Larson. Constitutive equations for thixotropic fluids. *Journal of Rheology*, 59(3):595–611, 2015.

[61] P. Moller, A. Fall, V. Chikkadi, D. Derks, and D. Bonn. An attempt to categorize yield stress fluid behaviour. *Philosophical Transactions of the Royal Society A*, 367:5139–5155, 2009.

[62] A. C. Pipkin. *Lectures on Viscoelastic Theory*. Springer, 2nd edition, 1982. ISBN 9780387963457.

[63] M. Renardy and Y. Renardy. Thixotropy in yield stress fluids as a limit of viscoelasticity. *IMA Journal of Applied Mathematics*, 81:522–537, 2016.

[64] A. Mujumbar, A. N. Beris, and A. B. Metzner. Transient phenomena in thixotropic systems. *Journal of Non-Newtonian Fluid Mechanics*, 102:157–178, 2002.

[65] K. L. Pinder. Time dependent rheology of the tetrahydrofuran-hydrogen sulphide gas hydrate slurry. *The Canadian Journal of Chemical Engineering*, 42(3):132–138, 1964.

[66] M. Houška. *Inženýrské aspekty reologie tixotropních kapalin [Engineering aspects of the rheology of thixotropic fluids]*. PhD thesis, České vysoké učení technické v Praze [Czech Technical University in Prague], 1980.

[67] J. Billingham and J. W. J. Ferguson. Laminar, unidirectional flow of a thixotropic fluid in a circular pipe. *Journal of Non-Newtonian Fluid Mechanics*, 47:21–55, 1993.

[68] K. Dullaert and J. Mewis. A structural kinetics model for thixotropy. *Journal of Non-Newtonian Fluid Mechanics*, 139:21–30, 2006.

[69] P. R. de Souza Mendes. Modeling the thixotropic behaviour of structured fluids. *Journal of Non-Newtonian Fluid Mechanics*, 164:66–75, 2009.

[70] P. R. de Souza Mendes. Thixotropic elasto-viscoplastic model for structured fluids. *Soft Matter*, 7:2471–2483, 2011.

[71] P. R. de Souza Mendes and R. L. Thompson. A unified approach to model elasto-viscoplastic thixotropic yield-stress materials and apparent yield-stress fluids. *Rheologica Acta*, 52:673–694, 2013.

[72] P. Coussot, Q. D. Nguyen, H. T. Huynh, and D. Bonn. Viscosity bifurcation in thixotropic, yielding fluids. *Journal of Rheology*, 46:573–589, 2002.

[73] J. Diani, B. Fayolle, and P. Gilormini. A review on the Mullins effect. *European Polymer Journal*, 45:601–612, 2009.

[74] R. G. Larson. A constitutive equations for polymer melts based on partially extending strand convection. *Journal of Rheology*, 28:545–571, 1984.

[75] G. Ovarlez, S. Rodts, X. Chateau, and P. Coussot. Phenomenology and physical origin of shear localization and shear banding in complex fluids. *Rheologica Acta*, 48(8):831–844, 2009.

[76] P. D. Olmstead. Perspectives on shear banding in complex fluids. *Rheologica Acta*, 47(3):283–300, 2008.

[77] C.-H. Jeon and B. R. Hodges. Comparing thixotropic and herschel–bulkley parameterizations for continuum models of avalanches and subaqueous debris flows. *Natural Hazards and Earth System Sciences*, 42:303–319, 2018.

[78] P. D. Patel and W. B. Russel. A mean field theory for the rheology of phase separated or flocculated dispersions. *Colloids and Surfaces*, 31:355–383, 1988.

[79] S. K. Wilson, B. R. Duffy, and R. Hunt. A slender rivulet of a power-law fluid driven by either gravity or a constant shear stress at the free surface. *The Quarterly Journal of Mechanics and Applied Mathematics*, 55(3):385–408, 2002.

[80] Y. M. Yatim, S. K. Wilson, and B. R. Duffy. Unsteady gravity-driven slender rivulets of a power-law fluid. *Journal of Non-Newtonian Fluid Mechanics*, 165(21–22):1423–1430, 2010.

[81] F. H. H. Al Mukahal, B. R. Duffy, and S. K. Wilson. A rivulet of power-law fluid with constant contact angle draining down a slowly varying substrate. *Physics of Fluids*, 27:052101, 2015.

[82] F. H. H. Al Mukahal, S. K. Wilson, and B. R. Duffy. A rivulet of power-law fluid with constant width draining down a slowly varying substrate. *Journal of Non-Newtonian Fluid Mechanics*, 224:30–39, 2015.

[83] S. D. R. Wilson. A note on thin-layer theory for Bingham plastics. *Journal of Non-Newtonian Fluid Mechanics*, 85:29–33, 1998.

[84] D. Pritchard, B. R. Duffy, and S. K. Wilson. Shallow flows of generalised Newtonian fluids on an inclined plane. *Journal of Engineering Mathematics*, 94:115–133, 2015.

[85] R. R. Huilgol. *Fluid Mechanics of Viscoplasticity*. Springer, 1st edition, 2015. ISBN 9783662456163.

[86] J. R. A. Pearson and P. M. J. Tardy. Models for flow of non-Newtonian and complex fluids through porous media. *Journal of Non-Newtonian Fluid Mechanics*, 102:447–473, 2002.

[87] H. Chanson, S. Jarny, and P. Coussot. Dam break wave of thixotropic fluid. *Journal of Hydraulic Engineering*, 132(3):280–293, 2006.

[88] D. Pritchard and J. R. A. Pearson. Viscous fingering of a thixotropic fluid in a porous medium or a narrow fracture. *Journal of Non-Newtonian Fluid Mechanics*, 135(2–3):117–127, 2006.

[89] F. Bautista, J. F. de Santos, J. E. Puig, and O. Manero. Understanding thixotropic and antithixotropic behavior of viscoelastic micellar solutions and liquid crystalline dispersions. I. The model. *Journal of Non-Newtonian Fluid Mechanics*, 80(2–3):93–113, 1999.

[90] S. Livescu, R. V. Roy, and L. W. Schwartz. Leveling of thixotropic liquids. *Journal of Non-Newtonian Fluid Mechanics*, 166(7–8):395–403, 2011.

[91] F. Moore. The rheology of ceramic slips and bodies. *Transactions of the British Ceramic Society*, 58:470–494, 1959.

[92] K. Dullaert and J. Mewis. Thixotropy: Build-up and breakdown curves during flow. *Journal of Rheology*, 49(6).

[93] E. S. Boek, J. T. Padding, V. J. Anderson, P. M. J. Tardy, J. P. Crawshaw, and J. R. A. Pearson. Constitutive equations for extensional flow of wormlike micelles: stability analysis of the Bautista–Manero model. *Journal of Non-Newtonian Fluid Mechanics*, 126(1):39–46, 2005.

[94] C. R. McArdle, D. Pritchard, and S. K. Wilson. The Stokes boundary layer for a thixotropic or antithixotropic fluid. *Journal of Non-Newtonian Fluid Mechanics*, 185–186:18–38, 2012.

[95] A. I. Croudace, D. Pritchard, and S. K. Wilson. Unsteady flow of a thixotropic fluid in a slowly varying pipe. *Physics of Fluids*, 29:083103, 2017.

[96] W. H. Herschel and R. Bulkley. Konsistenzmessungen von Gummi-Benzollösungen. *Kolloid-Zeitschrift*, 39(4):291–300, 1926.

[97] W. Huang and R. D. Russell. *Adaptive moving mesh methods*. Springer Science & Business Media, 2011. ISBN 978-1441979155.